Clock with 8×10^{-19} systematic uncertainty

by

Alexander Gerald Aeppli

B.A., Carleton College, 2018

M.S., University of Colorado Boulder, 2022

A thesis submitted to the

Faculty of the Graduate School of the

University of Colorado in partial fulfillment

of the requirements for the degree of

Doctor of Philosophy

Department of Physics

2025

Committee Members:

Jun Ye, Chair

Andrew Ludlow

Ana María Rey

Adam Kaufman

Penina Axelrad

Aeppli, Alexander Gerald (Ph.D., Physics)

Clock with 8×10^{-19} systematic uncertainty

Thesis directed by Professor Jun Ye

Optical atomic clocks have revolutionized time keeping, leading to the most accurate and precise measurements that humankind has ever made. The work in this thesis builds upon years of progress to construct the most accurate clock to date. Strontium atoms are trapped in a one-dimensional (1D) optical lattice formed within an in-vacuum build up cavity oriented along gravity. We probe the ultra-narrow, environmentally insensitive $5s^2\ {}^1S_0 \rightarrow 5s5p\ {}^3P_0$ electronic transition with a laser based upon a single-crystal silicon resonator. To build the best atomic clock, we need precise quantum control of the atoms as well as comprehensive stabilization of systematic shifts. We discuss how in-situ imaging allows us to measure frequency gradients within an atomic sample, including determining the gravitation redshift over less than a millimeter [22]. Through precision spectroscopy, we characterize the motional states of the atoms. In a tilted 1D optical lattice, atoms occupy Wannier-Stark external wavefunctions. Tuning the wavefunction using a "magic depth," we realize a density shift cancellation, allowing us to operate with 10^5 atoms with a negligible density shift [1]. Under strong interactions, an dynamical phase transition appears during a Rabi drive. We understand and tame the lattice light shift through a comprehensive campaign modulating the lattice depth, frequency, and external wavefunction [70]. We reduce the uncertainty in the largest systematic shift in room temperature Sr clocks, the black body radiation shift, by remeasuring the atomic response function and carefully determining the radiant temperature [2]. Other systematic shifts have much smaller uncertainties, and all together we achieve a systematic uncertainty of 8.1×10^{-19} in fractional frequency units–the lowest of any clock to date [2]. Lastly, we discuss recent work to push the strontium clock into new regimes. We reduce both the laser and atomic instability, mapping out the coherence limitations of both systems. We can combine atom interferometry techniques with optical clock techniques to realize a system that combines classical and relativistic geodesy

tools. Ongoing frequency comparisons with optical clocks at NIST allow us to test the veracity of our systematic uncertainty, perhaps aiding in the redefinition of the SI second.

Dedication

To my family.

Acknowledgements

In my first spring in Boulder, I decided to plant a small vegetable garden outside my residence on Elm Ave. Shortly after the tomatoes were in the ground, a few hard frosts and a small May snow storm decimated the poor plants. While the hardy kale survived and provided tough, leafy greens for a few years, the tomato plants were rather unhappy. Yet one plant persisted and eventually produced two small tomatoes by the early fall. Not super tasty, but real tomatoes nontheless.

My journey in physics would not have been nearly as enjoyable without so many wonderful people. Excellent science teachers in middle and high school started me down this path. The wonderful physics department at Carleton College solidified my love for the subject. Eric Hazlett first introduced me to experimental atomic physics, planting a seed that has continued to grow. Another formative experience was in Rob Scholten's lab at the University of Melbourne, working closely with Alex Wood, an amazing mentor. These few months solidified my desire to continue studying atomic physics in grad school.

The first time I met Jun was in April of 2018 during an visit weekend at CU. I was struck by his passion for physics, as well as his freindliness and humanity. When he offered me a spot in his lab, my grad school decision became an easy one. In the seven years following our first meeting, Jun has been a remarkable advisor. Through his guidance, support, teaching, and pushing, he has helped me become the best physicist I could be. I am still in awe of how Jun can lead multiple fields of physics: from frequency metrology to ultracold molecules, every experiment in his lab is world class.

I first joined the Stark decelerator experiment with Dave Reens, Hao Wu, Piotr Wcisło, and Anna McAuliffe. I was later join by post doc Lee Liu, who became a close friend and mentor. While

this experiment was perhaps not the most fruitful, it did result in two publications [124, 149]. More importantly, I learned an immense amount of physics and experiment techniques from this wonderful team. In the summer of 2020, I moved a few rooms north into S1B60, joining Toby Bothwell and Colin Kennedy on the recently rebuilt strontium clock. These two soon became good friends and teachers. Toby's dogs Heidi and Luna were excellent companions. I was joined in the fall of 2021 by Kyungtae Kim. In the past four years, Kyungtae has been an irreplaceable part of my PhD, helping me grow as a researcher with his constant support and guidance. Will Warfield joined in 2022, and I am supremely confident in his ability to lead the Sr clock into the next frontier. We have been joined by other excellent students including John, Melanie, Aidan, and Kai. I have had the pleasure of working closely with Ana Maria Rey's group and her excellent student Anjun and post doc David. Marianna Safronova has also been a close collaborator, lending her atomic wisdom.

I have also had the pleasure of working with a number of wonderful folks elsewhere in the Ye group. On the other side of S1B60, the Sr2 team made a number of breakthroughs on their 3D optical lattice clock during my time in lab. Lindsay Sonderhouse, Christian Sanner, Ross Hutson, Lingfeng Yan, Stefan Lannig, Max Frankel, and Yu Hyun Lee have all been wonderful presences. Will Milner is a close friend, with whom I've explored both physics and the bars in Boulder. The Sr3 team has made remarkable progress realizing a spin-squeezed strontium optical lattice clock. I have learned much from Maya Miklos, Yee Ming Tso, John Robinson, Benedikt Heizenreder, Yang Yang, Joonseok Hur, and Stella Kraus. The stable lasers team ensured we always had the best laser in the world, and I learned a lot about laser stabilization from Dhruv Kedar, Eric Oelker, Alex Staron, Zhibin Yao, Ben Lewis, Zoey Hu, and Dahyeon Lee. Outside of the Sr group, others in the Ye lab have had a profound impact on my time in JILA. Jack, Tian, Chuankun, Jake, Lars on XUV, Qizhong, Apoorva, Jutta, Lee (after our time on OH) on MIR. Kameron and Justin have been good fiends on the molecule side of the lab. Mengjie, Logan, Simon, Parul, Shiqian, Yewei, Ian, also on YO, were always great to talk with. When I first joined the lab, I got to know the 2018 iteration of KRb well, including Luigi, Giacomo, Kyle, and Will. Later important additions include Jun-Ru, Cal, Junyu, Tim, and Phil. Annie and Stephen were always a joy.

Elsewhere in JILA, the wonderful community has supported my research and mental wellbeing! Will and Dylan were early friends and officemates at JILA. Eric, Nelson, Yuval, and many more JILAns have been friends, mentors, and collaborators. The JILA staff are a truly special part of this institution. The machine shop had a large part in building much of what is reported in this document, and my PhD would not have been possible without their hard work. Hans, James, Calvin, Adam, Todd, Kim, and Kyle have all had hands in my PhD in addition to being great people to talk with and learn from. The electronics shop, including Terry, James, Ivan, Carl, and Felix, were instrumental in my education. Other staff including those in the purchasing office, building manager George, and payroll—Agnieszka always made sure I was paid on time. Amy and later Krista were wonderful admins, helping me travel, plan, and deal with Jun.

Connor and Zach have been long term roommates, with mystery man Anton replacing Connor my last year. Many ski trips with Zach and later Annie have been a true highlight of my time in Colorado. Of course, thank you to the powerful Kinga. I won't forget biking with Jonah and staying at the SilverCreek Inn, where some of this thesis was written. Other friends in Boulder and elsewhere are important parts of my story—thank you all.

This document would not be possible without my family. Grandparents Emily, Gerald, Dorothee, and Alfred have provided love and guidance, supporting me in my interest in science from and early age. I cannot begin to express my gratitude for my parents—thank you for everything. I've been lucky to have my twin Clem, who has been my best friend during my entire life. I'm so excited to see what you will do next.

Well, I think that's it. Thank you reader—I hope you enjoy my thesis!

Contents

Chapter

Appendix

Tables

Table

Figures

Figure

Chapter 1

Introduction

When Theodore Roosevelt said "comparison is the thief of joy," he must have never met a metrologist. Indeed, comparison is perhaps the most important aspect of measurement (and for some the most joyful!). Any measurement is inherently a comparison, typically against a known quantity. Whether that is a platinum-iridium test mass that previously served as the definition of the kilogram, the 1/8" ticks on a cheap ruler, or the microwave oscillations of a cesium clock that set the second, every measurement needs a reference. The quality of your measurement is ultimately limited by this reference, so building a better reference can lead to better measurements.

A system of units is a sort of measurement language. In order to have mutual measurement understanding, we need to "speak" with agreed upon unit definitions. Enter the Système international d'unités (SI), a globally used system of measurements maintained by the Bureau International des Poids et Mesures (BIPM). There are seven base units that make up the SI: the second (s) for measuring time, the meter (m) for measuring length, the kilogram (kg) for measuring mass, the ampere (A) for measuring electric current, the kelvin (K) for measuring temperature, the mole (mol) for measuring a number amount, and the candela (cd) for measuring luminous intensity. Using only these base units, one should be able to express all measured quantities. All the results I present in this document rely on the SI, with the hope of making at least the reported quantities intelligible to others in the timekeeping community.

Measurement is at the heart of physics, with each advancement in measurement precision or accuracy furthering the field. So it is of primary concern to physicists that measurement tools

continue to improve. Since 2019, all units have been linked to fundamental constants, highlighting the connection between physics and measurement science. The seven base units are now based upon some combination of seven defined quantities: the speed of light (c), the Planck constant (h), the charge of the electron (e), the Boltzmann constant (k), the Avogadro constant (N_a), a candela constant for luminous efficacy (K_{cd}), and the ground state hyperfine transition frequency of cesium-133 ($\Delta\nu_{\mathrm{Cs}}$). Each measurement tool should be ultimately tied to these defined constants. The second is defined as $9192631770/\Delta\nu_{\mathrm{Cs}}$, so measurement of the cesium hyperfine transition is directly a measurement the second. A GPS disciplined oscillator is tied to the SI second by referencing the atomic clocks aboard GPS satellites. National metrology institutes (NMIs) exist to support this system of units, housing and developing specialized technology that links units to these defined quantities. An accurate scale undergoes a calibration process using test masses that are weighed using Kibble balance, a large machine that links the kilogram to h, c, and $\Delta\nu_{\mathrm{Cs}}$.

The cesium transition is a rather arbitrary choice to define the second, tied more to historical decisions than perhaps the more "fundamental constants" such as c, h, e, and k. With a better realization of the second using a different atomic transition, the entire SI can be improved [126]. Better is of course subjective, but as will become clear in the following thesis, strontium is an excellent candidate to define the second. By using a visible transition in atomic strontium, we can create a more precise timing signal that is linked to an atomic standard. This means that with proper care, any researcher can measure the exact same frequency anywhere in the world.

To understand the very best clocks, you need to compare against the very best clocks, so almost every clock experiment is a comparison of some sort. This approach is necessary for using clocks to perform real science. We compared different atoms in our system to measure the gravitational redshift [22]. We compared atoms under different lattice conditions to determine the shift from holding the atoms against gravity [70]. Work is ongoing comparing our clock with clocks at the National Institute of Standards and Technology (NIST), reevaluating previous measurements [23]. Thus the story I will present here is one of comparison and how comparison allowed us to build the

best clock to date.[1]

1.1 Atomic Clocks

What makes a good clock? Or perhaps, how do we understand the uncertainty of a time measurement? Measurement uncertainty has two sources: uncertainty that is modified with repeated measurements, and fixed uncertainty that stems from the techniques used. These are statistical and systematic uncertainties, and quantify how "certain" the measurement is with respect to a common reference quantity. If uncorrelated, we can write the total measurement uncertainty $\delta\nu$ as a quadrature sum of these two sources:

$$\delta\nu = \sqrt{(\delta_{stat}\nu(t))^2 + (\delta_{sys}\nu)^2}, \tag{1.1}$$

where $\delta_{stat}\nu(t)$ and $\delta_{sys}\nu$ are the statistical and systematic frequency uncertainties, respectively. As more data is accrued, the statistical uncertainty is modified, so we treat it as having dependence on time t. For example, if measuring a normal distribution, the measurement uncertainty reduces with the number of measurements n as $1/\sqrt{n}$. Thus a longer duration of repeated measurements correspond with lower δ_{stat}. Of course the systematic uncertainty may vary over time, however this time dependence is often less deterministic than with statistical uncertainty.

Humans have become rather good at measuring frequency and phase, so precision time measurement is based upon a phase measurement of an oscillating signal. Since $\nu = 1/T$, where ν is the frequency and T is the time of one oscillation period, to measure a length of time, one must simply count the cycles of a periodic oscillation and multiply by the inverse of the oscillation frequency. For example, a grandfather clock is based upon a 1 Hz oscillation of a carefully made pendulum. A set of gears known as an escapement counts the passing of the pendulum arm, advancing the second, minute, and hour hands. A quartz oscillator forms the frequency basis of common wrist watches. The oscillating crystal creates a sinusoidal voltage with a frequency of 32 kHz, and a shift

[1] As of April 2025!

register counts the periods, updating the display with the current time. A precision microwave oscillator is typically based upon a temperature stabilized quartz crystal oscillator (OXCO). In the low frequency microwave domain, that is frequencies that oscillate from 10 MHz to 40 GHz, there are many commercial solutions for counting cycles of an oscillating voltage. A key issue with each of these frequency references is that they are manmade artifacts, with frequencies dependent on careful manufacturing. If a pendulum is not the right length or the quartz crystal is not cut perfectly, the resultant time will not be accurate. That is, these microwave oscillators often have poor $\delta_{sys}\nu$.

The best clocks are ones that combine both excellent statistical uncertainty under short measurement times and excellent accuracy. To achieve this goal, state of the art clocks typically contain two main components: a high stability "local oscillator" that quickly averages to low statistical uncertainty and a reference that steers the local oscillator to a low systematic uncertainty. Throughout this thesis we will use fractional units: frequency uncertainty or shifts will be expressed as a part of the primary or "carrier" frequency. A uncertainty of 1 Hz on a 100 Hz oscillator becomes a fractional uncertainty of 10^{-2}. Since period counting is typically perfect, this approach allows us to compare very different frequency standards.

The best microwave frequency based timescales use an ultra-stable microwave oscillator with an atomic reference. At NIST, a number of hydrogen masers are combined to output a stable time base. Hydrogen masers are active clocks that use stimulated emission of 1.4 GHz spin flip transition in atomic hydrogen, generating a microwave frequency that has remarkably low instability of 10^{-15} at an averaging time of 10^3 s. Despite being referenced to an atomic transition, masers have known drift issues that compromise long term frequency measurements [60, 118]. The standard approach to eliminating drift is to steer the maser frequency using a cesium (or rubidium) microwave clock. These systems take the microwave signal generated by the maser, compare it with a well controlled clock transition in cesium, and correct the maser drift. At long times, the output frequency now takes the noise characteristics and systematic uncertainty of the cesium clock, and is now tied to the primary definition of the SI second.

To measure the statistical uncertainty, or frequency stability, a commonly used tool is the

Allan variance or its root the Allan deviation [4, 127]. The Allan variance calculates the variance of measurements averaged over time τ, and is defined as,

$$\sigma_y^2(\tau) = \frac{1}{2(M-1)} \sum_{i=1}^{M-1} \left[\langle y(\tau)\rangle_{i+1} - \langle y(\tau)\rangle_i\right]^2, \tag{1.2}$$

where M is the number of measurements, and $\langle y(\tau)\rangle_i$ is the average frequency measured during the interval i of duration τ. The Allan deviation, or ADEV, allows one to characterize the instability of y at some measuring time. For example, an ADEV of 10^{-16} at 1 s means that successive frequency measurements of 1 s would have frequency differences with a root mean square of 10^{-16}. We normally use an improved method called an overlapping Allan deviation, or OADEV, which calculates the Allan deviation using overlapping bins of length τ. This provides far greater confidence at the small price of being more computational intensive–typically not an issue for our data sets.

The Allan variance is also a powerful tool for understanding the character and even the origin of noise in frequency measurements. In Fig. 1.1, we plot different types of frequency noise and their corresponding Allan deviations. By averaging for a longer time, the uncertainty from white frequency modulation (WFM) and white phase modulation (WPM) noise can be reduced, or "averaged down." Plotting frequency as a function of time, it is not immediately obvious the difference between WFM and WPM, however the Allan deviation makes this readily apparent. WFM averages $\propto \tau^{-1/2}$, whereas WPM averages faster as τ^{-1}. Conversely, if the frequency is drifting, longer averaging times will actually lead to larger uncertainties. At short times, drifting frequencies might appear white, while longer times the ADEV grows. Flicker frequency modulation (FFM) noise, commonly called $1/f$ noise, does not average with repeated measurements. Random walk frequency modulation (RWFM) has uncertainty that grows with time $\propto \tau^{1/2}$.

In timekeeping, many signals have a combination of different noise types, each having a particular origin. In an atomic clock, quantum projection noise, usually WFM or in rare cases WPM, may dominate at short timescales, while an uncontrolled systematic shift might lead to flicker at longer time scales. Plotting the Allan deviation as a function of τ, these behaviors can be teased out

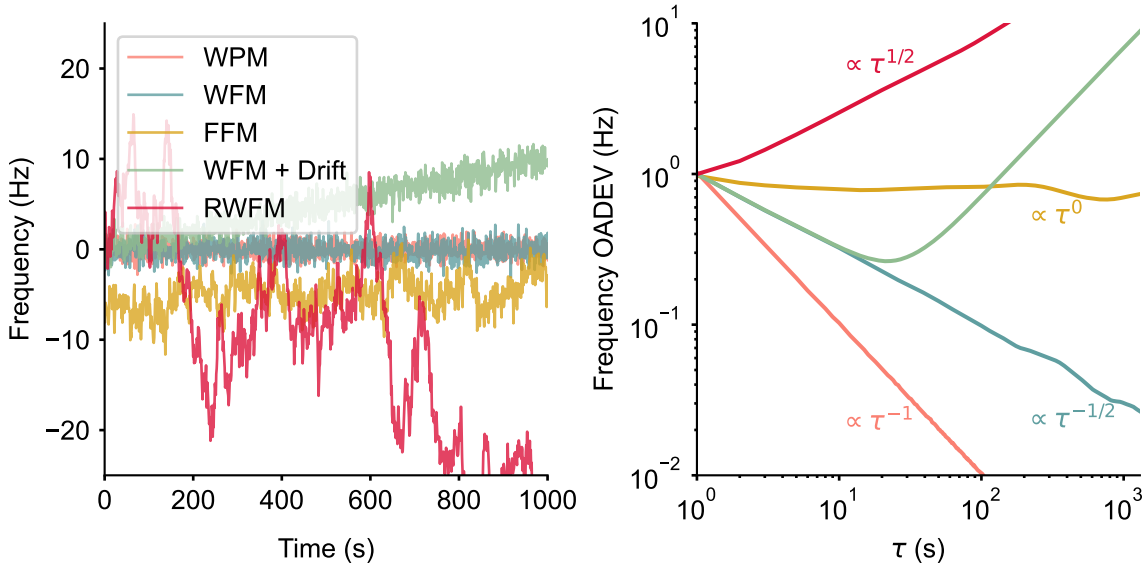

Figure 1.1: Different noise types and their Allan deviations. On the left are five types of noise: white phase modulation (WPM), white frequency modulation (WFM), flicker frequency modulation (FFM), WFM plus a drifting center frequency, and random walk frequency modulation (RWFM). The overlapping Allan Deviation (OADEV) of the five different shows how uncertainty varies as a function of averaging time τ. Different noise sources can be characterized with an exponent. For example, averaging of WPM scales $\propto \tau^{-1}$.

of a time record of frequency. Similar statistical techniques have been developed to better target specific noise characteristics. The modified Allan deviation, MDEV, allows distinction between white phase and flicker phase noise. Hadamard deviation removes linear drift from frequency noise. In sum, Allan deviations and related tools are powerful diagnostics for characterizing frequency noise. In this thesis, we will primarily use OADEVs, and occasionally MDEVs, to characterize frequencies as well as other repeated measurements, such as temperature.

While reporting a statistical uncertainty might be as simple as comparing against another clock and taking an Allan deviation, systematic uncertainty is often trickier. In atomic clocks, an accuracy budget is typically prepared to describe all sources of frequency shifts and their associated systematic uncertainties under nominal conditions. This represents the best known sources of shifts at the time of evaluation, but certain shifts can and have been overlooked [23, 47]. There are many ways systematic shifts are measured, from directly modifying the systematic and measuring a frequency

shift, to modeling the atomic response function and calculating the shift. Systematic shifts can also be reported dynamically, varying over time as the shift changes. For example, the density shift in a cesium clock will change as the atom number changes, so it may be corrected dynamically if the density is not constant.

While stability and accuracy are not necessarily correlated, the most accurate clocks typically need very low instability. Evaluating systematics accurately often relies on the measuring relative shifts with excellent precision. The practical side of clock building also necessitates a linking of these two performance metrics. If one needs a very accurate clock, the ability for that clock to quickly average to the systematic uncertainty is key.

1.2 Optical Clocks

Much like how upgrading from a simple ruler to a pair of precision calipers immediately improves length measurement, upgrading microwave to optical atomic clocks has revolutionized time measurements. Consider the following scenario: we would like to measure a time interval of roughly one minute with high accuracy. At our disposal are two clocks. One ticks once per second or 1 Hz, and the other ticks 100 times per second, or 100 Hz. To measure the duration of a given time interval, we need to count how many cycles pass in each clock. In one minute, the first clock measures 60 ticks and the second measures 6000 ticks. If each clock has a systematic uncertainty of 0.1 Hz, the the first clock will measure the minute with an uncertainty of 6 s, while the second clock has an uncertainty of only 0.06 s. Simply by increasing the ticking frequency of our clock we reduce the uncertainty of our interval measurement.

Optical clocks exploit this exact trick, scaling up the frequency of microwave atomic clocks from 10^{10} Hz to optical frequencies in the 10^{14} to 10^{15} Hz range. To create single frequency radiation in the 100s of THz, we trade in crystal oscillators and masers for visible wavelength lasers. The most stable lasers are currently diode lasers stabilized to optical cavities. The length of the optical cavity sets the frequency of the laser, so a more stable cavity will lead to less frequency noise.

To reference such a high frequency, optical clocks use an electronic transition in atom that

is excited with visible light. The best clock transitions are less sensitive to external perturbations that shift the frequency. Choosing the appropriate transition requires care, as the electron orbit can act as an antenna, converting external field fluctuations into deleterious frequency shifts. A narrow linewidth clock transition gives better frequency resolution that reduces instability, so long lived clock states are also necessary to build the best optical clocks. Our atom of choice, strontium (Sr), contains perhaps the most convenient clock transition type: two long lived states with zero total angular momentum realize a forbidden $J = 0 \rightarrow 0$ transition. This type of transition was proposed first as on optical reference in thallium ions (Tl^+) ions by Hans Dehmelt [35], and has since become widely used: both the aluminum ion (Al^+) and ytterbium neutral (Yb) optical clocks exploit a similar transition type to excellent effect. Synthetic $J = 0$ states can also be realized by averaging over many different transitions [6, 135].

Converting an optical frequency to a human usable frequency is a rather tricky task, and was a primary limitation of optical clocks before the advent of the frequency comb. The optical frequency comb is a pulsed laser that contains optical frequency tones spaced a constant microwave frequency apart. With proper stabilization, a frequency comb generates a microwave signal that inherits the low instability of an optical frequency. By referencing a comb to an optical transition, we construct an optically stabilized time scale that is still usable with microwave electronics [39].

Optical clocks have progressed rapidly since the advent of the frequency comb, with many critical components now commercially available. However, the most accurate atomic standards are still research projects. In Fig. 1.2, we plot clock accuracy over the past 25 years. Since overtaking the best microwave atomic clocks in 2008, optical clocks have consistently improved and are now over two orders of magnitude more accurate than microwave standards. The Ye lab in JILA has been consistently improving strontium optical lattice clocks over this time period, and work within this thesis has contributed to this march towards a more accurate optical standard.

Time ties together much of physics, so improving time measurement will have wide ranging implications. In the coming years, the SI second will be redefined on an optical standard, simultaneously improving a number of different SI units [40]. Optical clocks can provide precision tests

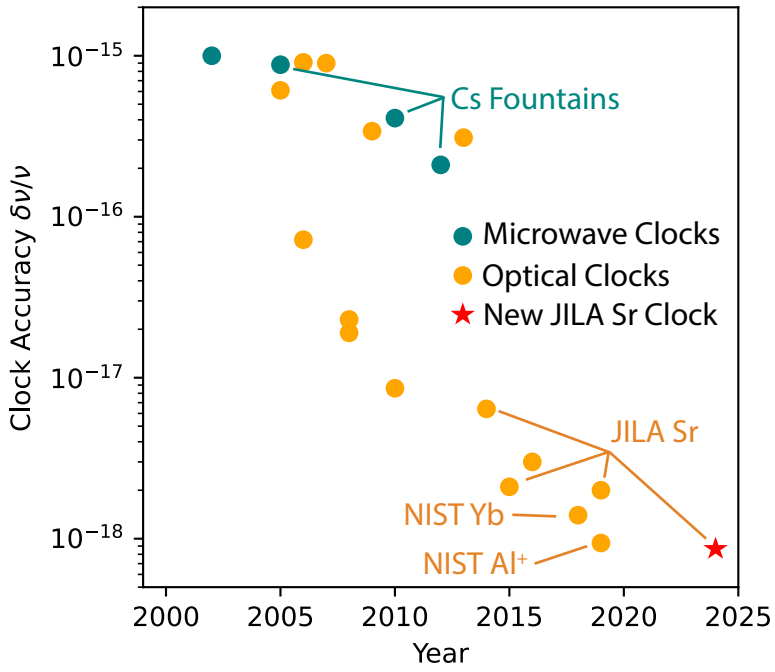

Figure 1.2: Fractional frequency accuracy ($\delta\nu/\nu$) of atomic clocks over the past few decades. Microwave standards, shown in teal, reach below 10^{-15} around 2000. Optical standards, shown in orange, have since far surpassed the most accurate microwave standards. The most accurate clocks are all located in Boulder, CO: the NIST Yb [98] and Al^+ [26] clocks and our JILA Sr1 system [2]. This thesis will discuss our record accuracy, the red star.

of relativity [140], have placed bounds on dark matter [69, 148], and may be used for measuring gravitational waves [75] or predicting volcanic eruptions [17]. Simply building better clocks can also lead to fundamental atomic physics discoveries, from motivating better atomic structure calculations [122, 123, 154], to understanding optimal use of quantum resources [30, 42, 44, 171]. Especially in the Ye lab, precise clocks have allowed exploration of many-body systems [1, 50, 95, 102]. Of course, we may build better clocks simply because we are curious–what is the fundamental limit of precision frequency measurement?

1.3 My Work

My time spent working on the strontium 1-dimensional (1D) optical lattice clock (Sr1) in the Ye lab has primarily focused on achieving record accuracy and stability. I joined the experiment in

the midst of the COVID-19 pandemic. The original strontium experiment had achieved the lowest systematic uncertainty in a Sr OLC a year prior [21], and was being reconstructed to push the limits even further. By August 2020, atoms were loaded in the lattice of this new system and the first narrow clock spectroscopy was measured, but there remained significant work to reach our accuracy and stability goals.

Much has been said about Sr OLCs. In this thesis, I hope to build upon this body of work and present what we have done to make Sr1 the most accurate and stable clock. We begin by discussing the experimental systems and general operation in Ch. 2. Broadly speaking, there are two limitations to optical lattice clock accuracy, single particle and multi-particle. Single particle shifts, such as the lattice light shift or the black body radiation shift, limit the achievable accuracy. The density shift arises from multiple atoms colliding. The lowest instability is achieved with many atoms, yet scaling up the atom number results in loss of atomic coherence and systematic shifts. Precise control of the atoms and the surrounding environment is critical to reducing instability and systematic uncertainty. In Ch. 3, we discuss how we understand and measure the motional states of the atoms. The first work published with Sr1 uses the excellent synchronous stability and large sample size to resolve the gravitational redshift [22]. This measurement removes the laser noise, allowing measurement instability that is not limited by the oscillator but rather the atomic noise. A key to this experiment was eliminating the density shift by operating at the "magic depth" [1]. The control and measurement of the density shift is discussed in Ch. 4.

After demonstrating excellent synchronous stability as well as control over shift gradients, our attention turned to reducing the absolute systematic uncertainty of the platform. Through careful measurements, we reduced the lattice light shift uncertainty to 3×10^{-19}, work presented in Ch. 5. This is an important systematic shift that has be a significant limitation in previous clocks [21, 109]. The largest systemic shift in room temperature Sr clocks is due to black body radiation (BBR). In Ch. 6, we make strides in taming this by remeasuring the atomic response to BBR as well as characterizing the radiation environment. Putting together all known systematic shifts, we find a total uncertainty of 8.1×10^{-19}, with additional shifts and the full uncertainty budget presented in

Ch. 7. As of writing, this is the most accurate clock ever constructed, as illustrated by the red star in Fig. 1.2.

We dedicate the final chapter, Ch. 8 to discussing the frontiers and ongoing experiments using Sr1. We investigate the clock stability limitations, including the atomic coherence time and laser system, to see how far we can push Sr1. We discuss some shallow lattice physics, including directly measuring local gravitational acceleration g. The three most accurate clocks, including the Yb OLC and Al^+ ion, are all located in Boulder, Colorado! With a fiber connection between these labs, we hope to verify clock performance [23].

Chapter 2

The Strontium System

Strontium as an optical clock candidate has been covered extensively in many papers [66, 88, 138, 163] and theses [18, 24, 87, 110]. A narrow, environmentally insensitive clock transition, advantageous laser cooling structure, and easily attainable wavelengths make it a key candidate for the redefinition of the SI second. In this chapter, I will discuss our intent building a next-generation optical lattice clock, how we utilize the strontium structure, and our how we operate to optimize accuracy and stability.

2.1 The Strontium Atom

Located in the second column and fifth row of the periodic table, strontium is an alkaline-earth metal with 38 protons. Isotopes naturally occur with atomic masses in the range of 84 to 90. We choose the only abundant stable fermionic isotope, ^{87}Sr.

As an alkaline-earth atom, strontium has two valence electrons, which form singlet and triplet electronic states. The strontium level structure is plotted in Fig. 2.1. Electronic transitions between singlet and triplet manifolds are strictly "forbidden" by LS coupling selection rules, yet can be driven through higher order coupling. A set of narrow transitions between the two lowest energy levels, the $5s^2\ {}^1S_0$ and the $5s5p\ {}^3P_J$, are a quantum physicist's playground. The ${}^1S_0 \rightarrow {}^3P_1$ intercombination transition is 7 kHz, allowing for low Doppler temperature cooling and easy ground motional state preparation in a lattice [146]. The ${}^3P_2$ state is exceedingly long-lived, with a 520^{+310}_{-140} s lifetime [161], and has been considered for quantum physics applications [57, 73, 143]. The beating heart of our

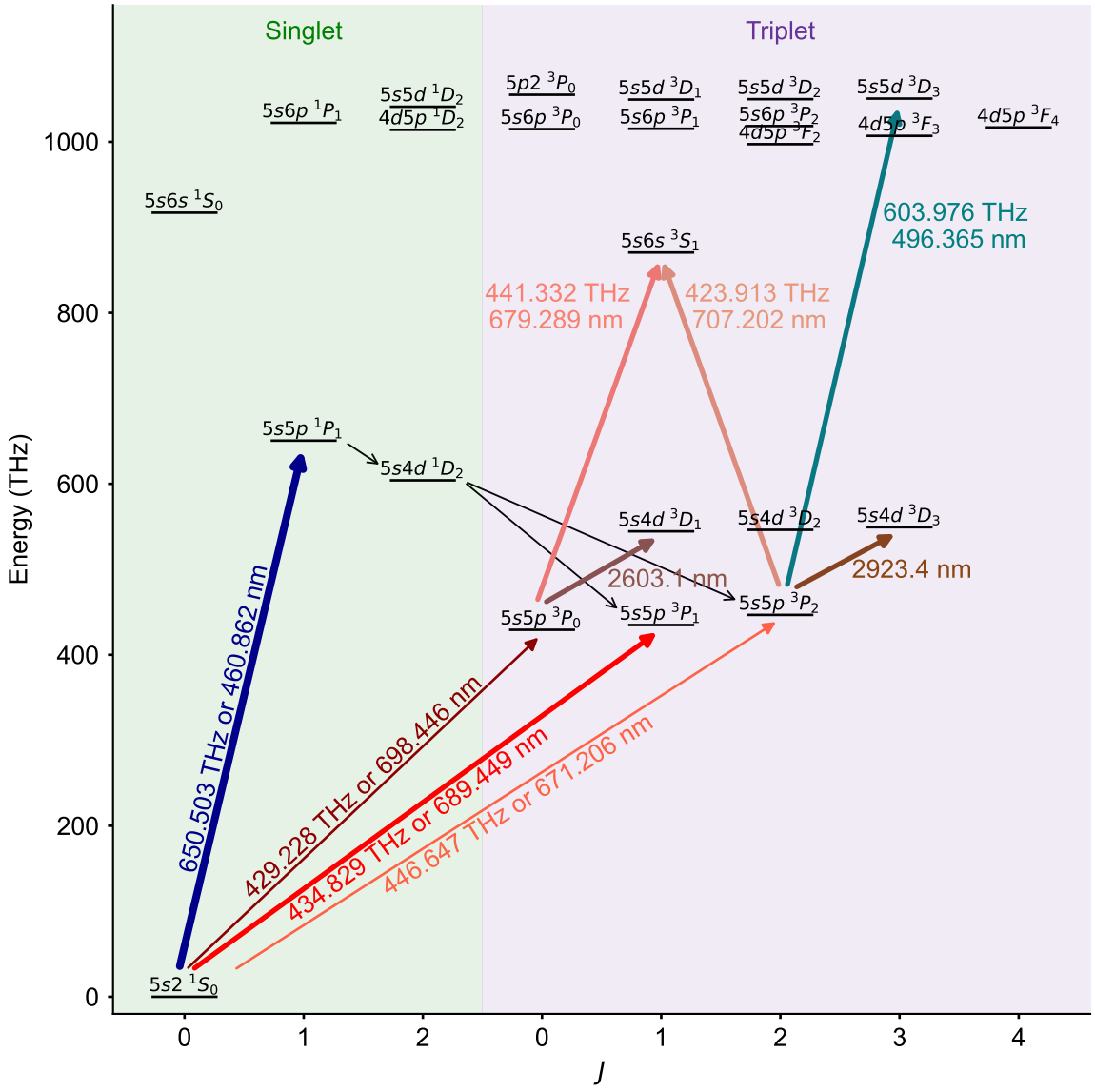

Figure 2.1: Strontium energy level structure. The two valence electrons create singlet and triplet states. The blue transition is dipole allowed and forms the first MOT sequence. The narrow ${}^1S_0 \rightarrow {}^3P_1$ intercombination transition allows Sr laser cooling down to < 1 μK. To bridge the linewidth difference, we use a SWAP MOT on the intercombination transition, while some groups form another MOT using the 496 nm transition from ${}^3P_2$ [3]. The ${}^1S_0 \rightarrow {}^3P_0$ transition at 429 THz forms the basis of the optical clock.

strontium clock is the mHz ${}^1S_0 \rightarrow {}^3P_0$ *clock* transition. In ^{87}Sr, the nuclear spin mixes states, so the clock transition is simply a strongly attenuated E1 transition [25]. With $J = 0$ for both states, these states are magnetically insensitive, making for reliable spectroscopy. Interrogating this narrow

transition in a dilute gas, we reference a laser frequency that forms the basis of the optical clock system.

Strontium spectroscopy systematics can largely be grouped into single particle shifts and multi-particle shifts. The new Sr1 system was constructed with both shift sources in mind. The wavelength dependent polarizability of the two clock states presents a roadmap to understanding some single particle shifts, shown in Fig. 2.2. By using Sr to create a clock, we necessarily perturb the atom from its natural state. While less of an issue with the weak intensity laser drive we typically use, the clock laser at 698 nm can nevertheless induce a small differential shift between the two states. We use an optical lattice to support the atoms against gravity, perform Doppler cooling, and recoil free spectroscopy. This is tuned to 813 nm, where the polarizability of the two clock states crosses and the differential polarizability vanishes [139]. Nevertheless, this "magic wavelength" lattice induces a small frequency shift that must be precisely characterized. The largest frequency shift is due to the blackbody radiation spectrum from the ambient environment. At 22 °C, or 295 K, this spectrum is centered at 10 μm, far away from any transition out of either clock states. To first order, this spectrum shifts the clock transition due to the differential polarizability at DC, with higher order shifts occurring due to other transitions. Similarly, residual static electric fields cause a DC Stark transition shift. Plenty of other systematic shifts are not represented in Fig. 2.2, such as magnetic field dependent shifts, collisional shifts, and many more.

2.2 Laser Cooling & Lattice Loading

At room temperature and pressure, strontium is a solid silver metal, not the dilute, cold gas we need for laser spectroscopy. In a commercially available oven and Zeeman slower system from AOSense, we heat a piece of strontium to a range of 370 to 500 °C. This creates a fast beam of atomic strontium traveling $\sim$ 500 m/s. Inside the Zeeman slower, permanent magnets apply a spatially varying magnetic field that modifies the energy of $^1P_1$ state. We cycle photons on the dipole allowed $^1S_0 \rightarrow {}^1P_1$ transition, a blue color light at 461 nm, slowing and focusing it into our primary experiment chamber. Two high current coils create a quadrupole field with zero field near

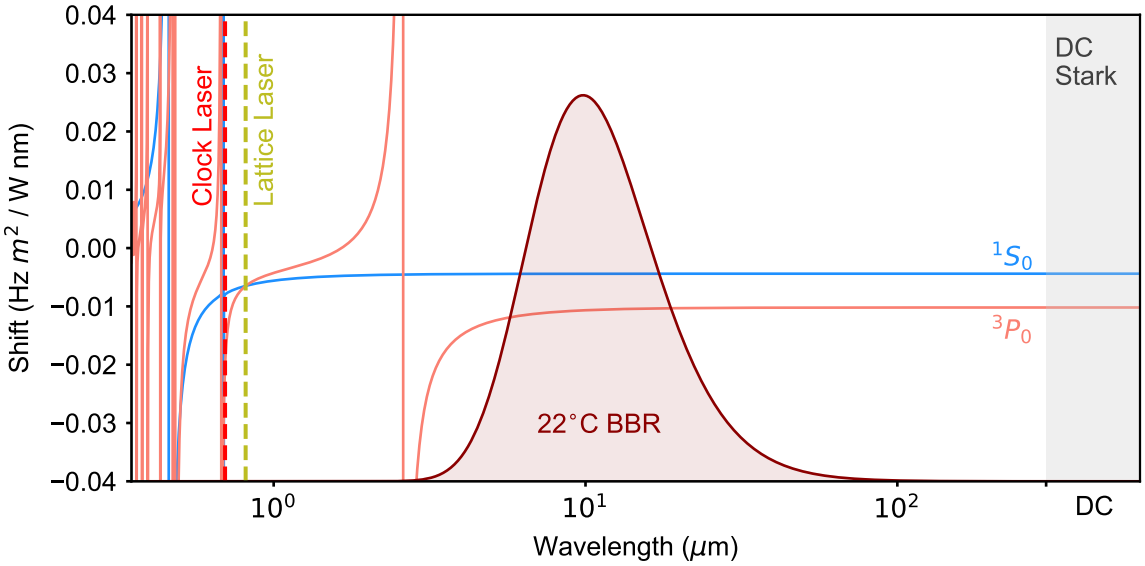

Figure 2.2: Strontium polarizability and systematic shifts. The differential polarizability at DC causes a DC Stark shift and is predominantly responsible for the shift due to the black body radiation spectrum. The clock laser at 698 nm and the lattice laser at 813 nm also induce systematic shifts.

the center of our chamber. Again using the broad $^1S_0 \rightarrow {}^1P_1$ transition, we collect the output of the Zeeman slower with a magneto optical trap (MOT). Depending on the desired number of atoms, we slow and trap for 0.02 to > 1 s, creating a sample of millions of atoms at mK temperatures. Our "blue MOT" has two stages, with a higher field, high intensity stage succeeded by a lower intensity, lower field stage for around 100 ms that allows us to better mode match with the subsequent cooling step using a narrower transition. Leakage from this cooling transition through the $5s4d\ ^1D_2$ state populates the metastable $^3P_2$ state, requiring repumping population through $5s6s\ ^3S_1$. Two repump lasers are modulated to address all hyperfine states along these transitions and prevent additional population accumulating in $^3P_0$.

Next, we make use of the 7 kHz $^1S_0 \rightarrow {}^3P_1$ transition at 689 nm in a "red" MOT [66]. For efficient laser cooling, we need to address the hyperfine structure of the $^3P_1$ state by cycling photons on both the $F = 11/2$ and the $F = 9/2$ states [159]. To capture a larger potion of the blue MOT, we modulate the frequency of the red lasers to effectively broaden the cooling transition. Following the work in the Thompson group, we implement a SWAP MOT [9, 113]. Modulating the lasers with

a sawtooth wave frequency profile replaces spontaneous emission with stimulated emission, leading to a colder, higher number sample. By switching to a single tone, we approach the recoil limit of the red MOT, resulting in a ~ 2 μK sample.

During all stages of cooling, the optical lattice remains at a peak depth of 300 lattice photon recoil energies (E_r). After the single frequency red MOT, most of the sample is cold enough to remain trapped in a lattice of this depth. The transfer efficiency is likely dominated by the spatial overlap between the MOT and lattice. In this conservative potential, we perform our final cooling and state preparation. With a weak bias field ~ 1 G, we Doppler cool along the MOT paths and sideband cool along the lattice direction using the $^3P_1$ $F = 11/2$ state. Polarizing in one of the stretched $m_F = \pm 9/2$ states occurs concurrently using a laser tuned to the $^1S_0 \rightarrow {}^3P_1$ $F = 9/2$ transition. The final temperatures we reach are around 600 to 700 nK in a deep lattice. We typically reduce the lattice depth to around 10 E_r adiabatically, achieving samples at 100 nK. More details about the exact motional state of the atoms are given in Ch. 3.

2.3 The System

A key enhancement of the Sr1 rebuild is an in-vacuum build-up cavity for the optical lattice, highlighted in Fig. 2.3. Operating a lattice at the magic wavelength requires high intensity at the rather inconvenient wavelength of 813 nm. Most Sr OLCs, including the previous generation Sr1, use a titanium-sapphire laser, tightly focussed and retroreflected to create a standing wave. Through a build up cavity with a finesse of 1020 ± 60, we create a large volume lattice with a simple 800 mW diode laser.[1] The cavity is formed by two 1 m radius of curvature mirrors mounted 16.9 cm apart in-vacuum with a resultant cavity waist of 260 μm [18]. The laser is locked to the cavity via a standard Pound-Drever-Hall (PDH) locking technique. One mirror is mounted on a piezo stack that allows us to stabilize the lattice wavelength to the frequency comb. Having a stable lattice intensity is important for reliable atom conditions, so we monitor cavity transmission

[1] We use a Toptica-Eagleyard EYP-RWL-0808-00800-4000-BFW09-0000 800 mW diode injection locked with an ECDL.

intensity and actuate on the input intensity using a two stage intensity servo. A fast electro-optic amplitude modulator stabilizes at high frequency, while a low frequency intensity lock actuates on an acousto-optic modulator (AOM). To vary the lattice depth, we change the intensity servo setpoint. To preserve the cavity lock stability, we separately intensity stabilize the light on the PDH photodiode.

A partial reflector is mounted below the lower cavity mirror and acts as a phase reference for our clock laser fiber noise cancellation. This reference plate is mounted outside of vacuum and before any ND filters. Any reflection of the clock laser light by the top cavity mirror would create a standing wave of clock light. The cavity mirrors are designed to be low reflectivity for 698 nm, nevertheless a $\sim 1\%$ reflection causes a small standing wave component, discussed in Ch. 3.7.

The first Sr OLC to use an in-vacuum lattice cavity was in the SYRTE group [82]. They noticed a significant DC stark shift from large patch charges on their mirror surfaces. The new Sr1 design process considered this effect and approached it in two ways. Copper cups around the mirrors are intended to reduce any stray field effects at the atoms. An in-vacuum quadrant electrode pair is designed to apply sufficiently large electric fields to the atoms to measure and remove any DC stark shift. These electrodes are illustrated as copper rings in Fig. 2.3.

The MOT coils are not directly mounted to the vacuum chamber, so switching them quickly does not unlock the lattice. A set of compensation coils also mounted separately allow us to correct for the earth's magnetic field and apply a bias field for Doppler cooling and coherent spectroscopy.

2.3.1 Temperature Stabilization

Active temperature stabilization is an important aspect of the rebuilt Sr1 system, leading to more reliable operation and more stable systematics. While the room temperature is stabilized to around 2 °C, additional layers of control are necessary. The system is stabilized through a number of different active loops, including the air circulating the system and liquid coolant pumped around the vacuum chamber and through the MOT coils.

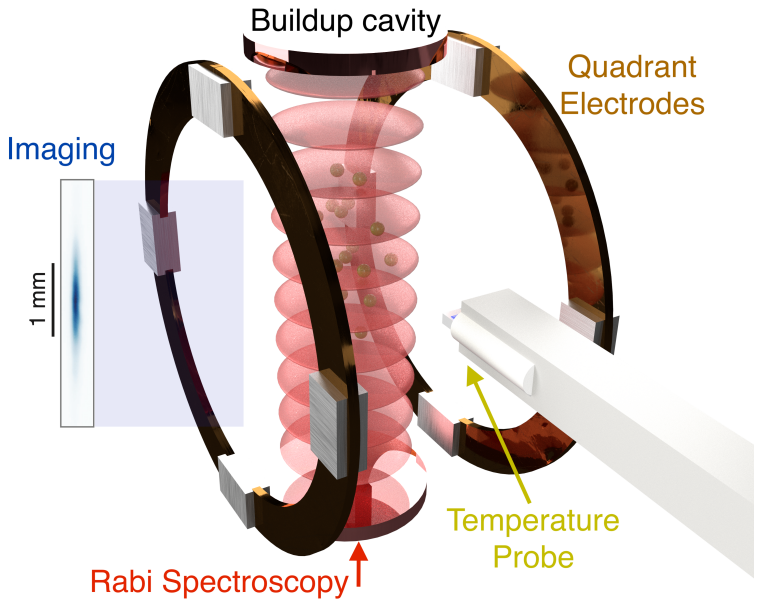

Figure 2.3: A simplified schematic of the Sr1 system, highlighting some important aspects. Two mirrors mounted in vacuum form a build up cavity for the lattice. This cavity is oriented along gravity. Quadrant electrodes mounted in vacuum allow us to apply an electric field to measure and correct for residual DC Stark shifts. We use imaging with a 6 μm resolution to read out the atomic state. An image of lattice trapped atoms spanning over 1 mm is shown on the left. An in-vacuum temperature probe measures the radiant temperature at the atom location.

Excluding supporting laser systems, the Sr1 clock occupies a single optics table surrounded by a 80-20 structure resting on the ground. The table is enclosed with panels, leading to some passive isolation from room temperature swings. Atop the enclosure, a HEPA filtered fan unit pulls in air at a constant speed. A liquid to air heat exchanger sits above this to control the intake air temperature. The temperature is stabilized by varying the flow of building process chilled water to this heat exchanger and using a temperature sensor inside the enclosure for feedback. This approach allows us to cool the table, and typically we stabilize 0 to 3 °C below the room temperature.

Unlike the NIST Yb clocks [11], we have no in vacuum radiation shields. Instead, the stainless steel chamber itself acts as a uniform radiative environment. Reliably controlling its temperature is paramount for creating a stable black body radiation environment. We circulate temperature stabilized coolant through roughly a dozen separate liquid loops surrounding the vacuum chamber. All windows that have direct line-of-sight to the atoms are surrounded by individual loops. Each

loop has two temperature sensors, commercial negative temperature coefficient (NTC) 50k sensors with a quoted uncertainty of 0.5 °C. The in-loop sensor feeds back to a control board to stabilize its temperature loop and the out-of-loop sensor is logged. Liquid chillers afford additional temperature control for the MOT coils as well as the camera, reducing inhomogeneity across the system. This comprehensive approach leads to a more uniform, stable temperature environment. Seldom do we need to adjust optics, and our in vacuum cavity has low drift despite using stainless steel as the spacer. In-vacuum temperature measurements confirm that the radiative environment the atoms see is very stable, generally changing < 5 mK over a day. Two thin-film platinum resistance thermometers are mounted to an in-vacuum translation stage, as shown in Fig. 2.3. We insert the sensors to the center of the vacuum chamber to measure the radiant environment at the atom location. In Ch. 6 we discuss this temperature measurement process and how our temperature control effects the stability of the black body radiation shift.

2.4 Clock Spectroscopy

Every atomic clock is simply a very careful spectroscopy experiment. The best atomic clock relies on the best spectroscopy. Two methods of coherent spectroscopy have become indispensable to the clock community, named after their creators Rabi and Ramsey. For most of this thesis, we will deal exclusively with Rabi spectroscopy. For reasons that will become apparent throughout this document, Rabi spectroscopy is superior technique in almost all cases.

Rabi spectroscopy involves coherently driving an two level transition between a ground state g and excited state e with a fixed intensity pulse of electromagnetic radiation. The excitation fraction ρ^{ee} is a function of pulse time T_{Rabi}, detuning from resonance δ, and a Rabi frequency Ω_0:

$$\rho^{ee}(T_{Rabi}, \delta) = \frac{\Omega_0^2}{\Omega_0^2 + \delta^2} \sin^2\left(\frac{T_{Rabi}\sqrt{\Omega_0^2 + \delta^2}}{2}\right). \tag{2.1}$$

With $\delta = 0$, the excitation oscillates or "flops" between g and e with a frequency of Ω_0. When $T_{Rabi} = \pi/\Omega_0$, the π-pulse time, the population can be entirely moved from g to e. In this case, the

lineshape as a function of detuning has one central peak with full width half maximum of $0.8/T_{Rabi}$. This lineshape is shown in Fig. 2.4 and Fig. 2.7.

Both the ground and excited clock states have $F = 9/2$ leading to 10 magnetic sublevels, $m_F = -9/2, \ldots, +9/2$. With a clock drive, we promote atoms from the ground state to the excited state with $\Delta m_F = \pm 1, 0$ with $\sigma\pm$ and π light polarization respectively. Using the magnetic sublevel structure and different light polarizations, we can measure the magnetic field.

In a weak magnetic field B, the Zeeman interaction Hamiltonian H_Z depends on the electron spin S_z, orbital momentum L_z, and nuclear spin I_z:

$$H_Z = (g_s S_z + g_l L_z - g_I I_z)\mu_0 B, \tag{2.2}$$

where $g_s \approx 2$, $g_l = 1$, and $\mu_0 = \mu_B/h$ with μ_B the Bohr magneton. The nuclear g factor $g_I = \frac{\mu_I(1-\sigma_d)}{\mu_0|I|}$, with $\mu_I = -1.088784(3)\mu_N$ [115, 142], μ_N is the nuclear magneton, $\sigma_d = 0.00345$, and I is the nuclear spin. As discussed, hyperfine interactions mix the state of $^3P_0$ with $^3P_1$, $^1P_1$, and $^3P_2$, leading to a different g_I for the excited clock state, $g_I^e = g_I + \delta g$. This effect introduces differential magnetic field sensitivity that resolves magnetic sublevels under transitions between clock states. Neglecting lattice light effects, the magnetic sublevel splitting $\Delta_{g(e)}$ for the ground (excited) states is thus,

$$\begin{aligned} \Delta_g &= m_F g_I \mu_0 B, \\ \Delta_e &= m_F (g_I + \delta g)\mu_0 B, \end{aligned} \tag{2.3}$$

with $\delta g \mu_0 = -108.4 \pm 0.4$ Hz/G [25]. When driving the clock transition between the same magnetic sublevels, this magnetic sensitivity is due entirely to δg. The implication of this differential magnetic sensitivity is the need to use a single magnetic sublevel for precise clock spectroscopy, as small field fluctuations can lead to a broadened line. Instead, we apply a ~ 0.5 G field to frequency resolve all transitions, so the ultimate linewidth is due to magnetic field gradients, not the field magnitude. Alternating between different sign m_F, we reject the first order Zeeman shift by taking the frequency average.

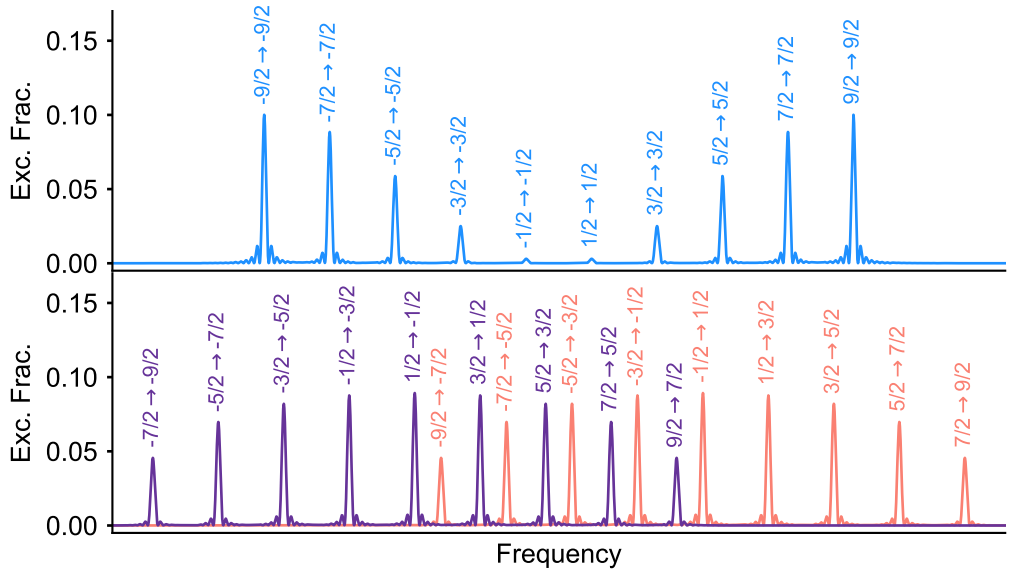

Figure 2.4: Calculated spectrum for π (top) and $\sigma\pm$ (bottom) clock transitions of a sample prepared in g. The rabi frequency for each line is modified by the relevant Clebsch-Gordon coefficient. The ground and excited m_F levels are noted in the figure.

Fig. 2.4 shows the calculated Rabi spectrum for a uniform m_F spin mixture with a bias field, driving from the ground state to the excited state. The Rabi frequency is adjusted by the Clebsch-Gordon coefficients between states governing the angular momentum coupling. The top plot shows the spectrum under a π polarization drive, where the clock laser is polarized along the bias field direction, and the bottom plot is with $\sigma\pm$ polarization.

The experimentally measured spectrum is shown in Fig. 2.5. By setting the clock polarization perpendicular to the bias field, we drive with both $\sigma+$ and $\sigma-$ light. On the top, we plot the spectrum of a spin mixture with a bias field of about 450 mG. The Clebsch-Gordon coefficients create two "envelopes" of transitions, with the stretched states having the lowest Rabi frequency.

To operate in a controlled manner, we use the differential magnetic sensitivity to correct for the background magnetic field. With a spin mixture in a very low magnetic field, we drive the clock transition and measure the line broadening, adjusting the current in the bias coils to reduce the linewidth and compensate for the background field. With care, we typically operate the gaussian width of this spin mixture lineshape to be ~ 1 Hz, corresponding to a residual magnetic field of

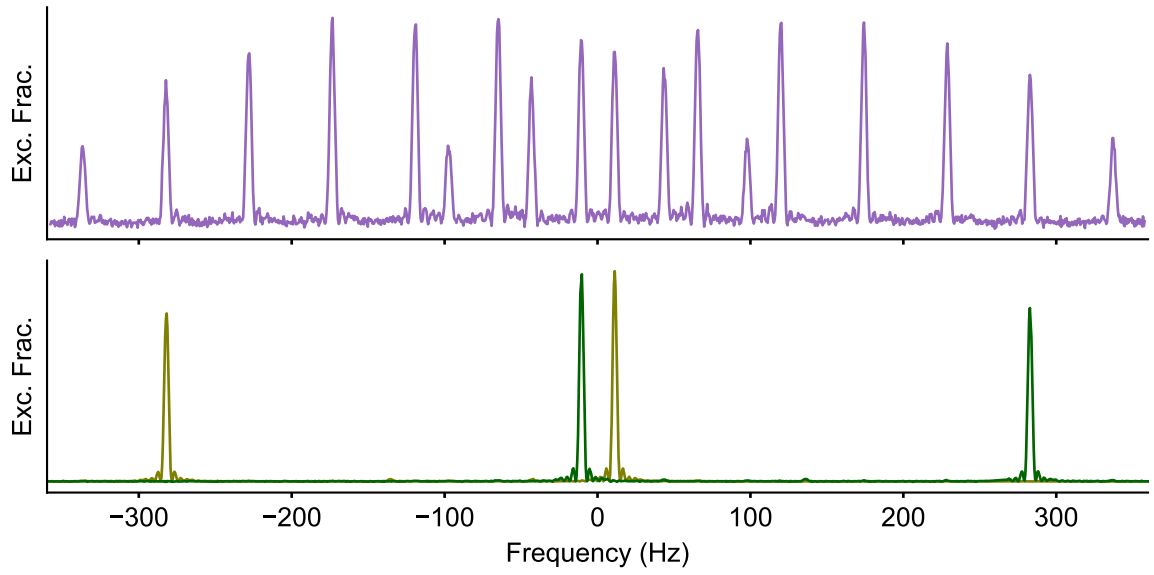

Figure 2.5: Measured clock spectrum with an unpolarized sample (top) and with the sample in our desired $m_F = \pm 5/2$ states. The clock laser is linearly polarized perpendicular to the bias magnetic field such that we can drive $\sigma+$ and $\sigma-$ transitions with the same light. By using $|m_F = \pm 5/2, {}^1S_0\rangle \rightarrow |m_F = \pm 3/2\, {}^3P_0\rangle$ transitions, magnetic field sensitivity is reduced by over 20 times compared with standard stretched state spectroscopy.

~ 1 mG. By compensating for field drifts every day, we ensure that the applied bias field does not rotate due to any other external field, a necessary step for controlling the tensor light shift.

To measure the true frequency of the strontium transition, we realize a synthetic $m_F = 0$ transition by taking the average of two opposite sign magnetic sublevels with an applied bias field. This generates a strong quantization axis for coherent Rabi spectroscopy on a single magnetic sublevel. The standard approach for Sr OLCs is to use the stretched $m_F = \pm 9/2$ states and drive with π polarization. Spin polarizing in either of these states can be accomplished by driving the ${}^1S_0 \rightarrow {}^3P_1$ $F = 9/2$ transition with either $\sigma+$ or $\sigma-$ polarization oriented along a magnetic bias field. The splitting between these states is about 1 Hz/mG. Since we observe ambient field fluctuations around 0.1 mG with occasional 1 mG jumps, this field sensitivity would limit our spectroscopy time to < 1 s.

To circumvent this, we choose to operate with the least magnetically sensitive magnetic sublevel transition, $|{}^1S_0, m_F = \pm 5/2\rangle \rightarrow |{}^3P_0, m_F = \pm 3/2\rangle$. This reduces field sensitivity by roughly a factor

of 22, removing field fluctuations as a limiting effect on spectroscopy. We use two fast clock pulses to transfer the atoms from $|m_F = \pm 9/2, {}^1S_0\rangle$ to $|m_F = \pm 7/2, {}^3P_0\rangle$ first, and then $|m_F = \pm 7/2, {}^3P_0\rangle$ to $|m_F = \pm 5/2, {}^1S_0\rangle$. The bottom plot in Fig. 2.5 shows what this spectroscopy signal looks like in our desired states, with the green spectrum prepared in $|{}^1S_0, m_F = \pm 5/2\rangle$ and the brown spectrum prepared in $|{}^1S_0, m_F = -5/2\rangle$. From $|m_F = +5/2, {}^1S_0\rangle$ we also have access to the second most magnetically sensitive magnetic sublevel transition to $|m_F = \pm 7/2, {}^3P_0\rangle$, which we make use of to measure the effect of field fluctuations in Ch. 7.2.

2.5 The "Clock Lock"

We are lucky to have one of the best lasers in the world to perform clock spectroscopy [114]. The Si3 laser is based upon a 1.5 μm laser stabilized to single crystal silicon cavity [97]. Si3 stabilizes a frequency comb, which transfers this IR stability at frequencies < 1 kHz to the 698 nm wavelength laser that is locked to a 40 cm ULE cavity [96]. This system generates exceptionally low instability $< 5 \times 10^{-17}$ from 1 to 1000 s, and drifts < 10 Hz/day. A long term frequency record is plotted in Fig. 2.6, demonstrating < 10 kHz drift over 6 years of operation. While we do not have a comprehensive understanding of drift in this system, we fit a phenomenological drift model for cavity frequency at time t, $\nu_{Si3}(t) \propto t \times e^{t/\tau_{Si3}}$. This appears to partially capture the drifting frequency, although the structured residuals, plotted in the lower panel, suggest a more complicated process.

Nonetheless, our clock laser system has some fundamental limitations that prevent the silicon cavity alone from operating as a reliable clock. Thermal flicker noise in the coatings limits the stability to $\sim 4 \times 10^{-17}$ from roughly $1 - 10^4$ s. Flicker noise, random walk noise, and long term nonlinear drift cause the silicon cavity to have worse performance than the best cesium disciplined Masers over about 10^5 s [103]. By feeding back on the silicon light with an error signal derived from the strontium atoms, we can generate a timing signal that inherits the stability of the strontium system at long times. We call this feedback process a "clock lock".

To generate an error signal for feedback, we probe the strontium clock transition twice, on either side of a Rabi, half a linewidth detuned from the peak. The "left" and "right" lockpoints on

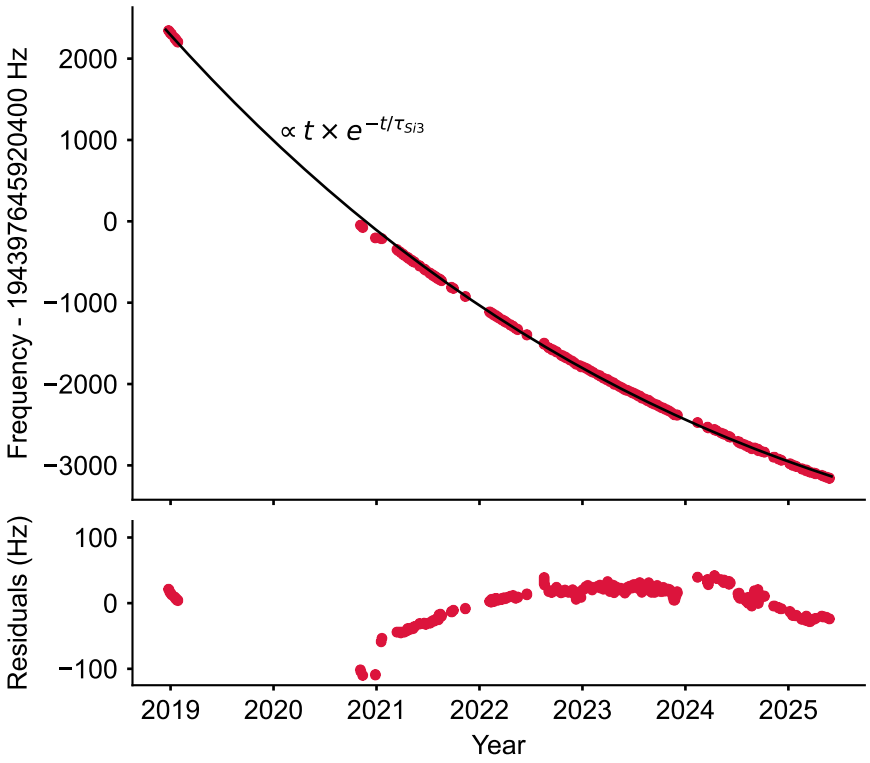

Figure 2.6: Si3 long term frequency record measured against Sr atoms. We fit a phenomenological drift model for cavity frequency as a function of time, shown as the black solid line. Fit residuals are plotted in the lower panel.

the Rabi lineshape are illustrated in Fig. 2.7. The error signal is the difference in excitation fraction between the left and right, as shown on the right of Fig. 2.7, with the servo feedback designed to zero the error signal at the red circle. Rabi spectroscopy generates a robust error signal, where the capture range is twice the linewidth of the spectroscopy line, shown as the blue region of the error signal. In the limit of a Lorentzian lineshape, the error signal has an infinite capture range. Due to multiple nearly identical fringes, Ramsey spectroscopy has about half the capture range of Rabi spectroscopy.

Feedback is applied to a steering AOM using a digital servo. The servo has a proportional term and two integrators, with servo parameters determined by the spectroscopy time. Rabi spectroscopy is sensitive to the laser noise, with the sensitivity evolving during the Rabi drive. This sensitivity function $r(t)$ is shown on the left of Fig. 2.8. As the atomic state evolves from g to e under a

constant intensity Rabi drive, the sensitivity to laser phase noise initially grows. Since the final readout involves projecting the evolved state, the phase noise sensitivity goes to zero at the end of the pulse as no evolution occurs. The final excitation fraction readout contains the integrated phase noise of this sensitivity function, acting as a low pass filter on laser frequency noise [78]. Taking the Fourier transform of $r(t)$ yields $R(f)$ which indicates the frequency sensitivity to laser noise, as shown on the right of Fig. 2.8. A clock lock control signal is a direct measurement of the laser noise convolved with the sensitivity function. Our typical Rabi frequencies are around 1 Hz, so our primary laser noise sensitivity is at very low frequencies. Operating with different Rabi frequencies and pulse sequences allows one to construct a laser noise model, as in Refs. [14, 160].

In Fig. 2.9, we plot a Si3 frequency record measured over an example clock lock. We use a $T_{rabi} = 1.15$ s, and each point is an average of four lock points measured over ~ 10 s, so the resulting frequency record rejects most frequency noise > 100 mHz. For all time scales plotted here, the atomic frequency stability is superior to the laser, so this measurement represents a near perfect frequency measurement of Si3. Over the course of a 5 hour clock lock, we observe laser drift of about 0.7 Hz at 698 nm. On the right of Fig. 2.9 we plot a modified Allan deviation of the dedrifted frequency record in red as well as the expected thermal noise floor of Si3 as a dashed black line. This remarkable laser performance of $\sim 4 \times 10^{-17}$ is what allowed us to perform many of the experiments described in this thesis.

When using this system as a clock, that is outputting a timing signal based upon an atom steered laser, the total noise performance is a combination of laser noise, atomic noise, and atomic servo response. We illustrated this process in Fig. 2.10. At times shorter than the first integrator, laser noise is the dominant noise source. Because we periodically measure the laser frequency, we inherit all the high frequency laser noise. The Dick effect, aliasing of laser noise from this approach, contributes statistical uncertainty [38]. Using a model of the Si3 laser system developed by Eric Oelker, we estimate this effect given different experimental parameters at 5×10^{-17} $1/\sqrt{\tau/\mathrm{s}}$ [114]. Once the atomic servo is engaged, the output frequency will average as $1/\tau$ until reaching the Dick effect limit, where it begins to average as white frequency noise.

The statistical uncertainty of a non-entangled atomic frequency measurement is limited by quantum projection noise (QPN). QPN arises since each frequency measurement involves projecting the atomic population into either the ground or excited clock states, leading to binomial population statistics. The variance σ^2 of the measured excitation fraction can be written as a function of the average excitation fraction $\bar{\rho}^{ee}$ [62]:

$$\sigma^2 = N\bar{\rho}^{ee}(1-\bar{\rho}^{ee}), \tag{2.4}$$

where N is the atom number. QPN is maximize when $\bar{\rho}^{ee} = 1/2$ and minimized at $\bar{\rho}^{ee} = 0, 1$. When applied to an atomic clock, excitation fraction noise is mapped onto frequency noise via the Rabi lineshape. The resultant frequency noise for Rabi spectroscopy of pulse time T_{Rabi} is,

$$\delta_{QPN} = \frac{0.264}{T_{Rabi}}\sqrt{\frac{T_{Rabi}+T_{dead}}{N}}\frac{1}{\sqrt{\tau}}, \tag{2.5}$$

where T_{dead} is the dead time between spectroscopy times and τ is the averaging time. For a small sample of 10^4 atoms, $T_{Rabi} = 1$ s, and $T_{dead} = 1$ s, the QPN limit is $< 10^{-17}/\sqrt{\tau/\text{s}}$, shown as the dashed black line in Fig. 2.10. Although we can reduce QPN by an order of magnitude, there will be no gains in noise performance as the output frequency will be Dick effect limited. After averaging $> 10^3$ s, the final uncertainty limit of the clock signal will now be dominated by the systematic uncertainty, 8×10^{-19} [2], plotted as a green line. For timing signals, the clock systematic accuracy is the ultimate frequency uncertainty limit.

2.6 Imaging Spectroscopy

Although standard practice in many cold atom experiments, imaging atomic samples is a rarely used technique in optical lattice clocks. Yet imaging has been a critical tool in allowing us to extend the performance of Sr1. We use a Andor EMCCD camera with an imaging objective that gives us 6 μm resolution, limited by the pixel size of the sensor. For every shot of the experiment,

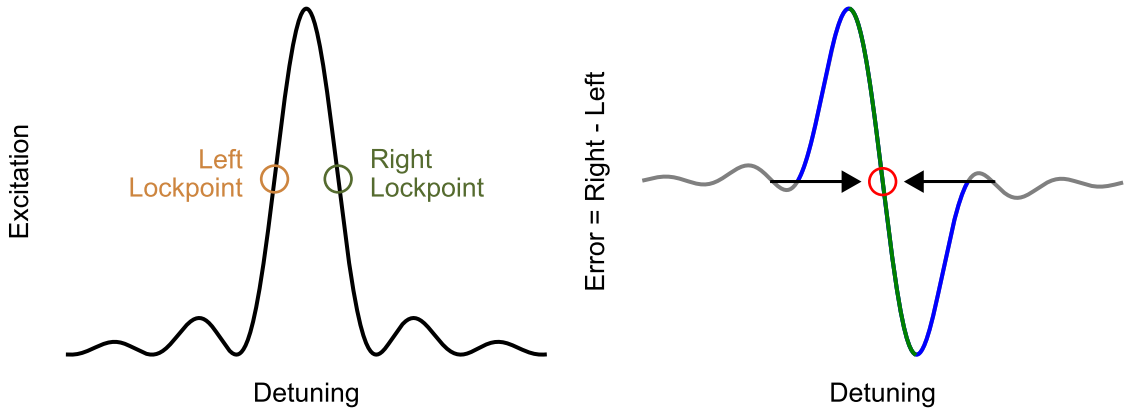

Figure 2.7: Rabi line feedback during spectroscopy. Each Rabi line is probed with two fixed frequencies detuned from resonance at the full width half maximum points. These "left" and "right" lock points are highlighted by circles on the Rabi lineshape on the left. The difference in excitation fraction forms the error signal, shown on the right, allowing us to determine the true transition frequency. A servo seeks to eliminate the difference in excitation. The blue indicates the full capture range of the servo and the green indicates the region of unambiguous frequency determination.

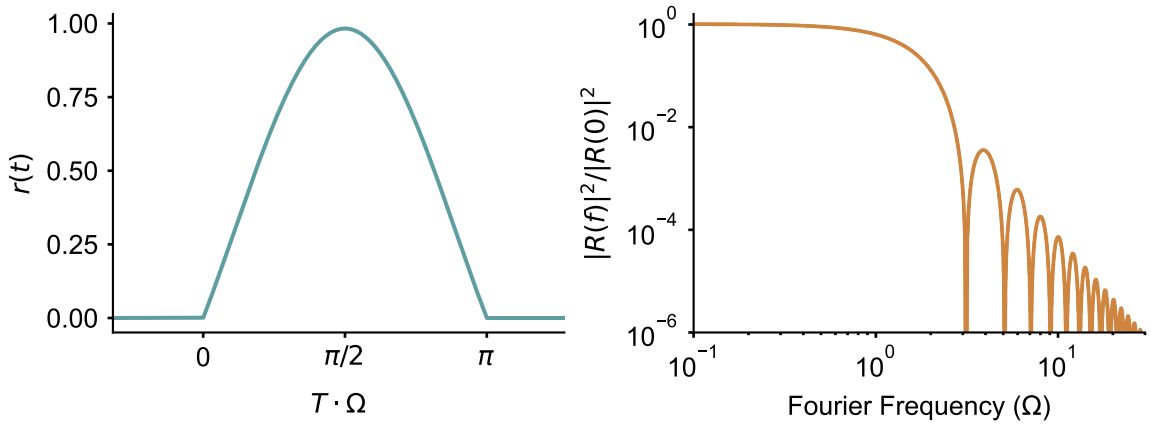

Figure 2.8: Rabi spectroscopy sensitivity. Left: the sensitivity $r(t)$ as a function of spectroscopy time T/Ω, where Ω is the Rabi frequency. Right: normalized Fourier transform of the sensitivity function, $R(f)$. Rabi spectroscopy acts as a low pass filter, with attenuated sensitivity to laser noise above the Rabi frequency.

we take a picture of the ground state atoms $\{g\}$, excited state atoms $\{e\}$, and a background image $\{b\}$. Performing all these steps carefully is critical to reliable, accurate imaging.

We calibrate the pixel size using a standard time of flight technique. We prepare a red MOT,

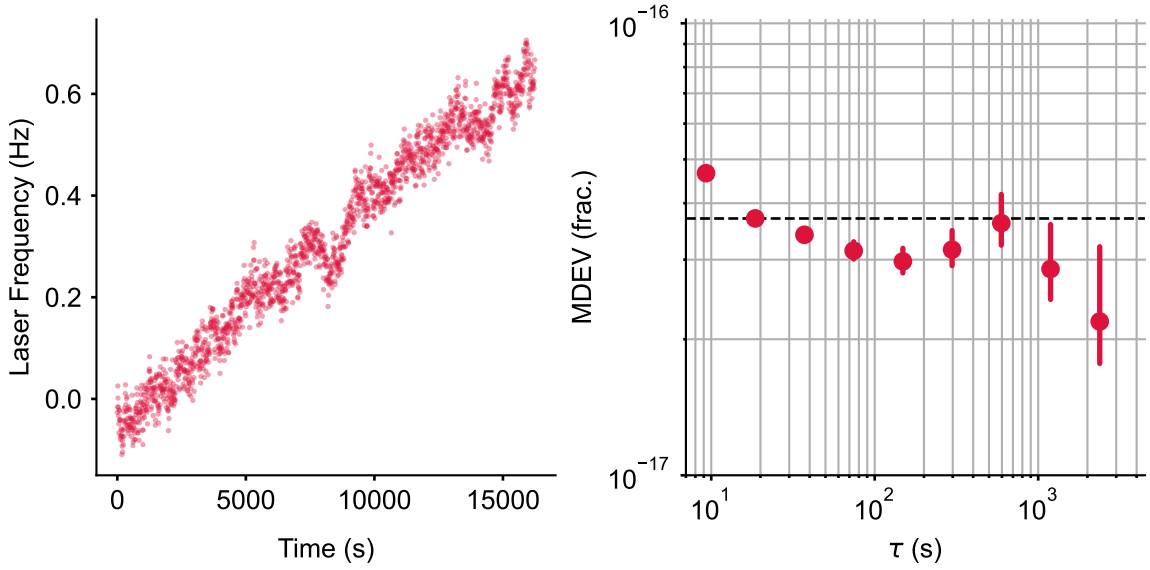

Figure 2.9: Even with no systematic corrections, the Sr atoms are typically a much better frequency reference than the clock laser at all averaging times. Thus clock spectroscopy is really a measurement of laser frequency stability. Left: the relative frequency of the silicon laser during a 5 hour clock lock. Right: a modified Allan deviation (MDEV) of the dedrifted frequency record. The dashed black line indicates the expected thermal noise floor of the Si3 laser [114].

release it into free fall, wait for some time, and then image on the $^1P_1$ transition. At each free fall time, we take an averaged picture over many shots and fit a gaussian along both dimensions. In a UHV system with a non interacting cloud of atoms, this motion is effectively perfect free fall, and allows us to precisely characterize a pixel size of 6 μm as well as any tilt of the imaging plane with respect to gravity. Through the spread of the cloud over time we determine a red MOT temperature of around 2 μK. We also see no correlations between neighboring pixels, meaning this size is the true resolution of our complete imaging system [94].

In standard operation, atom imaging takes place in the lattice. We scatter blue photons on the $^1S_0 \rightarrow {}^1P_1$ transition using a "probe" beam along one axis of the MOT, perpendicular to the imaging viewport. As more photons are scattered, the signal increases but spatial information is lost as the atoms heat up and move. We find an optimal imaging time of 25 μs, scattering as many photons as possible while preserving our resolution, and image in a 300 E_r deep lattice to keep the atoms confined as long as possible. We collect about 3 photons per atom. Since our sample is about

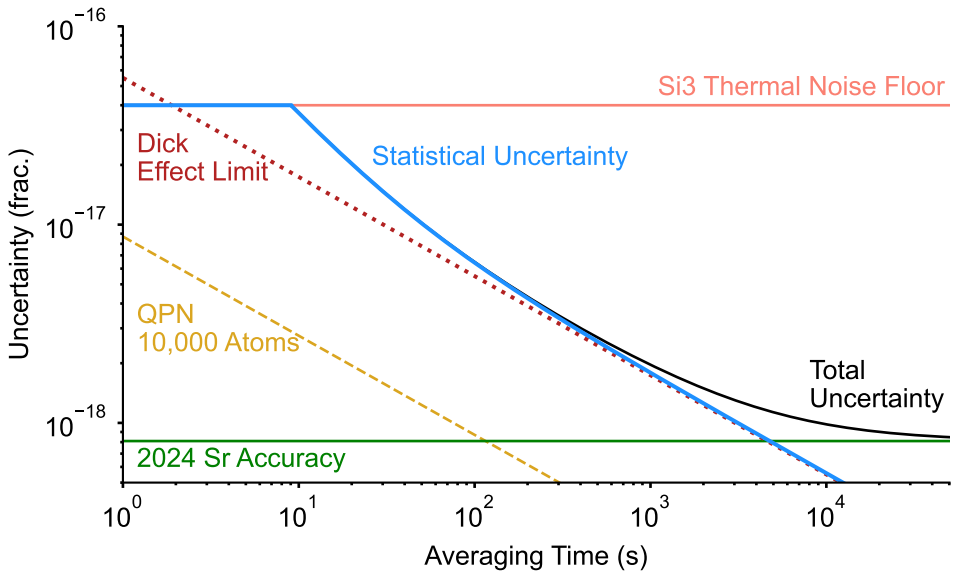

Figure 2.10: Projected clock uncertainty as a function of averaging time. At short times, the clock laser noise dominates, shown as the salmon colored line for the Si3 flicker noise floor. Once the "clock lock" servo is engaged, the frequency output is stabilized to the atoms and averages with a Dick effect noise limit determined by the operating parameters as $5 \times 10^{-17}\ 1/\sqrt{\tau/\mathrm{s}}$. Operating with just 10^4 atoms reduces quantum projection noise to $< 10^{-17}/\sqrt{\tau/\mathrm{s}}$. At long times, the largest source of uncertainty is due to the systematic accuracy of the clock, 8.1×10^{-19} for the new Sr1 system.

2 mm in length and 100 μm in width, we need a probe beam that is large enough to uniformly illuminate the atoms. A cylindrical lens pair adjusts the beam aspect ratio to increase the power along our atom axis. To measure the intensity of probe light, we observe how the counts vary as we attenuate the probe and fit a saturation intensity I_{sat}. Typically, the probe intensity is $20 - 30\ I_{sat}$, so intensity fluctuations across the sample lead to only small effects in the total number of collected photons. To calibrate the atom number, we measure the QPN noise as a function of $\bar{\rho}^{ee}$ [94]. Using Eq. 2.4, we determine an atom number per camera count over a range of different camera settings.

We have observed that for our short imaging probe time, about 0.1% of the imaged atoms are not heated out of the lattice. Without removing this population, it will skew the excitation fraction measurements. The imaging sequence begins by ramping the trap depth from the spectroscopy depth to $\sim 300\ E_r$. We first image the ground state $\{g\}$ and then turn on the probe for 10 ms to remove all atoms that were not heated out of the trap. Then we apply the repump lasers to shuffle atoms

out of ${}^3P_0$ to ${}^1S_0$, scattering a few photons per atom in the process. Imaging of $\{e\}$ occurs in much the same way, with the short imaging pulse and then a longer pulse to remove all the atoms. Lastly, the $\{b\}$ image is taken with the probe light on for the same duration. We use $\{b\}$ to subtract out any effects that are common to the ground and excited state images, including hot pixels on the camera, dark counts, ambient light, and reflected light from the imaging probe. We typically sum all counts along the radial direction, preserving only the axial information along the lattice direction. This is done on camera, reducing the total data we store and increasing the read speed of this older model.

For clock lock feedback, we use the average excitation fraction of the whole sample, effectively treating the camera like a single pixel. This keeps the feedback processing simple and efficient, however realtime spatial processing may be included for removing systematic shifts from an output frequency. In post processing, we use all the spatial information we collect along the axial direction to correct for systematic shifts and understand our system. There are two composite images we use, the total atom number, $\{n\} = \{g\} + \{e\} - 2\{b\}$, and the excited state fraction, $\{\rho^{ee}\} = (\{e\} - \{b\})/\{n\}$.

To illustrate our processing approach, we present a characteristic clock lock measured December 16, 2024. This is the same lock as the Si3 frequency record shown in Fig. 2.9. This lock uses about 5×10^4 total atoms, a 1.15 s spectroscopy time, and a total duration of 5 hours. We begin processing by applying data cuts to remove bad points, as shown in Fig. 2.11 for a characteristic lock run. We typically remove the first 10 to 20 cycles of the clock lock so that any transients from engaging the clock servo have settled. We then remove all cycles where one of the lock points had fewer atoms than a certain threshold, shown on the top plot of Fig. 2.11. We occasionally lose atoms due to unlocked lasers or system control issues. By setting this threshold to $10^3 - 10^4$ atoms, we remove cycles where we are actively locking lasers during the sequence leading to a reduced signal. Next, we remove cycles where the excitation fraction has large excursion, as shown on the bottom plot of Fig. 2.11. With a proper lock, the excitation fraction is centered around 0.5 with excursions due to magnetic field and laser noise. We want to exclude any times where the clock laser becomes unlocked and the excitation fraction goes to 0. Additionally, there is frequency ambiguity at the extremes of the lineshape, shown in the error signal plotted in Fig. 2.7, and applying cuts can reduce this effect.

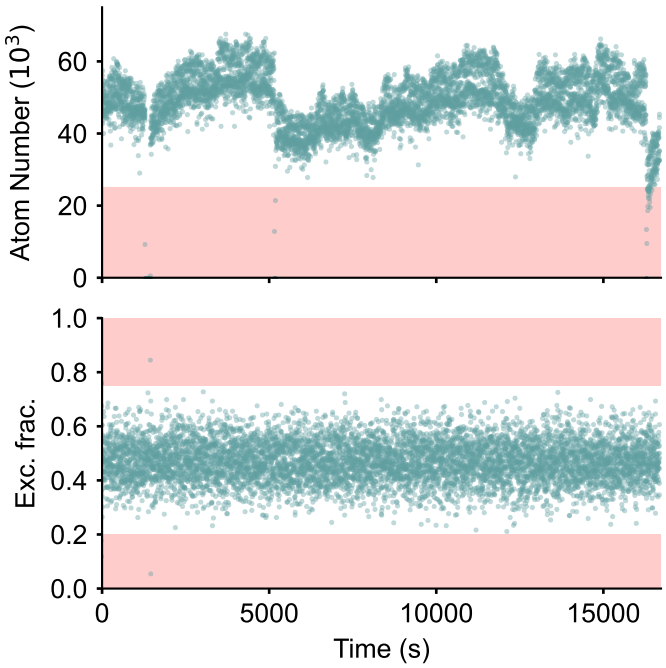

Figure 2.11: The measured atom number (top) and excitation fraction (bottom) for a representative clock lock where we track the clock laser. The red regions show the data points that we exclude, where the atom number is too low or the excitation fraction exceeds reasonable bounds.

For spatial analysis, we select only the central region of the sample and remove the low atom wings. Fig. 2.12 illustrates this process. We fit a gaussian to the averaged total atom number $\{\bar{n}\}$, and exclude pixels that are beyond some multiple of the gaussian width σ. Typically this multiple is 1.5 to 2.5, and is chosen to maximize the total number of usable pixels without having the camera read noise rise above the quantum projection noise.

In Fig. 2.13, we demonstrate how we use this filtered data to construct in-situ frequency maps of the sample. Each lock contains four lock points, $\sigma^{\pm}$ R and $\sigma^{\pm}$ L. These refer to the magnetic sublevel transition $m_F^g = \mp 5/2 \rightarrow m_F^e \mp 3/2$ and right (positively detuned) and left (negatively detuned) lock point dithers. The average excitation of these four points is plotted on the left of Fig. 2.13. The average excitation fraction is near 0.5, and it is immediately obvious that excitation is correlated across the sample.

Before each lock, we scan out and fit a Rabi lineshape for each transition. We use the fitted

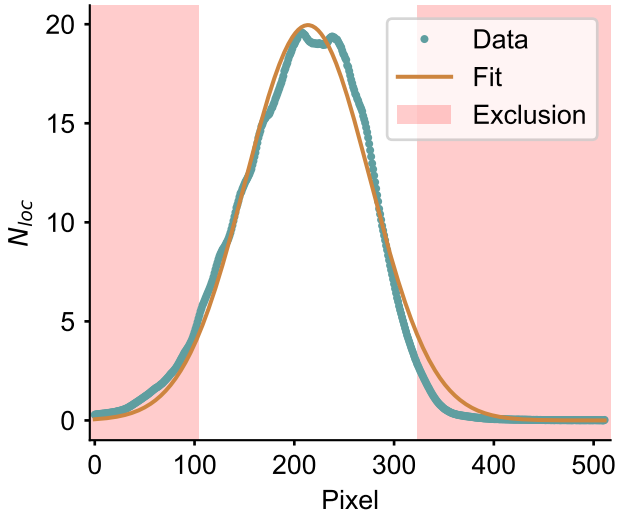

Figure 2.12: At the edges of our sample, noise can cause erroneous measurements. To reduce this effect we fit a Gaussian (rust colored line) to the cloud (teal points), plotted as on-site density N_{loc}. We exclude points which fall outside of 1.5 to 2.5 times the gaussian width σ, depending on operation conditions. Here, we use pixels within 1.75 σ.

parameters to construct an error signal that takes into account the line contrast, Rabi frequency, and spectroscopy time. Using a carefully measured and fit Rabi line is critical for proper conversion to frequency, and errors here become errors in all in-situ corrections, such as the density shift or second order Zeeman shift. In typical locks, the error signal is calculated for the laser, generating a frequency correction. Since the goal is to understand shifts within the sample, our error signal has the opposite sign. Through this error signal, we take the R and L excitation points and convert them to frequency at each pixel for each transition, shown in the center of Fig. 2.13. The largest gradient in our system is typically the magnetic field, so as expected the frequency of $\sigma^{\pm}$ transitions are anticorrelated.

From these frequency maps for each transition, we take the average and difference frequency, as shown on the right of Fig. 2.13. The average frequency $\nu_{center} = (\nu_{\sigma^-} + \nu_{\sigma^+})/2$ shown in blue rejects first order Zeeman shifts, allowing us to study shifts independent of m_F sensitivity. The difference frequency $\nu_{\Delta} = (\nu_{\sigma^+} - \nu_{\sigma^-})/2$ contains information about the magnetic field and rejects common shifts such as the density shift.

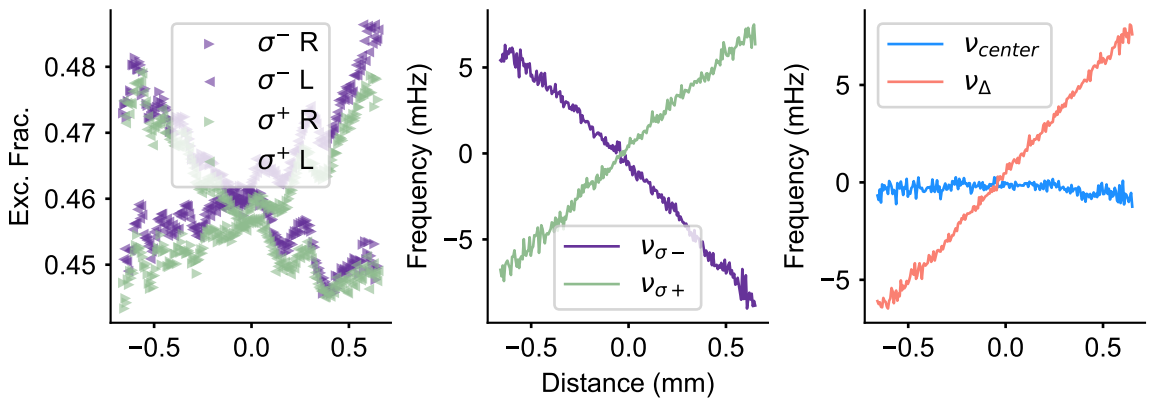

Figure 2.13: We begin processing a clock lock by constructing average maps of the sample. Left: the average excitation fraction for both spin state transitions and both sides of the line. From this map and the Rabi lineshape, we can extract the frequencies of the two transitions across the sample, $\nu_{\sigma\pm}$, shown in the center. Right: The transition average frequency, $\nu_{\text{center}} = \frac{1}{2}(\nu_{\sigma+} + \nu_{\sigma-})$ and difference frequency $\nu_\Delta = \frac{1}{2}(\nu_{\sigma+} - \nu_{\sigma-})$.

With ν_{center} and ν_Δ in hand, we now study systematic shifts throughout the sample. The density shift is proportional to the atom number. We fit a line to $\nu_{\text{center}}(n)$, and use this slope and the density information to calculate the shift at each pixel, shown in Fig. 2.14, with more details presented in Ch. 4. We correct for the second order Zeeman effect using the field gradient information from ν_Δ. Further details about the second order Zeeman effect are in Ch. 7.3. Corrected frequencies for each pixel are shown in blue on the right of Fig. 2.14. The error bars contain the standard error for each frequency combined with the uncertainty associated with each correction. The red line is a linear fit to the data, with a fitted fractional frequency slope of $-(1.31 \pm 2.0) \times 10^{-19}$ $(\text{mm})^{-1}$.

After properly applying frequency corrections to each pixel, the resultant gradient across the sample is due to the gravitational redshift. The gravitational redshift creates a frequency difference $\delta\nu$ between two clocks:

$$\frac{\delta\nu}{\nu} = \frac{gh}{c^2}, \tag{2.6}$$

where g is the local gravitational acceleration, h is the height difference between clocks, and c is the speed of light. In our lab where $g = -9.796$ m/s^2 [152], $\delta\nu/\nu - 1.09 \times 10^{-19}$ mm^{-1}, so this example lock is has a gradient consistent with the gravitational redshift across the sample. I will not discuss

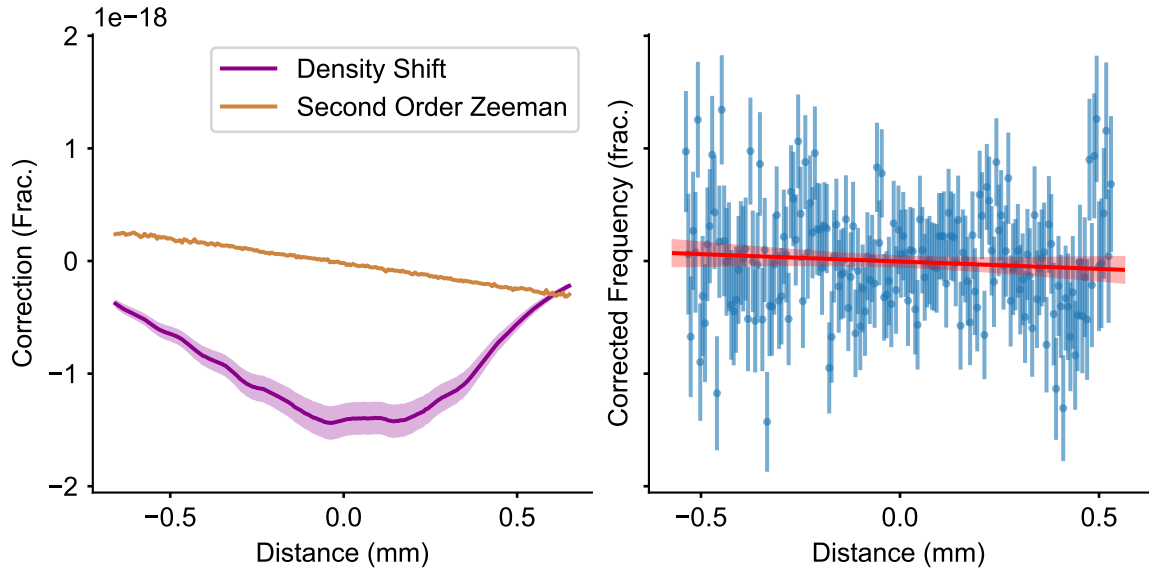

Figure 2.14: Using in-situ frequency imaging, we correct for spatial gradients throughout the sample. Left: we fit a linear slope to ν_{center} as a function of atom number and remove this effect at each pixel, shown in purple with the highlighted area showing the uncertainty. The second order Zeeman gradient is calculated using ν_Δ and plotted in gold. Right: after correcting the density shift and second order Zeeman effect, the corrected frequencies are shown in blue with error bars indicating the standard error plus correction error. To this, we fit a linear slope of $-(1.3 \pm 2.0) \times 10^{-19}$ $(\text{mm})^{-1}$, shown in red, which contains the gravitational redshift.

in-situ measurement of the gravitational redshift further, as the data processing described here is the same technique we used to measure the gravitational redshift reported in Ref. [22].

Other shifts can appear in this corrected signal, so care must be taken. For example, if the spin states have different atom number or different temperature, the density shifts differ. Thus the ν_Δ signal will be polluted by the density shift, and ν_{center} will contain magnetic field information, leading to improper gradient corrections. Additionally, thermal gradients throughout the chamber, lattice light shift gradients from radial temperature variation, and DC stark shift gradients can all cause redshift measurement errors. These error sources and more are discussed in the supplement of Ref. [22].

The self-synchronous stability between two regions of the sample removes common laser noise, so the fundamental noise source should be due to the atomic signal, ideally QPN. Fig. 2.15 illustrates

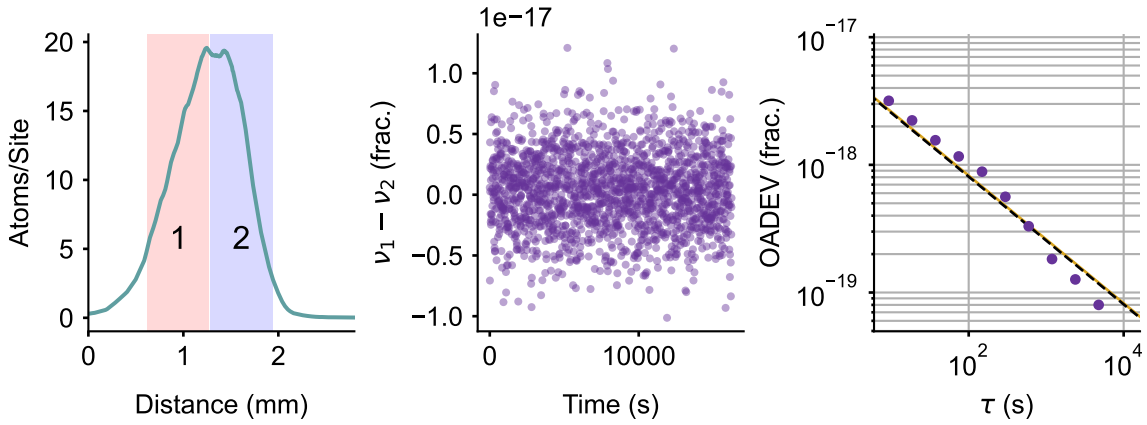

Figure 2.15: Self-synchronous stability for a clock lock. Left: we divide the sample into two equal size and atom number regions, 1 and 2 highlighted in red and blue. Center: the frequency difference between the two regions, $\nu_1 - \nu_2$. Right: an overlapping Allan deviation of the frequency difference, indicating no flicker and averaging below 10^{-19} for this lock. The black dashed line is the expected quantum projection noise, $8.1 \times 10^{-18}/\sqrt{\tau/\mathrm{s}}$, and the gold line is a fit to the OADEV, $8.2 \pm 0.1 \times 10^{-18}/\sqrt{\tau/\mathrm{s}}$. In this lock, our frequency instability is consistent with a QPN limit, with the total instability $< 7 \times 10^{-20}$ at full averaging time.

how we study synchronous stability within the system. We split the sample into two equal size and atom number regions, labeled 1 and 2 on the left plot of Fig. 2.15. For each region, we calculate the frequency $\nu_{1,2}$ and then take the difference, shown in the center. Since the laser noise is common between the two regions, $\nu_1 - \nu_2$ contains only atomic noise. On the right of Fig. 2.15 we take an overlapping Allan deviation (OADEV) of the frequency difference. The dashed black line is the expected quantum projection noise, $8.1 \times 10^{-18}/\sqrt{\tau/\mathrm{s}}$, and the gold line is a white frequency noise fit, $8.2 \pm 0.1 \times 10^{-18}/\sqrt{\tau/\mathrm{s}}$. This result indicates that for this lock, synchronous measurements are quantum projection noise limited.

Under certain conditions, the synchronous stability does not match the QPN expectation. For example, in our redshift measurement work, Ref. [22], the measured instability was over a factor of 2 larger than the calculated QPN limit. We theorized that readout noise could contribute to higher than expected instability. While this is certainly possible, we now understand this excess instability as stemming from frequency excursions into the ambiguous region of the Rabi lineshape error signal, leading to poor frequency reconstruction. Increase the spectroscopy time reduces the

capture range of the lock as well as increasing the total phase excursion of Si3. In Ref. [22], we used a 3 s spectroscopy time. Since Rabi spectroscopy generates a robust locking signal, the clock lock still tracks the laser drift, but spectroscopy points occasionally occur beyond the intended side of the line. Reconstructing the frequency using the error signal, these points add noise to the frequency record as they flip the sign of the gradient. This can greatly increase the measured instability. With more aggressive excitation fraction cuts removing these points, we can often recover the expected QPN performance. By reducing the spectroscopy time to < 2.5 s, we generally observe instabilities consistent with QPN. The lowest instabilities with Rabi spectroscopy we have observed between two regions are $< 4 \times 10^{-18}/\sqrt{\tau/\mathrm{s}}$.

Chapter 3

Atoms In A Lattice

Where are my atoms? And what are they doing? Understanding the motional state of atoms is critical for precise spectroscopy. Key to our system is the use of a shallow, 1D optical lattice oriented vertically. Atoms are supported against gravity, allowing us to probe the clock transition for prolonged periods of time to reduce QPN. By tightly confining the atoms, we are able to drive the optical clock transition with no photon recoil or thermal Doppler broadening, but this modifies atom-atom interactions and introduces a lattice light shift. Characterizing these shifts requires knowledge of the external atomic state. We use the clock transition to probe these energy scales far below the recoil or Doppler broadening limit.

The motion of particles in a lattice has been extensively researched throughout condensed matter physics [16]. As cold atom tools were refined in the 1990s, physicists could directly study the dynamics of atoms in lattices [63, 90, 150]. Certain considerations arise when applying this physics to understand optical lattice clocks, as more recent work has shown [27, 74, 165].

A simple 1D lattice system realizes Bloch bands. By lifting the energy degeneracy between lattice sites, atoms are localized in Wannier-Stark eigenstates. The advantageous nature of a Wannier-Stark optical lattice clock was first discussed theoretically by Pierre Lemonde and Peter Wolf in 2005 [79]. This work has served as a guiding text for much of our understanding of the Sr1 system. While a 1D approximation is generally appropriate for the majority of our studies, occasionally it becomes necessary to consider the radial degree of freedom. Atoms are confined via a standing wave Gaussian beam with the wave vector $\vec{k}$ oriented along gravity. Expressed in

cylindrical coordinates, (Z, r), the potential U is:

$$U(Z,r) = -U_0 \cos^2(kZ) e^{-2r^2/w_0^2} + MgZ. \tag{3.1}$$

U_0 is the peak lattice depth, ω_0 is the lattice waist, 260 μm in our system, M is the mass of strontium, and g is the local gravitational acceleration. We will denote motional states in this potential with the quantum number $n_{X,Y}$ for the radial direction and n_Z along $\hat{Z}$. The index n identifies the lattice site where the particle is localized.

3.1 Bloch Bands

A well studied problem in condensed matter physics, the free electron model of metals is a good place to start in understanding our system. In this model, electrons in a metal are assumed to be free particles, having a quadratic relationship between energy and momentum k and energy E that can take any real value. In 3-dimensions, the energy E is

$$E_{\vec{k}} = \frac{\hbar^2}{2M} \left(k_X^2 + k_Y^2 + k_Z^2 \right). \tag{3.2}$$

The solutions to this model are running waves:

$$\psi_k(\vec{r}) = \exp(i\vec{k} \cdot \vec{r}), \tag{3.3}$$

where $\vec{r}$ is the position and the momentum of the wave $\vec{p} = \hbar\vec{k}$.

As confinement is added, such as a positively charged lattice with an electron gas or an optical lattice filled with neutral strontium, the dispersion relationship is modified. Consider a particle trapped in a 1-dimensional potential along the Z axis. The Hamiltonian H describing this system is

$$H = \frac{p^2}{2M} + V(Z), \tag{3.4}$$

where p is the momentum operator, M is the mass of the particle, and $V(Z)$ is the potential at position Z. A periodic potential, like optical lattice, has translational symmetry such that

$$V(\vec{r}) = V(\vec{r} + \vec{a}), \tag{3.5}$$

where $\vec{a}$ is the lattice vector. Felix Bloch proved the solution to such a periodic potential can be written as a plane wave incorporating this translation symmetry momentum [16]:

$$\psi_{\vec{q}}(\vec{r}) = e^{i\vec{q}\cdot\vec{r}/\hbar} u_{\vec{q}}(\vec{r}), \tag{3.6}$$

where $\vec{q} = \hbar\vec{k}$ is the crystal momentum. To respect the translational symmetry, $u_{\vec{q}}(\vec{r}) = u_{\vec{q}}(\vec{r} + \vec{a})$.

Applying the momentum operator $\vec{p}$ we find:

$$\vec{p}\psi_{\vec{q}}(\vec{r}) = e^{i\vec{q}\cdot\vec{r}/\hbar} (\vec{q} + \vec{p}) u_{\vec{q}}(\vec{r}), \tag{3.7}$$

allowing us to write the Schrödinger equation as:

$$H_{\vec{q}} u_{n\vec{q}} = \left(\frac{1}{2M} (\vec{p} + \vec{q})^2 + V(\vec{r}) \right) u_{n\vec{q}} = E_{n\vec{q}} u_{n,\vec{q}}. \tag{3.8}$$

Here, we restricted the solutions to the first Brillouin zone, indexing this with integer n. $E_{n,\vec{q}}$ is the eigenenergy of band n at quasimomentum $\vec{q}$. This periodic potential generates allowable energy bands, with forbidden energy bands between. In our 1D lattice system, we will index the bands with integer n_Z and consider the quasimomentum q along only Z.

To solve Eq. 3.8, we begin by writing the Bloch wavefunctions $u_q^{(n_Z)}(Z)$, in a Fourier expansion with coefficients $c_l^{(n_Z,q)}$ as:

$$u_q^{(n_Z)}(Z) = \sum_l c_l^{(n_Z,q)} e^{iqZ/\hbar}. \tag{3.9}$$

First, we expand the kinetic energy term:

$$\frac{1}{2M}(p+q)^2 u_{n_Z \vec{q}} = \frac{1}{2M}\sum_l (p+q)^2 e^{2ilkZ} c_l^{(n_Z,q)} = \frac{1}{2M}\sum_l (2\hbar kl+q)^2 e^{2ilkZ} c_l^{(n_Z,q)}. \tag{3.10}$$

Next, we will consider our potential in the lab which we expand, $V(Z) = -U_o \cos(kZ)^2 = -\frac{U_0}{4}\left(e^{2ikZ} + e^{-2ikZ} + 2\right)$, where here k is the wavenumber of the lattice. We expand the potential energy term, product of the potential and $u_q^{(n_Z)}(Z)$:

$$V(Z) u_{n_Z \vec{q}} = -\frac{U_0}{4}\sum_l c_l^{(n_Z,q)} \left(e^{i2(l+1)kZ} + e^{i2(lk1)kZ}\right). \tag{3.11}$$

Combining both terms, we can rewrite Eq. 3.8 as an infinite $l \times l$ matrix:

$$\sum_{l'} H_{l,l'} c_l^{(n_Z,q)} = E_q^{n_Z} c_l^{(n_Z,q)}, \tag{3.12}$$

with $H_{l,l'}$ matrix elements as,

$$\begin{aligned} H_{l,l} &= (2l + q/\hbar k) E_r, \\ H_{l,l\pm1} &= -1/4 U_0, \end{aligned} \tag{3.13}$$

and all other elements $H_{l,m} = 0$. E_r is the lattice photon recoil energy, and U_0 is the lattice depth. This governing equation is known as the "central equation" [72]. We can solve for $c_l^{(n_Z,q)}$ numerically by simply restricting the number of lattice sites, as is the case below.

With no confinement $U_0 = 0$, so $H_{l,l\pm1} = 0$ and H becomes diagonal, thus recovering the free particle case. With a small perturbing U_0, band gaps begin to appear at the Brillouin zones, modifying the free particle dispersion curve. With large U_0, particles become confined to specific energy levels known as Bloch bands. The resultant Bloch band energies at three different lattice depths are plotted in Fig. 3.1. Each band is plotted in a different color and U_0 is plotted as a dashed black line. With a shallow lattice depth, the free particle dispersion relationship is only slightly

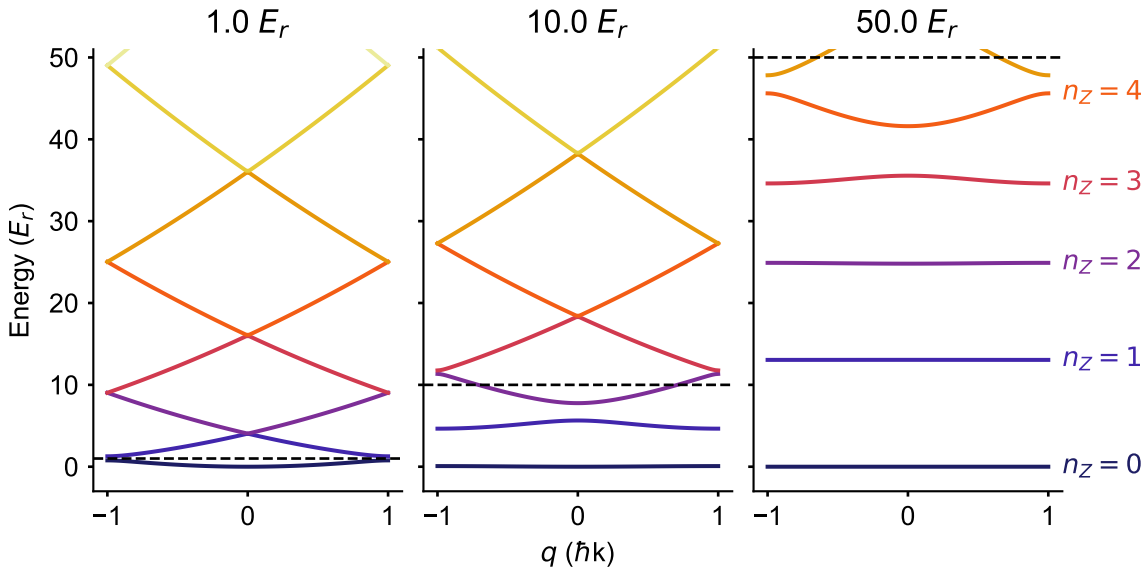

Figure 3.1: Bloch bands at three different lattice depths given in units of lattice photon recoil energies (E_r). At 1 E_r, the lattice perturbs the ground band, with higher energy bands essentially describing free particles. As confinement increases, bands become flatter and the gap between bands grows. The dashed black line indicates the lattice depth in each case.

modified, with the ground band and first excited band gap opening slightly. Where the particle energy is greater than U_0, the particle is unconfined by the potential and experiences only a slight modification of its dispersion. At very deep lattice depths, the bands are flatter and the band spacing is much larger. The tunneling energy, J_0, describes the tunneling coupling between neighboring lattice sites. It is related to the energy width of the ground band, $J_0 = (\max(E_q^0) - \min(E_q^0))/4$, and grows with shallower lattice depth.

3.1.1 Clock Spectroscopy

Using a degenerate lattice (where each lattice site has the same minimum energy) immediately leads to linewidth broadening. The clock photon carries momentum k_c along the lattice direction. Driving from the ground $|g\rangle$ to the excited state $|e\rangle$ necessitates the excited state carry this k_c momentum kick. In free space, this is apparent as the recoil shift. Because a lattice is periodic in q, this is simply a momentum translation of the $|e\rangle$ band with respect to the $|g\rangle$ band. In our system,

$k_c/k_l \approx 7/6$, generating "spin orbing coupling" (SOC) where $|e\rangle$ is offset from $|g\rangle$ in quasimomentum space. In order to drive from $|g\rangle$ to $|e\rangle$, the photon energy must span this difference. Fig. 3.2 illustrates this effect for three different lattice depths. At very shallow depths, the band widths are large, so $|e\rangle - |g\rangle$ becomes large.

SOC creates line broadening, first measured experimentally in a strontium clock in Ref. [74]. We illustrate the origin of this effect in Fig. 3.3. The top set of plots indicate the energy broadening due to spin orbit coupling for three lattice depths, with a calculated line shape plotted in the bottom panels. At very shallow lattice depths, the density of states (DOS) is spread out over $\sim 1\ E_r$, which means that the clock transition frequency becomes split over a similar scale and the resultant linewidth is many kHz broader than the fourier limit. The DOS peak near the edges of the band, leading to the characteristic winged lineshape. To reduce the linewidth due to this effect, operating at a deep lattice is imperative. In Fig. 3.4, we plot the linewidth broadening due to SOC as a function of lattice depth. With a depth below about 100 E_r, SOC broadening exceeds the natural linewidth of Sr, indicated by the dashed line.

Since higher bands have larger bandwidths, even at deep lattice depths, SOC can induce line broadening. With no cooling along the lattice direction, the sample with thermally populate n_Z modes, so the resultant line shape will be an average of these bandwidths. In Fig. 3.5, we plot the line shape of a 2 μK sample at 60 E_r, the typical temperature one might expect out of a red MOT. While most of the sample is in $n_Z < 3$, additional structure emerges at the base of the Rabi line due to higher band SOC, and the line becomes broad.

3.1.2 Wannier States

Wannier functions are eigenstates of Eq. 3.12, typically maximally localized to a single lattice site in contrast to Bloch states. For a lattice site i and band n_Z, the Wannier function is given by

$$w_{n_Z}(x - x_i) = \mathcal{N}^{-1/2} \sum_q e^{-iqx_i/\hbar} \phi_q^{(n_Z)}(x), \tag{3.14}$$

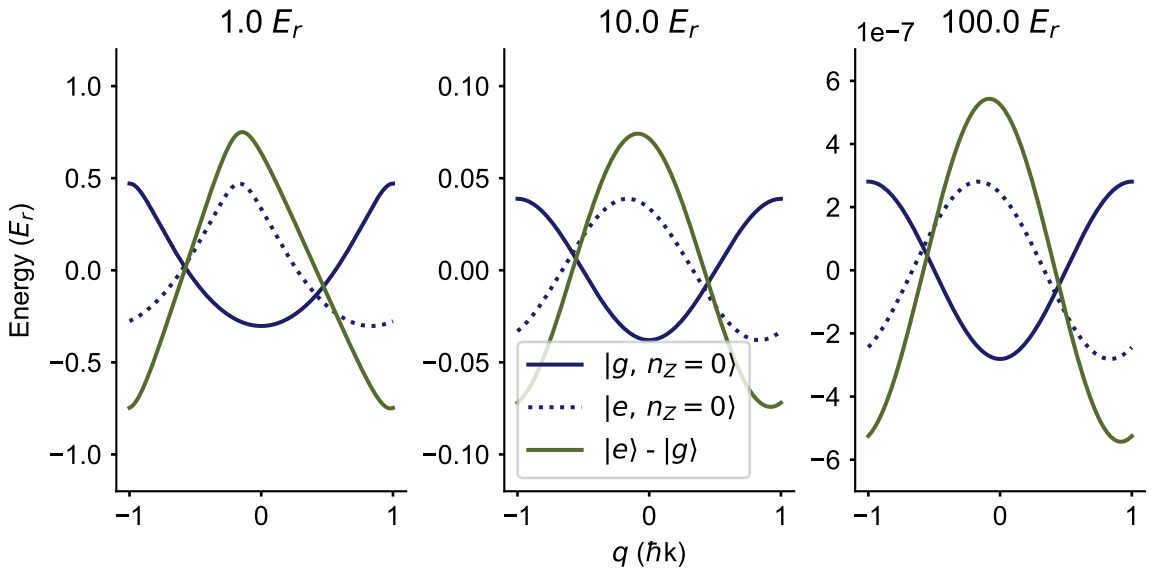

Figure 3.2: Driving clock transition in a degenerate lattice trapped strontium system translates the excited clock state $|e\rangle$ band with respect to the ground clock state $|g\rangle$ band in quasimomentum space q. The clock photon must provide the energy difference between these two bands, $|e\rangle - |g\rangle$. This is plotted for three different lattice depths, with the 100 E_r case showing over 10^6 reduction in broadening with respect to the 1 E_r depth.

where $\mathcal{N}$ is a normalization constant. In Fig. 3.6, we plot the ground band Wannier function $w_0^0(Z)$ of three different lattice depths. As expected, at higher lattice depths, the states become tightly confined to a single lattice depth.

3.2 Wannier-Stark Lattice

So far, we have highlighted the line broadening issues that might plague an optical lattice clock. Fortunately, the solution is rather simple: remove the energy degeneracy between lattice sites. By orienting the lattice against gravity, there now is a potential energy difference between lattice sites, Mga_L, where M is the mass of the particle, g is the gravitational acceleration, and the lattice spacing $a_L = \lambda_L/2$. This action localizes particles to specific sites unless there is sufficient energy to overcome this potential barrier. Now, the eigenstates of this system are described by Wannier-Stark states. Wannier-Stark eigenstates $W_n(Z)$ are given as a sum of Wannier states weighted by the ratio

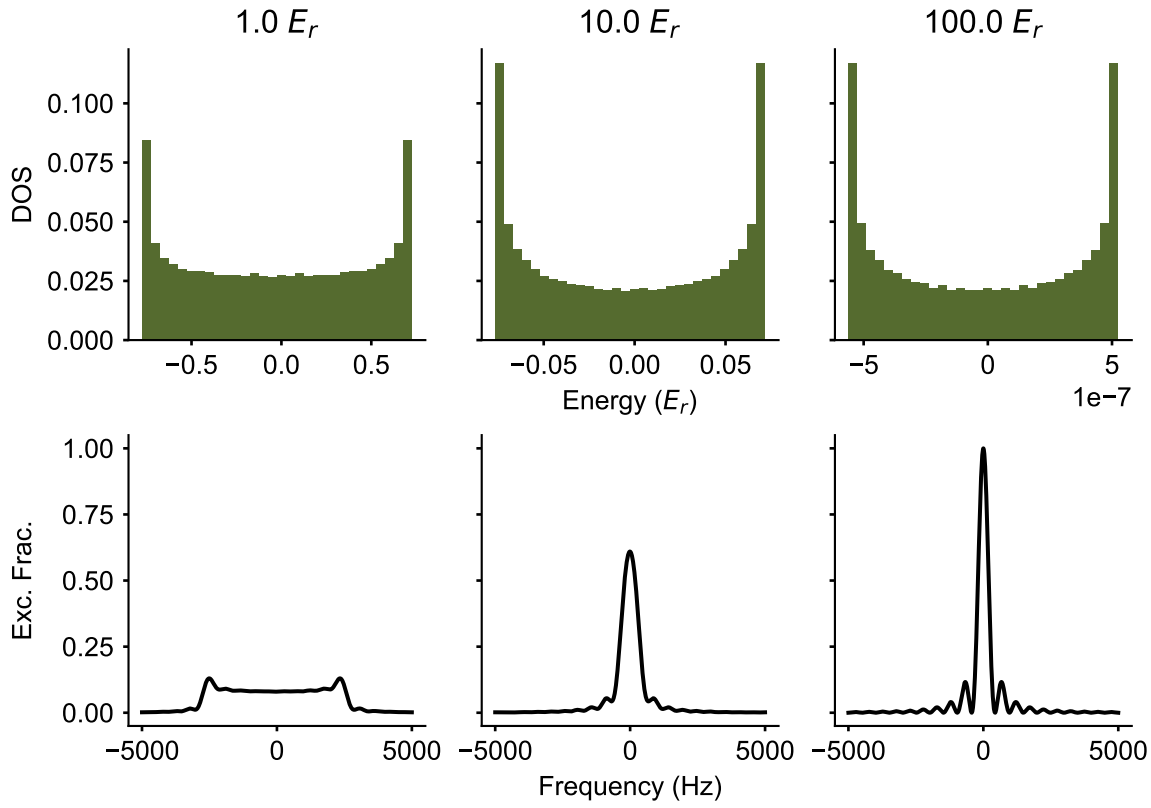

Figure 3.3: Due to the band curvature and coupling under a clock drive, the line shape is broadened. Top: the density of states (DOS) under a clock drive for three different lattice depths. Bottom: the resultant line shape with SOC broadening.

of the tunneling energy to the energy offset between neighboring lattice sites [49]:

$$W_n(Z) = \sum_m \mathcal{J}_{m-n}\left(\frac{2J_0}{Mga_L}\right) w_{n_Z}(Z - ma_L), \tag{3.15}$$

where n is the site index, $\mathcal{J}$ is a Bessel function, and J_0 is the ground band nearest-neighbor tunneling energy:

$$J_0 \approx (4/\sqrt{\pi}) E_{rec}^{1/4} V_0^{3/4} \exp[-2\sqrt{V_0/E_{rec}}]. \tag{3.16}$$

In Fig. 3.7, we plot the ground band Wannier-Stark states for three different lattice depths. At deep depths, the wavefunction is strongly localized to a single lattice site and closely resembles a Wannier state. At very shallow depths, the wavefunction extends over a number of neighboring lattice sites.

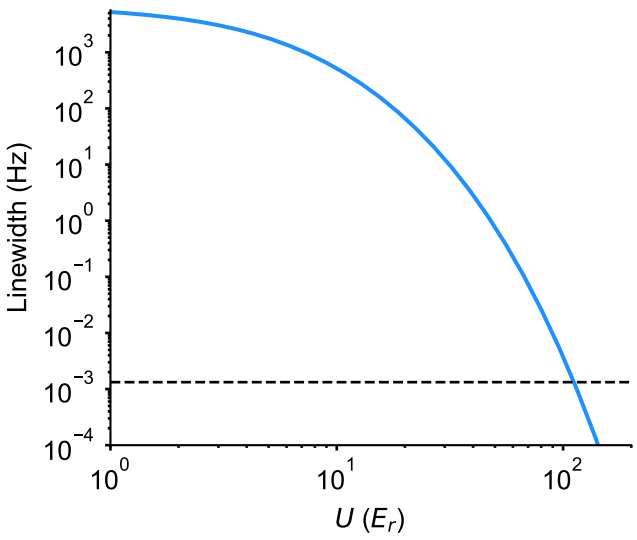

Figure 3.4: The linewidth broadening due to spin orbit coupling as a function of lattice depth U for a $n_Z = 0$ sample. The natural linewidth of ^{87}Sr is plotted as a dashed black line [105]. One of the long term goals, clock spectroscopy near the excited state lifetime, is only feasible with $U > 100\ E_r$.

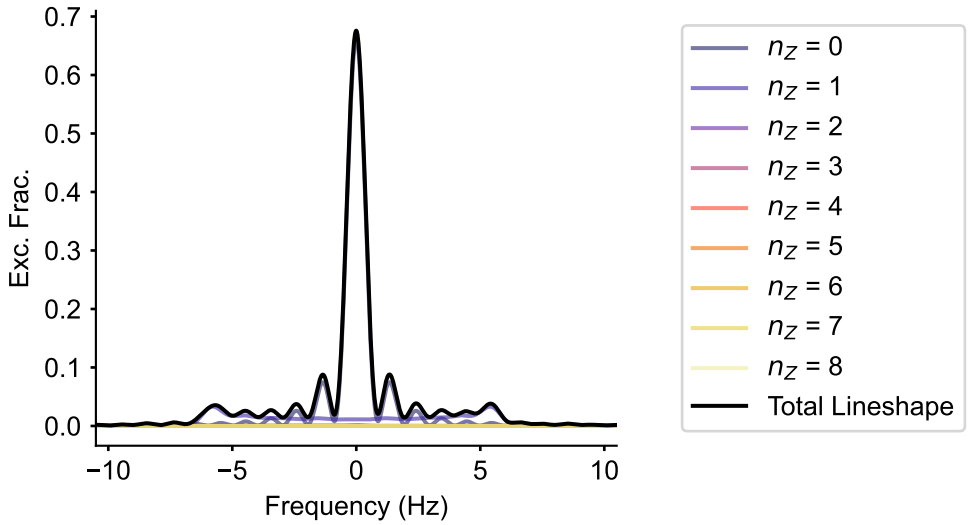

Figure 3.5: Broadening due to higher band population. With a thermal distribution of n_Z states at 2 μK and 60 E_r, higher band populations broaden the resultant line shape, apparent as an excitation pedestal around the line shape base.

Nevertheless, particles remain pinned to a single lattice site. Wannier-Stark wavefunctions are metastable; the particle will eventually tunnel to the continuum [90, 112]. However this timescale for

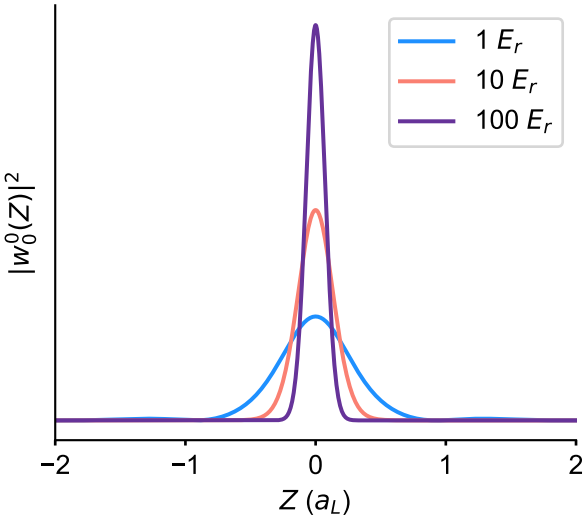

Figure 3.6: The localized states of a degenerate 1D optical lattice are described by Wannier functions, Eq. 3.14, plotted here for three different lattice depths.

our system is generally very long, and for all practical purpose we can treat the atoms as occupying static eigenstates. There are a number of other approaches for calculating Wannier-Stark states, including numerically solving for eigenstates of a finite lattice potential as we did in Ref. [70], treating the problem with scattering formulism as in Ref. [48], or solving a modified differential equation as in Ref. [79].

Like in the degenerate case, there are higher bands denoted by n_Z localized to each lattice site. At higher energies, the bands are more delocalized than the ground band. In a deep lattice, $W(Z)$ approaches a single site w_{n_Z} function, so band spacing is the same as in a degenerate lattice. The spectroscopic signal of shallow lattice excited bands is shown in subsequent sections.

In a clock system, we drive $|g\rangle \rightarrow |e\rangle$, so the resultant Rabi frequency is an integral over these states linked with a clock photon. Since the available energies are discrete values and not broad bands, there is no lineshape broadening except where the energy scales are not resolvable, when $\Omega_0 > Mga_L/h$. To good approximation, the clock laser is a plane wave, so the Rabi frequency Ω_i

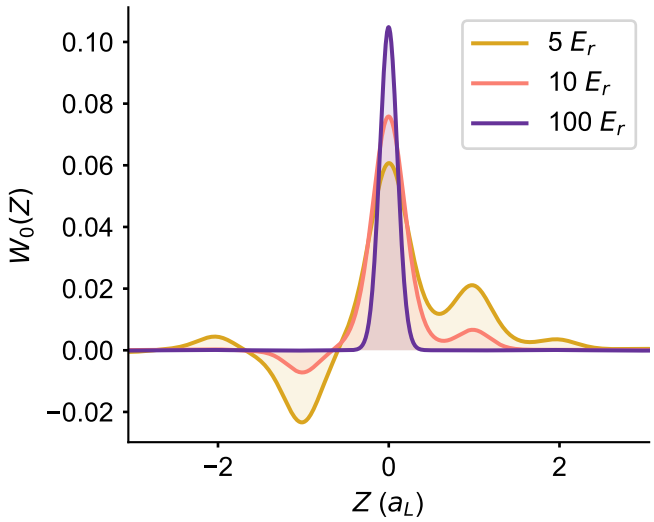

Figure 3.7: Wannier-Stark wavefunctions at different lattice depths. At deep depths, the wavefunction resembles Wannier states, see Fig. 3.6. At shallow depths the particle is still confined to a single lattice site but has wavefunction extent over neighboring sites.

between Wannier-Stark states W_n and W_{n+i} becomes,

$$\Omega_i = \Omega_0 \langle W_{n+i} | e^{ik_c Z} | W_n \rangle, \tag{3.17}$$

where Ω_0 is the peak Rabi frequency and k_c is the clock laser wave number. We label these transitions "WS+i." The relative Rabi frequencies between these different transitions over a range of experimentally achievable depths U is plotted in Fig. 3.8. At deep lattice depths where the wavefunction is strongly confined to a lattice site, only the $i = 0$ carrier transition can be feasibly driven. At lower lattice depths, offsite $|i| > 0$ transitions have much stronger Rabi frequencies, even surpassing the carrier transition $U < 5\ E_r$. Since higher bands are more delocalized, the off-site Rabi frequencies increase as n_Z increases.

3.3 Radial Motion

Until now, we have only considered a 1D system, yet reality is a bit messier, and we must discuss the radial axis. We begin by treating the radial and axial degrees of of freedom as separate.

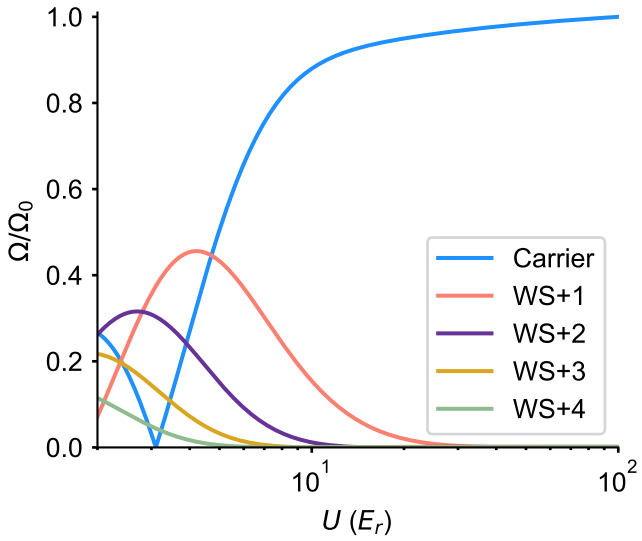

Figure 3.8: Relative Rabi frequencies Ω/Ω_0 as a function of lattice depth. Off-site transitions, WS+i where $i > 0$, increase in strength at lower lattice depths.

With a cold atomic sample, to good approximation we can treat the Gaussian trapping potential in Eq. 3.1 to first order in r:

$$U(r) = U_0 e^{-2r^2/w_0^2} \approx U_0 \left(1 - \frac{2r^2}{w_0^2}\right). \tag{3.18}$$

This gives us a quadratic potential in the radial direction with trapping frequency $\nu_r = \sqrt{U_0/M\pi^2 w_0^2}$. While this simplification is often adequate, higher order corrections are necessary for precision measurements of the lattice trapped sample. Following the approach in Ref. [15], we write the confining potential to quartic order incorporating axial and radial coupling as:

$$U(Z,r) \approx U_0(-1 + k^2 z^2 + \frac{2}{w_0^2} r^2 - \frac{k^4}{3} z^4 - \frac{2k^2}{w_0^2} z^2 r^2). \tag{3.19}$$

The eigenenergies of this system are,

$$E_{\mathbf{n}}/h \approx \nu_z \left(n_z + \frac{1}{2}\right) + \nu_r(n_x + n_y + 1) - \frac{\nu_{rec}}{2}\left(n_z^2 + n_z + \frac{1}{2}\right) - \nu_{rec}\frac{\nu_r}{\nu_z}(n_x + n_y + 1)\left(n_z + \frac{1}{2}\right), \tag{3.20}$$

where $\nu_Z = 2\nu_{rec}\sqrt{U_0/E_r}$ is the axial trapping frequency. With this energy spectra, we write an effective radial trapping frequency that depends on both the radial state n_r and the axial state n_Z:

$$\bar{\nu}_r^{n_Z}(n_X+n_Y) = \left(\nu_r - \nu_{rec}\frac{\nu_r}{\nu_Z}\left(n_Z+\frac{1}{2}\right)\right)(n_X+n_Y) = 2.44\,\mathrm{Hz}\left(2\sqrt{\frac{U_0}{E_r}} - \left(n_Z+\frac{1}{2}\right)\right)(n_X+n_Y). \tag{3.21}$$

The 2.44 Hz prefactor is the specific energy scale for the Sr1 system.

The radial degree of freedom also modifies the axial state. Since the radial modes are thermally populated, this gives rise to an effective lattice depth that is shallower than the peak lattice depth and depends on the temperature of the sample. Expanding the trapping potential to second order of r, we have

$$U(r,Z) \approx \left[V_0 - \frac{1}{2}M\omega_r^2(r^2)\right]\sin^2(k_L Z) + \frac{1}{2}M\omega_r^2(r^2), \tag{3.22}$$

An atomic gas with radial temperature T_r feels an effective lattice depth given by $V_0 - k_B T_r$. Although $k_B T_r \ll V_0$, it may still lead to non-negligible corrections to the nearest-neighbor tunneling rate, which shows exponential dependence on lattice depth. To take into account the leading order effects of the thermal distribution, we modify the ground band tunnel coupling by

$$J_0(T_r) \approx \frac{4}{\sqrt{\pi}}E_{rec}^{1/4}(U_0 - k_B T_r)^{3/4}\exp\left(-2\sqrt{\frac{U_0 - k_B T_r}{E_{rec}}}\right). \tag{3.23}$$

Using the radial temperature scaling we have measured on the system, we plot this change in ground band tunneling energy as a function of lattice depth in Fig. 3.9. This change increases the tunneling energy across all lattice depths, and modifies the resultant Wannier-Stark wavefunctions, as shown for 5 E_r on the right of Fig. 3.9. The dashed black lines are calculated with $T_r = 0$, and the solid green lines are calculated using the experimentally measured T_r as a function of U in a Doppler cooled sample. While this appears to be a small effect, the radial temperature must nevertheless be considered in evaluating the lattice light and density shifts.

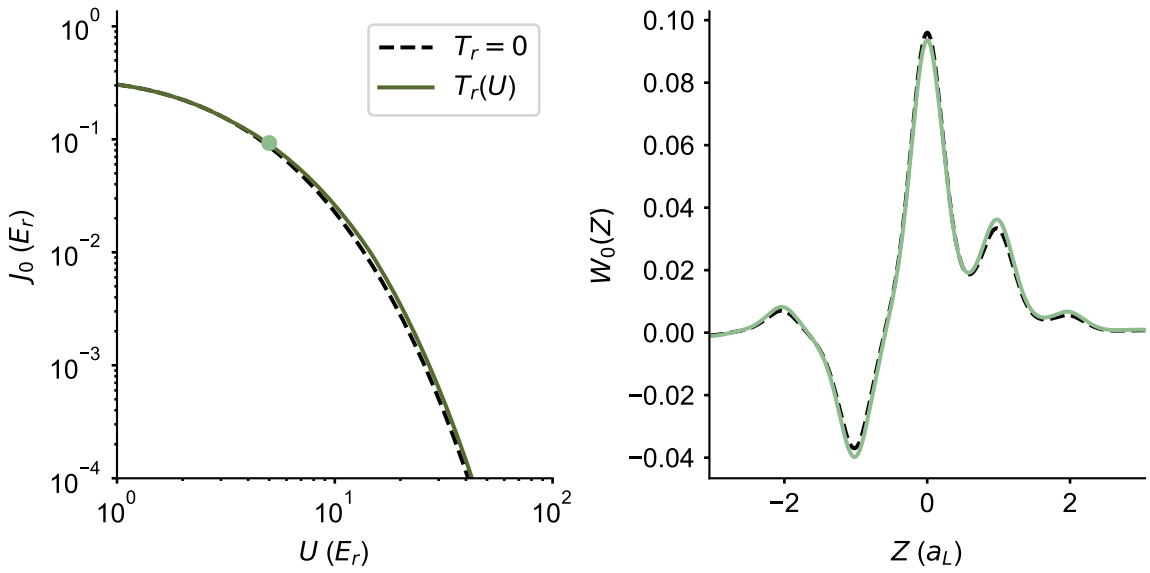

Figure 3.9: We treat the finite radial energy as modifying the tunneling energy. On the left we plot the tunneling energy as a function of lattice depth, with the solid green curve modified by the experimentally measured radial temperature T_r as a function of lattice depth U. Using this modified tunneling energy, we can see that it generates modified Wannier-Stark states as the tunneling energy increases, plotted on the right for a lattice depth of 5 E_r.

3.4 Energy Scales

Before we delve into the spectroscopic signals of these motional states, it may be helpful to summarize all the energy scales in context. In Tab. 3.4, we list in descending order the energy scales of our 1D lattice system. The motional energy scales contribute to a broad range of frequencies from 5 Hz to $\sim$ 125 kHz. The axial trapping frequency is typically the largest of these energy scales. The Doppler broadening and recoil shift are the next largest energy scales, highlight the need for a lattice to probe energy scales below this level. Wannier-Stark transitions are in the kHz range, depending on the number i of lattice sites driven. As discussed in Ch. 2, we typically drive the $|^1S_0, m_F = \pm 5/2\rangle \rightarrow |^3P_0, m_F = \pm 3/2\rangle$ transition. The $|^1S_0, m_F = \pm 5/2\rangle \rightarrow |^3P_0, m_F = \pm 7/2\rangle$ transition has a similar Rabi frequency and is typically $\sim$ 200 Hz away, under our standard applied bias field. The radial trapping frequency is the lowest motional energy scale. Interactions are typically < 1 Hz, as will be discussed in Ch. 4.

Table 3.1: Sr1 Energy Scales. The axial trapping frequency, radial trapping frequency, and Doppler broadening due to the radial temperature, and interactions depend on the lattice depth. The $|^1S_0, m_F = \pm 5/2\rangle \rightarrow |^3P_0, m_F = \pm 7/2\rangle$ frequency is the splitting with respect to our operational $|^1S_0, m_F = \pm 5/2\rangle \rightarrow |^3P_0, m_F = \pm 3/2\rangle$ transition.

Mechanism	Energy Scale	Formula
${}^1S_0 \rightarrow {}^3P_0$, ν_{Sr}	429,228,004,229,872.99 Hz	CIPM, Ref. [92]
Axial Trapping Frequency, ν_z	5 kHz - 125 kHz	Eq. 3.20
Doppler Broadening, σ_{Doppler}	10 kHz - 100 kHz	Eq. 3.27
Clock recoil, ν_{recoil}	4.701 kHz	$h/(2M\lambda_C^2)$
Lattice recoil, E_{rec}/h	3.465 kHz	$h/(2M\lambda_L^2)$
Wannier-Stark Site Changing Transition, WS+i	$868 \times i$ Hz	$Mg\lambda_L i/(2h)$
$\lvert^1S_0, m_F = \pm 5/2\rangle \rightarrow \lvert^3P_0, m_F = \pm 7/2\rangle$	0.1 - 2 kHz	Eq. 2.3
Radial Trapping Frequency, ν_r	5 - 100 Hz	Eq. 3.21
Rabi Frequency, Ω	0.2 - 100 Hz	
Interactions, $U_{\alpha\beta}$ $V_{\alpha\beta}$	< 1 Hz	Eqs. 4.5,4.6
Strontium natural linewidth, $1/(2\pi\tau_{Sr})$	~ 1 mHz	Ref. [85, 105]

In Fig. 3.10, we plot many of these energies as a function of lattice depth. The axial and radial energy scales increase with lattice depth. In the case of the Doppler FWHM, this scaling comes from the increased lattice depth leading to an increase in temperature. The WS+1 and higher order transitions in light green do not change in energy with higher lattice depth, but the Rabi frequency reduces, as shown in Fig. 3.8. The axial trapping frequency ν_Z is plotted for $n_Z = 0$ in blue, with lighter blues indicating ν_Z for $n_Z > 0$. Thanks to the exceedingly long live excited state lifetime, all of these energy scales are resolvable with the appropriate clock drive. In the next section we will discuss how we experimentally approach characterizing and understanding these energies.

3.5 Motional Spectroscopy

The narrow clock transition is a powerful tool for probing the motional states of the atoms. Using a number of different measurement techniques, we can construct a near-complete picture

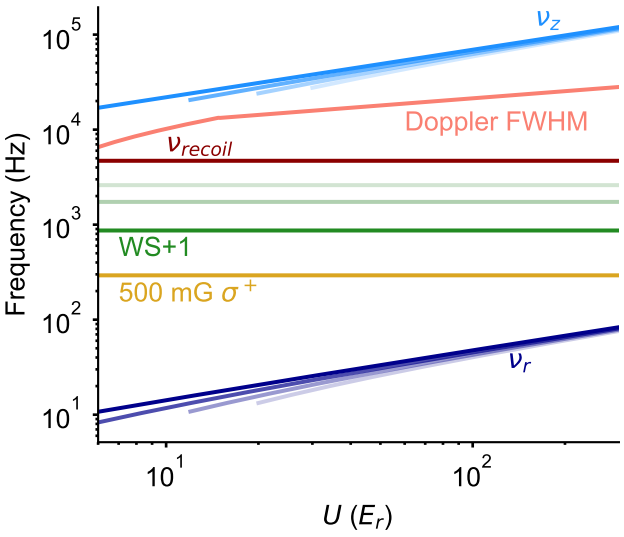

Figure 3.10: Energy scales as a function of lattice depth U. For the axial and radial trapping frequencies, ν_Z and ν_r, the darkest line represents the $n_Z = 0$ frequency, with lighter lines indicating $n_Z > 0$ frequencies. The Doppler full width half maximum (FWHM) is scaled by the measured radial temperature in our system. The WS+1 transition is shown in green, with WS+i where $i > 1$ transitions are in lighter green. The orange line represents the frequency difference between the σ^- and σ^+ transitions from the $|^1S_0, m_F = 5/2\rangle$ state at 500 mG.

of atomic motion. With the clock oriented along the tightly confined direction, we perform recoil free spectroscopy of the axial states, including the carrier transition, off-site transitions of the Wannier-Stark ladder, and motional quanta changing transitions. We probe how the Rabi frequency changes as a function of lattice depth, motional state, and final state. Using a clock oriented along the weakly confining radial direction, we measure a Doppler broadened profile as well as the recoil shift of the clock photon. In the following section, we discuss and interpret the experimental signals of atomic motion.

3.5.1 Rabi Spectroscopy

The Wannier-Stark system allows us to address the clock transition with no motional broadening or recoil shift. Historically, this has been known as the Lamb-Dicke regime [35], where the confinement dimension is far smaller than the wavelength of the incident radiation. However at shallow depths, the wavefunction extends over many neighboring lattice sites, violating the Lamb-Dicke assumption.

Instead, we rely on operating in the resolved sideband regime, where all motional energy scales are resolvable through the laser frequency. By driving with a Rabi frequency less than the relevant energies, such as ν_r or ν_Z, the atoms remain in the same external state while changing electronic state.

Nevertheless, the external state of the atom does affect this spectroscopy. We have already demonstrated how the Wannier-Stark state modifies the clock excitation coupling, shown in Fig. 3.8. Experimentally, we drive the carrier transition and observe how the Rabi frequency changes with lattice depth. We observe Rabi oscillations, and fit an exponentially damped sine wave to the resulting signal. As will be discussed later (Ch. 3.7), this does not perfectly capture the Rabi flopping dynamics but is adequate for comparing the relative Rabi frequencies between depths. We plot the square of the Rabi frequency Ω normalized by the peak Rabi frequency Ω_0. By detuning the laser with some multiple of the potential energy difference between lattice sites (868 Hz), we address off-site transitions. The relative Rabi frequencies on all these transitions scale differently with lattice depth, so we can use this measurement to experimentally determine U. At deep depths, the wavefunction is strongly localized and off-site transitions are attenuated. Operating with a sample in the first excited band, $n_Z = 1$ shown in red, leads to larger wavefunction spread and higher off-site Rabi frequencies. We used this approach to determine lattice depth in the light shift evaluation, Ref. [70]. In that work, the Rabi frequencies were calculated numerically solving for wavefunctions in a finite lattice system.

3.5.2 Axial Spectroscopy

If we detune the laser 5 to 125 kHz from the clock transition, we drive axial state changing transitions. Fig. 3.12 presents a simplified 1D schematic of the emergence of the axial spectrum. The transition from $n_Z \rightarrow n_Z + 1$ is known as the blue sideband (BSB) and has frequency ν_{BSB}. Conversely, the red sideband (RSB) involves removing an axial quanta, $n_Z \rightarrow n_Z - 1$, and has frequency ν_{RSB}. Resolved sideband cooling involves driving the RSB on $^3P_1$ along the Z direction during the final sample preparation step [53]. The structure of the BSB and RSB are rather

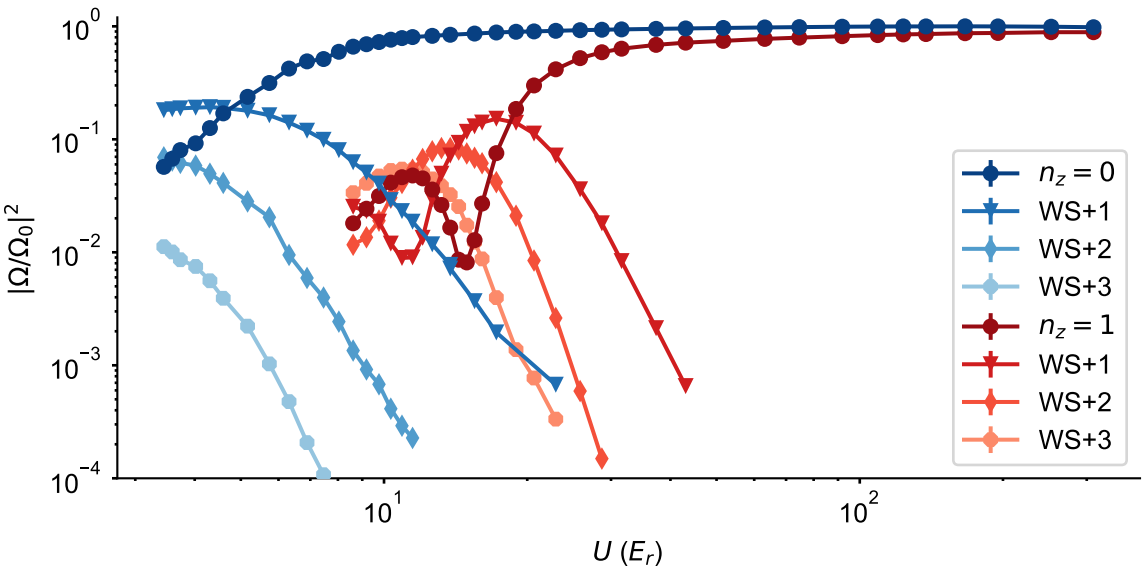

Figure 3.11: Measured Rabi frequency ratios for the ground motional state ($n_Z = 0$) shown in blue, and the first excited motional state ($n_Z = 1$) shown in red. Rabi frequencies Ω are normalized by the peak rabi frequency, Ω_0, which occurs for the $n_Z = 0$ state at deep depths. We drive carrier and site changing WS+n transitions for both states.

complicated: the axial state, radial temperature, and lattice site potential energy difference all contribute to a unique spectroscopic signal.

To first order, the frequency of both sidebands varies as a function of lattice depth. In Fig. 3.13, we plot axial scans as a function of lattice depth, from 9 E_r to 320 E_r. These scans are measured starting with an $n_Z = 0$ population, so excited state atoms are in $n_Z = 1$. Each BSB has a sharp edge of excitation fraction that delineates the axial frequency ν_Z at the peak lattice depth, U_0. The standard way to calibrate the lattice depth is to measure the position of the blue sideband and use this relationship to determine U. To derive a functional lineshape for the BSB, we assume a thermal distribution of radial modes with temperature T_r. This generates an array of axial transition frequencies, with the highest frequency occurring at the coldest part of the sample. Following Ref. [15], we write the excitation fraction along the blue sideband as a function of clock detuning δ:

$$\rho^{ee}_{BSB}(\delta) = \frac{\alpha^2}{\tilde{\gamma}(n_Z)}\left(1 - \frac{\delta}{\tilde{\gamma}(n_Z)}\right) e^{-\alpha(1-\delta/\tilde{\gamma}(n_Z))}\Theta\left(\tilde{\gamma}(n_Z) - \delta\right), \tag{3.24}$$

where $\alpha = \frac{\tilde{\gamma}(n_z)}{\nu_{rec}} \frac{h\nu_Z}{kT_r}$, $\tilde{\gamma}(n_Z) = \nu_Z - \nu_{rec}(n_Z + 1)$, and Θ is the Heaviside function. Using Eq. 3.24, we extract ν_Z and T_r from the blue sideband lineshape. While Eq. 3.24 generally holds well, it becomes apparent at shallow lattice depths that the sideband structure is too complicated to be properly captured by this formula, leading to depth calibration errors.

At very shallow lattice depths, site changing transitions can occur along with an axial transition, illustrated as the lighter blue and red lines in Fig. 3.12. In Fig. 3.14, we plot the blue sideband at 10 E_r. At this shallow lattice depth, the $n_Z = 1$ state is sufficiently delocalized where the Rabi frequency is similar for on-site and off-site Δn_Z transitions. This leads to peaks on the sideband structure spaced by 868 Hz. Evaluating the relative Rabi frequency of these different transitions and then applying radial depth reduction, we calculate an expected lineshape, shown in dashed black in Fig. 3.14. The gray lines indicate the constituent transitions that make up the overall spectrum. Significant work to understand the motional spectrum has also been completed in Yb [20, 168].

As apparent in Eq. 3.24, the BSB signal is linked to the radial character of the sample. We can investigate this by modifying the cooling sequence, shown in Fig. 3.15 at 320 E_r. With our standard Doppler and axial cooling engaged, we achieve a narrow blue sideband at 122 kHz, indicating the $|^1S_0, n_Z = 0\rangle \rightarrow |^3P_0, n_Z = 1\rangle$ transition. Broadening towards the carrier indicates radial reduction of the axial trapping frequency and a radial temperature around 700 nK. At this deep depth, off-site transitions are strongly attenuated, so the atoms remain on a single site. Without axial cooling, the axial state n_Z^g is in a thermal distribution, and the blue sideband contains transitions $n_Z^g \rightarrow n_Z^e = n_Z^g + 1$. Since the band spacing is reduced as n_Z increase, each n_Z blue sideband is 1 E_r shifted closer to the carrier. This is readily apparent in the spectrum in Fig. 3.15, with the axial transitions labeled. Using the relative difference between n_Z axial states allows proper characterization of the exact axial populations, see Ref. [20]. With axial cooling and no radial cooling, the blue sideband spreads over a much wider energy, as different atoms see different effective depths. With neither axial nor radial Doppler cooling, the different axial transitions are still visible, now with a broader radial pedestal. Modifying the cooling sequence will also create a red sideband that contains some of this character.

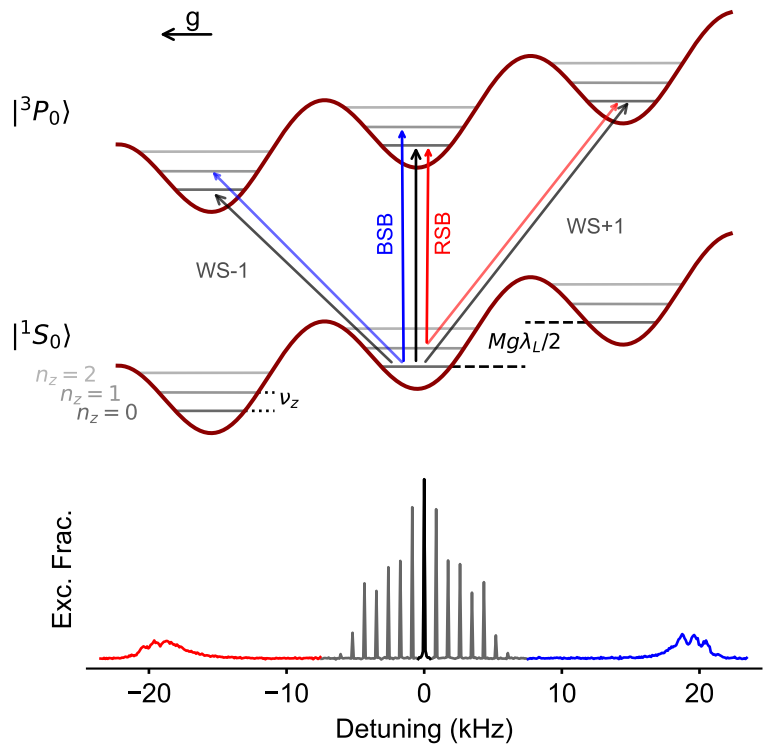

Figure 3.12: Axial spectrum. The two internal clock states each contain a ladder of motional state, axial quantum states n_Z, and lattice sites n. The carrier transition, in black, contains no external state change. Offsite transitions, WS+i, appear at a frequency spacing of 868 Hz, corresponding to the potential energy difference between lattice sites, $Mg\lambda_L/2$. Transitions with $\Delta n_Z \neq 0$, the red and blue sidebands (RSB, BSB), correspond with removing or adding a motional quanta of frequency, and are detuned from the carrier by approximately the axial trapping frequency. These are shown in the spectrum below as broad, jagged sidebands $\pm 15 - 22$ kHz from the carrier. This spectrum here is from a sample with no axial cooling, leading to a $\langle n_Z \rangle \approx 1$.

3.5.3 Radial Spectroscopy

To characterize the radial temperature, we typically measure a Doppler broadened excitation profile using a clock beam oriented perpendicular to the lattice. A schematic of this procedure and an example line scan of a 100 nK sample is shown in Fig. 3.16. The Doppler shift can be written for a distribution of velocities P_v, generating a frequency distribution:

$$P_\nu(\nu)d\nu = \frac{c}{\nu_0} P_v\left(c(\nu/\nu_0 - 1)\right) d\nu, \tag{3.25}$$

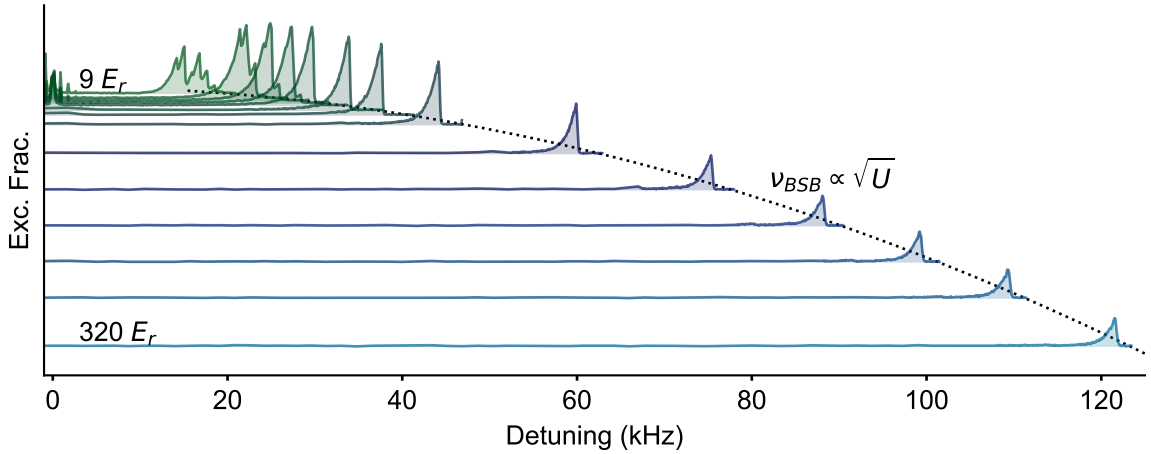

Figure 3.13: Blue sidebands at different lattice depths. Excitation spectra of a $|^1S_0, n_Z = 0\rangle$ sample driving positively detuned from the carrier, at 0 kHz. The frequency of the blue sideband ν_{BSB} scales with the root of the lattice depth.

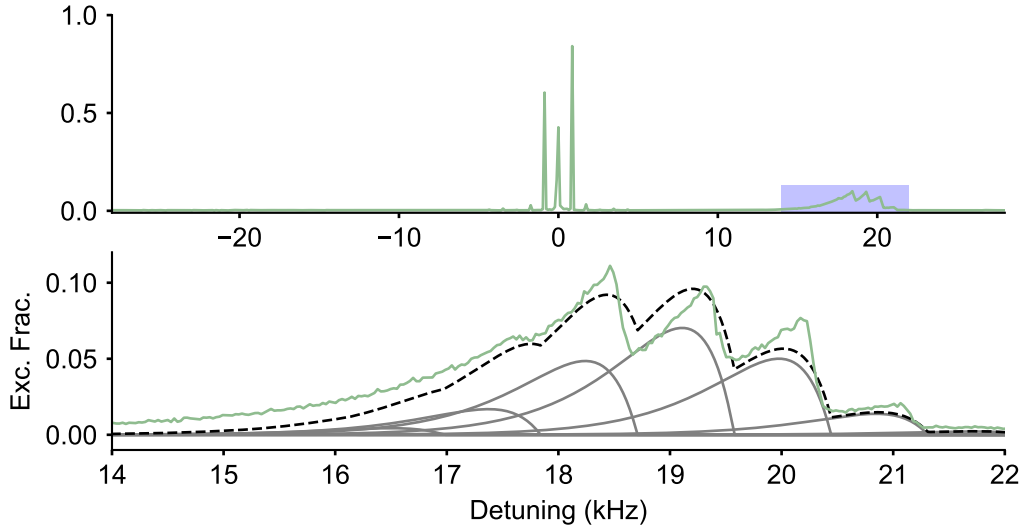

Figure 3.14: At shallow lattice depths, shown here at 10 E_r, the blue sideband structure is modified by other energy scales. The top plot is a broad scan of the axial spectrum of a $^1S_0$ $n_Z = 0$ sample. We highlight the BSB, shown in detail in the lower plot. Axial and off-site transition can occur at the same time, that is $|^1S_0, \mathrm{WS}_n, n_Z = 0\rangle \rightarrow |^3P_0, \mathrm{WS}_{n+i}, n_Z = 1\rangle$, leading to peaks at 867 Hz. Calculated BSB transitions for each WS transition are shown in gray, with the total sum in dashed black roughly approximating the measured BSB.

where ν_0 is the transition frequency at rest. In a thermal gas, the velocity v is a function of T_r and given by the Maxwell distribution:

$$P_v(v)dv = \sqrt{\frac{M}{2\pi k T_r}} \exp\left(-\frac{mv^2}{2kT_r}\right) dv. \tag{3.26}$$

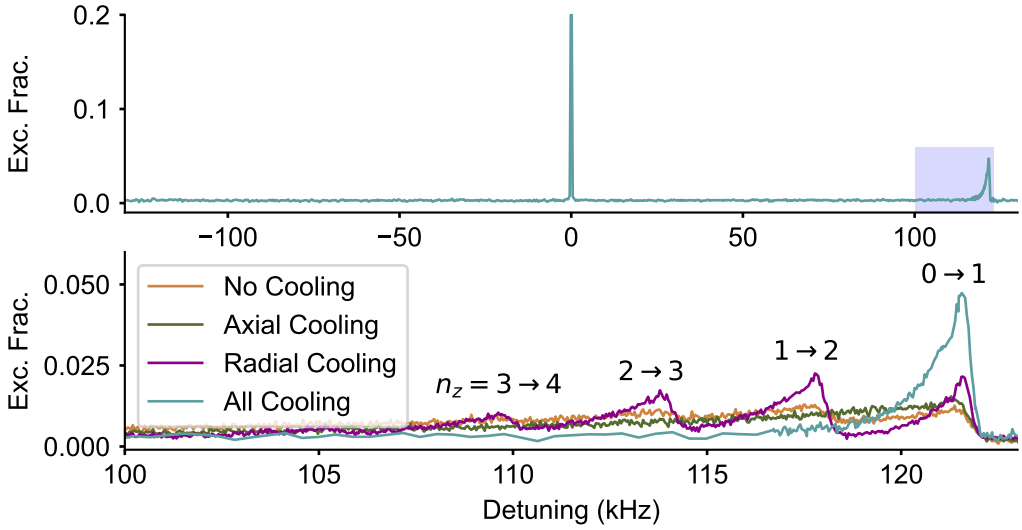

Figure 3.15: Blue sideband at 300 E_r with different cooling configurations. The sideband spectrum of a Doppler and axial cooled sample near 300 E_r is plotted on the top. The blue highlighted region in the top panel is shown in greater detail below. BSB spectrum at 300 E_r under different cooling conditions noted in the plot key. The axial state changes are labeled above each sharp feature.

Using this distribution in Eq. 3.25, we notice that the distribution of Doppler broadened frequencies has a Gaussian profile, with Gaussian width σ:

$$\sigma_{\text{Doppler}} = \sqrt{\frac{kT_r}{Mc^2}}\nu_0. \tag{3.27}$$

Thus, our standard approach is to measure the Doppler broadened profile, fit a gaussian to find σ_{Doppler}, and solve for the temperature. The profile center is shifted by the recoil energy of the clock photon, a frequency shift $\nu_{recoil} = 4.7$ kHz. We measure T_r over the entire range of accessible lattice depths and fit T_r as a piecewise function:

$$T_r(nK)(U) = \begin{cases} -45.2 + 14.1\ U/E_{rec} & (U < 15E_r), \\ 42\sqrt{U/E_{rec}} & (U > 15E_r). \end{cases} \tag{3.28}$$

This function represents an adiabatic temperature reduction with a shallow depth correction. Since radial clock spectroscopy involves absorbing a clock photon, it can fail to fully capture T_r at shallow

lattice depths where trapping and ν_{recoil} energy scales are comparable. We notice that for $U < 3\ E_r$ the lineshape appears asymmetric: the hottest population can be kicked out of the trap via the clock photon momentum. This may explain the departure from true adiabatic temperature scaling where $U < 15\ E_r$ We also notice that the lattice is about 2° misaligned from vertical, perhaps leading to additional loss and T_r modification at shallow depths. Nevertheless, this function works well to describe the physics we observe.

Another approach to measuring the radial temperature is to image the ground state atoms. The spread σ_i in a given direction i of a thermal sample is described by

$$\sigma_i = \sqrt{\frac{\hbar}{M\omega_i}} \times \sqrt{2\langle n_i \rangle_{T_r} + 1}. \tag{3.29}$$

where ω_i is the trapping frequency, and

$$\langle n_i \rangle_{T_r} = \left(\exp(\frac{\hbar\omega_i}{k_B T_r}) - 1 \right)^{-1}. \tag{3.30}$$

Thus we can use the width of an imaged sample to determine the radial temperature. In Fig. 3.17, we take images of lattice trapped samples over a range of depths and fit the gaussian width to determine the temperature. This temperature metric is consistent with Doppler spectroscopy, as shown on the right of Fig. 3.17. At shallow depths, the imaging probe blurs the image, leading to a hotter extracted temperature. The probe beam duration was reduced for shallow lattice depths, but below about 10 E_r even a few scattered photons leads to a blurry image.

Unfortunately, we do not have state resolved spectroscopy along the radial direction. Instead, if the axial clock is slightly misaligned, we can drive radial motional sidebands as $\vec{k}_c$ has projection along the radial direction. In Fig. 3.18, we observe radial mode changing transitions detuned by $\nu_r^{n_Z}$ from the carrier for $n_Z = 0$ and $n_Z = 1$ over a range of shallow lattice depths $< 17\ E_r$. To observe these without a significant clock misalignment, we overdrive the Rabi line, leading to the messy spectrum near 0 detuning. The radial projection results in small increases in excitation

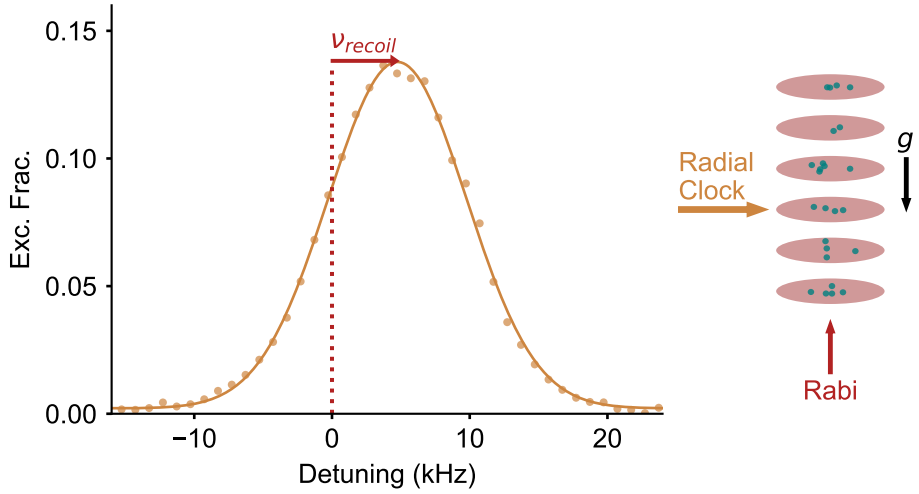

Figure 3.16: Radial clock spectroscopy. Using a clock path perpendicular to the lattice the clock transition is Doppler broadened and has a recoil shift. Fitting a Gaussian to this spectrum, we extract the radial temperature T_r. This is experimental data measured with a Doppler cooled, spin polarized $|^1S_0, m_F = -9/2\rangle$ sample in a 10 E_r lattice.

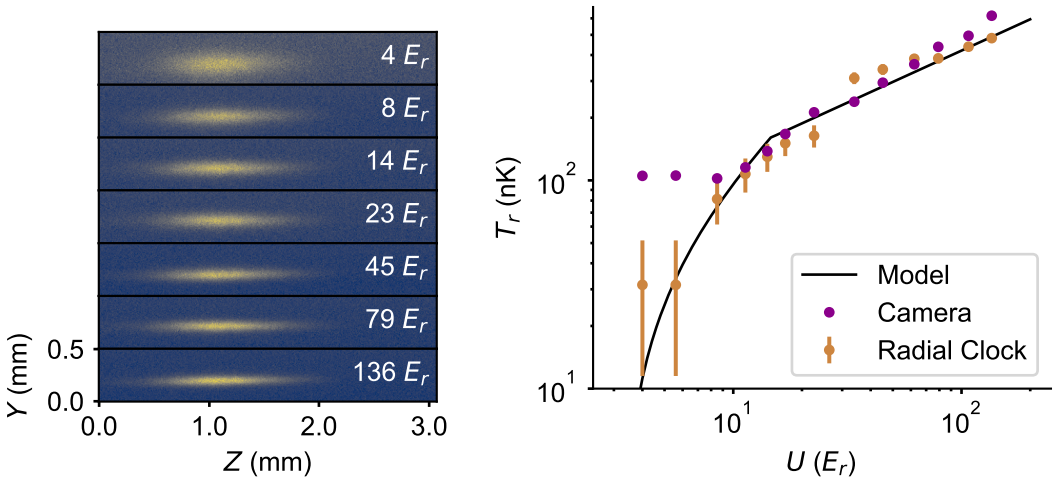

Figure 3.17: Using imaging to determine the radial temperature. Left: images of lattice trapped samples at different lattice depths. At shallower depths, the spread along $\hat{Y}$ is greater as ω_Y relaxes. Right: Comparing imaging spectroscopy to clock spectroscopy along the radial direction. At all but the shallowest depths, the radial temperature follows adiabatic scaling, Eq. 3.28, plotted as the black line.

fraction near integer multiples of the radial trapping frequency. Using Eq. 3.21, the calculated sidebands are plotted with a solid black line for the $n_r \to n_r \pm 1$ transition and a dashed black line

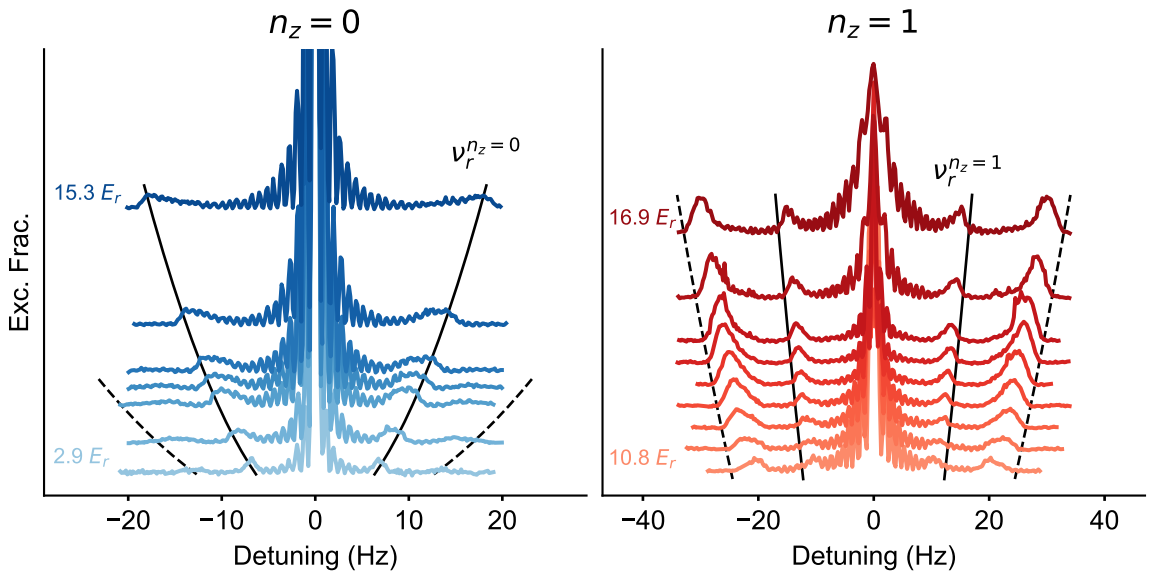

Figure 3.18: Radial sidebands on the carrier transition for $n_Z = 0$ (left) and $n_Z = 1$ (right) over a range of depths. In order to make the radial sidebands apparent, the carrier transition addressed for time $T >> T_{rabi}$, leading to an overdriven Rabi lineshape near 0 Hz. The calculated radial trapping frequency $\nu_r^{n_Z}$ is shown as a solid black line, with $2\nu_r^{n_Z}$ plotted as a dashed black line.

for the $n_r \rightarrow n_r \pm 2$ transitions. Interestingly, the $n_Z = 1$ sample has higher amplitude second order sidebands than first order. These sidebands contain information about the radial states, and we have observed modifying the cooling results in different sideband spread. We do not yet have a complete model for extracting T_r or n_Z from this spectroscopic signal.

3.6 Radial Sloshing

At shallow lattice depths and short spectroscopy times, we notice the radial profile appears asymmetric or detuned from the expected frequency. To quantify this asymmetry, we calculate the first moment of the Gaussian profile, subtracting off the known recoil shift. With a short probe time < 100 ms, we vary the hold time between lowering the lattice depth and the spectroscopy window and observe the first moment oscillate between $\sim +2$ to -2 kHz. This oscillation is at the radial trapping frequency and varies with U.

On Sr1, Doppler cooling proceeds along the MOT paths, using the same waveplates and relying

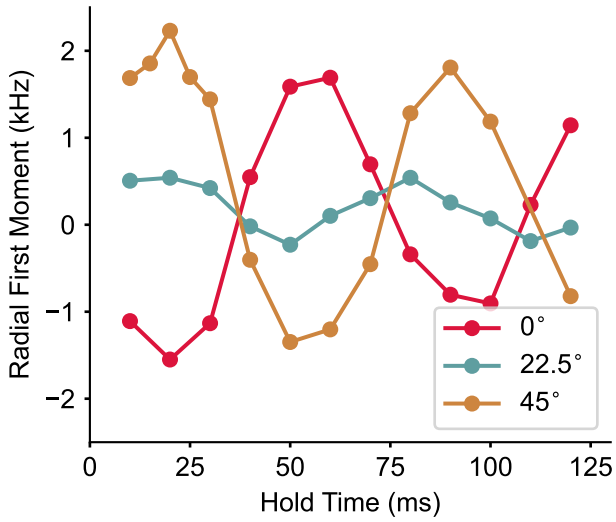

Figure 3.19: Radial sloshing as a function of waveplate angle for a $m_F = -9/2$ Doppler cooled sample. We calculate the first moment of the radial spectroscopy signal and observe collective oscillations at the radial frequency. We control the radial sloshing through the input polarization of the Doppler beam along the $\hat{X}$-direction, reported here as the angle of a $\lambda/2$ waveplate.

on the frequency detuning due to the applied 1 G bias field to resolve the magnetic sublevels of the $^3P_1$ $F = 11/2$ state. With the same polarization as the MOT light, the Doppler cooling along the X-direction, parallel to the bias field, has σ^+ polarization in one direction and σ^- in the other. As we polarize in one of the stretched states, only one direction of light will address the sample. This leads to a net radiation force that displace the entire sample along $\hat{X}$. Once the cooling is removed, the sample collectively "sloshes" at the radial frequency.

We control sloshing by varying the polarization of the $\hat{X}$ Doppler beam, as shown in Fig. 3.19. Here we plot the first moment of the Radial spectrum as a function of hold time, varying the angle of a $\lambda/2$ waveplate. With this control, we can reverse the sign or eliminate the radial sloshing.

We made many clock measurements before we first noticed this radial sloshing, leading to the possibility of an uncontrolled shift polluting all previous data. With an interleaved lock, we measure the frequency shift between different hold times, presented in Fig. 3.20. To observe this effect without averaging over a significant potion of the radial period, we measure a 6 E_r sample with $T_{Rabi} = 20$ ms. In the top panel of Fig. 3.20, we plot the frequency difference between no hold time

and a variable hold time for the $m_F = +5/2$ and $m_F = -5/2$ locks. The lock indicates a significant frequency oscillation ($>10^{-15}$) between the different spin states, with a π phase shift consistent with the radial sloshing measurements. There also appears to be oscillation in the density shift correction, plotted in the center panel of Fig. 3.20. This remains a mystery: perhaps a clock laser phase gradient across the sample leads to distinguishable atoms and on-site s-wave interactions. As the atoms slosh back and forth, they gain a degree of distinguishability depending on their position with respect to the clock laser. Additionally, density modulation during this sloshing will generate a time varying density shift. By taking an average of spin states and applying density shift corrections, plotted in the bottom panel of Fig. 3.20, we seem to broadly reject frequency oscillations. The density shift is a relatively minor correction, but it does seem to reduce the overall amplitude of the raw center frequency shift.

While averaging over more radial periods with a longer spectroscopy time and a higher depth reduce the lock frequency oscillation, this effect is still measurable for the different spin states and in the density shift coefficient. This mechanism raises concern with using Ramsey spectroscopy where the $\pi/2$ pulse time $T_{\pi/2} < 1/\nu_r$ leading to some uncontrollable frequency shift even with a reduced sloshing amplitude. While the data presented in Fig. 3.20 suggests that radial sloshing did not significantly affect our previous results, more investigation regarding this mechanism and resultant effects on clock operation are needed.

3.7 Rabi Inhomogeneity

Typical 1D OLCs use a single mirror to form the trapping potential. Creating a buildup cavity necessitates placing an additional mirror with the high reflectivity side facing the incident clock laser. Achieving high reflectivity for 813 nm while very low reflectivity for 698 nm is a rather challenging task; our mirrors are specified as having a 1% reflectivity at 698 nm.

Consider a full contrast standing wave created by perfect reflection of the clock light. At the nodes the intensity is zero and the corresponding Rabi frequency is zero. With trapped atoms arranged in a standing wave of light with a incommensurate period, atoms see a fixed Rabi frequency

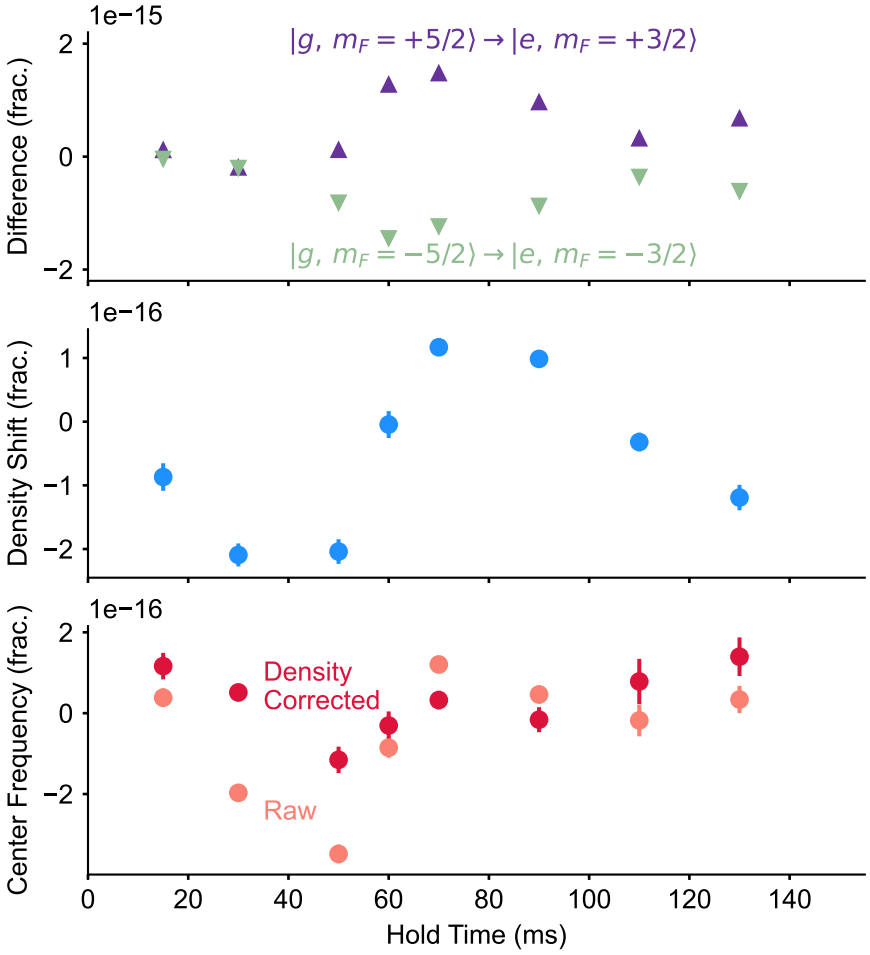

Figure 3.20: Clock shift from radial sloshing. Top: we compare the transition frequency difference between standard operation and after holding the sample in a shallow lattice for a given "hold time." We observe oscillations in the two magnetic sublevel transitions of opposite sign, consistent with radial sloshing measurements. Center: the density shift correction as a function of hold time seems to echo this radial motion. Bottom: the uncorrected "raw" frequency average of the two spin states and the density corrected frequency indicate about an order of magnitude reduction in the frequency shift.

that ranges between 0 and 2 times the non-reflected Rabi frequency across the sample. With a partial reflection, the Rabi frequency is centered around a nominal value Ω_0, with peaks and minima $\pm\epsilon$ modifying Ω_0. This scenario is illustrated in Fig. 3.21, with the left illustrating how a standing wave of light creates an inhomogeneous Rabi frequency. Over many lattice sites, the Rabi frequency has a spectrum illustrated on the right.

We probe the Rabi inhomogeneity in our system by measuring a Rabi flopping spectrum,

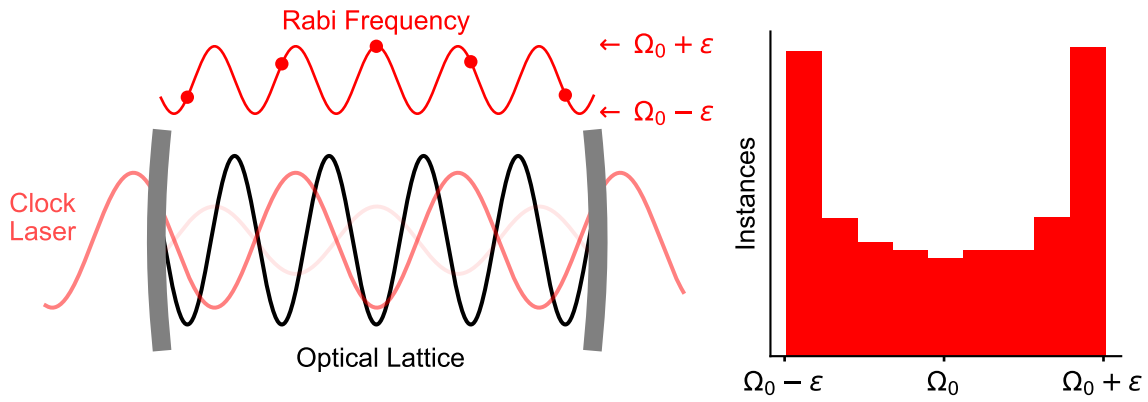

Figure 3.21: A standing wave of clock light is formed inside the cavity. This leads to a modulated Rabi frequency $\Omega = \Omega_0 + [-\epsilon, \epsilon]$ The incommensurate clock and lattice wavelengths mean that each lattice site samples a different Rabi frequency, as shown on the right.

shown in Fig. 3.22. After about 6 flopping cycles, the Rabi flopping collapses only to revive over the next few cycles. This beating occurs for many cycles, indicating good atom-light coherence but inhomogeneity in the Rabi spectrum. Taking a Fourier transform of this spectrum, we observe the Rabi frequency spectrum has two peaks, as shown on the right of Fig. 3.22.

Motivated by our understanding of a standing wave of clock light, we fit this spectrum with a model that takes into account the variation of Rabi frequencies:

$$\bar{\rho}^{ee} = \sum_{n}^{N} A \sin\left(\Omega_0 t(1 + \epsilon \sin^2(2\pi n \lambda_l/\lambda_c))\right). \tag{3.31}$$

To fit the averaged excitation fraction ρ^{ee}, we sum over N lattice sites with a Rabi contrast A. The fit to the flopping and a Fourier transform of this fit are shown as dashed black lines in Fig. 3.22. This simple model with no atom-light decoherence seems to capture the flopping signal well, indicating that Rabi inhomogeneity is a primary issue in our system. The Rabi frequency spread depends on the cavity reflectivity at 698 nm, $\epsilon^2/2 \approx R$, and with the fit we find $R = 0.9\%$, near the mirror coating specifications.

While this standing wave of clock light poses a challenge for many pulse spectroscopy sequences, we can use it to imprint a particular density profile along the axial direction. If this standing wave

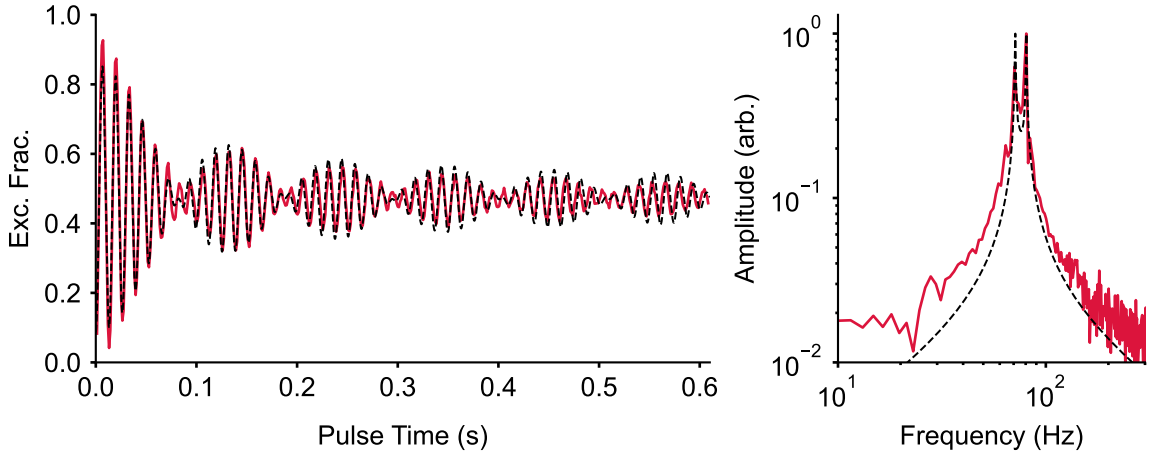

Figure 3.22: Left: the excitation fraction as a function of clock drive time. The red line is experimental data taken at 100 E_r, and the dashed black line is a simple model fit to this result, Eq. 3.31. Right: A fourier transform of this signal lends insight into the origins of this Rabi nutation. A fourier transform of the fitted function, in dashed black, further illustrates how well the model captures this Rabi behavior.

was intentional, perhaps we might call this technique "subwavelength spatial selection!" Since the Rabi frequency varies from site to site, over the course of many Rabi flops, the clock will imprint an excitation pattern along the lattice direction. By illuminating the sample with blue 461 nm light, we remove atoms that are in the ground state while preserving the excited state atoms and distilling the sample to a smaller spread of Rabi frequencies.

Fig. 3.23 shows how we use this approach to control the Rabi flopping spectrum. We begin by driving the atoms many Rabi cycles until the excitation fraction collapses to ~ 0.5, as shown on the left. After 88, 90, or 92 ms of a Rabi drive, we remove the ground state atoms. On the right, we show the flopping signal after this initial preparation. Through this process, we homogenize the Rabi frequency throughout the sample, leading to a longer coherent Rabi flopping signal. Small differences in the timing of the first Rabi drive significantly alter the distilled Rabi frequency, with the 92 ms preparation increasing the average Rabi frequency, and the 90 ms preparation leading to the highest contrast Rabi frequency at long time.

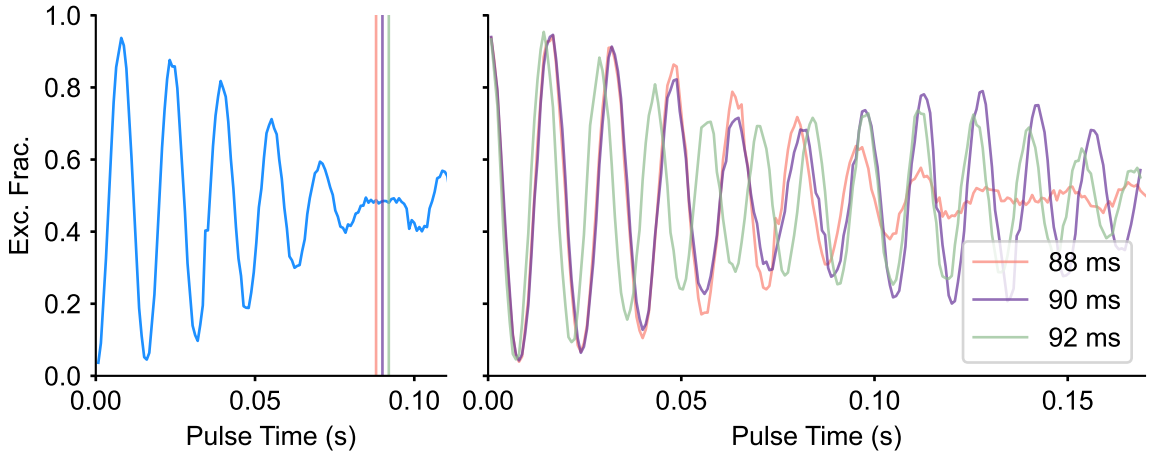

Figure 3.23: Atoms located at the peak light intensity flop faster than those at the minima. After roughly 5 periods, the sample has a maximal spread of excitation fractions and the average excitation fraction is 50%. Using 461 nm light, we remove the ground state population, selecting the portion of the lattice trapped sample that sees either the highest or lowest clock laser intensity. On the left, the blue line is measured excitation fraction as a function of Rabi flopping time. On the right, we prepare a sample after flopping for a given amount of time and removing the ground state population. This effectively narrows the spread of Rabi frequencies, altering the Rabi nutation.

Chapter 4

Density Shift

The more atoms the better! Of course, there is no free lunch. ^{87}Sr is a fermion, so while atom-atom interactions are weak, they still pose a problem for building the most stable and accurate clock. To circumvent this issue, most Sr clocks operate with fewer than 10^4 atoms, significantly reducing the density shift yet increasing quantum projection noise. These systems periodically check the residual density shift by modulating the atom number and measuring the frequency shifts. In this chapter, I will present a new technique to measure the density shift as well as work to identify a fortuitous cancellation of the entire shift, a specific lattice depth we call the "magic depth." Most of this work was published in our Science Advances paper entitled "Hamiltonian Engineering of Spin-Orbit Coupled Fermions in a Wannier-Stark Optical Lattice Clock," Ref. [1].

4.1 Atomic Interactions

Interactions and density dependent frequency shifts in the strontium optical lattice clock have been well described by a simplified "spin model" and a mean field approximation. This spin model has been extensively discussed theoretically [50, 147] and investigated experimentally [27, 29, 95, 136, 169]. In this section, I will summarize for experimentalists the density shift calculations Anjun Chu discussed in the supplement of [1].

Atoms are trapped in a motional state of the Wannier-Stark lattice described by $\vec{n} = (n, n_X, n_Y, n_Z)$, where n is the lattice site index, X, Y are the weakly confined radial directions, and

Z is the strongly confining axial direction. Their evolution is governed by the Hamiltonian H,

$$H = H_0 + H_{\text{laser}} + H_{\text{int}}, \tag{4.1}$$

where H_0 describes the single particle motion, H_{laser} contains the evolution between the two internal states under a laser drive, and H_{int} contains p-wave and s-wave interactions.

We treat the spin model with a mean field approach resting on a "frozen mode" approximation. During Rabi evolution, we assume atoms remain in their external single particle eigenstates of the optical trap and collisional relaxation is negligible. While we challenge this assumption later, the results here are valid for the carrier transition under laser limited spectroscopy times (< 4 s). For simplicity, we also treat only the case where $n_Z = 0$, although this model works with higher band populations. For each atom we define a two level system, $|\downarrow_{\vec{n}}\rangle \equiv |{}^1S_0, n_X, n_Y, W_n\rangle$ and $|\uparrow_{\vec{n}}\rangle \equiv |{}^3P_0, n_X, n_Y, W_n\rangle$. For each two level system, we have the fermionic annihilation (creation) operators, $c^{(\dagger)}_{\vec{n}\uparrow}$ and $c^{(\dagger)}_{\vec{n}\downarrow}$. This allows us to define spin operators $S^{x,y,z}_{\vec{n}}$ and the number operator $N_{\vec{n}}$.

Due to the partial delocalization of the Wannier-Stark states along Z, the dominant density shift terms are due to on-site and nearest-neighbor interactions. Since the s-wave interaction strength is considerably larger than the p-wave interaction strength, we neglect p-wave interactions on neighboring sites. All these approximations allow us to write a simplified large-spin Hamiltonian:

$$\begin{aligned}
H &= H_{\text{on-site}} + H_{\text{off-site}} + H_{\text{laser}}, \\
H_{\text{on-site}}/\hbar &= \sum_n \Big[J_0^{\perp} \vec{S}_n \cdot \vec{S}_n + \chi_0 S_n^z S_n^z + C_0 N_n S_n^z \Big], \\
H_{\text{off-site}}/\hbar &= \sum_n \Big[J_1^{\perp} \vec{S}_n \cdot \vec{S}_{n+1} + \chi_1 S_n^z S_{n+1}^z + D_1 (S_n^x S_{n+1}^y - S_n^y S_{n+1}^x) \Big], \\
H_{\text{laser}}/\hbar &= \sum_n \Big[-\delta S_n^z + \Omega_0 S_n^x \Big].
\end{aligned} \tag{4.2}$$

The interaction parameters defined for the collective spin operators are calculated using a thermal

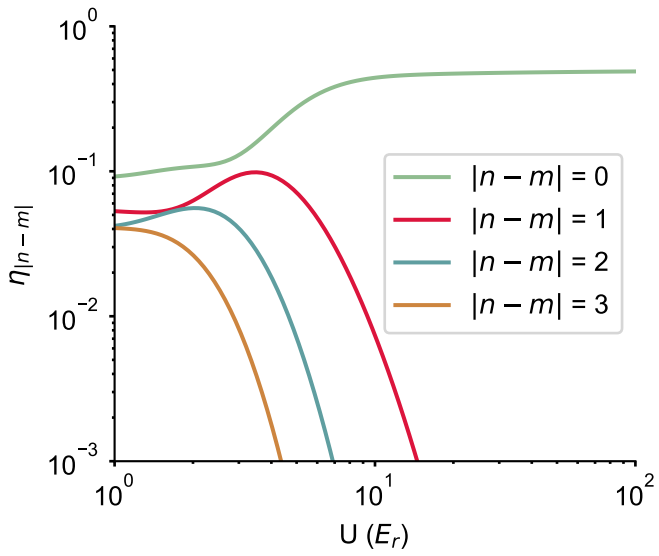

Figure 4.1: The dimensionless $\eta_{|n-m|}$ parameter that governs the density shift strength. Onsite interactions dominate at deep depths while the off-site integral ($\eta_{1,2,3}$) grows at shallower depths.

average over radial modes,

$$\begin{aligned} J_0^{\perp} = \eta_0(V_{eg} - U_{eg})/2, \quad \chi_0 = \eta_0(V_{ee} + V_{gg} - 2V_{eg})/2, \quad C_0 = \eta_0(V_{ee} - V_{gg})/2, \\ J_1^{\perp} = -\eta_1 U_{eg}\cos\varphi, \quad \chi_1 = -\eta_1 U_{eg}(1 - \cos\varphi), \quad D_1 = -\eta_1 U_{eg}\sin\varphi. \end{aligned} \tag{4.3}$$

The spin orbit coupling phase $\varphi = k_C a_L = \pi\lambda_L/\lambda_C$. The parameter $\eta_{|n-m|}$ is a dimensionless overlap integral that scales the wavefunction overlap along Z of two atoms:

$$\eta_{|n-m|} = \frac{\lambda_L}{\sqrt{2\pi}}\left(\frac{V_0}{E_{rec}}\right)^{-1/4}\int dZ (W_n(Z))^2 (W_m(Z))^2. \tag{4.4}$$

In Fig. 4.1, we plot $\eta_{0,1,2,3}$ as a function of lattice depth. We typically consider only on-site and nearest-neighbor interactions, so η_0 and η_1. Above 20 E_r, the on-site ($n - m = 0$) overlap dominates all other overlap strengths, so considering only on-site p-wave interactions is valid, as has been previously treated. At shallow lattice depths, η_i for $i > 0$ grows and off-site interaction must be included.

The $U_{\alpha\beta}$ and $V_{\alpha\beta}$ terms are s-wave and p-wave interaction strengths respectively, defined

between states $\alpha, \beta \in \{g, e\}$:

$$U_{\alpha\beta} = \frac{8\pi\hbar a_{\alpha\beta}}{M} \frac{M\omega_R^2}{4\pi k_B T_r} \frac{k_L}{\sqrt{2\pi}} \left(\frac{V_0}{E_{rec}}\right)^{1/4}, \tag{4.5}$$

$$V_{\alpha\beta} = \frac{6\pi\hbar b_{\alpha\beta}^3}{M} \frac{1}{\pi} \left(\frac{M\omega_R}{\hbar}\right)^2 \frac{k_L}{\sqrt{2\pi}} \left(\frac{V_0}{E_{rec}}\right)^{1/4}. \tag{4.6}$$

The a and b parameters are scattering lengths, with $a_{eg} = (a_{eg}^+ + a_{eg}^-)/2$ and $b_{eg}^3 = ((b_{eg}^+)^3 + (b_{eg}^-)^3)/2$ The s-wave and p-wave scattering lengths are recorded in Tab. 4.1.

Table 4.1: s-wave and p-wave scattering lengths for ^{87}Sr in Bohr radius (a_0) [1].

Channel	s-wave (a_0)	p-wave (a_0)
gg	96.2 ± 0.1	74.5 ± 0.3
eg^+	161.3 ± 2.5	-215.9 ± 28.2
eg^-	69.1 ± 0.9	-41.3 ± 2.7
ee (elastic)	176.3 ± 9.5	-155.8 ± 21.1
ee (inelastic)	17.3^{+14}_{-8}	152.5 ± 16.4

In Fig. 4.2 we plot U and V as a function of lattice depth. As expected, V is much smaller that U for all depths. Generating on-site s-wave interactions can and does lead to a much stronger density shift, as we will discuss in Ch. 4.4.

For the carrier transition, we alternate sides of the Rabi lineshape as described in Sec. 2.5. The measured density shift per atom per site (N_{loc}) is:

$$\Delta\nu_{\mathrm{dens}} = \frac{\delta_l + \delta_r}{4\pi N_{\mathrm{loc}}}, \tag{4.7}$$

where $\delta_{l,r}$ are the negative and positive detunings from the center of the line as described in Ch. 2. Under a Rabi spectroscopy lock, the laser drives continuously from the initial states to a superposition state of g and e.

Using the mean field approximation, we can rewrite Eq. 4.2 simply as a spin evolving under an

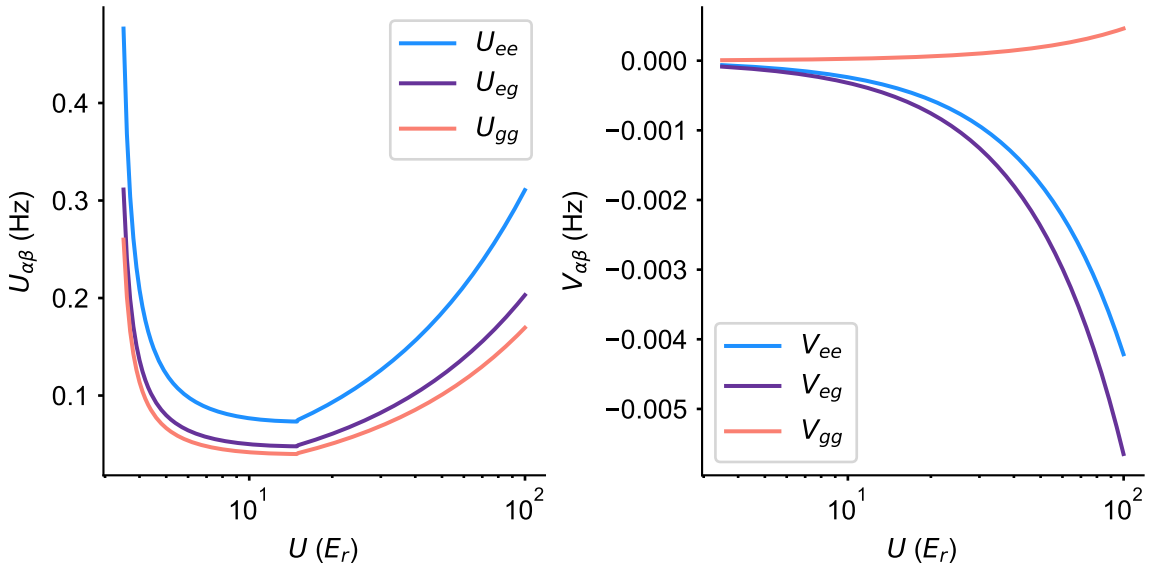

Figure 4.2: The p-wave (V) and s-wave (U) interaction strengths as a function of depth for ee, eg, and gg interaction channels, see Eqs. 4.5 and 4.6. U is calculated using the experimentally measured radial temperature.

effective magnetic field $\vec{B}_{\text{eff}}$ that contains an averaged density interaction. For simplicity, we assume a constant density within a local region. Because we are concerned with only the mean field effect, we also neglect the parallel component of $\vec{B}$. Thus, for time t,

$$\frac{d}{dt}\langle \vec{S}_n \rangle = \vec{B}^{\perp} \times \langle \vec{S}_n \rangle, \tag{4.8}$$

where $\langle \vec{S}_n \rangle$ is the Bloch vector and $\vec{B}^{\perp}$ is the synthetic magnetic field perpendicular to $\langle \vec{S} \rangle$. $\vec{B}^{\perp}$ can be written,

$$\vec{B}^{\perp} = \{\Omega_0, 0, -\delta + 2(\chi_0 + \chi_1)\langle S^z \rangle + C_0 N_{\text{loc}}\}, \tag{4.9}$$

where Ω_0 is the bare Rabi frequency, δ is the laser detuning, $\langle S^z \rangle$ is the average magnetization, and N is the number of atoms on the site. Expanding this further, we write the dynamics as a set of

coupled differential equations:

$$\begin{aligned}
\frac{dS^x}{dt} &= -(2(\chi_0+\chi_1))S^zS^y + \delta S^y - C_0N_{\rm loc}S^y, \\
\frac{dS^y}{dt} &= (2(\chi_0+\chi_1))S^zS^x - \delta S^x + C_0N_{\rm loc}S^x - \Omega_0 S^z, \\
\frac{dS^z}{dt} &= \Omega_0 S^y.
\end{aligned} \tag{4.10}$$

We can use any differential equation solver to observe the dynamics of this mean field density shift. For Rabi spectroscopy, the initial state is a sum of all spins: $\langle S_N^z\rangle = \pm N_{\rm loc}/2$ for e and g states.

Since our clock lock servo seeks to track the lineshape, it dynamically adjusts the laser detuning δ to compensate for the density shift. Thus, the observed density shift $\nu_{\rm dens} = \delta$ is where $B_z^\perp = 0$. Using Eq. 4.9, we find:

$$\begin{gathered}
\Delta\nu_{\rm dens}^{\alpha\to\beta} = \Delta\nu_{\alpha\to\beta}^s + \Delta\nu_{\alpha\to\beta}^p, \\
2\pi\Delta\nu_{\alpha\to\beta}^p \approx 2\chi_0\varsigma_{\alpha\to\beta}^z + C_0, \qquad 2\pi\Delta\nu_{\alpha\to\beta}^s \approx 2\chi_1\varsigma_{\alpha\to\beta}^z.
\end{gathered} \tag{4.11}$$

We have simplified the $\vec{S}$ dynamics under the mean field to a simple fitting parameter $\varsigma_{\alpha\to\beta}^z$, on-site p-wave, and off-site s-wave terms. This fitting parameter depends on the Rabi pulse area, excitation fraction, and the initial and final states of the spectroscopy, either $g\to e$ or $e\to g$. For the data presented in Ref. [1], we have $\varsigma_{g\to e}^z = -0.12$ and $\varsigma_{e\to g}^z = -0.095$. In Fig. 4.3, we plot the calculated s-wave, p-wave, and total density shift for both initial states over a range of lattice depths. The points are experimental data which show good agreement. Data gathering and processing are discussed in the next section.

4.2 Density Shift Imaging

We have already highlighted the power of in-situ imaging to measure and correct for spatial frequency gradients, see Ch. 2. The data presented in Fig. 4.3 harnesses this capability to make fast, synchronous measurements, as we naturally sample different densities throughout the atomic sample.

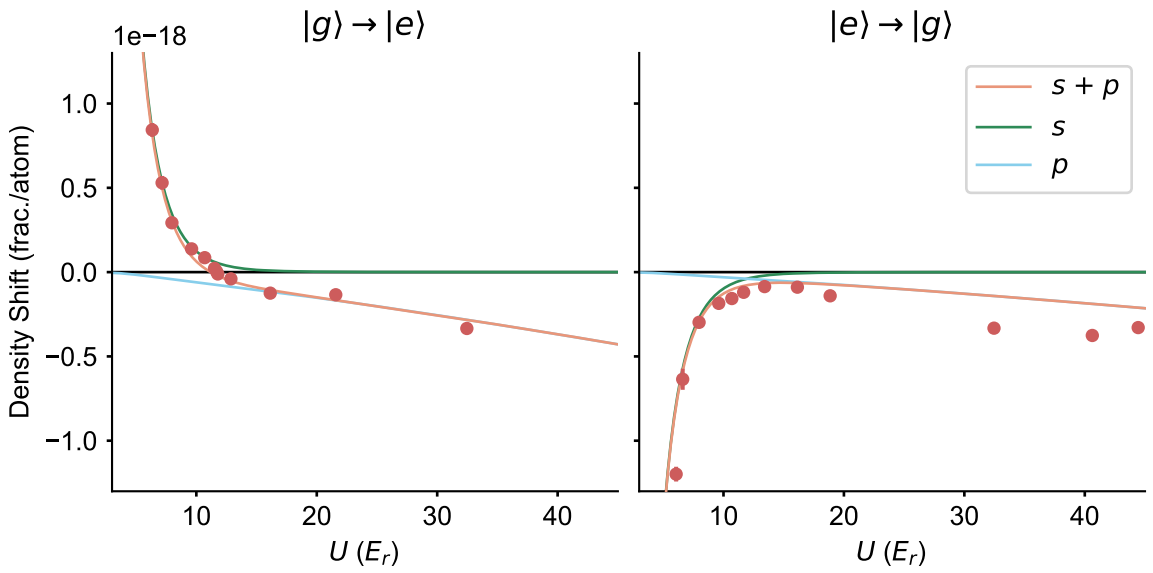

Figure 4.3: The density shift as a function of lattice depth. The density shift is due to two components, on-site p-wave interactions shown in blue, and off-site s-wave interactions shown in green. The total density shift is a sum of both components, shown in red. The points and error bars are experimental data with standard error, which match well with the calculated values. On the left, the sample is prepared in ${}^1S_0$, $|g\rangle$, and driven to ${}^3P_0$, $|g\rangle$. On the right, the scheme is reversed, leading to a different sign s-wave interaction shift.

One approach is to measure the average density gradient over a long clock lock, and then fit a line to the ν_{center} as a function of N_{loc}. While this technique works and was used for the gravitational redshift paper [22], we have moved to determining and correcting the density shift for each 4 point lock sequence. This allows us to correct for density shift variations in real-time, further reducing the flicker floor of the clock.

In Fig. 4.4 we show how this processing technique is applied. For each 4 point sequence, we construct a density map and a frequency map of the sample, shown in the left and middle plots, respectively. The density shift is well approximated by a linear function:

$$\nu_{center} = \nu_{dens} \times N_{loc} + b, \tag{4.12}$$

where b is the laser frequency offset from the single particle transition. While there is dependence

on S_z that varies throughout the sample with density, assuming a linear response allows us to reliably correct the density shift under standard operation. For each lockpoint, we use Eq. 4.12 to fit $\nu_{center}(N_{loc})$ and extract ν_{dens} and b, as shown on the right of Fig. 4.4.

Using the same lock data presented in Ch. 2, Fig. 4.5 shows a record of this density shift correction technique over the 15000 s run. On the left is the fractional density shift coefficient, ν_{dens}, with the average of all coefficients shown in black. In the center is a record of the intercept, b. In addition to a density shift free transition frequency, this parameter also contains the laser servo correction, including the Dick effect, leading to a noisier spread of frequencies than the synchronous measurement of ν_{dens}. On the right of Fig. 4.5 is an overlapping Allan deviation (OADEV) of the intercept and the peak total density shift, roughly $20\nu_{dens}$. As expected, the intercept determination is laser limited, $\sim 5 \times 10^{-17} \, / \sqrt{\tau/\mathrm{s}}$, while the ν_{dens} noise is limited only by QPN. Thus, we rapidly determine and correct for the density shift with negligible added noise.

Dynamic density shift corrections are critical for reliable clock measurements. Previous approaches to measuring the density shift necessitated varying the density and measuring the resultant frequency shift in an interleaved fashion [21]. Not only is this a Dick effect limited measurement, but any variation in ν_{dens} or the atom distribution would lead to a correction error. Lattice light shift measurements also benefit directly from this approach. As will be discussed in Ch. 5, we vary the lattice depth to measure the effect of the lattice light on the transition frequency. This inherently changes the density shift from 10^{-20} to 10^{-16}, which we measure and correct for during the light shift measurement campaign.

4.3 The "Magic Depth"

A fortuitous feature in our 1D Wannier-Stark lattice is the ability to operate with 0 density shift. Since the density shift is a combination of on-site p-wave and off-site s-wave interactions, we can tune our lattice depth to where these two mechanisms cancel in the mean field. As shown on the left of Fig. 4.3, the density shift crosses 0 around 10 E_r in the $|g\rangle \rightarrow |e\rangle$ case. This "magic depth" was critical in allowing us to resolve the gravitational redshift across the sample, as we could

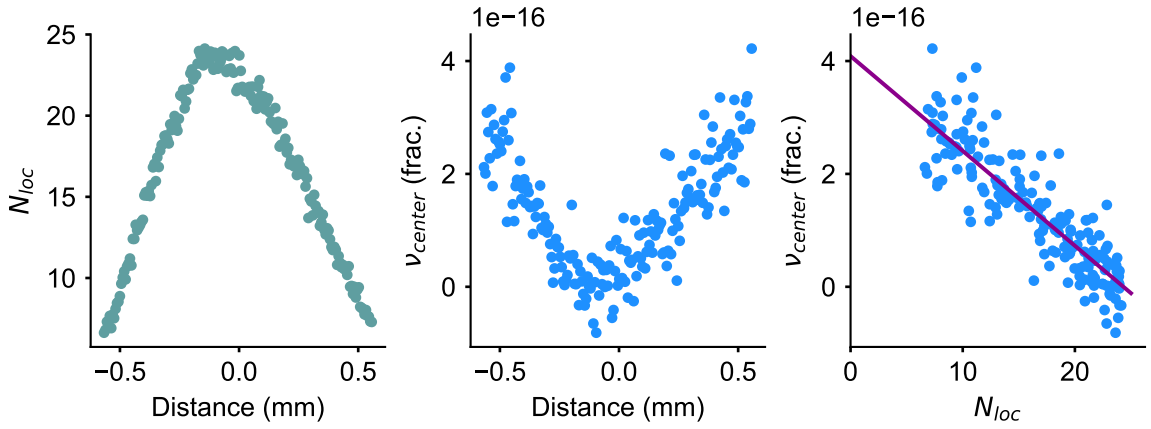

Figure 4.4: We determine the density shift using a single lockpoint during a standard "clock lock" sequence. The average of atom numbers during these four experimental shots is shown on the left. Using the excitations from the positive and negative detuned sides of the clock transition, we calculate the frequency at each pixel. The center panel shows the average of the $m_F = \pm 5/2 \rightarrow \pm 3/2$ transitions, rejecting spatial Zeeman gradients. Next, we fit a line to the frequency as a function of on-site density. By linearly extrapolating to zero density, we reject the density shift both spatially and temporally.

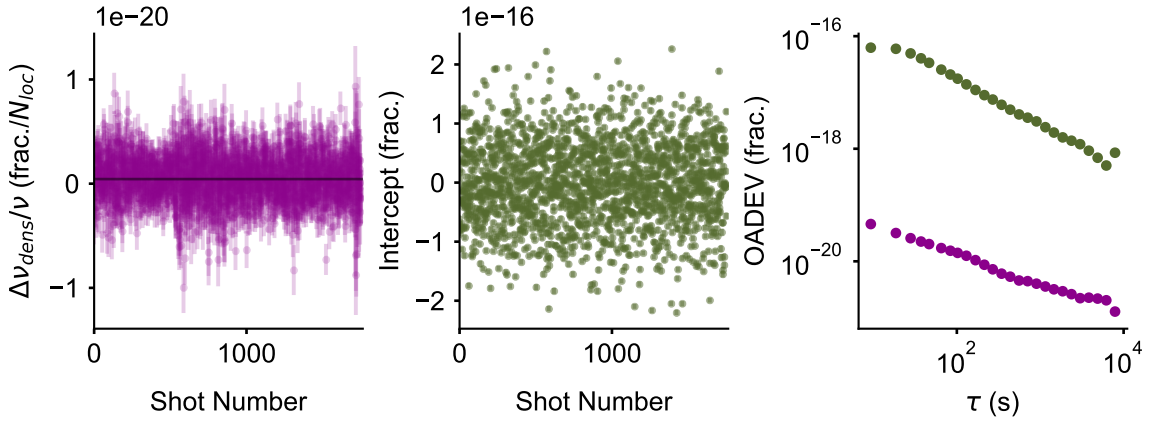

Figure 4.5: Point by point density shift correction. Left: the extracted density shift coefficient, $\Delta\nu_{\text{dens}}/\nu$ (frac./N_{loc}). Center: the probe correction, which includes both a density shift correction and a servo correction. Right: OADEVs of the probe correction (green) and the total density shift (purple) at the peak density ($N_{loc} = 20$). $\Delta\nu_{\text{dens}}$ is an in-situ measurement, so it is QPN limited with an additional lever arm due to the density variation. The intercept is a Dick effect limited correction.

operate with 10^5 atoms to reduce QPN and have a total density shift $< 10^{-18}$. Unfortunately, since the magic depth requires $\langle S_z \rangle < 0$, it does not exist for the $|e\rangle \rightarrow |g\rangle$ case or standard Ramsey

spectroscopy. By modifying the initial $\pi/2$ pulse and preparing a sample below the Bloch sphere equator, one can cancel the density shift in Ramsey [95]. This magic depth is also only valid for the ground band, as modifying the axial state will lead to a different magic depth as $\eta_{0,1}$ varies for n_z. During the lattice light shift evaluation, see Ch. 5, we modify the n_Z state and observe modified collisional shifts.

4.4 Dynamical Phase Transition

While the primary purpose of Sr1 is to operate as the most accurate and stable clock, the necessary quantum control in our system provides opportunities to study interesting features of the spin model. With this work, we do not seek to operate as an accurate clock, rather we use clock spectroscopy to understand emergent behavior, further verifying the spin model.

In the strongest density shift regimes in our system, we can achieve a dynamical phase transition where the spin dynamics vary dramatically at different laser detunings. Since the shift is dependent on $\langle S^z \rangle$, as one drives Rabi oscillations, the density shift varies. When the shift is strong, this can greatly suppress Rabi oscillations as the transition quickly becomes detuned from the laser as $\langle S^z \rangle$ increases. Varying the laser detuning, there is a sharp change in this behavior, indicating a dynamical phase transition (dpt). To generate strong interactions, we can drive an off-site transition (WS$\pm i$ for $i > 0$), creating s-wave interactions which scale as η_0. Following a similar approach to the carrier transition, we write a mean-field Hamiltonian for this off-site transition:

$$H_{\text{off-site}}/\hbar = \sum_n \vec{S}_n \cdot \vec{B}, \tag{4.13}$$

where the perpendicular component of the synthetic field is

$$B^{\perp}_{l=1} = \{\Omega_1, 0, -\delta_1 + 2\chi_1^{l=1}\langle S^z \rangle\}. \tag{4.14}$$

As with the carrier transition, mean-field equations can be written in terms of normalized expectation

value of collective spin operators on a single site $s^{x,y,z} = 2\langle S^{x,y,z}\rangle/N_{\mathrm{loc}}$,

$$\begin{aligned} \frac{\mathrm{d}}{\mathrm{d}t}s^x &= -N_{\mathrm{loc}}\chi_1^{l=1}s^z s^y + \delta_1 s^y, \\ \frac{\mathrm{d}}{\mathrm{d}t}s^y &= N_{\mathrm{loc}}\chi_1^{l=1}s^z s^x - \delta_1 s^x - \Omega_1 s^z, \\ \frac{\mathrm{d}}{\mathrm{d}t}s^z &= \Omega_1 s^y. \end{aligned} \tag{4.15}$$

Note that Eq. (4.15) takes the same form as the mean-field equations obtained in [32, 104].

With much stronger interactions, mode-changing collisions are now possible as the interaction energy can exceed the motional energy level spacing in the trap. As this dramatically increases the dimensionality of the problem, violating the frozen mode approximation, a full solution is complicated. Fortunately, we treat mode-changing simply as a density-dependent decoherence term, γ_z, leading to a shorter Bloch vector under evolution. We extract γ_z experimentally; fitting lineshapes at different densities we find $\gamma_z = 0.35 + 0.009 \times N_{\mathrm{loc}}$ (1/s) (see the supplement of Ref. [1]). Rewriting Eq. 4.15 with this effect:

$$\begin{aligned} \frac{\mathrm{d}}{\mathrm{d}t}s^x &= -N_{\mathrm{loc}}\chi_1^{l=1}s^z s^y + \delta_1 s^y - \gamma_z s^x, \\ \frac{\mathrm{d}}{\mathrm{d}t}s^y &= N_{\mathrm{loc}}\chi_1^{l=1}s^z s^x - \delta_1 s^x - \Omega_1 s^z - \gamma_z s^y, \\ \frac{\mathrm{d}}{\mathrm{d}t}s^z &= \Omega_1 s^y. \end{aligned} \tag{4.16}$$

In a dynamical phase transition, a critical point exists separating phases with different dynamical properties. Atoms are initially prepared in the ground state before a clock drive generates evolution of the spins. We study the long-time average excitation fraction $\bar{\rho}^{ee}$ of this dynamical system after a sudden quench, that is, after the clock drive is removed. Two emergent spin behaviors correspond to a ferromagnetic phase where atoms remain in the ground state, $\bar{\rho}^{ee} \approx 0$, while a paramagnetic phase $\bar{\rho}^{ee} = (\bar{s}^z + 1)/2$, where $\bar{s}^z = \lim_{T\to\infty} \frac{1}{T}\int_0^T s^z(t)\mathrm{d}t$. In contrast to a standard Rabi drive under a low density shift, the ferromagnetic phase is largely independent of δ, while $\bar{\rho}^{ee}$ dynamically adjusts as with δ_1 in the paramagnetic phase. More details investigating the behavior of this dpt are presented in the Supplement of Ref. [1].

We calculate the lineshape for two different densities in Fig. 4.6. This lineshape is calculated

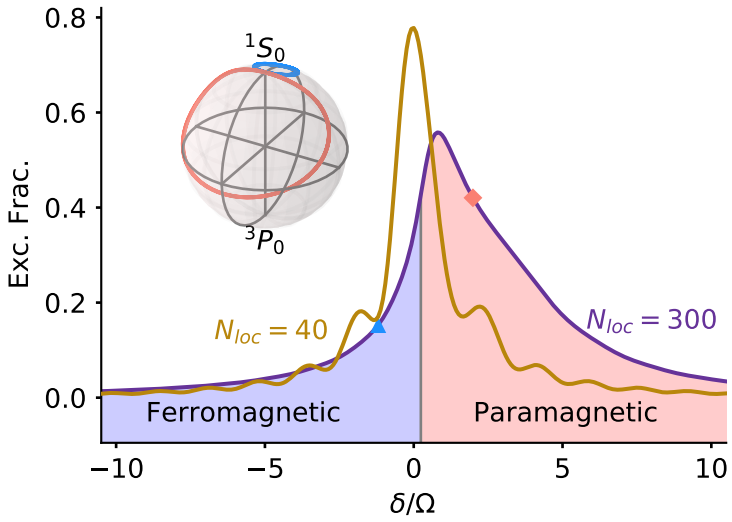

Figure 4.6: The dynamical phase transition lineshape and trajectories on the Bloch sphere. We plot the average excitation fraction of a long duration clock pulse as a function of detuning δ normalized by the Rabi frequency Ω. With $N_{\mathrm{loc}} = 40$, the line resembles a Rabi signal with additional decoherence. With $N_{\mathrm{loc}} = 300$, the line is asymmetric and has little Rabi character. On the negative detuning side, the sample is in a "ferromagnetic" state, with Bloch sphere trajectories remaining close to the origin, as with the blue line. Positively detuned, the sample is in a "paramagnetic" phase, with spin trajectories wrapping around the Bloch sphere.

include the experimentally determined γ_z and averaging over multiple Rabi drives $T_{\mathrm{Rabi}} > \pi/\Omega$. This gives an average excitation fraction that captures the long term dynamics of this dynamical system. For $N_{\mathrm{loc}} = 40$, the lineshape is roughly symmetric, and appears similar to a Rabi line with additional decoherence related broadening. When N_{loc} is increased above a threshold value, the sample now has two defined phases, a ferromagnetic phase where spins are aligned to one pole of the Bloch sphere, and a paramagnetic phase where spin trajectories have wider excursions and wrap around the Bloch sphere. This behavior is observed in the lineshape for $N_{\mathrm{loc}} = 300$ in Fig. 4.6. The line is very asymmetric, with the negatively detuned side having suppressed excitation and the right having higher excitation. The inset Bloch sphere shows two trajectories detuned from the center of the line, with the light blue showing the ferromagnetic phase and the salmon color showing the paramagnetic phase.

To probe this effect experimentally, we drive the $|^1S_0, W_i\rangle \rightarrow |^3P_0, W_{i+1}\rangle$ transition in a dense

sample. Again, making use of our imaging spectroscopy technique, we resolve the effect of different densities. To observe the dpt, we use a high density sample of $> 10^6$ atoms, with N_{loc} peaking around 250 atoms/site. We take multiple line scans and average the results together. In Fig. 4.7 C we plot this data as a heat map with the color showing the excitation fraction, organized by the onsite density on the vertical axis.

For a given N_{loc} we extract the lineshape asymmetry A_{LR} defined as $(n_R - n_L)/(n_R + n_L)$ from experimental data, and normalize by the maximum value of A_{LR}. Here, $n_R = \int_{\delta_{max}}^{\delta_{max}+f} n_\uparrow(\delta)\mathrm{d}\delta$, $n_L = \int_{\delta_{max}-f}^{\delta_{max}} n_\uparrow(\delta)\mathrm{d}\delta$, where δ_{max} is the detuning for the peak value of the Rabi lineshape, and $f/2\pi = 1$ Hz covers almost the entire frequency range of the Rabi lineshape. The lineshape asymmetry allows us to characterize the dynamical phases. For $N_{loc} < 63$, below the dashed black line in Fig. 4.7 C, the system is in a crossover regime featuring a linear density shift and asymmetry A_{LR} that becomes more pronounced as the atom number increases. With $N_{loc} > 63$, the lineshape is near maximally asymmetric, and distinct ferromagnetic and paramagnetic dynamical phases are identified. The phase boundary is experimentally determined by finding the maximum derivative of the lineshape as a function of detuning, plotted as green points in Fig. 4.7 C, with A_{LR} indicated by the shade. The points lie very close to the theoretically calculated phase boundary shown as a solid black line.

The asymmetry in the lineshape becomes apparent viewing the excitation at a constant atom number, as in Fig. 4.7 D. At densities well below the crossover boundary, the lineshape is only slightly distorted from that of an ideal Rabi response. Above the crossover density, the excitation displays very different behaviors for the two opposite signs of detuning, and the excitation becomes highly insensitive to changes of detuning deep in the ferromagnetic phase. The constant detuning profiles presented in Fig. 4.7 E further illustrate this dynamical phase transition. At $\delta_1/2\pi = 0$ Hz, the laser drive is on resonance with the non-interacting transition. Above the crossover regime, the ensemble features both dynamical phases, evolving from a dynamical paramagnet to a dynamical ferromagnet for $N_{loc} > 82$. At $\delta_1/2\pi = -0.72$ Hz the system is in the dynamical ferromagnetic phase above the crossover region. However, with $\delta_1/2\pi = 0.72$ Hz detuning, the excitation fraction initially

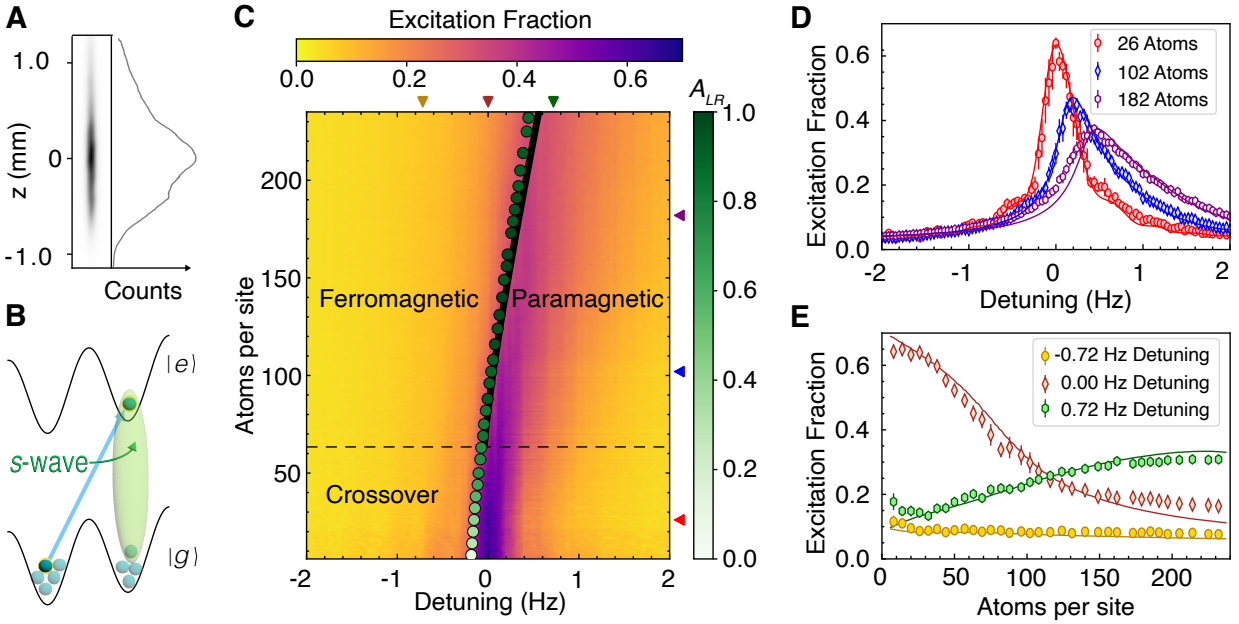

Figure 4.7: (A) An image of lattice trapped atoms, indicating a spatial extent over a millimeter in length. Within a single image, we can study lattice site density regimes ranging over two orders of magnitude, shown here as camera counts. (B) Addressing the $|^1S_0, W_i\rangle \rightarrow |^3P_0, W_{i+1}\rangle$ transition, s-wave interactions effectively become on-site, leading to a strong collisional shift. (C) Excitation fraction as a function of detuning and atom number on the $|^1S_0, W_i\rangle \rightarrow |^3P_0, W_{i+1}\rangle$ transition at 22 E_r. Above $\sim$ 63 atoms per site, denoted by the dashed black line, the system features a DPT between ferromagnetic and paramagnetic phases when varying the laser detuning and atomic density. The phase boundary is denoted by a solid black line from theoretical calculations and green points from the experimental data. The normalized asymmetry of the lineshape A_{LR} is indicated by the shade of these points. Arrows on the right and top axis indicate data plotted in (D) and (E) at constant atom number and detuning. (D) Excitation fraction as a function of detuning at different atom numbers demonstrates the notable distortion and asymmetry that arises in the strongly interacting regime. (E) Excitation fraction as a function of atom number in the ferromagnetic phase (-0.72 Hz), across the phase transition (0 Hz), and in the paramagnetic phase (0.72 Hz). Solid lines in (D) and (E) indicate theoretical calculations.

rises with atom number when the system is in the paramagnetic phase and saturates close to the phase boundary. In both panels D and E the solid lines are theoretical predictions from the mean field spin model with the additional decoherence term using Eq. 4.16.

Chapter 5

Lattice Light Shift

While trapping atoms in an optical lattice is key to performing narrow spectroscopy, this process necessarily shifts the spectroscopy states. The goal of a magic wavelength lattice is to match the light shifts for both clock states, leading to no net shift to the transition as well as no light shift induced motional broadening [138, 163]. Understanding of the lattice light shift is an ongoing endeavor, with each new benchmark in lattice clock accuracy often requiring a reevaluation of this systematic. In addition to finding the proper scalar polarizability, effects such as magnetic dipole and electric quadrupole moments complicate this shift. Additionally, we verify the lattice light shift model in a very shallow lattice for the first time. In the following chapter, we discuss the lattice light shift model we use and our work evaluating the lattice light shift on the Sr1 system. Much of this work was published in the Physical Review Letters paper entitled "Evaluation of Lattice Light Shift at Low 10^{-19} Uncertainty for a Shallow Lattice Sr Optical Clock," Ref. [70]. We also discuss a reevaluation completed in July 2024, as well as the light shift using different magnetic sublevel transitions.

5.1 Atom-Light Interactions

Under the electric dipole approximation, light of intensity I_0 interacting with an atom in hyperfine state F and magnetic sublevel m_F, creates an AC Stark shift U that depends on scalar,

vector, and tensor contributions. With light intensity I_0, this can be written as [151],

$$U(I_0) = I_0 \left(\kappa_s + \kappa_v m_F \xi \hat{k} \cdot \hat{B} + \left[3m_F^2 - F(F+1) \right] \left(3|\hat{\epsilon} \cdot \hat{B}|^2 - 1 \right) \kappa_t \right), \tag{5.1}$$

where ξ is the light ellipticity, $\hat{\epsilon}$ is the light polarization direction, $\hat{k}$ is the light propagation direction, $\hat{B}$ is the magnetic field direction, and κ_s, κ_v, and κ_t are the scalar, vector, and tensor strengths. The scalar component is rotationally invariant. The vector component appears when $F \geq 1/2$ and acts as a synthetic magnetic field, so it is canceled by taking the average of opposite sign m_F states. The tensor component gives rise to a light polarization dependent polarizability, appearing when $F \geq 1$. Since ytterbium-171 has $F = 1/2$, it has an attractively simple light shift that does not depend on polarization direction [28]. Taking the proper weighting of two different magnetic sublevel clock transitions, a Sr clock can reject the tensor contribution to the light shift. We find our tensor shift to be stable enough there is no need to implement this scheme for our accuracy goals.

For our lattice light shift evaluation, we seek to determine the effect of Eq. 5.1 on the clock transition. We must determine the differential strength $\Delta\kappa_{s,v,t}$ between the two clock transitions. We alternate m_F signs, using the difference transition frequencies between magnetic sublevel signs to measure the vector effect and the average to reject this effect. We combine the scalar and tensor light shift components into a single effective dipole polarizability for our specific state i that depends on the lattice frequency ν_{lat}: $\alpha_i^{E1} \equiv \alpha^{E1}(i, F^i, m_F^i, \hat{\epsilon}, \hat{B}, \nu_{lat})$.

In a one-dimensional lattice formed by a standing wave of light along Z, the intensity $I = I_0 \cos^2 k_L Z$, where I_0 is the incident intensity and k_L is the lattice light wavenumber. The electric dipole ($E1$) polarizability is the strongest interaction, so $U \approx \alpha_i^{E1} I_0 \cos^2 k_L Z$ for state i. To reach our desired light shift uncertainty, we must also consider higher order light shift effects. Hyperpolarizability is a fourth order in field process, so it goes as $I_0^2 \cos^4 k_L Z$ and has strength described by the coefficient β_i. The magnetic dipole interaction ($M1$) is due to the interaction of the atom with the magnetic field, which is simply the derivative of the electric field and goes as $\sin^2 k_L Z$. Similarly, the electric quadrupole interaction ($E2$) is due to the curvature of the electric

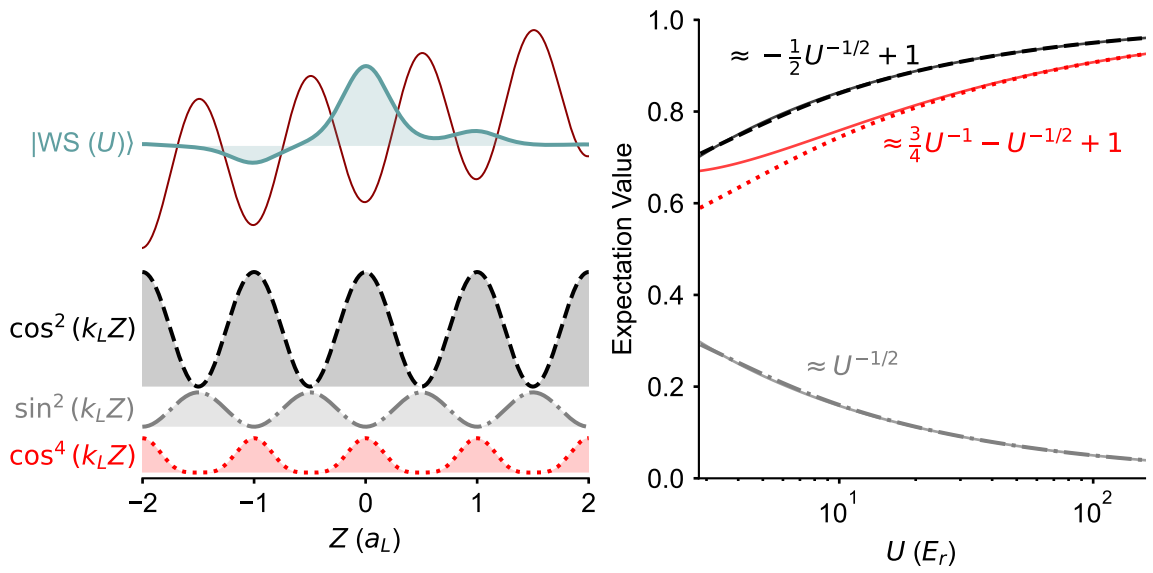

Figure 5.1: Origin of the lattice light shift. Left: the atoms are confined to the peak intensities of the lattice, shown as a red potential, creating Wannier-Stark wavefunctions $|\mathrm{WS}(U)\rangle$ along Z that depend on lattice depth U. The atoms spatially sample the lattice electric and magnetic fields, causing a light shift. The electric dipole polarizability depend on the light intensity, and goes as $\cos^2(k_L Z)$. The electric quadrupole and magnetic dipole go as $\sin^2(k_L Z)$. The higher order hyperpolarizability term goes as $\cos^4(k_L Z)$ Right: to calculate the total shift, we need to know the expectation value of all three terms. The dashed lines are calculated with the numerically evaluated $|\mathrm{WS}(U)\rangle$, with the solid lines a harmonic approximation using Eq. 5.4.

field, again $\sin^2 k_L Z$. We combine the $M1$ and $E2$ terms into a single coefficient, α_i^{qm}. Thus, for an atom in state i, we write the lattice light shift U as a sum of three terms,

$$U_i(I_0) \approx -\alpha_i^{E1} I_0 \cos^2(k_L Z) - \alpha_i^{qm} I_0 \sin^2(k_L Z) - \beta_i I_0^2 \cos^4(k_L Z). \tag{5.2}$$

Higher order light shift processes do exist, however for our system this is a valid approximation. Atoms are trapped in this lattice near the peak intensity of the light, strongly confined by the $E1$ shift.

With a two level system, the lattice light shift is due to the difference between the energy shift of both states, $\Delta\nu_{LS} = U_e(I_0) - U_g(I_0)$. In a "magic" lattice, we attempt to match the shift of both states, $U_e(I_0) = U_g(I_0)$ by adjusting the lattice frequency such that $\alpha_e^{E1} = \alpha_g^{E1}$. The resultant

error of the $E1$ term is from the differential slope between e and g and the detuning from magic, δ_L: $\alpha_e^{E1} - \alpha_g^{E1} = \frac{\partial\tilde{\alpha}^{E1}}{\partial\nu}\delta_L$. The other parameters are effectively δ_L independent, so the parameter difference between the two states is $\tilde{\alpha}^{qm} = \alpha_e^{qm} - \alpha_g^{qm}$ and $\tilde{\beta} = \beta_e - \beta_g$. This allows us to express the total light shift as a function of atomic parameters and expectation values of the motional wave function:

$$\Delta\nu_{LS}(U) \approx -\frac{\partial\tilde{\alpha}^{E1}}{\partial\nu}\delta_L U\langle\cos^2 k_L Z\rangle - \tilde{\alpha}^{qm}U\langle\sin^2 k_L Z\rangle - \tilde{\beta}U^2\langle\cos^4 k_L Z\rangle. \tag{5.3}$$

To evaluate the effect of the lattice confinement on the energy of the atom, we must determine the effect of each term in Eq. 5.2 on the state of the atom, illustrated in Fig. 5.1. To calculate the motional state, we assume first that confinement is due entirely to the $E1$ term. As derived in Ch. 3, the resultant wave functions in our tilted lattice are Wannier-Stark states, $|\mathrm{WS}(U)\rangle$, plotted for a shallow depth as the top trace on the left of Fig. 5.1. Next, we calculate the expectation value of the wave function for each of the terms. On the right, we plot the numerically evaluated terms as dashed lines on the right.

While it is possible to use numerically evaluated expectation values for calculating the light shift, if we make the approximation that the atoms are harmonically confined we can write $\Delta\nu_{LS}$ in an analytical form. Following the approach outline in Ref. [67], we write these as functions of the lattice depth and the axial motional state, n_Z:

$$\begin{aligned}
\langle\cos^2 k_L Z\rangle &\approx -\left(n_Z + \frac{1}{2}\right)U^{-1/2} + 1 \\
\langle\sin^2 k_L Z\rangle &\approx \left(n_Z + \frac{1}{2}\right)U^{-1/2} \\
\langle\cos^4 k_L Z\rangle &\approx \frac{3}{2}\left(n_Z^2 + n_Z + \frac{1}{2}\right)U^{-1} - 2\left(n_Z + \frac{1}{2}\right)U^{-1/2} + 1
\end{aligned} \tag{5.4}$$

On the right of Fig. 5.1, we plot with solid lines the expectation values for $n_Z = 0$ using these approximations. The agreement between the numerically evaluated and harmonic expectation values is generally quite good. The $\cos^4$ term contains the strongest disagreement where $U < 10\ E_r$. Fortunately, since the hyperpolarizability coefficient is small, this effect is negligible at such shallow

depths.

Lastly, we need to adjust for the effect of the radial extent modifying the lattice intensity. We do this by introducing an effective lattice depth u of power j such that $u^j = (1+jkT_r/U_0)^{-1}(U_0/E_r)^j$, where U_0 is the peak lattice depth. As the radial temperature T_r increases, this term generates a shallower effective depth to compensate. Since we do not observe any line broadening from radial temperatures, we abstain from using a state resolved radial description. With these approximations we write the final form of the "harmonic model," as derived in Ref. [67]:

$$\begin{aligned} h\Delta\nu_{LS}(u,\delta_L,n_Z) \approx &\left(\frac{\partial\tilde{\alpha}^{E1}}{\partial\nu}\delta_L - \tilde{\alpha}^{qm}\right)\left(n_Z+\frac{1}{2}\right)u^{1/2} \\ &- \left[\frac{\partial\tilde{\alpha}^{E1}}{\partial\nu}\delta_L + \frac{3}{2}\tilde{\beta}\left(n_Z^2+n_Z+\frac{1}{2}\right)\right]u^1 \\ &+ 2\tilde{\beta}\left(n_Z+\frac{1}{2}\right)u^{3/2} - \tilde{\beta}u^2. \end{aligned} \tag{5.5}$$

Thus, we have four parameters that describe the atomic response to lattice light, $(\delta_L, \partial_\nu\tilde{\alpha}^{E1}, \tilde{\alpha}^{qm}, \tilde{\beta})$, and three parameters that describe the atomic motion, (U_0, T_r, n_Z). This approach simplifies the lattice light shift problem while still preserving the effect of hyperpolarizability and $M1$ and $E2$ shifts.

Additional models and variations of this model have attempted to better capture the radial coupling to the light shift. A more sophisticated approach using measured motional signals was implemented in a Yb OLC [107], however this sample is at a much higher temperature than in our system, necessitating this technique. The Born-Oppenheimer and WKB model (BO + WKB), derived in Ref. [12], applies a Born-Oppenheimer approximation to the radial modes, and then the WKB approximation to solve the resultant differential equations. In practice, we have found Eq. 5.5 to adequately capture the experimental data we gather and allows us to reach our target light shift uncertainty. This is partly due to the low radial and axial temperatures as well as the very shallow lattice we use in standard operation. Further advances in clock accuracy may require fewer approximations to determine the light shift, or even more sophisticated lattices [153].

Since we are aiming to operate at shallow lattice depths, it is worthwhile to determine if the

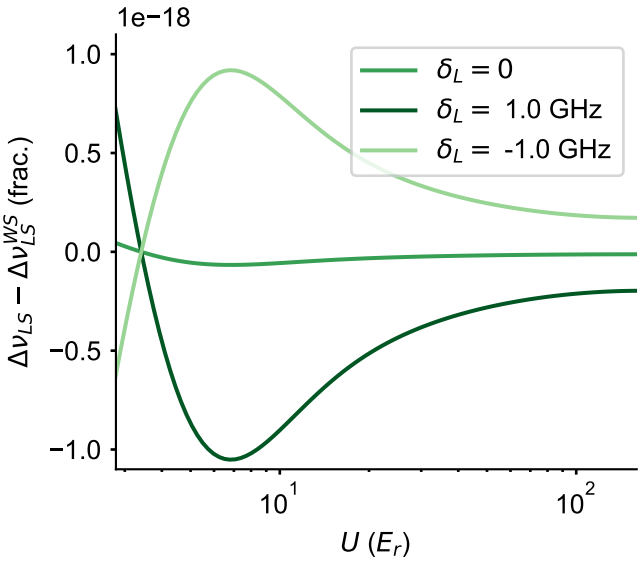

Figure 5.2: The difference between the light shift calculated using Eq. 5.5, $\Delta\nu_{LS}$, and the light shift calculated using numerically evaluated Wannier-Stark states, $\Delta\nu_{LS}^{WS}$. We assume $n_Z = 0$ and $T_r = 0$ for both cases, and plot for three detunings from magic, δ_L. Disagreement between the two light shift calculations stems primarily from the $E1$ term as it is strongly δ_L dependent.

Wannier-Stark state modifies the light shift. As we have already shown in Fig. 5.1, the harmonic approximation captures the expectation values where $U > 10\ E_r$. What is the effect on $\Delta\nu_{LS}$? In Fig. 5.2, we plot the difference between Eq. 5.5 and the light shift calculated using numerically evaluated $|\mathrm{WS}(U)\rangle$, $\Delta\nu_{LS}^{WS}$, for three different δ_L. We calculate this under the assumption $n_Z = 0$ and $T_r = 0$. The harmonic approximation error primarily appears in the $E1$ term as it depends on δ_L. The $M1 + E2$ and hyperpolarizability terms account for errors $< 10^{-19}$, shown in $\delta = 0$. At deep lattice depths, $|\mathrm{WS}(U)\rangle$ approaches the harmonic wavefunction, and different light shift approaches agree well. With errors $< 10^{-18}$ for $\delta_L < 1$ GHz, this calculation supports the use of the harmonic model in our system, even at shallow depths. With even sampling of δ_L about $\delta_L = 0$, this effect will slightly modify the fit $\partial_\nu \tilde{\alpha}^{E1}$ but not significantly change the overall light shift near magic. Further work using numerically evaluated wavefunctions is straightforward to implement, and may be necessary for light shift evaluations with accuracy goals $< 10^{-19}$.

Eq. 5.5 sets a roadmap for evaluating the light shift. While the atomic parameters are fixed,

the three simple controls we have are n_Z, U, and δ_L. Carefully varying these will allow us to back out the atomic coefficients with great precision. The coefficients in this model *should* be identical for all Sr^{87}, with δ_l depending only on the magnetic sublevel transition as we compensate for different tensor polarizabilities. Through this measurement process, we can compare against the precise measurement performed in RIKEN [145], as well as future precision light shift measurements in Sr. These atomic coefficients can also be calculated, allowing us to benchmark these methods.

5.2 Experimental Measurements

During the spring and summer of 2022, we completed the first lattice light shift measurement campaign with the rebuilt Sr1 system [70]. The previous generation Sr1 used the thermal model [21], so this is the first use of the harmonic model in the Ye lab. The first set of measurements involved preparing a ground band, $n_Z = 0$ sample, and varying the depth and lattice detuning, (U, δ_L). We performed these measurement via an interleaved comparison, alternating between two atomic servos at different lattice conditions, continuously averaging the difference frequency between these servos [108]. This relies on using Si3 as the short time frequency reference, leading to a Dick effect limited self-comparison stability of about 2×10^{-16} at 1 s with a 380 ms Rabi pulse and near 1 s duty cycle. The frequency shift is the average of the frequency differences, with the statistical uncertainty derived from a fit to the overlapping Allan deviation taken at 1/3 of the total measurement time τ. We typically average until the statistical uncertainties are less than 3×10^{-18}.

As we modulate the lattice depth, the density shift varies significantly, from near zero to $> 10^{-16}$ at deep depths. To prevent this from polluting the lattice light shift measurement by introducing another U-dependent systematic, it is critical to correct for the density shift effect. We implement synchronous density shift correction for each lock point, removing this effect from the light shift measurement and allowing us average for longer times, demonstrated in Fig. 5.3. Plotted on the top left, we gather an interleaved frequency record of the two lattice conditions, shown here at $U = 12.2\ E_r$ and $320\ E_r$. On the top right, we apply density shift and linear laser drift corrections to each frequency series. Since the two locks occur a few seconds apart on average, laser

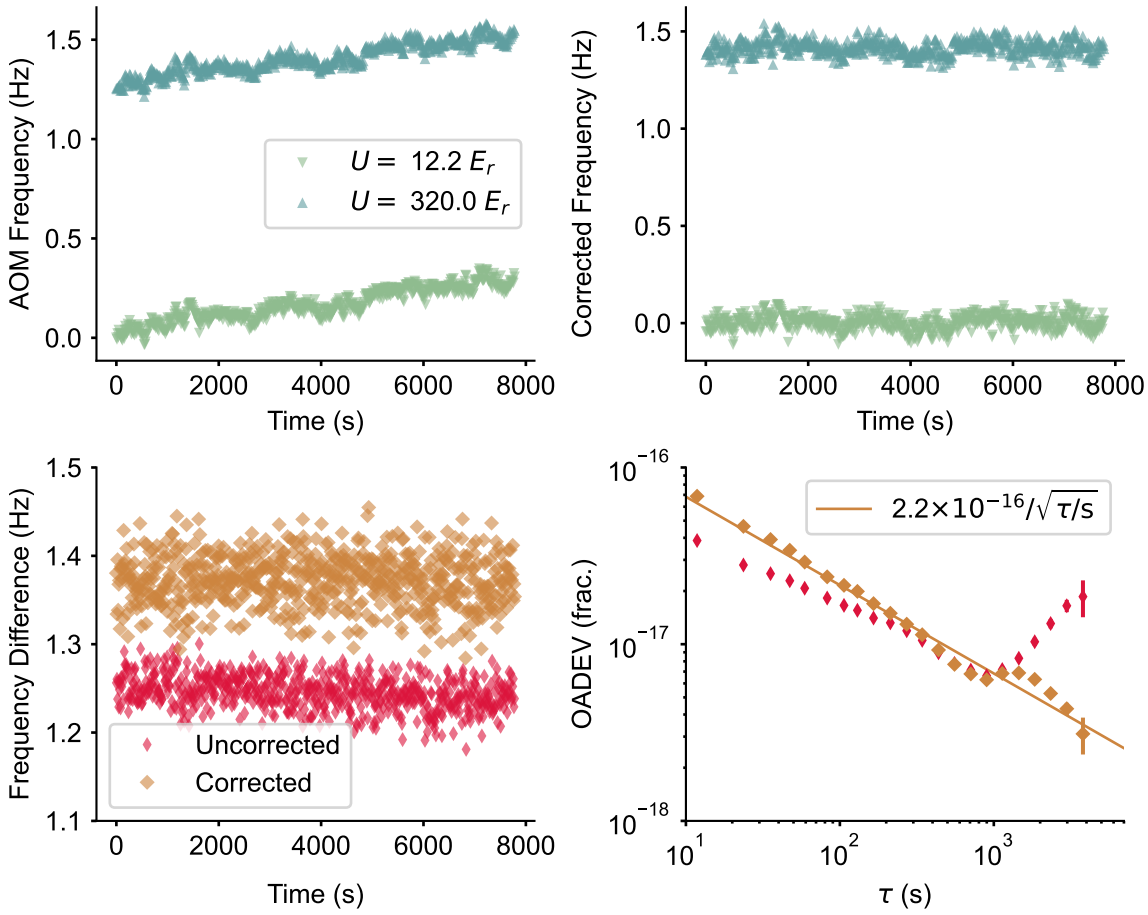

Figure 5.3: Example of an 8 point lock to measure the lattice light shift. We probe two different lattice depths, 12.2 E_r and 320 E_r, with separate clock servos in an interleaved fashion. The top left plot shows the frequency applied to the AOM to steer to the atomic resonance over the course of this 8000 s lock, with the initial 12.2 E_r frequency subtracted. We apply two frequency corrections to this data, the density shift and laser drift. Corrected frequencies are shown in the top right. The frequency difference between the two lattice depths is shown in the bottom left. On the bottom right, an overlapping Allan deviation (OADEV) highlights the stability difference between the corrected and uncorrected frequency differences. The corrected frequency averages down as white frequency noise with a stability of $2.2 \times 10^{-16}/\sqrt{\tau/\mathrm{s}}$ at averaging time τ. The uncorrected frequency difference flickers and drifts as the atom number changes.

drift skews the frequency difference at the low 10^{-19} level. Typically, we dedrift by subtracting from the frequency difference a fitted drift rate multiplied by the average time difference of the two locks. On the bottom left, we plot the frequency difference between the two lattice conditions for the uncorrected and corrected data. In this case, the density shift correction removes a shift of

around 150 mHz. The corrected frequency contains the servo error for each point, removing the low pass effect of the atomic servo and leading to higher noise at short time. This is apparent in the overlapping Allan deviation plotted in the bottom right, with times < 200 s. As the density varies by upwards of 10% over the course of a measurement, the density shift at deep depths can set a frequency noise floor above 10^{-17}. With this approach, we consistently observe Allan deviations of the density corrected frequency difference following the expected white frequency noise trend of $1/\sqrt{\tau}$. For the first dataset, (U, δ_L), we always use a reference depth $U \approx 10\ E_r$, near the magic lattice depth for additional robustness in taming the density shift.

It is critical to keep record of the atomic conditions during data collection. Before each measurement, T_r is recorded to be used in the final fit. We implement Rabi frequency lattice depth calibration described in Ch. 3 for robust characterization at shallow depths. Periodically, we measure the axial sideband structure, ensuring a constant depth and axial population distribution. Over the data campaign, we find the mean axial population $\langle n_Z \rangle < 0.03$, which we take as n_Z uncertainty for the fit.

Preparing a "clean" lattice laser with a stable spectrum, spatial mode, and polarization is important for a reliable light shift, as background light near the lattice frequency can cause deleterious frequency shifts. In the Ye group, this was noted early on as a potential issue with the high amplified spontaneous emission (ASE) background of tapered amplifiers (TAs). Significant works has gone into understanding this effect in both Sr OLCs [64] and Yb OLCS [43], with various schemes presented to ensure the background emission is attenuated as to not shift the clock frequency. Sr2 and Sr3 have used low background Ti:Sa lasers and now both use fiber lasers instead of TAs. On Sr1, the buildup cavity allows us to use a simple diode laser injection locked by an ECDL. The cavity provides some background suppression, and we insert a volume Bragg grating (VBG) before the cavity to further clean the optical spectrum. We measure the light shift with 0, 1, and 2 VBGs as well as different diodes and diode temperatures, and do not observe any unexplained light shifts. Thus, we are confident that background emission does not affect these light shift results.

The results of the (U, δ_L) modulation data are presented in Fig. 5.4. The top left plot shows

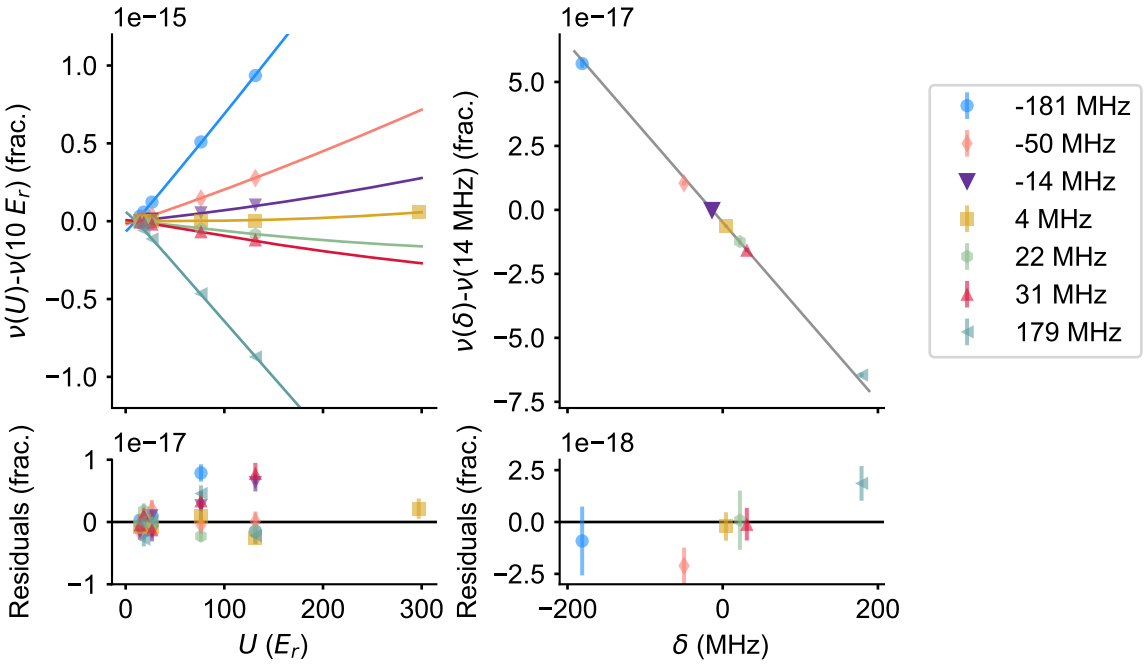

Figure 5.4: Lattice light shift measurement varying the lattice detuning from magic, δ_L, and lattice depth U. Left: difference between strontium transition frequencies at the reference depth, $\nu(10\ E_r)$, and at depth U, $\nu(U)$, at 7 different lattice frequencies. Solid lines show a fit using Eq. 5.5. The bottom panel shows fit residuals. Right: difference between strontium transition frequencies at the reference frequency $\nu(\delta_L = 14$ MHz) and at detuning δ_L at a 10 E_r. The gray line is the model fit, with the residual shown on the lower panel.

the results of the U modulation measurements. Each color represents a different lattice frequency, with the detuning δ_L from a fitted magic frequency indicated in the plot key on the right. The solid lines are fits to the data using Eq. 5.5, with the fit residuals plotted in the lower panel. On the right are the results for lattice frequency modulation, δ_L, with the gray line showing the fit and residuals in the bottom panel. The reference frequency $\delta_L = 14$ MHz is shown in purple and is not experimentally measured. The model appears to properly capture the data, with residuals $< 10^{-17}$.

Higher order polarizability effects due to the lattice light are relatively small, so determining $\tilde{\alpha}^{qm}$ with great precision is difficult. The approach first used in Ref. [145] utilizes the differential sensitivity to $\tilde{\alpha}^{qm}$ between different n_Z states. As the axial wavefunction extends further at higher n_Z, the atom samples more electric field curvature and magnetic field magnitude, increasing the differential $E2$ and $M1$ shifts. With $\delta_L = 0$, the difference in transition frequency between $n_Z = 0$

and $n_Z = 1$ becomes:

$$h\Delta\nu_{n_Z} = h(\Delta\nu_{LS}(n_Z = 1) - \Delta\nu_{LS}(n_Z = 0)) \approx \tilde{\alpha}^{qm} u^{1/2} + \tilde{\beta} u^1 (2u^{1/2} - 3). \tag{5.6}$$

Since $\tilde{\beta}$ is about three orders smaller than $\tilde{\alpha}^{qm}$, the frequency difference between n_Z states is dominated by the multipolar component at shallow lattice depths.

As in Ref. [145], we compare the frequencies between $n_Z = 0$ and 1 at different lattice depths with the lattice detuning near magic, $\delta_L < 1$ MHz. The $n_Z = 0$ population is prepared in the same way as the first data set, with resolved sideband cooling ensuring $\langle n_Z \rangle < 0.03$ and two clock transfer pulses to initialize the sample in $|^1S_0, m_F = \pm 5/2, n_Z = 0\rangle$. To prepare an $n_Z = 1$ sample, we cool as typical but then detune the $|^1S_0, m_F = \pm 9/2\rangle \rightarrow |^3P_0, m_F = \pm 7/2\rangle$ transfer by $\sim +30$ kHz, driving the blue sideband for 300 ms. This creates a $|^3P_0, m_F = \pm 7/2, n_Z = 1\rangle$ sample that we transfer to $|^1S_0, m_F = \pm 5/2, n_Z = 1\rangle$ before spectroscopy. The spin and motional transfer pulses are all completed at 20 E_r to ensure repeatable sample preparation. The process is rather inefficient, transferring about 20% of the population and increasing the dead time, adversely affecting the Dick effect limited measurement stability. The statistical uncertainty of the individual $\Delta\nu_{n_Z}$ light shift measurements measurements is typically around 5×10^{-18}.

As before, it is critical to correct for the density shift. Since the density interactions depend on the wavefunction overlap between atoms, the η parameter defined in Ch. 4, different motional states experience different frequency shifts. Off site interactions increase, leading to a magic depth near 20 E_r for the $n_Z = 1$ state. At deeper depths where this data was taken, interactions are on-site p-wave dominated, so the higher axial state leads to a lower effective density and lower shift per atom. We observe a roughly 20% reduction in density shift for the $n_Z = 1$ state where $U > 100$ E_r.

We collect (n_Z) modulation data between 50 and 300 E_r, with the final results presented in Fig. 5.5. The solid line is derived from a global fit to all of the data, with all residuals again $< 10^{-17}$. The $U^{1/2}$ behavior of $\Delta\nu_{n_Z}$ is clearly visible.

Key to a robust light shift evaluation is simultaneously fitting the data. While this may seem

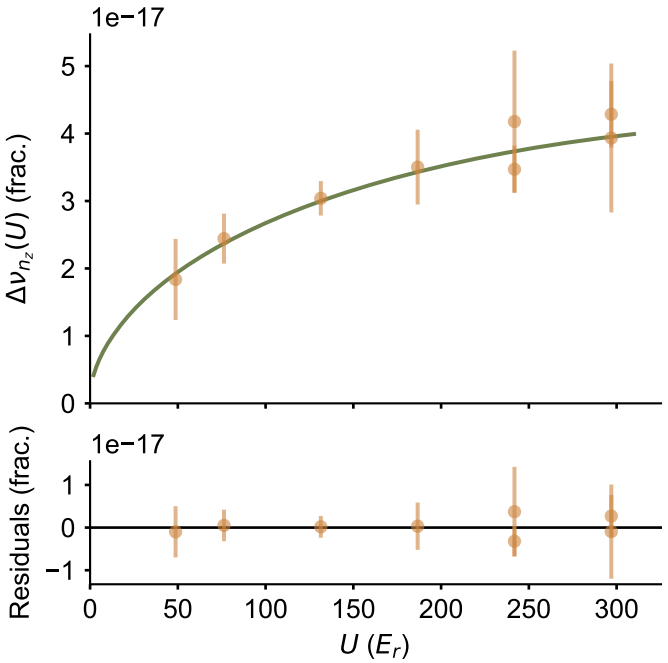

Figure 5.5: Differential light shift measurement between $n_Z = 0$ and $n_Z = 1$ axial states, $\Delta\nu_{n_Z}$, with $|\delta_L| < 1$ MHz. The solid line shows the results of a global fit to all light shift data with fit residuals shown in the bottom panel. Notice the $\sim U^{1/2}$ behavior of $\Delta\nu_{n_Z}$, characteristic of the $\tilde{\alpha}^{qm}$ term.

obvious, this approach is not always implemented due to perceived complexity [145]. We began our light shift evaluation separately fitting the (U, δ_L) modulation data and the n_Z modulation data, using the second data set to exclusively determine $\tilde{\alpha}^{qm}$. However, the (U, δ_L) modulation data still contains useful information about $\tilde{\alpha}^{qm}$ not used in our first attempt. This initial approach, as well as fitting with a constant reference condition, is described extensively in the supplement of Ref. [70]. Switching to a comprehensive fit allows us to determine fitting parameters with better precision, using the light shift model to describe all data simultaneously. We generically write all light measurements $\Delta\nu_{meas}$ as the frequency difference between two different sample and lattice configurations, A and B:

$$\Delta\nu_{meas} = \Delta\nu_{LS}(u(U^A, T_r^A), \delta_L^A, n_Z^A) - \Delta\nu_{LS}(u(U^B, T_r^B), \delta_L^B, n_Z^B). \tag{5.7}$$

Table 5.1: Summary of the light shift characterization. We perform a single fit to the data including data in both Fig. 5.4, 5.5 to extract the coefficients. Uncertainties in measured frequency differences and the lattice depth are used in the fit [70].

Quantity	Value
$\partial_\nu \tilde{\alpha}^{E1}/h$	$1.859(5) \times 10^{-11}$
ν^{E1} (MHz)	$368,554,825.9(4)$
$\tilde{\alpha}^{qm}/h$ (mHz)	$-1.24(5)$
$\tilde{\beta}/h$ (μHz)	$-0.51(4)$

The differential measurements only change one of (u, δ_L, n_Z) between the two locks, but this fitting procedure can involve any combination of differential locks. As long as the measured frequency shift is well described by the light shift model, the data can be incorporated in the fit.

Proper treatment of uncertainties is also important for the fitting procedure. The frequency measurements are dominated by statistical uncertainties. For each measurement, we fit a white noise $1/\sqrt{\tau}$ model to the overlapping Allan deviation and calculate the uncertainty at 1/3 the total measurement time. Since we observed no flicker in these measurements, we believe this approach properly captures the statistical uncertainty. The other significant source of uncertainty is in U, which comes from errors in the lattice depth calibration. This scales from 0.1 E_r at near zero depth to 0.6 E_r at 300 E_r. Smaller sources of uncertainty include uncertainty arising from sample preparation, with radial temperature uncertainty, $\delta T_r \approx 0.1 \times T_r$, and axial state uncertainty, $\delta n_Z = 0.03$. Lattice frequency uncertainty primarily arises from a loose lattice lock to the frequency comb, with $\delta\nu_{lat} = 100$ kHz. Using orthogonal distance regression (ODR), we are able to properly account for uncertainties in all fitting parameters. The final results including total uncertainty from the global fit are shown in Tab. 5.1.

Since the publishing of Ref. [145], the $\tilde{\alpha}^{qm}$ term has come under scrutiny. Eq. 5.5 relies on fundamental atomic properties $(\nu_{magic}, \tilde{\alpha}^{qm}, \partial_\nu \tilde{\alpha}^{E1}, \tilde{\beta})$ that should be calculable. Nevertheless, sophisticated theory work initially reported $\tilde{\alpha}^{qm}$ wholly inconsistent with the first experimentally measured value [123, 155]. Since Ref. [145], our measurement along with a measurement in PTB [41]

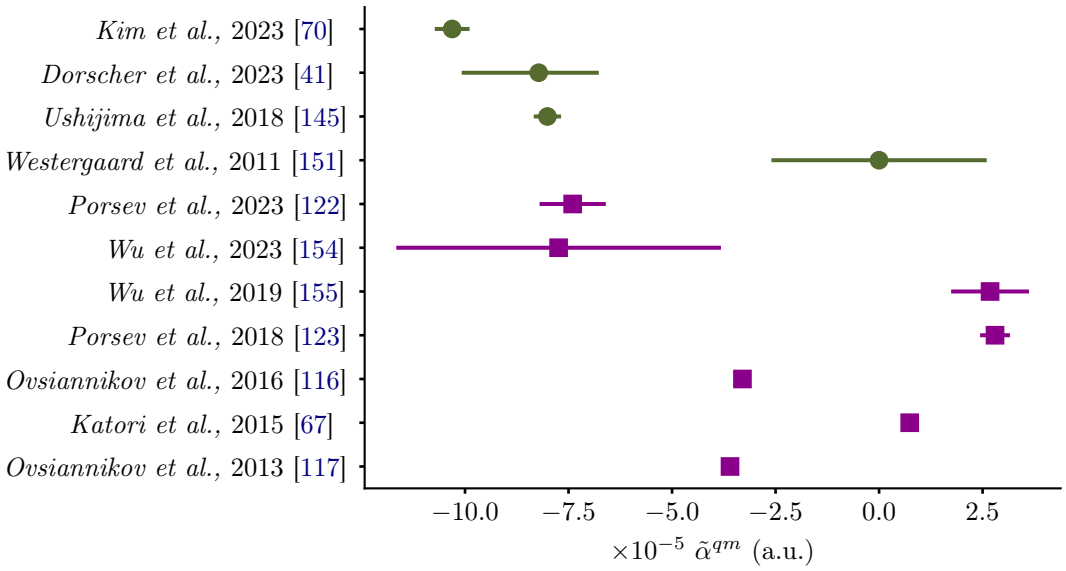

Figure 5.6: Values of $\tilde{\alpha}^{qm}$ in atomic units. The green circles are experimentally determined values results, and the purple squares are theoretical calculations. The three most recent experimental $\tilde{\alpha}^{qm}$ measurements [41, 70, 145] and two theory calculations [122, 154] converge around a narrow range of negative values.

have added confidence to a narrow range of values of negative $\tilde{\alpha}^{qm}$. As we were responding to referee comments on our light shift evaluation, new theory approaches considering the negative energy states revised the $M1$ contribution [122, 154]. Multipolar polarizability is calculated using a sum over states approach. Negative energy states, which arise from using Dirac theory to solve for Sr spectra and correspond to a positron state, have previously been disregarded in the M1 sum as it was believed that these had little effect on the calculation. Elsewhere, negative energy states have played an important role in accurate calculations of atomic g factors [80]. Righting this error, two theory teams now generally agree with these three experimental $\tilde{\alpha}^{qm}$ measurements. Experimental and theoretical values of $\tilde{\alpha}^{qm}$ are plotted in Fig. 5.6. Perhaps this should be regarded as a triumph of the optical lattice clock, leading theoretical calculations through precision spectroscopy!

5.3 Operational Conditions

To operate with the lowest possible light shift uncertainty, care must be taken for reliable operation. Fig. 5.7 demonstrates the effect of the lattice depth U and uncertainties in δ_L and n_Z on

the light shift uncertainty. Each plot shows the light shift uncertainty under our standard operation conditions, varying a single parameter. The gold stars indicate our standard operational conditions, $\delta_L = 7$ MHz with a lattice frequency uncertainty of 100 kHz, $n_Z = 0^{+0.01}_{-0}$, $U = 10 \pm 0.1\ E_r$, and $T_r = 100 \pm 10$ nK. By setting $\delta_L = 7$ MHz, we reduce the absolute light shift to $< 10^{-19}$ at the expense of slightly increasing the light shift uncertainty. Increase the magnitude of δ_L can significantly increase light shift uncertainty. In Sr1, the lattice frequency is locked to the Si stabilized comb, ensuring our lattice frequency is well known and drifts < 5 Hz/day, so the primary δ_L uncertainty arises from a loose frequency lock and the cavity linewidth.

Using a ground band sample is critical to reducing light shift uncertainty, as shown in the center panel. We reduce the lattice depth to the single band regime $U < 6\ E_r$ before readout, removing all atoms with $n_Z > 0$. This ensures that regardless of the relatively delicate sideband and Doppler cooling process, the light shift will not significantly change. We measure the attenuation of the blue sideband with this readout scheme, and typically observe > 40 times reduction in blue sideband amplitude with respect to our standard scheme, limited by readout noise. We quote a conservative uncertainty $\delta n_Z = 0.01$.

Lastly, operating at a shallow depth is typically the most convenient way to reduce light shift uncertainty. With our light shift evaluation, we can operate with a light shift uncertainty below 10^{-18} at depths below 50 E_r, plotted on the right of Fig. 5.7. Our standard operation is at the magic depth zero density shift point near 10 E_r. As the lattice depth calibration is common between the evaluation and standard operation, treating depth uncertainty in both the fit and the light shift calculation necessarily increases the shift uncertainty. The proper uncertainty to include is due to lattice depth repeatability between shift characterization and operation. While we have not extensively measured this, we believe it is considerably better than the absolute depth uncertainty.

Under standard operation, our light shift uncertainty is 3×10^{-19}, still limited by uncertainty in the atomic parameters, and not our understanding of the motional states or experimental conditions. Thus improvement must come from better parameter determination from longer measurement campaigns or clever measurement techniques. Running synchronously with another Sr clock would

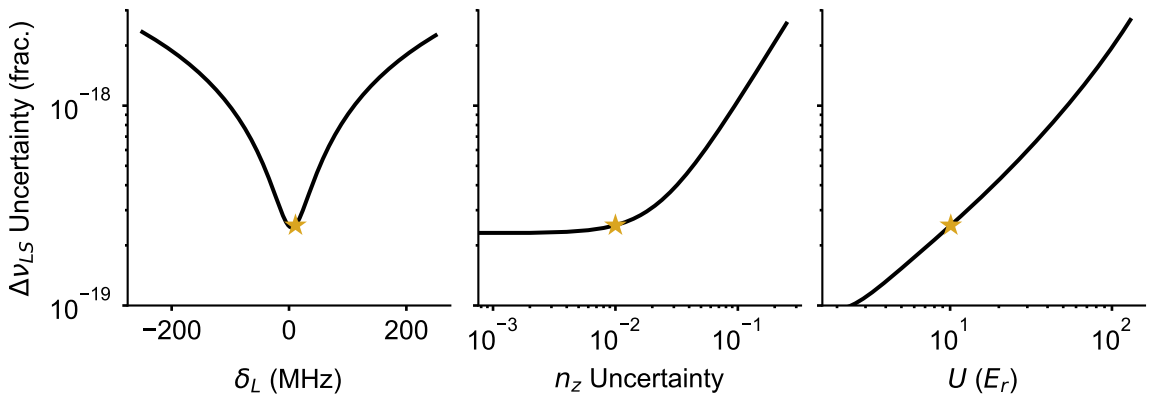

Figure 5.7: Light shift error from different parameters, with the gold stars indicating our typical operation. The light shift uncertainty is calculated for our standard operation, varying only one parameter for each plot. Left: the light shift uncertainty as a function of detuning from magic, δ_L. Uncertainty is minimized with $\delta_L = 0$. Center: the light shift uncertainty as a function of axial state n_Z uncertainty. Right: the light shift uncertainty as a function of lattice depth U.

allow us to measure with stabilities below the Dick effect limit of interleaved comparisons, a current evaluation speed limit. More inventive approaches have been tried elsewhere. Additional running waves have been used in both Sr [156] and Yb [20], leading to unique techniques for measuring the resultant light shift. In Yb, synchronous spectroscopy of an $n_Z = 0$ and $n_Z = 1$ sample allow for QPN limited $\Delta\nu_{n_Z}$ measurements [20]. With a blue detuned lattice, the atoms are trapped at light intensity minima, reducing the $E1$ effect and possibly leading to a reduction the overall light shift uncertainty [137, 153]. This is not the end of the lattice light shift story!

5.4 Vector Shift

We apply a static bias field $\vec{B}_s$ for clock spectroscopy, splitting the magnetic sublevels. As written in Eq. 5.1, the vector component of the lattice light creates a synthetic magnetic field that works much the same way. Thus the total splitting between magnetic sublevels is a vector sum of these two components. Following the convention in Ref. [134], we write the measured splitting between magnetic sublevels of state α:

$$\Delta^{\alpha}_{meas} = m^{\alpha}_F g^{\alpha} ||\vec{B}^{\alpha}_{eff}||, \tag{5.8}$$

where $\vec{B}^{\alpha}_{eff}$ is an effective magnetic field and g^{α} is the g-factor. Expanding this, the total splitting with a vector shift component becomes:

$$\Delta^{\alpha} = m^{\alpha}\sqrt{(g^{\alpha}B_s\cos\theta + \kappa_v^{\alpha}\xi U_0)^2 + (g^{\alpha}B_s\sin\theta)^2}, \tag{5.9}$$

where θ is the angle between the lattice wave vector and the bias field, κ_v^{α} is the vector strength, and ξ is the lattice ellipticity. In strontium, $\kappa_v^g = -6.5\times10^{-5}$ Hz/E_r, $\kappa_v^e = -2.55\times10^{-1}$ Hz/E_r, $g^g =$ 1.8438 MHz/T, and $g^e = 2.9828$ MHz/T [134]. This equation is often approximated in a quadratic form but there is no need. The experimentally relevant quantity is the difference in m_F splitting on the clock transition, $\Delta_{meas} = (\Delta^{e(m_F=-3/2)} - \Delta^{g(m_F=-5/2)}) - (\Delta^{e(m_F=+3/2)} - \Delta^{g(m_F=+5/2)})$.

This formula does not properly capture the motional state of the atom, and we observe vector shift dependence on n_Z. Using the harmonic model approach, we replace U_0 with the expectation value, $U_0 \to U_0(1-(n_Z+\frac{1}{2})U_0^{1/2})$, as in Eq. 5.4. This gives a harmonic approximation of the vector shift formula, which we will use in the following section.

To determine the lattice light vector shift on the clock transition, we need to measure how the splitting between different magnetic sublevel transitions varies as a function of lattice depth. Fortunately, our lattice light shift measurement data already contains all the needed information. Since the vector shift is dependent on the applied magnetic field, it is important that the magnetic field is kept constant for this measurement. We first determined the vector shift using the initial light shift evaluation. Since this data campaign took a few months and the bias field changed over time, this data set is over scattered. The much shorter light shift evaluation completed in July 2024 results in more reliable vector shift fits, although it is still over scattered.

The vector shift data and fitting results measured in July 2024 are shown in Fig. 5.8. During this lattice light shift campaign, we measured three different lattice detunings from magic, δ_L, and four lattice depths with respect to a reference depth $U = 12.2\ E_r$. The results are shown on the left, with fits plotted as solid lines and the fit residuals in the lower panel. The cavity ellipticity ξ, angle between the magnetic field and lattice $\hat{k}$-vector θ, and the magnetic field B are used as fitting

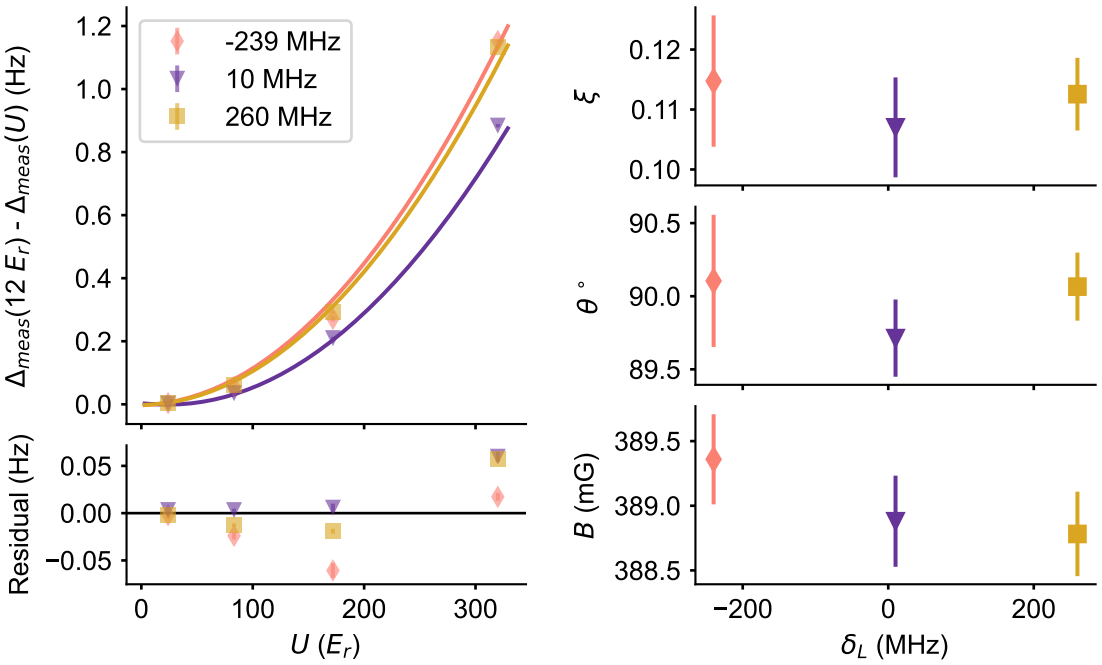

Figure 5.8: Vector shift data and fit from the July 2024 light shift evaluation. Left: The difference between spin state transition frequencies, Δ_{meas}, at depth U and the reference depth 12.2 E_r. Three different lattice frequencies, reported as detuning from magic in the key are separately fit with the vector shift formula, Eq. 5.9, plotted as solid lines. The fit residuals are plotted in the bottom panel. Right: The results from the vector shift fits shown for each lattice detuning from magic, δ_L, with error bars arising from the fit. The cavity ellipticity, ξ, angle between magnetic field and lattice k vector, θ, and magnetic field B agree for the three fits.

parameters for the vector shift data. The fitted values are plotted on the right and indicate no dependence on δ_L, as expected. Using ξ and θ, we calculate Δ_{vec} over different B and U to correct for the second order Zeeman shift, described in Ch. 7.3.

The ellipticity $\xi = 0.11$ is relatively large for a 1D Sr OLC, where standard single retro reflected lattices can have exceedingly pure polarization. This highlights one of the greatest downsides of using an in-vacuum cavity: the inability to directly control the polarization. Upon each reflection, the light experiences a small twisting of the polarization axis, creating a large average ξ after many round trips. Without modifying the cavity, this effect is unavoidable. However, the cavity provides a well defined optical axis and fixed birefringence, making this a generally static effect.

Due to the cavity ellipticity, the vector component of the light shift slightly rotates the effective

bias field. This in turn modifies the tensor component of the light shift and appears as a shift that goes as U^2. This is dangerous, as it appears as a hyperpolarizability-like magentic field dependent shift on ν_{Sr}. Again, following the convention in Ref. [134], we write this shift:

$$\Delta\nu_{vt} = -\gamma_{vt}|\vec{\epsilon}\cdot\vec{e}_B|^2\xi\cos\theta U_0^2, \tag{5.10}$$

with

$$\gamma_{vt} = [3m_F^e - F(F+1)]\frac{6\kappa_t^e\kappa_v^e}{g^e B_s}, \tag{5.11}$$

where $\kappa_t^e = -60.9\times10^{-6}$ Hz$/E_r$ is the excited state tensor strength. We neglect the ground state shift as it is significantly smaller than in the excited state. In Fig. 5.9, we plot the associated shift of this term as a function of lattice depth for three different bias fields. Increasing the bias field reduces this effect, and for our system it remains over an order lower than the hyperpolarizability ($\tilde{\beta}$) shift. Under standard operational conditions, shown as a gold star, this is a 5×10^{-22} effect. We do not incorporate this systematic in the lattice light shift evaluations: it should reduce $\tilde{\beta}$ by roughly 1%, well below the uncertainty.

We were initially surprised to observe different vector shifts in the (n_Z) data sets, as motional dependence has not been reported elsewhere. Due to a larger ξ in our system, n_Z dependence in the vector shift is finally visible. In Fig. 5.10, we plot the difference of Δ_{meas} between $n_Z = 0, 1$ over four different lattice depths and three frequency detunings from magic, listed in the key. At deeper lattice depths, Δ_{meas} is reduced for $n_Z = 1$ states as the atoms sample a lower effective intensity lattice. Since the (n_Z) data was measured during the 2024 light shift reevaluation, the parameters ξ, θ, B should be very similar to those reported in Fig. 5.8. Using the harmonic modification to Eq. 5.9, we calculate the n_Z dependence as a function of U, plotted as the gray line. The agreement is not perfect, perhaps due to a changing bias field, but it suggests the validity of this first order harmonic motional correction.

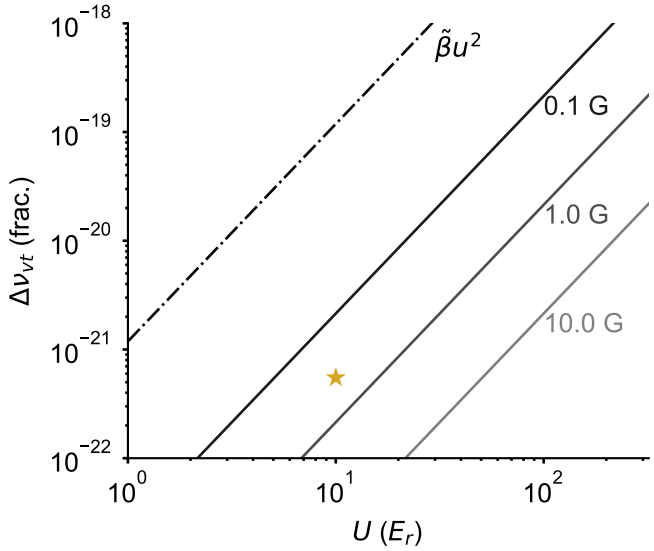

Figure 5.9: The vector shift rotates the effective bias field, leading to a tensor shift $\Delta\nu_{vt}$ that scales as U^2, as in Eq. 5.10. We plot this effect for three different bias fields as well as the hyperpolarizability contribution, β. The star indicates the shift at our normal operational bias field and lattice depth.

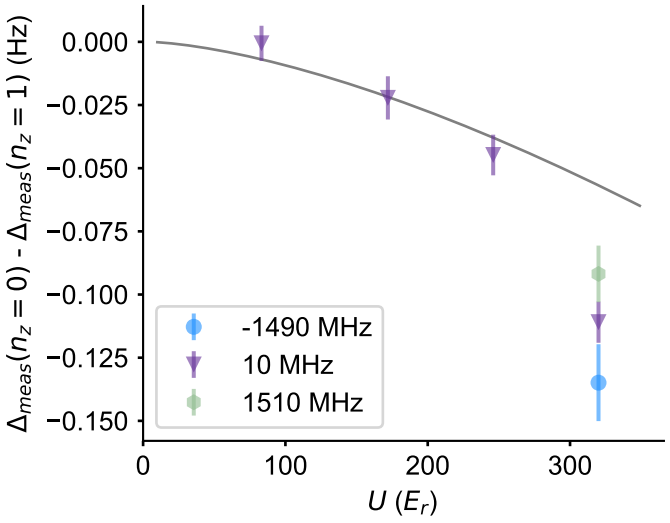

Figure 5.10: The difference between spin state transition frequencies Δ_{meas} in the ground state $n_Z = 0$ and the first excited axial motional state $n_Z = 1$ over a range of lattice depths U. The lattice frequency detuning from magic is shown in the key and plotted with different colors. The gray line is the calculated vector shift difference between $n_Z = 0, 1$ using Eq. 5.9 and the parameters reported in Fig. 5.8.

5.5 Other Magnetic Sublevel Transitions

Our light shift results disagree significantly with other precise strontium light shift measurements. Both $\partial_\nu \tilde{\alpha}^{E1}$ and $\tilde{\alpha}^{qm}$ are inconsistent with the measurements made in RIKEN, the most precise measurements of these quantities to date. One possible explanation is different lattice depth calibration, with a $\sim 7\%$ lattice depth error on either measurement bringing $\partial_\nu \tilde{\alpha}^{E1}$ into agreement. Another possible explanation is our use of different magnetic sublevels. While the light shift dependence on m_F states should be highly suppressed, our curiosity was nevertheless piqued, and we decided to measure this effect.

In addition to our standard $|^1S_0, m_F = \pm 5/2\rangle \rightarrow |^3P_0, m_F = \pm 3/2\rangle$ transition, we also measured the light shift on the $|^1S_0, m_F = \pm 5/2\rangle \rightarrow |^3P_0, m_F = \pm 7/2\rangle$ and $|^1S_0, m_F = \pm 9/2\rangle \rightarrow |^3P_0, m_F = \pm 9/2\rangle$ transitions. To measure $\partial_\nu \tilde{\alpha}^{E1}$ on other transitions, we modulate lattice depth and detuning, keeping $n_Z = 0$. We fit $\partial_\nu \tilde{\alpha}^{E1}$ and an operational magic wavelength detuning δ_L. The results of these measurements are shown in Fig. 5.11. The top panel shows the magic frequency detuning from our standard $|^1S_0, m_F = \pm 5/2\rangle \rightarrow |^3P_0, m_F = \pm 3/2\rangle$ transition. The extracted $\partial_\nu \tilde{\alpha}^{E1}$, shown in the bottom panel, has no dependence on the magnetic sublevel within our statistical uncertainty and continue to disagree with the RIKEN measurement [145]. Thus, the results are as expected—no scalar light shift dependence on the magnetic sublevels and strong disagreement with other $\partial_\nu \tilde{\alpha}^{E1}$ remains. Perhaps lattice depth calibration is indeed the primary culprit. Fortunately, this disagreement does not directly affect our operational accuracy as the light shift depth calibration and our operational depth calibration are identical. More measurements using the harmonic model are need to settle this, as well as the $\tilde{\alpha}^{qm}$ disagreement.

5.6 Light Shift Reevaluation

In preparation for the clock comparison with NIST starting in 2024, we decided to reevaluate the lattice light shift in our system, which was initially performed in 2022. The polarization of the lattice is set by a polarizing beam splitter mounted atop the chamber. If this cube changes

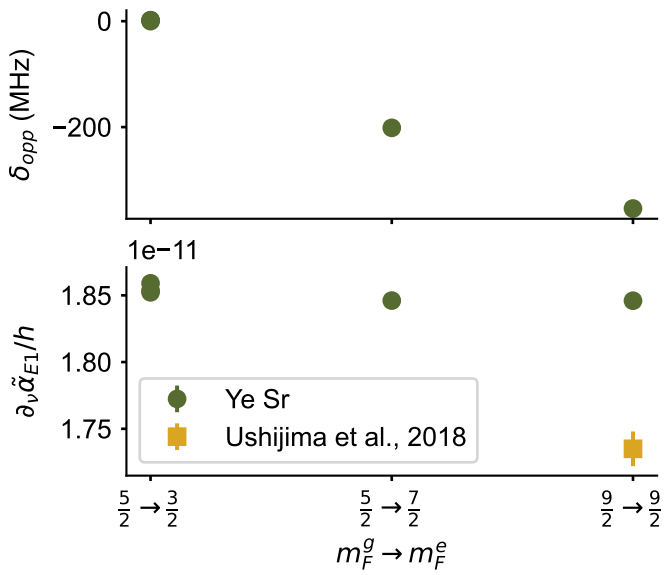

Figure 5.11: We measure the light shift for three different magnetic sublevel transitions. Top: the difference in magic wavelength from our standard $|^1S_0, m_F = \pm 5/2\rangle \to |^3P_0, m_F = \pm 3/2\rangle$ transition, δ_{opp}. Bottom: the differential E1 polarizability slope $\partial_\nu \tilde{\alpha}^{E1}$ for different magnetic sublevels. Our results, in green, disagree significantly with measurements made in RIKEN [145] measured for the $|^1S_0, m_F = \pm 9/2\rangle \to |^3P_0, m_F = \pm 9/2\rangle$ transition.

orientation, or the magnetic field rotates, the tensor shift will change and the overall light shift must be remeasured. With this concern, we remeasured the light shift in much the same way, varying the lattice depth U, the detuning from magic δ_L, and the axial state n_Z. Learning from our previous evaluation, we decided to measure with larger δ_L and U, generating a much stronger light shift. We also change δ_L with n_Z modulation measurements, further testing the robustness of the light shift model. We opted not to modulate the lattice frequency within a single lock to simplify this measurement.

The data and fits are shown in Fig. 5.12. On the top left is the (U, δ_L), with solid lines fits of Eq. 5.5 to the data. Each color represents a different detuning from magic, as indicated by the key. The bottom panel shows the fit residuals. On the top right is the n_Z modulation data, with solid lines indicating the fit. The bottom panel shows fit residuals.

In Fig. 5.13 we plot the light shift parameters determined during the 2024 reevaluation along with the results measured two years prior, Ref. [70], and in RIKEN, Ref. [145]. All JILA

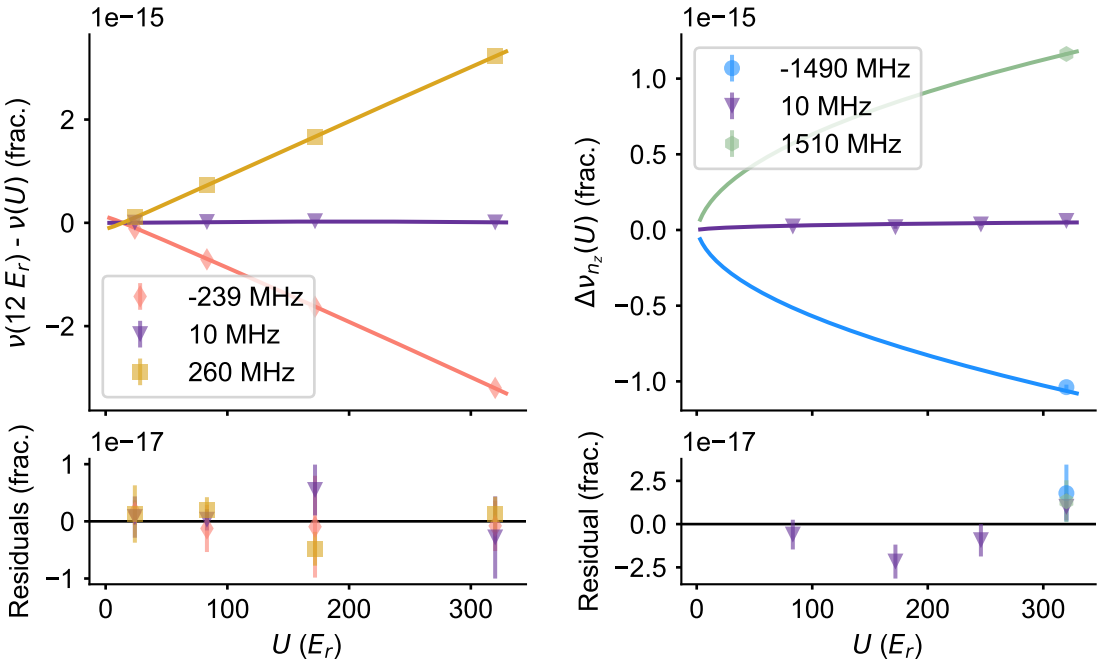

Figure 5.12: Lattice light shift reevaluation in July 2024. Left: light shift results for the (δ_L, U) modulation data set. The points are data with error bars showing the statistical uncertainty and color indicating the detuning from magic determined by the fit and shown in the key. The solid lines are fits to Eq. 5.5 with fit residuals shown on the bottom panel. Right: n_Z modulation data set with three different lattice detunings from magic, shown in the key. The solid lines are fits, with fit residuals plotted in the bottom panel.

measured parameters agree within their uncertainty. The operational magic wavelength difference $\nu^{2023}_{magic} - \nu^{2024}_{magic} = -0.5 \pm 1.5$ MHz is also consistent with zero. This adds confidence to the robustness of our experimental apparatus, specifically the tensor shift, remained constant despite the gap of two years between evaluations. The disagreement with the RIKEN measured $\partial_\nu \tilde{\alpha}^{E1}$ and $\tilde{\alpha}^{qm}$ measurements persists. The lattice light shift was remeasured after the comparison in May of 2025, and the results remain consistent with the 2024 evaluation.

5.7 Thermal Model Comparison

One of the first widely used light shift models to capture the effect of hyperpolarizability originated from the NIST ytterbium group [28]. Since deprecated by the more robust harmonic model discussed earlier in this chapter, the thermal model is still widely used due to its simplicity.

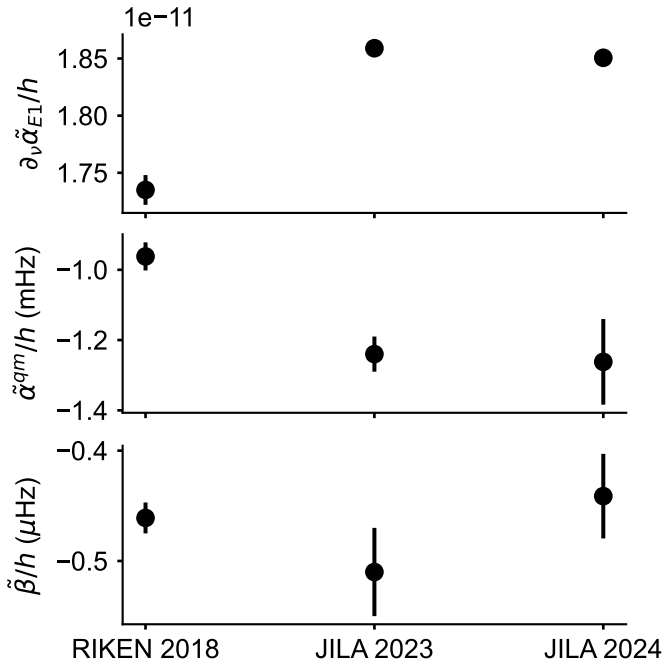

Figure 5.13: A comparison of light shift evaluation results. The JILA 2023 [70] and JILA 2024 measurements agree within uncertainty. The RIKEN 2018 measurement [145] $\tilde{\alpha}^{qm}$ and $\partial_\nu \tilde{\alpha}^{E1}$ terms disagree significantly with our measurements.

Much like the RIKEN light shift model, the thermal model writes the light shift as an expansion in lattice depth U to powers of 1/2, 1, 3/2, and 2, with additional dependence on transverse and axial motional states. In the thermal model, a key simplification is that the axial and radial states also scale with U and powers of U. This allows rewriting the light shift $\Delta\nu_{LS}^{therm}$ as:

$$\Delta\nu_{LS}^{therm} \approx -\frac{\partial\alpha^*}{\partial\nu}\delta_L U - \beta^* U^2, \tag{5.12}$$

where α^* and β^* are experimentally determined parameters that incorporate the motional state of the atoms. These coefficients are akin to the $\partial\tilde{\alpha}^{E1}/\partial\nu$ and $\tilde{\beta}$ coefficients in Eq. 5.5, but incorporate implicit motional state dependence. Thus the fit requires no knowledge of the atomic motion, making it far simpler to use in practice. Unfortunately, this means that evaluations using this method are not broadly comparable as cooling and trapping geometries vary between systems.

Our system is no longer thermal, as we perform resolved sideband cooling along the tightly

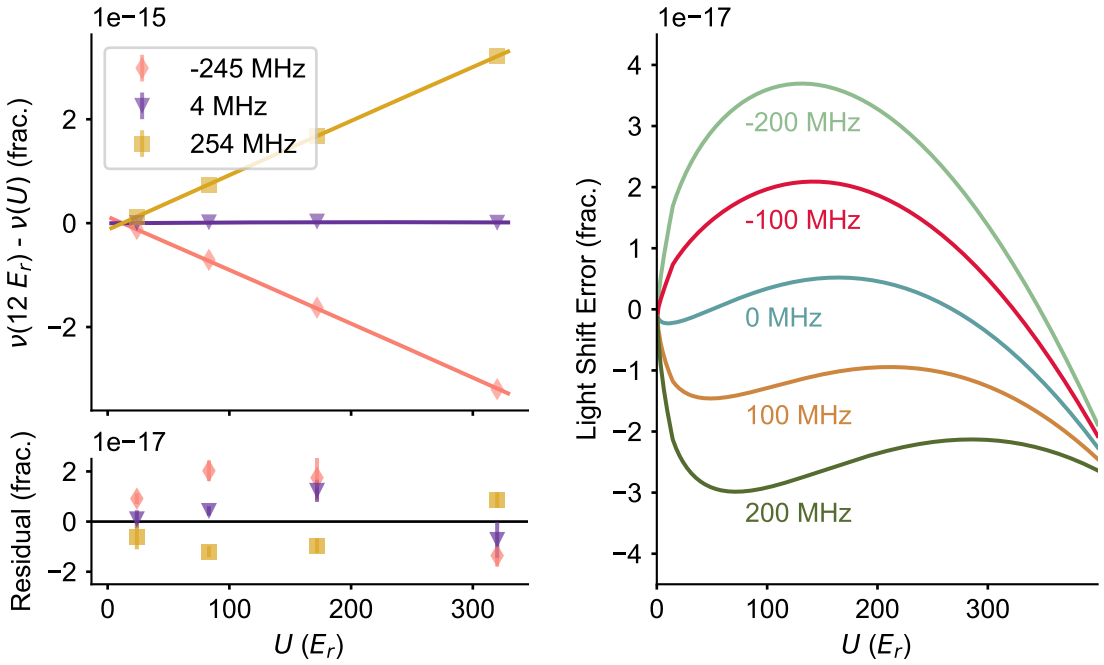

Figure 5.14: Using the thermal light shift model. Left: fit of the thermal model to the light shift data measured in July 2024. Points are data with error bars reporting 1σ data. Solid lines are fits using Eq. 5.12, with fit residuals reported in the lower left panel. Right: The difference in calculated light shift between the thermal model and the harmonic model for a number of different lattice detunings from magic.

confined direction. Nevertheless, it is interesting to see the effect of this commonly used model on explaining our light shift results. Fig. 5.14 shows the results of fitting Eq. 5.12 to the light shift data collected in July 2024. The fit immediately seems to not fully capture the behavior of the light shift in our system, with residuals a few parts in 10^{-17} and structured as a function of lattice depth. As expected, we need the $U^{1/2}$ and $U^{3/2}$ terms to properly capture the light shift behavior in our system. Using the fitted parameters, we calculate the light shift error using the thermal model with respect to the harmonic model, plotted on the right of Fig. 5.14 for different δ_L. Near magic, the resultant error is $< 5 \times 10^{-18}$ for $U < 200\ E_r$, with the error growing at larger detuning. Thus the thermal model is adequate for low 10^{-18} light shift evaluations, but should not be used for more stringent accuracy goals.

Chapter 6

Black-body Radiation

The largest source of uncancelled shift in room temperature Sr optical lattice clocks is due to black-body radiation (BBR) from the surrounding environment. Unlike systematic shifts that can be measured by modulating the shift source, such as the lattice light shift we previously discussed, varying the BBR environment enough to precisely measure the atomic response is prohibitively challenging without a cryogenic system [11, 144]. Instead, we determine the BBR shift by understanding the atomic response and the spectrum of light that the atoms sample. At room temperature, the BBR spectrum is centered around 10 μm. Over the BBR wavelength range, most components in our system are good BBR emitters, so the atoms experience an ideal BBR environment at room temperature T described by Planck's law. The atomic response is given by the differential polarizability between the $^1S_0$ and $^3P_0$ states over this spectrum. The total BBR shift has been historically written as a sum of a static component that scales as T^4 and a higher order dynamic component that scales as T^6:

$$\Delta\nu_{BBR} = \nu_{\text{stat}} \left(\frac{T}{T_0}\right)^4 + \nu_{\text{dyn}} \left(\frac{T}{T_0}\right)^6 + \mathcal{O}(T^8), \tag{6.1}$$

where T_0 is a reference temperature that scales the coefficients, ν_{stat}, ν_{dyn}, typically 300 K [131]. Recent work has shown that higher order powers of T or the true integral form of the shift must be included for accurate $\Delta\nu_{BBR}$ determination, with only a T^6 term leading to a correction error at 10^{-18} [81].

Accuracy in previous generations of room temperature Sr OLCs has been limited by the

uncertainty in ν_{dyn}, which is directly tied to the $5s4d\ ^3D_1$ oscillator strength [131]. We set out to remeasure the $5s4d\ ^3D_1$ lifetime, reducing its uncertainty by a factor of two for operation with a BBR shift uncertainty $< 10^{-18}$. This work is described in the first half of this chapter, as well as interesting observations of Zeeman beats and density related interactions. We also make accurate measurements of the radiative temperature using an in-vacuum temperature probe. Combined, we reduce our uncertainty in $\Delta\nu_{BBR}$ to 7.3×10^{-19}.

6.1 $^3D_1$ Lifetime

A direct measurement of the $5s4d\ ^3D_1$ lifetime is rather challenging, as this is a 2.6 μm wavelength transition out of $^3P_0$. This state decays to all states in the ^3P_J manifold, two of which are metastable. So to resolve the lifetime of the $^3D_1$ state, we collect 689 nm photons from the $^3P_1$ decay. As in Refs. [13, 109], we prepare a sample of Sr atoms in $^3P_0$ within a shallow lattice along $\hat{Z}$. A 2.6 μm laser pulse perpendicular to the lattice along $\hat{X}$ excites a portion of the sample to the $^3D_1$ state. Some excited atoms decay to $^3P_1$ and then to the $^1S_0$ ground state, releasing a 689 nm photon in the process. We collect this fluorescence with a cooled hybrid photomultiplier assembly (PMA) nearly coaxial with the 2.6 μm laser and time tag the incident photons with 5 ns resolution.[1] This process is shown on the left of Fig. 6.1. In the single particle regime, the photon rate y at time t is well characterized by a cascaded double exponential process,

$$y(t) = A \times \Theta(t - t_0) \left(e^{-(t-t_0)/\tau_{^3D_1}} - e^{-(t-t_0)/\tau_{^3P_1}} \right) + y_0, \tag{6.2}$$

where A is the flux amplitude, Θ is a Heaviside function for instantaneous excitation at time t_0, $\tau_{^3D_1}$ and $\tau_{^3P_1}$ are the $^3D_1$ and $^3P_1$ lifetimes respectively, and y_0 is an offset due to background counts. In Fig. 6.1 we plot all collected photon counts and fit with Eq. (6.2). Since Eq. (6.2) assumes instantaneous excitation of atoms to $^3D_1$, we do not fit data within a 500 ns window about the excitation pulse, indicated by the red exclusion area [109, 110]. The characteristic signal from this

[1] The detector is a Picoquant PMA Hybrid 40 cooled hybrid photomultiplier detector assembly. The counter is a Picoquant TimeHarp 260 PCIe board in the "NANO" configuration run with "long range mode."

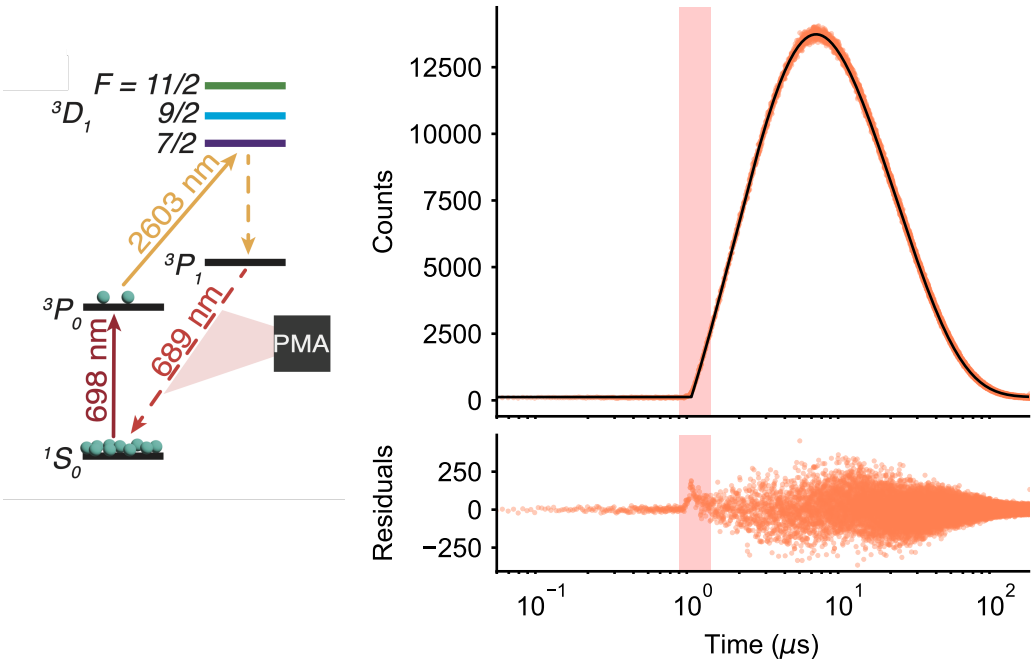

Figure 6.1: To measure the $^3D_1$ lifetime, we prepare sample in $^3P_0$ before a brief 2.6 μm pulse excites atoms to one of the $^3D_1$ hyperfine states, $F = 7/2, 9/2, 11/2$. Atoms decay from $^3D_1$ to the ground state via $^3P_1$. We collect photons on this decay using a photomultiplier assembly (PMA), and time tag their arrival with 5 ns resolution using a multichannel scalar. On the right we plot all the experimental data used for lifetime determination with the double exponential model. The black line is a fit to the data using Eq. (6.2) with the red area indicating exclusion around the excitation pulse. The bottom panel shows the fit residuals.

double exponential decay is shown in Fig. 6.1. The photon flux initially rises as population decays into $^3P_1$ before falling with a long exponential tail governed by $\tau_{^3P_1}$. The black line is a fit to the data using Eq. (6.2), with fit residuals plotted in the lower panel. While all the data we used to extract the $^3D_1$ lifetime is contained within Fig. 6.1, the fit does not represent the true atomic state lifetimes.

6.1.1 Quantum Beats

Since previous research measuring the $^3D_1$ lifetime in Sr and Yb made no observation of Quantum or Zeeman beats [13, 109], it came as a bit of a surprise when we first observed an oscillating fluorescence signal. By applying a magnetic field, the magnetic sublevels in each hyperfine

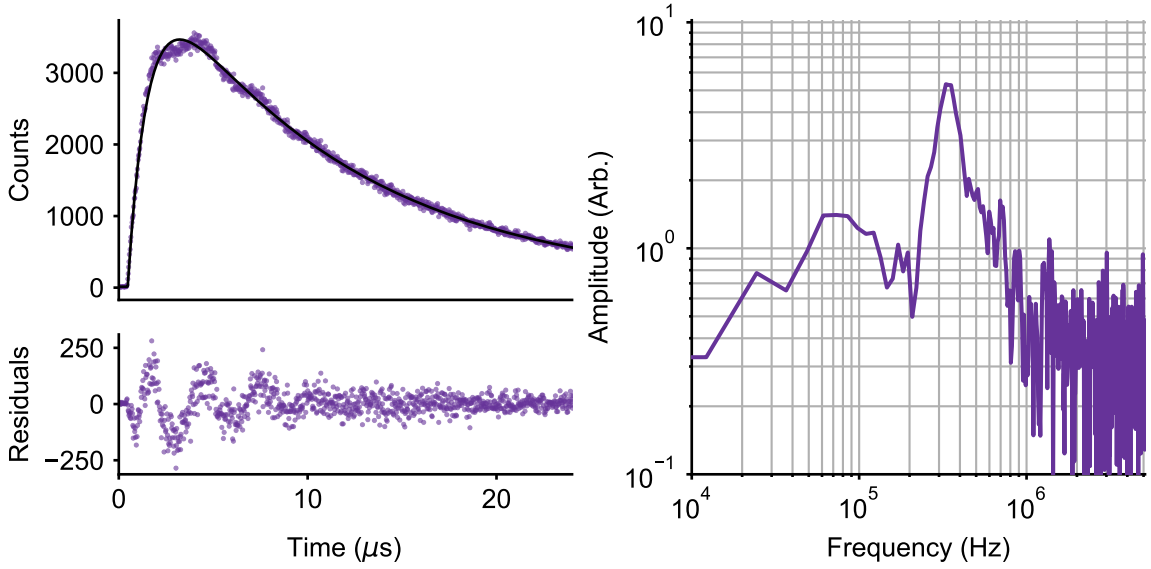

Figure 6.2: Observation of the Zeeman beats. A 2.5 G magnetic field is applied using the MOT coils, leading to an oscillation in the exponential decay signal, shown on the top left. The black line is a fit to Eq. 6.2 assuming no Zeeman beating, with the fit residuals on the lower panel indicating this periodic signal. An Fourier transform of the residuals is shown on the right, indicating a strong tone around 350 kHz.

state of $^3P_1$ manifold split. The excited atom decays quickly from the $^3D_1$ state into a superposition of magnetic sublevels in $^3P_1$ before decaying down to $^1S_0$ and emitting a 698 nm photon. The different decay pathways interfere, leading to a oscillating signal at the energy spacing of magnetic sublevels [34]. In Fig. 6.2, we plot the observed decay under a 2.5 G magnetic field applied using our MOT coils. We are unsure of the exact direction of this applied bias field and there is a 700 mG/mm gradient across the 250 μm sample, so this is a rather uncontrolled experiment. The solid line is a fit to Eq. 6.2 assuming no Zeeman beats. The oscillating signal is visible in the fit residuals, shown on the bottom panel. Taking a Fourier transform of the residuals, we observe a strong tone at the oscillating frequency near 350 kHz. As expected, this oscillation frequency reduces with a smaller MOT field. The observed frequency is twice the Larmor precession frequency of $^3P_1$ $F = 9/2$, 85 kHz/G.

The Zeeman beat structure in this double exponential decay is rather fragile. Atoms must decay to a superposition of $^3P_1$ magnetic sublevels that are split at the right energy scale and

uniformly across the system such that beating can be observed [34]. If the splitting is too large, the atom will decay into only one magnetic sublevel, while if it is too small, the effect will not be visible. All three hyperfine levels within $^3D_1$ are resolvable, and each has different magnetic sensitivity. Individual magnetic sublevels within each hyperfine manifold are unresolvable in our system, so we populate a spin mixture. We begin by preparing a $|^3P_0,\ F = 9/2,\ m_F = -7/2\rangle$ state before driving to $^3D_1$ with a laser along $\hat{X}$, linearly polarized along $\hat{Z}$. Depending on the hyperfine state in $^3D_1$ and the applied bias field, we populate some superposition of $m_F = -9/2, -7/2, -5/2$ in one of $F = 11/2, 9/2, 7/2$.

With the goal of controlling this effect, we observe how this precession frequency changes as a function of field direction. Classically, this Zeeman beat phenomenon can be described as a rotating dipole radiation pattern. The atom will preferentially emit along the two dipole lobes, with the dipole pattern rotating under Larmor precession. If this rotation axis is perpendicular to the collection axis, the detector will see a periodic increase in flux consistent with twice the precession frequency. If the applied field is along the photon collection axis, the rotating radiation pattern is perpendicular to the collection axis and there should be no observed time dynamics outside of the standard decay process. We use our bias coils to apply a more uniform magnetic field than our MOT coils along one of three axis, and use the clock transition frequency to measure the strength of the field. On the left of Fig. 6.3, we plot the FFTs of the double exponential fit with ~ 1.1 G bias fields applied along all three axis. The $\hat{Y}$ and $\hat{Z}$ bias fields, nearly perpendicular with our collection axis, have strong tones in the residuals around 150 kHz. With a 1 G field, the Larmor frequency of the $^3P_1$ $F = 9/2$ state is 85 kHz, so this beating is consistent with twice this precession rate. The $\hat{Y}$ direction has an additional tone around 400 kHz, which is the Larmor frequency of the $^3P_1$ $F = 11/2$ state, 385 kHz/G. Perhaps a wobbling precession pattern could cause emission at this frequency. With an applied field along $\hat{X}$, the collection axis, the Zeeman beats are suppressed as the dipole emission pattern rotates along the same axis.

We further control the quantum beat signal by modifying decay channels or the light shift environment. The decay from $^3D_1$ into $^3P_1$ hyperfine levels has different branching ratios depending

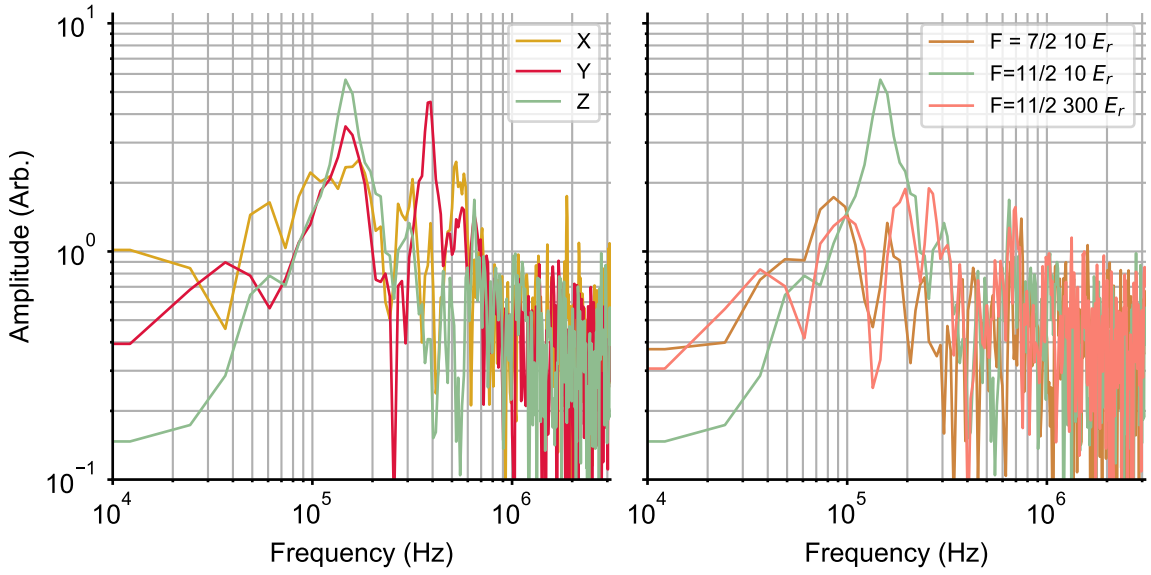

Figure 6.3: Zeeman beats occur when the radiation pattern rotates during decay. Right: FFT of the residuals in the double exponential decay for three different magnetic field axes, listed in the caption. The photon collection axis is along $\hat{X}$, so the Zeeman beat amplitude is attenuated with a $\hat{X}$ bias field. Left: FFT of the residuals in the double exponential decay for three different configurations. A 1 G bias field along $\hat{Z}$ is applied, and the double exponential decay is observed for initially populating $^3D_1$ $F = 7/2$ and $F = 11/2$, as well as for a high lattice depth of 300 E_r.

on the initial state. If we select the $^3D_1$ $F = 7/2$ state, decay to the $^3P_1$ $F = 9/2$ and $F = 7/2$ is allowable. On the right of Fig. 6.3 we plot the FFTs of the residuals under different experimental conditions. This data is collected with a 1 G bias field applied along $\hat{Z}$. Using the $^3D_1$ $F = 7/2$ state seems to remove the Zeeman beating present in the $^3D_1$ $F = 11/2$ initial state data.

All the data presented so far has used a shallow lattice depth of 10 E_r near the standard clock magic wavelength. However this frequency is not magic for $^3P_1$, and strong vector and tensor shifts can modify the magnetic sublevel energies. To test this effect on the Zeeman beating, we repeat the experiment using a high lattice depth of 300 E_r, shown in salmon on the right of Fig. 6.3. We expect the tensor light shift on $^3P_1$ to be of order 10-200 kHz for the different spin states [134]. This causes a spread of frequencies across the trap on the same order as the Larmor frequency, so no collective Zeeman beat signal is observable.

While observation of the Zeeman beat signal was certainly exciting, it introduces another

systematic we must bound for the ultimate $^3D_1$ lifetime determination. To reduce this effect, we periodically check that the field is near 0 and use a shallow lattice depth of 10 E_r. We model the effect of residual magnetic fields causing low frequency Zeeman beats that pull the lifetime by numerically simulating the double exponential decay. This process is discussed in the supplement of our accuracy paper, Ref. [2]. With a 10 E_r lattice and a magnetic field < 2 mG, Monte Carlo simulations estimate a $^3D_1$ lifetime error of 3.2 ns, and a 11 ns $^3P_1$ lifetime error.

6.1.2 High Density Interactions

Our initial goal in revisiting the lifetime measurement performed in Ref. [109] was to reduce the limiting statistical uncertainty by measuring a larger sample. This quickly proved challenging, as at high densities the decay profile departs significantly from the double exponential decay, Eq. 6.2. The NIST Yb measurement reported density dependent lifetimes, however still used the same fitting procedure and simply measured the lifetime using different sample sizes [13]. In Ref. [109], no density related effects were observed. Collective effects typically scale as the wavelength volume, λ^3, so perhaps it is unsurprising that the long 2.6 μm radiation can generate all sorts of collective systematics. In Fig. 6.4 we plot data collected using about 10^5 atoms in a 1 mm sample length. The black line is a fit to the data using Eq. 6.2, with the fit residuals plotted in the lower panel. At times less than 10 μs, the fit clearly does not capture the decay effects, with photon counts about 2% higher or lower than the fitted value, depending on the time.

While we attempted to understand the dynamics in this decay process fully,[2] it became apparent that the system was too complicated. The initial pulse was uncontrolled, the magnetic sublevels were not resolved, the decay channels were too numerous, and the populations and densities were changing during the course of the experiment. Eq. 6.2 cannot be simply modified by one or two parameters to properly capture the high density decay signal. Some combination of superradiance, subradiance, and radiation trapping along many different transitions is likely responsible for this observed photon flux. The only way around this was to reduce the atomic density.

[2]Thank you, David Wellnitz, for your hard work attempting to understand this system!

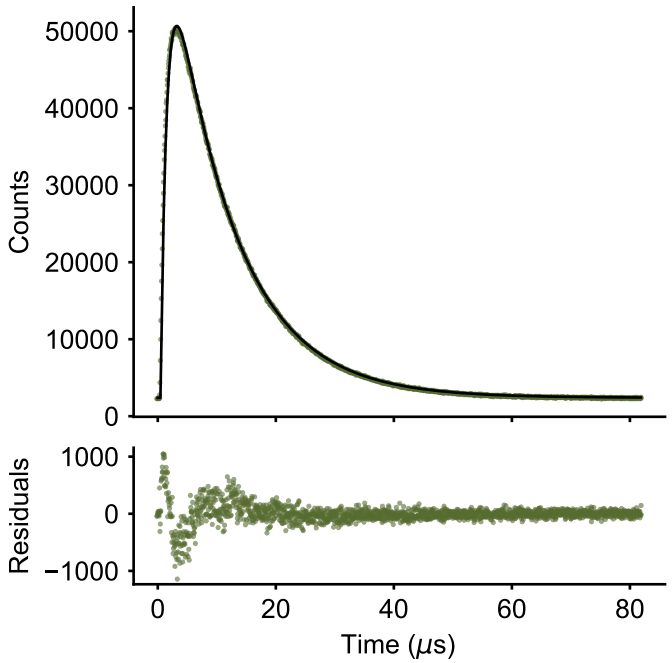

Figure 6.4: At high densities, the decay profile is modified. The green data are points collected with a 1 mm long sample of 10^5 atoms. The black line is an ideal double exponential fit to the data, Eq. 6.2. The residuals, plotted on the lower panel, indicate departure from this model.

6.1.3 Experimental Approach

How were we to reduce the lifetime uncertainty if we cannot operate with many atoms? The task seemed daunting as I contemplated how many years I would have to extend my PhD just to reach the accuracy goals we desired. The $^3D_1$ lifetime directly impacted my own! And even if we were to reduce the density systematic by operating with far fewer atoms, how do we account for the modified lifetime due to residual interactions between atoms?

An important understanding of this collective decay process is that the modification to the decay primarily came from population in the $^3P_0$ state, the strongest decay channel for $^3D_1$. The model in Eq. (6.2) fits properly if the population in $^3P_0$ is low, as it is the primary state that contributes to collective effects in the $^3D_1$ decay. Reducing the population in $^3P_0$ and holding a larger sample in $^1S_0$, we reduce the complicated collective effects on the decay we cared about. The large reservoir of atoms in $^1S_0$ would allow us to repeatedly populate $^3P_0$ and excite to $^3D_1$,

periodically refilling the lattice with a new MOT. The MOT and lattice loading contribute most to the dead time, so increasing the number of decays we measure between MOTs reduces the total averaging time. By creating a large reservoir of atoms in $^1S_0$, this introduces significant radiation trapping on the $^3P_1$ decay. In a sense, we trade increased uncertainty on the $^3P_1$ decay for reduced uncertainty on $^3D_1$ decay.

Our final data was taken with this revised experimental procedure. We begin by loading a large number of atoms in $^1S_0$ and promote a small portion of the atoms to $^3P_0$. This is done with a spin mixture and near zero bias field, meaning the maximum population we can load into $^3P_0$ is about 40% of the total population. We then excite these atoms to $^3D_1$ with a 100 ns laser pulse. Since most of the atoms decay back to $^3P_0$, we repeat this process 15 times before again exciting a portion of the $^1S_0$ atoms to $^3P_0$. After 10 clock pulses and a total of 150 $^3D_1$ decay cycles, we Doppler cool the remaining sample. We repeat this excitation and cooling sequence 5 times before loading a new sample into the lattice. In sum, for each MOT sequence we collect photons from 750 decay cycles. On average we capture less than one photon from the sample per decay cycle, so pile-up effects, where multiple photons strike the detector within one time bin, are effectively eliminated.

On the left of Fig. 6.5 we plot the collected photons for each intrashot index, that is the number of 2.6 μm pulses after a MOT. There are five clear sections of this plot, each corresponding to 150 $^3D_1$ excitations. The drop in number of photons occurs due to some atom loss from Doppler recooling. Within each of these regions are 10 spikes that correspond to repopulation of the $^3P_0$ state. Over the subsequent 15 $^3D_1$ excitations, this population is depleted and the photon rate is reduced. We use this characteristic photon count rate to align the data. Each photon we collect is assigned a trigger number that can be tied to an intrashot index after the MOT. We noticed the counting board would occasionally skip a trigger. Through a pattern matching algorithm, we were able to ensure that we accounted for these slipped shots and could properly attribute each photon to an intrashot index.

Although the population that contributes to non-linear collective effects is significantly reduced,

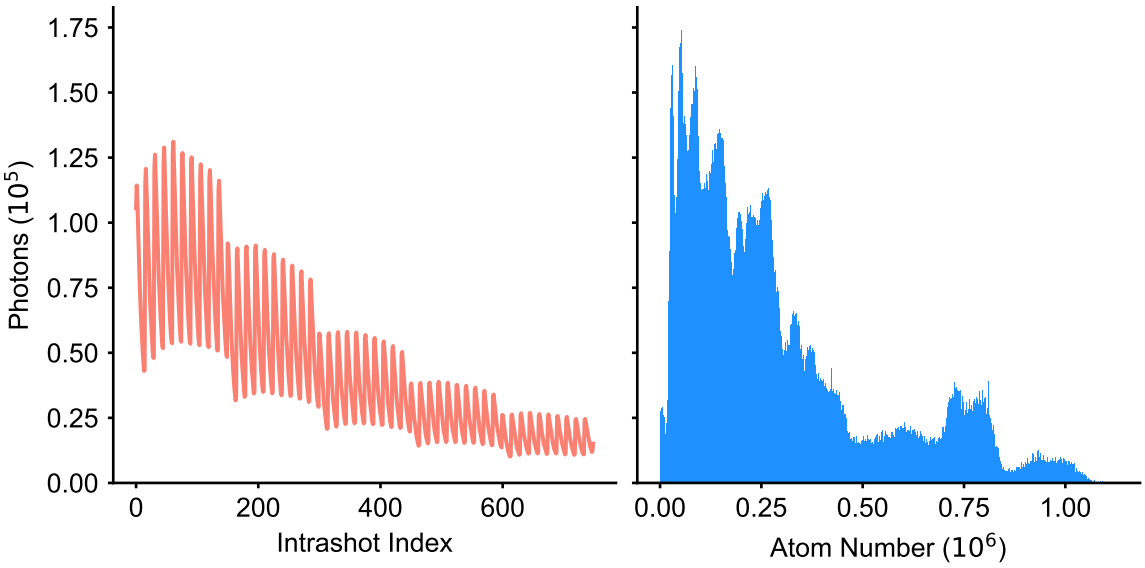

Figure 6.5: Implementing the new approach to reduce density effects on the $^3D_1$ decay. Left: the number of photon collected at each point after the MOT, the intrashot index. Five regions of 150 indices correspond to recooling the sample. Each of the ten spikes in each region corresponds to repopulation of the $^3P_0$ state, which is depleted after 15 pulses of 2.6 μm light. Right: a histogram of all the collected photons at each atom number. We use the intrashot index as well as images of the sample to assign an effective atom numbers to each photon.

weaker collective effects are still present. To understand how density affects the measured lifetime, we measure the total atom number at the beginning and end of the sequence and assign an atom number to each decay event using the intrashot index. Over the course of the measurement campaign, we collect 8×10^7 photons with a total atom number ranging from 10^3 to 10^6. We collect data with different proportions of atoms in $^3P_0$ and iterate over all three hyperfine levels in $^3D_1$, for a total of six separate data sets, observing if there are any effects that skew the lifetime. A histogram of all photons at each atom number is plotted on the right of Fig. 6.5.

6.1.4 Results

With this large set of time and density tagged photon counts, there are numerous techniques for processing to determine the true lifetime. After evaluating different approaches, we settled on the analysis framework presented here. Photon counts are sorted into bins by atom number with

widths of 50 thousand atoms, such that there is one bin for atom numbers from $0 - 50,000$, one for $50,000 - 100,000$, and so on. To each bin, we fit the ideal double exponential decay model, Eq. 6.2, excluding 500 ns around the excitation pulse. We found it critical to use a maximum likelihood approach to fitting, as it properly accounts for the Poisson statistics governing time steps with low or no counts. The results of the fits for all measured hyperfine levels and proportion of atoms in the excited state are shown in Fig. 6.6. On the left (right) we plot the $^3D_1$ ($^3P_1$) lifetime at different mean atom numbers for each bin. Each plot is a different initial hyperfine level in $^3D_1$, with different markers indicating the proportion of total population in the $^3P_0$ state at the beginning of the sequence, either 5%, 20%, or 40%. The error bar for the atom number indicates the width of the atom number bin. The error bars for τ are from the statistical uncertainty of the maximum likelihood fit to Eq. 6.2.

It is apparent in the data that there is still a significant dependence on density, and that dependence varies under different conditions. As in Ref. [13], we fit the lifetime density dependence $\tau(n) = \tau_0/(1 + cn)$, where n is the camera measured atom number and is proportional to density, τ_0 is the single atom lifetime, and c is the density dependence coefficient. At very high density, we notice that the data deviates from the linear model, so we choose to exclude data above 8×10^5 atoms in these fits. This choice does not change the final reported value. These fits are shown for all data sets in Fig. 6.6, with the shaded area indicating the fit uncertainty. The fits use orthogonal distance regression to properly account for the atom number bin width.

With small population in the $^3P_0$ state, the measured lifetime is shorter at higher density. However, by initially placing 40% of the population in $^3P_0$ the trend is reversed and higher density results in a longer observed lifetime, as shown for the $F = 11/2$ data in Fig. 6.6. As with the $F = 11/2$ decay data, the $F = 7/2$ data shows a shallower slope with an increased population ratio in the $^3P_0$ state. As expected, the ratio of population in $^3P_0$ has a smaller effect on the $^3P_1$. For the $F = 11/2$ 40% data, the ground state has a smaller population on average, so radiation trapping effects are reduced and the corresponding overall density dependence is reduced.

We use these fits to extrapolate to a single particle lifetime, shown in Fig. 6.7. The error bars

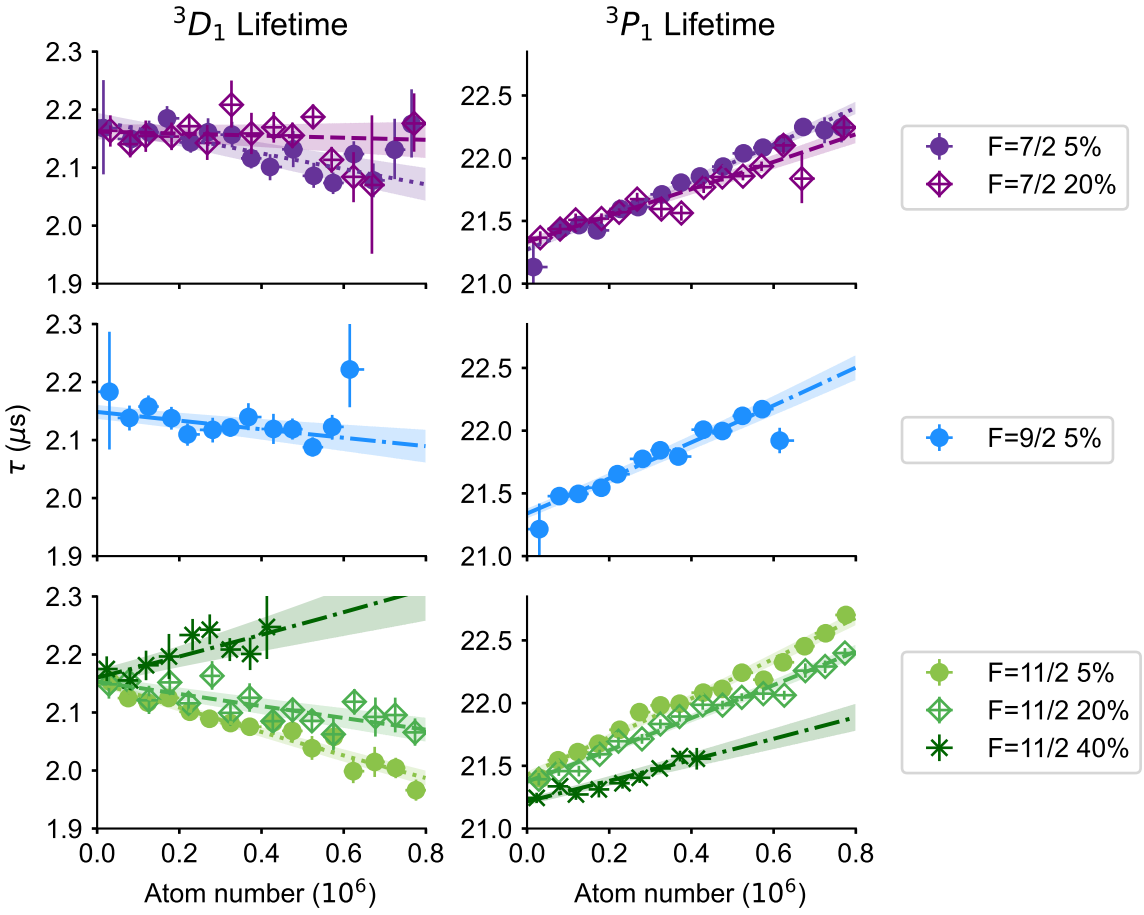

Figure 6.6: Density dependence for the $^3D_1$ and $^3P_1$ lifetime over different hyperfine states (F) and initial population proportions in the $^3P_0$ state, indicated as a % in the legend. To each data set, we fit a density dependent lifetime, shown as the lines on each plot with the shaded region indicating the fit uncertainty.

for each of the points is from the statistical uncertainty of the density dependence fit. The solid orange line indicates the weighted average of all points, and the dashed orange lines indicate the statistical uncertainty. The solid light orange lines represent the combined statistical and systematic uncertainty of each lifetime. The $\tau_{^3D_1}$ data is well scattered around the mean, but it is clear that the $\tau_{^3P_1}$ data is overscattered. This may be a result of the trade off we made to determine the $^3D_1$ lifetime, increasing the radiation trapping effect on the second decay.

The total uncertainty in the $^3D_1$ lifetime is dominated by statistics and quantum beats, as shown Table 6.1.4. We consider two other smaller sources of uncertainty, photon counter timing and

finite pulse duration. The multi-channel scaler quotes a < 710 ps rms timing jitter, which we take as a conservative bound on the timing error. As described in Ref. [109], finite pulse duration modifies the decay dynamics from a true double exponential. To circumvent this, we cut out 500 ns about this laser pulse, with a residual error from this approach is below 0.1 ns. The final $^3D_1$ lifetime is 2.1560 ± 0.0052 μs. Similar sources of uncertainty exist for the $^3P_1$ lifetime, presented in Tab. 6.1.4. We find $\tau_{^3P_1} = 21.327 \pm 0.033$ μs.

Table 6.1: $^3D_1$ lifetime uncertainty.

Effect	Uncertainty (ns)
Statistical	4.0
Quantum beats	3.2
Photon counter timing	0.7
Finite pulse duration	0.1
Total	5.2

Our result here notably differs from the measurement in Ref. [109], which found $\tau_{^3D_1} = 2.18(1)$ μs. This discrepancy may be explained by the different regimes of these measurements. In Ref. [109], the experiment was performed with the population entirely in the $^3P_0$ state, leading to a higher effective optical depth (OD) on the $^3D_1 \rightarrow^3 P_0$ decay along the collection axis. With a similar OD we observe longer lifetimes. For our measurements, we estimate an OD on the $^3D_1$ decay with 100% of the atoms in $^3P_0$ to be roughly 12 per million atoms. In Ref. [109], we estimate an OD of 1000 per million atoms.

6.2 Evaluating The Dynamic Coefficient

With a properly measured $^3D_1$ lifetime, we need a reevaluated dynamic term. Since this lifetime dominates the dynamic term, this shift has been calculated exclusively using this lifetime, as in Ref. [109]. In Ref. [81], the authors develop a technique to incorporate many atomic observables to calculate the dynamic shift. Our understanding and observations of the strontium atom should be self-

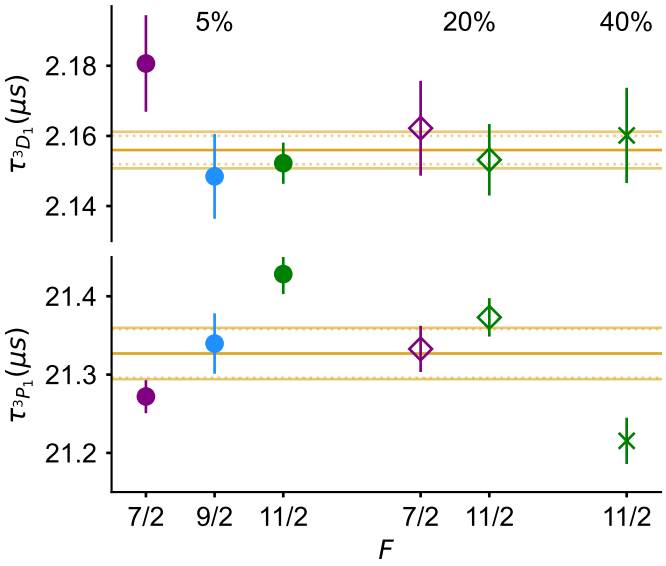

Figure 6.7: Single particle $^3D_1$ and $^3P_1$ lifetimes over different hyperfine states (F) and initial population proportions in the $^3P_0$ state, listed as a % above the data. The gold line is the weighted average for each lifetime. The dashed gold lines represent the statistical uncertainty and the solid light gold lines indicate the combined statistical and systematic uncertainties, as reported in Tabs. 6.1.4 and 6.1.4.

Table 6.2: $^3P_1$ lifetime uncertainty.

Effect	Uncertainty (ns)
Statistical	31.1
Quantum beats	10.5
Photon counter timing	0.7
Finite pulse duration	0.1
Total	32.8

consistent, so the calculation of ν_{dyn} should be based upon more than one measurement. For example, the $^3D_1$ oscillator strength directly affects the magic wavelength [132], so both measurements should help constrain each other. The sum-over-states polarizability formula links observables across the frequency spectrum:

$$\alpha_i(\nu) = \alpha_i^{\mathrm{core}} + \frac{\epsilon_0 c^3}{(2\pi)^3} \sum_k \frac{2J_k + 1}{2J_i + 1} \frac{A_{ki}}{\nu_{ik}^2 \left(\nu_{ik}^2 - \nu^2\right)}. \tag{6.3}$$

For state i, α_i^{core} is the core polarizability, A_{ki} are the Einstein A coefficients to states k, ν_{ik} are the transition frequencies, and J_i and J_k are the angular momentum of the states. The sum is over all the intermediate transitions. With this formula we compute various observables $\{y_j'(\{A_k\})\}$ that depend on $\alpha_i(\nu)$, including the magic wavelength and DC polarizability of $^1S_0$ state in addition to measured A coefficients. Our goal is to determine a set of fitted A_k that minimize a χ^2 function:

$$\chi^2 = \sum_j \left(\frac{y_j'(\{A_k\}) - y_j}{\sigma_j} \right)^2, \tag{6.4}$$

where y_j is the experimental value and σ_j is its uncertainty. Through this χ^2 minimization, we determine a set of A coefficients that best describes the observed quantities $\{y_j\}$. The observables used to calculate the dynamic shift are presented in Tab. 6.2. Appropriately propagating uncertainty through this linked fit is an opaque task. We vary the observables within their uncertainty using a Monte Carlo sampling technique, systematically remove observables from the fit, and vary the number of fitted A_k to create a distribution of ν_{dyn}. More details about this procedure are in the

Table 6.3: Observables used for calculating ν_{dyn}. More details of this selection process are described in Ref. [70]

y_j	Value	Reference
$A[(5s5p)^1P_1 \rightarrow (5s^2)^1S_0]$ at 461 nm	$1.9001(14) \times 10^8\ s^{-1}$	[162]
$A[(5s5p)^3P_1 \rightarrow (5s^2)^1S_0]$ at 689 nm	$46888(68)\ \mathrm{s}^{-1}$	[2]
$A[(5s4d)^3D_1 \rightarrow (5s5p)^3P_0]$ at 2603 nm	$2.7619(64) \times 10^5\ \mathrm{s}^{-1}$	[2]
$A[(5s5s)^3S_1 \rightarrow (5s5p)^3P_0]$ at 679 nm	$8.348(66) \times 10^6\ \mathrm{s}^{-1}$	[57]
$\alpha((5s^2)^1S_0, \nu = 0)$	$3.07(24) \times 10^{-39}\ \mathrm{Cm^2V^{-1}}$	[133]
$\Delta\alpha(\nu = 0)$	$4.07873(11) \times 10^{-39}\ \mathrm{Cm^2V^{-1}}$	[101]
Magic wavelength near 813 nm, $\nu_{813}^{\mathrm{magic}}$	368 554 825.9(4) MHz	[70]
$\partial\Delta\alpha/\partial\nu(\nu = \nu_{813}^{\mathrm{magic}})$	$1.859(5) \times 10^{-11}$	[70]
Magic wavelength near 390 nm, $\nu_{390}^{\mathrm{magic}}$	768917(18) GHz	[137]
Tune-out wavelength near 689 nm, ν^{to}	434 972 130(10) MHz	[57]
$\alpha(^3P_0, \nu = \nu^{\mathrm{to}})$	$2.564(13) \times 10^{-38}\ \mathrm{Cm^2V^{-1}}$	[57]

supplement of Ref. [2]. Through this procedure, we determine $\nu_{\mathrm{dyn}} = -153.06 \pm 0.33$ mHz at 300 K. This procedure was recently reproduced at NTSC in China, with further investigation into the minimization algorithm [31].

At our accuracy goals, the dynamic correction cannot be used with a simple T^6 scaling as done previously. This shift should be done by evaluating the integral across the BBR spectrum. A higher order power expansion does suffice, as was demonstrated in Ref. [81]. Between 200 K and 300 K, we fit a power expansion to the numerically calculated integral of the form:

$$\Delta\nu_{\mathrm{dyn}} = \eta_6 \left(\frac{T}{T_0}\right)^6 + \eta_8 \left(\frac{T}{T_0}\right)^8 + \eta_{10} \left(\frac{T}{T_0}\right)^{10}, \tag{6.5}$$

with $\eta_6 = -0.132606$ Hz, $\eta_8 = -0.011413$ Hz, and $\eta_{10} = -0.009013$ Hz, and $T_0 = 300$ K.

6.3 Measuring Temperature

With a properly determined atomic response function, we now need to measure the temperature the atoms experience. Two approaches have been used to measure the radiant temperature at the atoms: an in-vacuum BBR shield, and in-vacuum thermometry at the atoms. In the NIST YB group, a BBR shield made of copper creates a uniform radiation environment for the atoms, with sensors on this shield used to determine the boundary temperature of the system [11, 13]. The Ye Sr group has historically used in-vacuum probes that allow determination of the radiant temperature at the atomic location, see Ref. [21, 109]. The group at KRISS uses a combination of an in-vacuum probe and a in-vacuum shield to precisely characterize the black body environment in a Yb clock [58].

For the rebuilt Sr1 system, we decided to measure temperature using an in-vacuum probe mounted on a translation stage [36]. Periodically inserting the sensor during operation allows us to check for temperature drifts. Additionally, with many active temperature loops stabilizing the vacuum system and all viewports, the outer vacuum acts as a reliable BBR shield. Two sensors are mounted on the end of a translatable arm. This arm is mounted on an auxiliary vacuum chamber connected to the main chamber via a gate valve. We close the gate valve during regular operation, opening it to extend the sensor arm and measure temperature.

For the in-vacuum sensors, we choose thin film platinum resistance thermometers (TFPRTs), which have a resistance that is a function of temperature. By precisely measuring this resistance, we deduce the temperature of the resistor. The Callendar–Van Dusen equation describes this effect [52]:

$$R(T) = \left(A + BT + CT^2\right)(\Omega), \tag{6.6}$$

where A, B, and C are are resistor dependent fitted coefficients. Note this form is only valid for temperatures between 0 °C and 661 °C. We reparamatarize this equation by factoring out a resistance offset, typically at a fixed point realization, R_0, giving the form:

$$R(T) = R_0\left(1 + aT + bT^2\right)(\Omega), \tag{6.7}$$

where a and b are modified fitting constants. To determine the temperature given a resistance, we simply factor eq. 6.7:

$$T = \frac{-aR_0 \pm \sqrt{(aR_0)^2 - 4(bR_0)(R_0 - R)}}{2bR_0}. \tag{6.8}$$

Note that R_0 does not necessarily have to be at 0 °C, and by moving our offset we can modify the total temperature uncertainty.

We employ a standard four wire measurement technique to determine the thermistor resistance, where two leads provide an excitation current and two leads with no current are used to measure the voltage drop. To determine the current, we interleave measurements of a stable resistance standard $R_{std} = 100\ \Omega$ with measurements of the thermometer R_{PRT}. The resistance of the PRT is not the only thing that changes as a function of temperature. Thermoelectric voltages, especially at connections, can cause measurement errors. To combat this, we alternate between positive and negative currents and measure the respective voltages $V^{+(-)}$. The final resistance value R_{PRT} is determined by four voltage measurements:

$$R_{\mathrm{PRT}} = \frac{V^+_{PRT} - V^-_{PRT}}{V^+_{std} - V^-_{std}} R_{std}. \tag{6.9}$$

Another source of error is self heating of the sensors. Since the NIST calibrated sensors and the in-vacuum TFPRTs have very different self heating, we need to accurately determine what the effect of the excitation current is on the measured temperature. With the self heating proportional to the power through the resistor, we extrapolate to 0 current with two different current measurements. Labeling the currents as conditions A and B, we extrapolate the resistance R at $I = 0$A:

$$R(I = 0) = R_A - P_A \left(\frac{R_B - R_A}{P_B - P_A} \right), \tag{6.10}$$

where $P_{A,B}$ is the power dissipated at currents A, B. The term in the parenthesis is the slope of the R as a function of P curve linearly extrapolated from currents A and B. With Ohm's law, we

simplify to find:

$$R(I=0) = \frac{(I_A^2 - I_B^2)R_A R_B}{I_A^2 R_A - I_B^2 R_B}. \tag{6.11}$$

We interleave resistance measurements at 100 μA and 200 μA for the calibration and 50 μA and 100 μA for standard operation. Nevertheless, we have not observed any self-heating at these low currents, and both current measurements agree within uncertainty.

The two in-vacuum temperature sensors are TFPRTs from YAGEO-Nexensos (part no. 32208519). The two chosen sensors were selected from a batch of 10 sensors after observing the measurement stability after numerous thermal cycles up to 200 °C. We use a dry-block technique to calibrate the TFPRTs. Two NIST-Gaithersburg calibrated platinum wire wound temperature sensors, labeled R17 and R18 in Ref. [141], are mounted in a temperature controlled copper block. These sensors were re-calibrated in 2020, and once mounted in the block agree within their uncertainty. For calibration, the TFPRTs are inserted between the two wire wound sensors. The block and environment are varied from 16 to 31 °C, and the results are fit with Eq. 6.6. The total calibration uncertainty for both sensors at 20 °C is 2 mK. The environment of the dry block is controlled to 200 mK, leading to a differential immersion error between the three sensors of 1.2 mK. Once installed in-vacuum and baked over a prolonged period at 150 °C the sensors continue to agree within their combined uncertainty. Further details about this calibration process are in Appenix A.

In Fig. 6.9, we plot the measured temperature at the atoms. In standard operation, we alternate measurements of both sensors and take the average, plotted as gold points. The black line is a binned average over 10 minutes. Periodic oscillations in the temperature on the hour timescale are likely due to weak coupling to room temperature, that oscillates up to 2 °C on a similar timescale. An overlapping Allan deviation of the data on the right shows this behavior, with the temperature uncertainty averaging down as white noise to 0.2 mK in 100 s before rising at longer times. Despite this oscillation, the temperature is very stable over long times, and we repeatedly measure < 10 mK variations over weeks.

With two correlated sensors and two calibration curves for each sensor, we cannot simply sum

uncertainty and divide by 2, so instead we use a linear pooling technique. In Fig, 6.10, we present the linear pooling approach to determine sensor uncertainty. Each Gaussian represents a sensor and calibration curve, with the Gaussian width given by the calibration uncertainty. The gold line is an area-normalized sum of these four curves, with the red star indicating the mean value. We use 95% confidence intervals, indicated by the shaded region, to give the error bars on the total calibration uncertainty. Typically, this results in a $3-4$ mK temperature uncertainty.

Immersion error arises when the act of measuring a temperature sensors modifies the measured temperature, such as conductive coupling along the sensor support structure. Using an in-vacuum translation stage, we bound immersion error by measuring temperature gradients along the translation axis. Our standard operation procedure is to match the temperature at the retracted position with the temperature at the fully extended position, where the atoms are located. The auxiliary chamber supporting the translation arm has separate temperature control loops, allowing us to modify its temperature without strongly affecting the main system. In Fig. 6.11, we plot the extended temperature as a function of the retracted temperature. The slope of the measurement is 0.13 °C/°C, so if the retracted temperature within the auxiliary chamber is 10 mK below the extended measurement at the atom location, the true temperature is 1.3 mK higher than the temperature measured in the extended state. Under standard operation, we are able to keep the retracted position < 20 mK different than the extended temperature. We typically treat this effect as pure error, and do not correct the measured temperature.

Images of the temperature probe are shown in Fig. 6.8. The two temperature sensors on the translation stage have different lines-of-sight to the vacuum chamber and thus are sensitive to thermal gradients, so rotating the probe modifies this differential temperature coupling. Within the sensor uncertainties, we have noticed no temperature differences in any orientation, confirming the lack of thermal gradients.

The wire wound sensors are calibrated to the ITS-90 temperature scale, which deviates from true thermodynamic temperature. Near room temperature, this correction is quadratic in temperature [141]. At our operational temperature, this is a 2.8 mK correction with a 0.4 mK

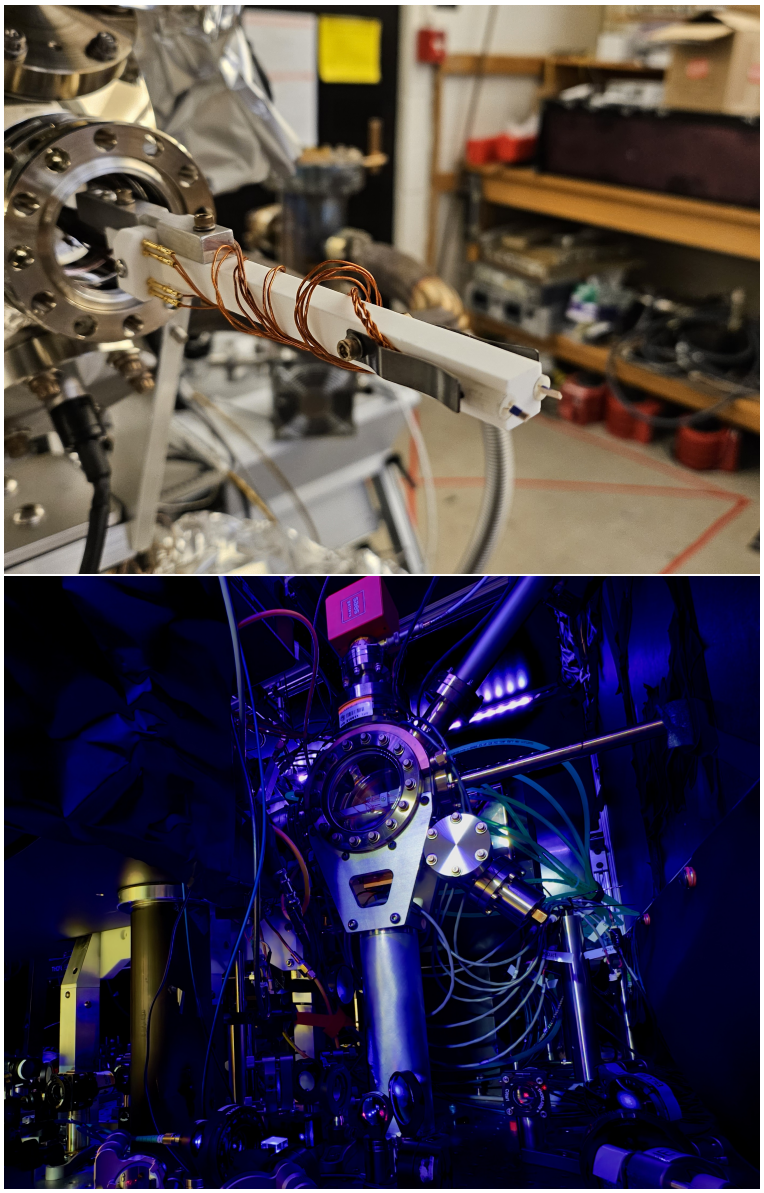

Figure 6.8: The thermal probe system. Top: the thermal probe under contruction. Two thin film platinum resistance thermometer are mounted to the end of a ceramic arm mounted on a magnetically coupled in-vacuum translation stage. We can fully extend this system in vacuum to measure the temperature at the atomic sample. Bottom: image of the thermal probe auxiliary chamber. This is mounted adjacent to the main system and can be closed off with a gate valve. The auxiliary chamber has its own pump, the red SAES box, and an RGA to determine the background gas composition.

uncertainty.

The total uncertainty budget is presented in Tab. 6.3. The operational temperature is

295.267 ± 0.0041 K, with the measurement uncertainty alone account for a BBR fractional shift uncertainty of 2.8×10^{-19}. It is important to periodically measure the radiant temperature. As will be discussed in Ch. 8, for high accuracy operation in a clock comparison, we choose to measure the temperature before and often after each comparison run. We have not noticed significant disagreement between daily measurements, but the temperature does change 10 mK over the course of weeks. The oven has no direct line of sight to the atoms, and we notice no fast coupling between the oven temperature and the measured temperature. However it does represent a heat load, so we notice that the radiant temperature will increase by a few mK as its surroundings heat up. We also observe some heating of the chamber from the bias coils and leave them on during temperature measurements. There appears to be no thermal coupling between the MOT coils and the in-vacuum measurement under a standard MOT current and duty cycle. For the most accurate temperature reading, as in the NIST comparison campaign, we leave the system on overnight before each measurement to ensure a fully thermal and stabilized environment. Thermometry before and after each comparison measurement indicates minimal temperature drift < 5 mK.

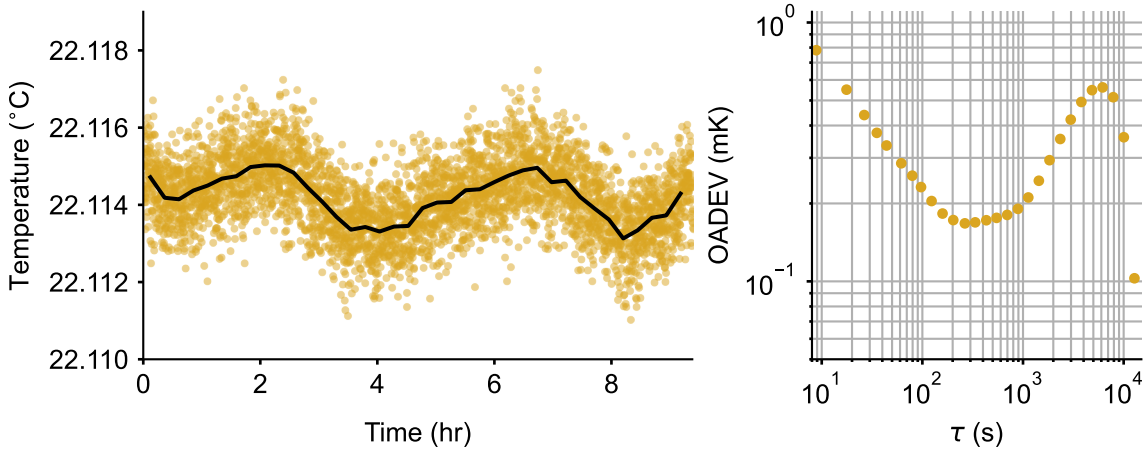

Figure 6.9: The temperature measured at the atoms. The gold points are an average of the two sensors using two calibration curves. The black line is a binned average over a 10 minute interval. On the right, we plot an overlapping Allan deviation of the temperature. Over short time scales, the temperature averages as white noise. At longer times, $T > 10^3$ s, temperature flicker and drift lead to greater instability.

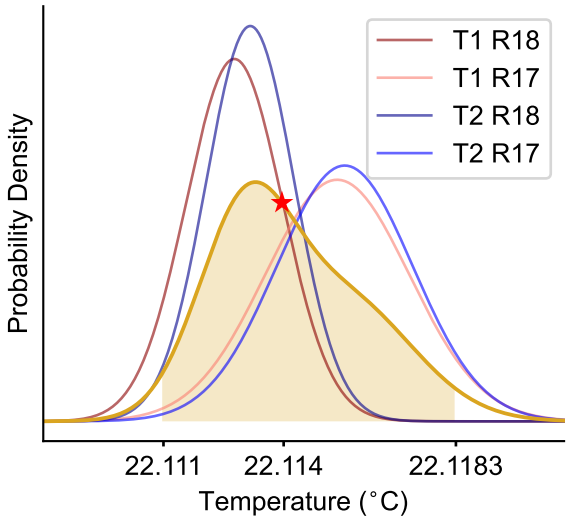

Figure 6.10: We use a linear pooling technique to calculate the average temperature and uncertainty. There are two sensors, labeled T1 and T2, and two NIST calibrated reference sensors, R17 and R18. Each sensor and calibration curve gives a slightly different temperature and uncertainty. We plot the probability density for each sensors and calibration, with the normalized sum distribution plotted in gold. The uncertainty is calculated using the 95% confidence interval, shown in the shaded region and labeled on the horizontal axis. The mean value is the red star.

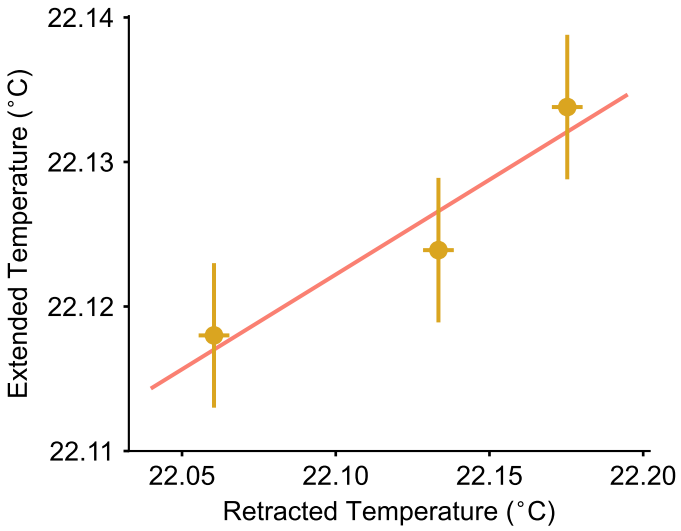

Figure 6.11: To understand the immersion error of the temperature probe, we modulate the temperature of the auxiliary chamber and measure the temperature at the atoms and in the retracted position. The salmon colored line is a fit to this data, and has a slope of 0.13 °C/°C.

Table 6.4: Temperature uncertainty for the in-vacuum radiant measurement. This table is for the measurement presented in Fig. 6.9, measured October 16, 2024 and differs from the measurement presented in Ref. [2]. The calibration error arises from the linear pooling 95% confidence interval shown in Fig. 6.10. The 2 hour temperature instability is calculated using an overlapping Allan deviation, presented on the right of Fig. 6.9.

Uncertainty source	Uncertainty (mK)
Calibration error	3.7
JILA calibration immersion error	1.2
Immersion error	1.3
ITS-90 correction	0.4
2 hour temperature instability	0.5
Total uncertainty	4.1

Chapter 7

Accuracy

So far, we have tackled some of the largest sources of systematic uncertainty in a Sr OLC: the blackbody radiation shift in Ch. 6, the lattice light shift in Ch. 5, and the density shift in Ch. 4. Only a few sources of small systematic shifts remain. In this chapter, we will discuss completing the systematic evaluation of Sr1, making it the most accurate clock built to date. In order to operate accurately, we need to identify an appropriate set of operational conditions. This will then guide the remaining evaluation of systematic shifts, including the first and second order Zeeman, tunneling, and background gas shifts. All these shifts are tabulated in Tab. 7.9, summing to 8.1×10^{-19}. Much of the work presented in this chapter is covered in our Physical Review Letters article entitled "Clock with 8×10^{-19} Systematic Uncertainty," Ref. [2].

7.1 Operational Conditions

To properly characterize and control systematic shifts, measurement precision together with repeatable and reliable operation are key. The most distinguishing feature of the new Sr1 system is the operation using a 10 E_r shallow lattice depth, nearly zero density shift, and low 100 nK radial temperatures. We have already discussed the approaches we use to ensure a reliable BBR correction, including table and chamber temperature stabilization, and frequent measurement of the radiant temperature at the atoms. Reliable and repeatable sample preparation is also key, with the motional and spin states directly impacting the density shift, lattice light shift, and many others. While our blue and red MOTs are standard among strontium experiments, the additional Doppler and resolved

sideband cooling allows us to prepare a ground band, 700 nK sample in a 300 E_r lattice. Through the frequency comb, this cooling light is stabilized at low frequency to the same cryogenic silicon resonator that stabilizes the clock light. The $^3P_1$ linewidth is 7 kHz, which is a similar scale to the daily drift rate of a good ULE resonator. Tieing the Doppler cooling light to the silicon cavity results in a few Hz/day drift, so there is no appreciable change to our atomic temperatures over many days. After spin polarizing in the stretched states, we transfer the population to the $m_F = \pm 5/2$ states to make use of the least magnetically sensitive transition. As discussed in Ch. 4, we operate near the "magic depth" around 10 E_r to reduce collisional effects. After adiabatically reducing the lattice depth, our sample is consistently around 100 nK in radial temperature. We briefly reduce the lattice depth to the single band regime (~ 3 E_r) before readout to ensure that the only measured atoms are in the $n_Z = 0$ state. This robust procedure mitigates potentially poor sample preparation as well as heating during spectroscopy, ensuring reliability and low uncertainty of the lattice light shift.

Between sample preparation and readout, the dead time is 1 s during standard operation. Based upon a noise model of the clock laser, Dick effect noise is minimized with a 2.43 s Rabi interrogation time [114]. A long clock interrogation time also reduces the light shift associated with clock light as well as line pulling from neighboring transitions. A digital servo with two integrators tracks the atomic transition by alternating spin states and sides of the Rabi lineshape. Using the Si3 laser model, we expect a Dick effect limited single clock stability of $5 \times 10^{-17}/\sqrt{\tau/\mathrm{s}}$ for averaging time τ [114].

7.2 First Order Zeeman

While we use the least magnetically sensitive Sr clock transition, drifting magnetic fields and low frequency noise may lead to an uncompensated first order Zeeman shift [114]. Our typical clock measurement sequence alternates between $|^1S_0, m_F = +5/2\rangle \rightarrow |^3P_0, m_F = +3/2\rangle$ and $|^1S_0, m_F = -5/2\rangle \rightarrow |^3P_0, m_F = -3/2\rangle$ transitions with two different atomic servos. The average frequency of the two servos rejects static Zeeman shifts.

Consider a 1 mG jump in the magnitude of the magnetic field occurring within the dead time

between the two locks, shifting the second frequency ~ 50 mHz or 10^{-16}. This will appear as a center frequency shift of 25 mHz, far above the desired systematic uncertainty. The clock servo will be able to track this, so the frequency shift of a static change in field will appear in a single lock point. If this point remains, the clock frequency will take a while to average away this jump. The lab magnetic field environment is more complicated than just a single jump, with many magnetic items such as power supplies, optomechanics, and two other running Sr clocks. How does the noisy magnetic field environment aliased by the clock lock affect frequency stability?

To characterize the magnetic field environment, we use the 26 times more magnetically sensitive $|^1S_0, m_F = -5/2\rangle \rightarrow |^3P_0, m_F = -7/2\rangle$ transition. This allows us to use the same sample preparation technique as in our standard operation, maintaining an identical duty cycle and field switching dynamics. We look at the frequency difference between successive measurements of the same transition, which contains the first order Zeeman coupling at our duty cycle. As in our standard scheme, two separate atomic servos ensure that this measurement is not correlated via the lock. An overlapping Allan deviation of this frequency series is shown in Fig. 7.1. The average difference is consistent with 0, and the measured noise floor of 1.8×10^{-18} represents an upper bound on the magnetic field noise. After scaling to the operational transition, we find a 7×10^{-20} uncertainty on the first order Zeeman shift.

This systematic shift certainly presents an obstacle for building a next generation Sr system with uncertainty $< 10^{-19}$, indicating that better magnetic field isolation is necessary. Borrowing techniques from other precision measurement fields, we might approach < 1 ppm field stability [100]. Without modifying our field environment, simultaneous spectroscopy of two spin states may allow for full rejection of the first order Zeeman shift. By preparing two regions of the cloud in two different spin state, driving the clock transition with two frequency tones, and using imaging readout, temporal variations in the magnetic field are trivial to reject. The NIST Yb group has pursued this technique, loading two opposite sign magnetic sublevels in separate atomic clouds during a single cycle [55]. This does require a more complicated experimental sequence as well as real time processing to implement, but is an attractive approach to solving this systematic.

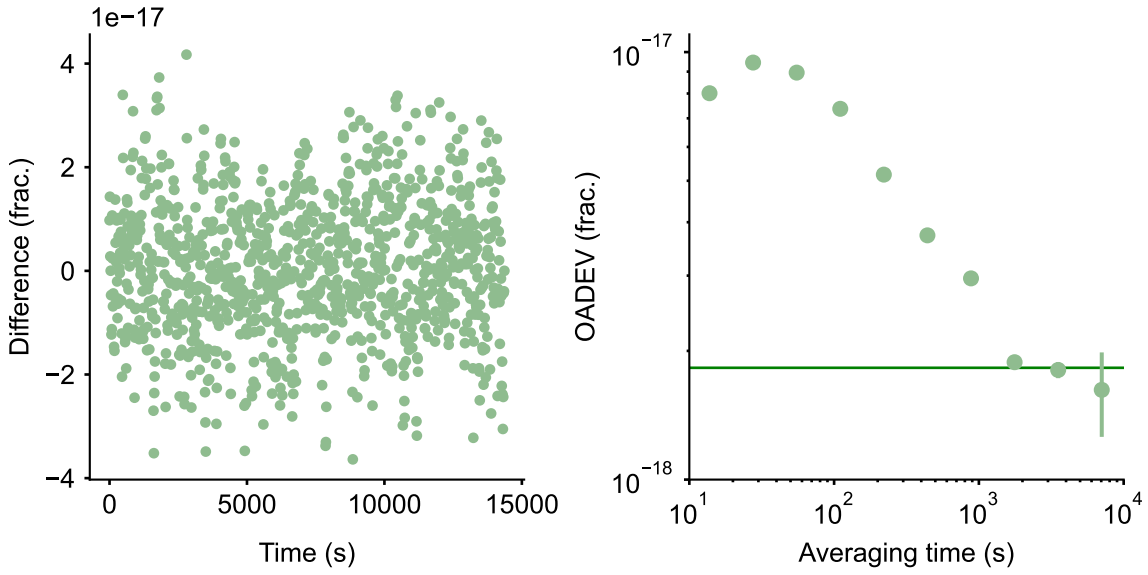

Figure 7.1: First order Zeeman systematic measurement. Left: the frequency difference between subsequent measurements of the $|^1S_0, m_F = -5/2\rangle \rightarrow |^3P_0, m_F = -7/2\rangle$ transition. Right: the overlapping Allan deviation (OADEV) of this frequency record. The solid green line represents a flicker floor of this measurement at 1.8×10^{-18}. Our standard $|^1S_0, m_F = \pm 5/2\rangle \rightarrow |^3P_0, m_F = \pm 3/2\rangle$ has 26 times less magnetic sensitivity, so the operational flicker floor should be 7×10^{-20}. We treat this flicker floor as the first order Zeeman shift uncertainty.

7.3 Second Order Zeeman

In the $J = 0$ strontium clock states, the second order Zeeman effect arises from mixture with other fine structure states, leading to a shift $\propto B^2$. The ground state is far away in energy from other levels, so the primary source of this effect is the interaction between $^3P_0$ and $^3P_1$. Under the Zeeman Hamiltonian H_Z, the second order Zeeman shift [25]

$$\Delta_B^{(2)} = -\sum_{F'} \frac{|\langle {}^3P_0, F, m_F | H_Z | {}^3P_1, F', m_F \rangle|^2}{\nu_{{}^3P_1, F'} - \nu_{{}^3P_0}}, \tag{7.1}$$

where ν is the energy of the state in the subscript. While this shift can be written as a function of measured atomic parameters and the applied magnetic field, the standard approach has been to measure a coefficient for the frequency of the clock transition as a function of magnetic sublevel splitting. The second order Zeeman shift can then be corrected on the fly, compensating for drifting

magnetic fields. This coefficient has been measured precisely over the years, including recently in Ref. [21], as well as precisely calculated in Ref. [84].

Operation on the $|^1S_0, m_F = \pm 5/2\rangle \rightarrow |^3P_0, m_F = \pm 3/2\rangle$ transition requires reevaluation of the second order Zeeman coefficient for our desired accuracy goal. This shift $\Delta\nu_{Z2}$ goes as

$$\Delta\nu_{Z2} = \xi_{\sigma^\pm\, m_F=\mp 5/2} \left(\Delta_{\text{meas}} - \Delta_{\text{vec}}\right)^2, \tag{7.2}$$

where $\xi_{\sigma^\pm\, m_F=\mp 5/2}$ is the second order Zeeman coefficient on our operational transition, Δ_{meas} is the measured frequency difference between the operational transitions, and Δ_{vec} is the splitting due to the lattice vector shift.

To determine $\xi_{\sigma^\pm\, m_F=\mp 5/2}$ precisely, we perform self-comparison measurements, similar to the lattice light shift measurement technique presented in Ch. 5.2. We compare the frequency difference between a static reference field near 0.7 G and a variable field from 0.3 to 1.5 G. Experimental results are shown in Fig. 7.2. Δ_{vec} is measured independently by modulating the lattice depth, see Ch. 5. We measure this effect in a shallow 10 E_r lattice depth, so the lattice light vector shift remains small for all applied bias fields. We find a $\xi_{\sigma^\pm\, m_F=\mp 5/2} = (-0.12263 \pm 0.00014)$ mHz/Hz^2. At the operational field near 397 mG, the second order Zeeman shift $\Delta\nu_{Z2} = (-85.51 \pm 0.10) \times 10^{-18}$. Further reducing the bias field does reduce the second order Zeeman shift and uncertainty. For significant reduction in shift uncertainty, a more precise determination of $\xi_{\sigma^\pm\, m_F=\mp 5/2}$ is needed, ideally using a stronger bias field to increase the lever arm.

Operating at different lattice depths and bias fields yields a different vector shift. While this is negligible for the coefficient measurement depth near 10 E_r, for locks where we significantly modify operational conditions, we implement realtime calculation of Δ_{vec}. Using Δ_{meas} as well as the lattice depth, lattice ellipticity, and the angle between the angle between the lattice k vector, measured in Ch. 5.4, we can correct for a varying Δ_{vec} without reevaluating the lattice light shift.

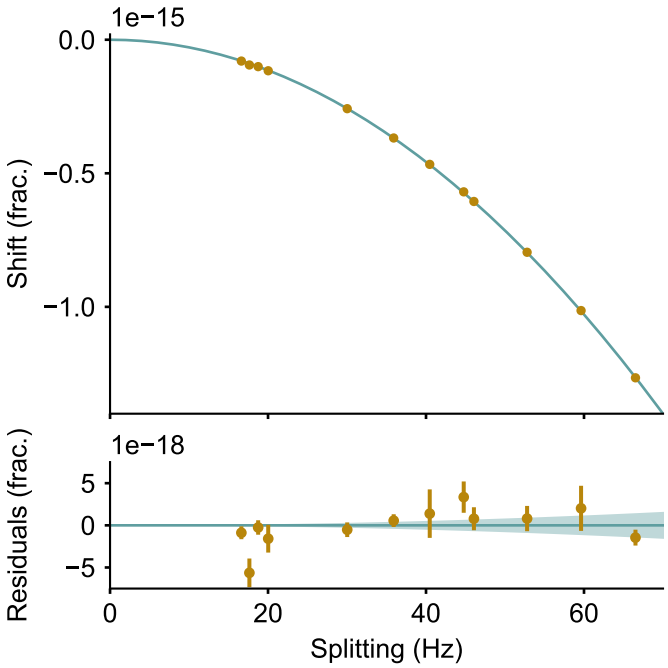

Figure 7.2: Second order Zeeman shift coefficient measurement. We vary the applied magnetic field and measure the splitting and the frequency shift. We fit the data with Eq. (7.2) and plot this fit in green. The lower panel shows the fit residuals with the shaded green region representing the fit uncertainty.

7.4 Tunneling

At shallow depths, superposition of states in neighboring sites can cause frequency shifts. First identified in Ref. [79], the maximum possible frequency shift due to this effect goes as $\Omega_0\Omega_1/\Delta_g$, where Ω_0 and Ω_1 are the Rabi frequencies of the carrier and first Wannier-Stark sideband and Δ_g is the frequency difference between neighboring lattice sites. At the operational depth near 10 E_r, the off-site Rabi frequency is appreciably large, leading to a maximum shift of $\sim 2 \times 10^{-19}$. While the coherent superposition of neighboring states is likely small, it is difficult to directly measure and control this effect. Instead, we opt to use a Rabi pulse time that is a half integer multiple of the oscillation period of the tunneling shift, which is the inverse of the energy offset between neighboring sites [79]. The shift has a sinusoidal envelope, going to zero at each oscillation period. We measure the splitting between neighboring lattice sites to be 867.7461 ± 0.0004 Hz. With a pulse

time of 2.4298583 s and a conservative timing uncertainty of 1 μs, the maximum tunneling shift is 2×10^{-21}.

7.5 Background Gas Shift

Collisions between trapped strontium atoms and background gas result in a systematic frequency shift [46]. Glancing collisions with residual gas elements in the vacuum create phase shifts, that in sum generate an overall frequency shift. As demonstrated in [5], the shift is inversely proportional to the vacuum lifetime τ_{vac}, and goes as:

$$\Delta\nu_{\text{BG}} = (\delta\nu_{bg}/\nu) \times 1/\tau_{\text{vac}}, \tag{7.3}$$

with the shift coefficient $\delta\nu_{bg}/\nu = (3.0 \pm 0.3) \times 10^{-17}$ s measured in Ref. [5]. τ_{vac} is measured as the $1/e$ decay time of an exponential decay fit to the atomic population to determine the vacuum loss rate. This coefficient was measured by modifying the vacuum hydrogen level by heating an non-evaporable getter, and thus the frequency shift is due primarily to collisions with molecular hydrogen.

We use a residual gas analyzer (RGA) with an electron multiplier stage to measure the partial pressures of the vacuum up to 300 atomic mass units. The RGA does not have direct line of sight to the atoms, so the absolute pressure values it reads are likely inaccurate. Mounted in an auxiliary chamber that also holds the temperature sensor and translation arm, we believe the local pressure and non-hydrogen vacuum contaminants the RGA measures to be significantly higher than in the primary chamber. However, the relative pressures are indicative of the gas makeup in our system. The partial pressures for each atomic mass are shown in Fig. 7.3. We confirm that the dominant species in the vacuum is hydrogen, with a partial pressure of 2×10^{-10} Torr at the RGA. Other significant vacuum contaminants include H_2O, N_2, CO, and CO_2, all with partial pressures below 5×10^{-11} Torr. The background gas coefficient reported in [5] was measured in a hydrogen dominated system, so it is valid in this environment.

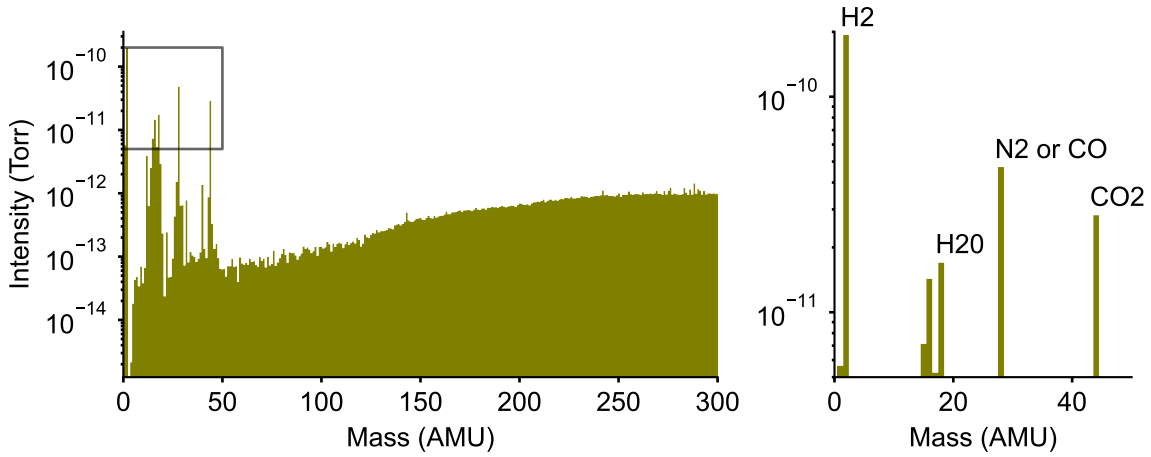

Figure 7.3: Background gas composition of the vacuum system. Using a residual gas analyzer equipped with an electron multiplying stage, we measure partial pressures of vacuum contaminants up to 300 atomic mass units (AMU), as shown in the top plot. The right plot highlights the predominant species in the vacuum. As expected, hydrogen molecules dominate the residual gas composition of our vacuum system.

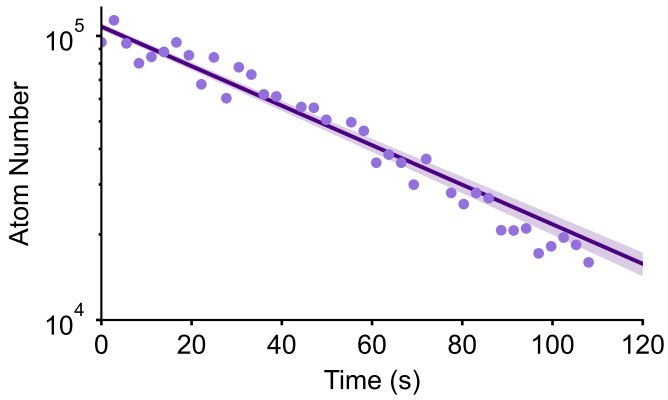

Figure 7.4: To measure the vacuum lifetime, we hold an atomic sample in the lattice and measure the atom number decay over time. The solid line shows an exponential fit to the atom number, and the shaded area shows the fit uncertainty. The vacuum lifetime is 63.6 ± 2.5 s.

We measure the vacuum lifetime by measuring the atom number as a function of hold time in a deep lattice. Background gas collisions with this trapped sample lead to atom loss over time. We fit this data to an exponential decay and find a vacuum lifetime of 63.6 ± 2.5 s. The results are presented in Fig. 7.4. This measurement is vacuum limited, as slightly increasing pressure leads to a shorter measured lifetime. With this lifetime, the background gas shift is $(-4.7 \pm 0.5) \times 10^{-19}$.

Despite the long vacuum lifetime in Sr1, the background gas shift remains one of the largest sources of uncertainty. This is a difficult systematic to fully characterize, as the interactions between Sr and background gas particles are poorly understood. A more comprehensive measurement of $\delta\nu_{bg}$ is needed, including dependence on background gas composition. Research using cold atoms to precisely characterize UHV environments has developed techniques that might be implemented on the next Sr1 system [8]. A reduction in the background gas is also a worthwhile endeavor for reducing this systematic. Vacuum lifetimes in other cold atom experiments have exceeded 1000 s [91], and cryogenic operation may further reduce collisions [170].

7.6 DC Stark

Differential DC polarizability between the clock states results in the DC Stark shift, where static electric fields shift the clock transition frequency. While our vacuum chamber is conductive stainless steel, insulating windows and cavity mirrors can accrue charges [110]. The first in-vacuum build up cavity for a 1D lattice clock experience patch charges on the cavity mirrors, leading to an untamable systematic shift [82]. Any insulating surfaces have the possibility to accrue patch charges, and using a piezoelectric actuator for one of the cavity mirrors caused additional concerns. Due to this history, the DC Stark shift was top of mind during the design of Sr1. Through Comsol modeling, John Robinson designed "Faraday cups," copper pieces that ring each mirror, acting as Faraday cages to shield atoms from patch charges. Tobias Bothwell's thesis contains more details [18]. To measure the DC stark shift and possibly apply a field correction, a set of two in-vacuum quadrant electrodes surround the atoms, illustrated in the schematic in Fig. 2.3. Simply by swapping the conductor configuration, we can apply electric fields at the atoms in all three directions.

With this hardware, measuring the background DC stark shift is a rather easy task. The frequency shift $\Delta\nu_{bg}$ in a background electric field E_{bg} is:

$$\Delta\nu_{bg} = \alpha(0)E_{bg}^2, \tag{7.4}$$

where $\alpha(0)$ is the differential polarizability at DC. To measure E_{bg}, we apply a much stronger electric field using the in-vacuum electrodes and measure the resultant clock shift. A schematic of this approach is shown on the left of Fig. 7.5. In our measurement, we alternate between three configurations, a positive field, a negative field, and the background field with grounded electrodes. With an applied electric field E_{app} the frequency shift is due to a vector sum of the applied field and the background field. In one direction, this is,

$$\nu_{\pm} = \alpha(0)(E_{bg} \pm E_{app})^2 + \nu_{Sr}. \tag{7.5}$$

The grounded electrode configuration results in the strontium frequency ν_{gnd}. The frequency differences between positive and negative fields,

$$\nu_+ - \nu_- = \alpha(0)\left((E_{bg} + E_{app})^2 - (E_{bg} - E_{app})^2\right) = \alpha(0)\left(4E_{bg}E_{app}\right). \tag{7.6}$$

Solving for the background field shift, Eq. 7.4, we find,

$$\Delta\nu_{bg} = \frac{(\nu_+ - \nu_-)^2}{16\alpha(0)E_{app}^2}. \tag{7.7}$$

Here $\alpha(0)E_{app}^2$ is simply the applied electric field shift absent a background field. The total background field shift becomes,

$$\Delta\nu_{bg} = \frac{(\nu_+ - \nu_-)^2}{8\left(\nu_+ + \nu_- - 2\nu_{gnd}\right)}. \tag{7.8}$$

An attractive feature of this approach is that the larger the applied field the better the background field determination. With the in-vacuum electrodes, we can apply large fields to quickly measure small background shifts.

An experimental measurement of the field along the $\hat{Z}$ direction is plotted in Fig. 7.5. In the center panel, we apply an electric field along $\hat{Z}$ and alternate the polarity of the 80 V applied between electrodes. This generates a roughly 5 Hz frequency shift between the background configuration

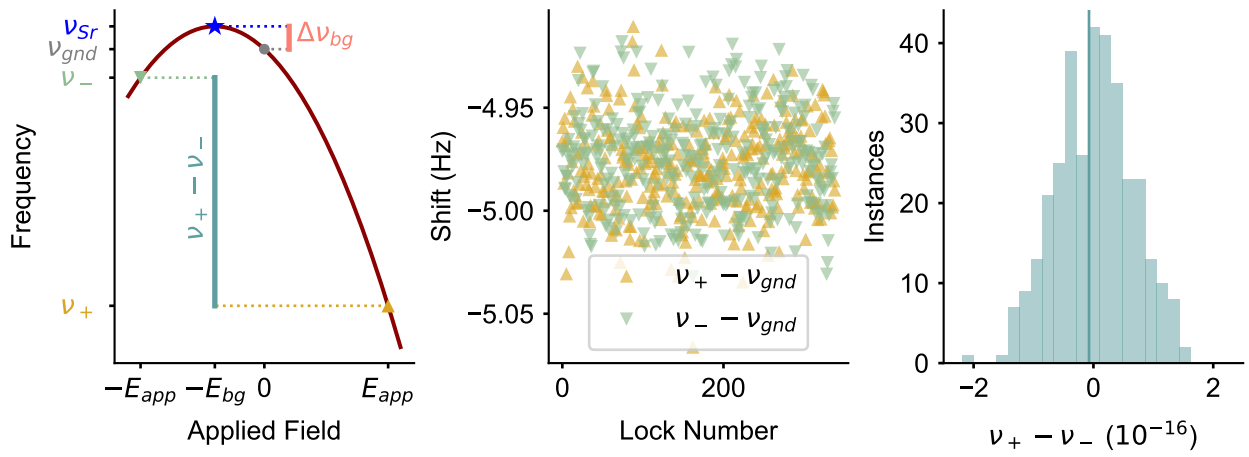

Figure 7.5: DC Stark shift measurement. A background electric field, E_{bg}, causes a frequency shift $\Delta\nu_{bg}^{Z}$ from the true strontium frequency ν_{Sr}. We apply an electric field, $\pm E_{app}$, and measure the resultant frequency shifts $\nu_{+,-}$ as well as the grounded field frequency, ν_{gnd}. This shift is quadratic with applied field, as shown on the left. A DC stark shift measurement record along $\hat{Z}$ is presented in the center and left panel. The applied field generates a 5 Hz shift for both field polarities. The average frequency difference between the two configurations, $\nu_+ - \nu_- = -7.4 \times 10^{-18}$, shown as the solid teal line. Using Eq. 7.8, we find $\Delta\nu_{bg}^{Z} = -(3 \pm 6) \times 10^{-22}$. The total DC stark shift is a vector sum along all three axes, reported in Tab. 7.6.

and the high field configuration. This frequency shift is stable and averages as white noise. On the right, a histogram of $\nu_+ - \nu_-$ shows a very small frequency difference between the two polarities, indicating a small background field. The average frequency difference is 10^{-17}, indicated by the solid blue line. Using Eq. 7.8, this measurement indicates a background DC Stark shift of 3×10^{-21}.

Since Sr1 was constructed, we have made 4 DC Stark shift measurements, all indicating $\Delta\nu_{bg} < 10^{-18}$ along all directions. As of writing, the most recent measurements were completed in July 2024, shown in Tab. 7.6. In this measurement set, the total DC stark shift is $< 10^{-20}$. Additionally, using in-situ imaging to study gradients across the sample resulted in no clear DC stark shift gradient [22].

7.7 Room Light

Much like how the broad, incoherent radiation from the room temperature chamber causes a frequency shift, we expect ambient room light to also cause a differential shift. Calculating this effect

Table 7.1: DC Stark shifts measured July 2024.

Axis	$\Delta\nu_{bg}$ (10^{-21})	Uncertainty (10^{-21})
$\hat{X}$	-4.2	3.2
$\hat{Y}$	-0.9	1.3
$\hat{Z}$	-0.3	0.6
Total Shift	-4.3	3.2

is much like the BBR correction: we need to know the atomic response function and the spectrum and intensity of the light hitting the atoms. Now seldom used, incandescent light bulbs are near ideal BBR emitters. A hot filament around 3000 K emits broad thermal radiation, some of which is visible, while much of the IR light is absorbed and heats the bulb glass. On the left of Fig. 7.6 we plot the wavelength dependence of the strontium shifts to $^1S_0$ and $^3P_0$ as well as the spectrum of a 3000 K black body. Unlike the room temperature BBR correction which is dominated by the DC polarizability, broad visible light addresses many transitions in Sr. To calculate the effect of this spectrum on the atoms, we must sum the contributions of all visible transitions weighted by the spectrum of the light. This ends up being rather imprecise, as the polarizability of Sr at shorter wavelengths is less well known. Additionally, we do not have precise knowledge of the spectrum or intensity of ambient visible light the atoms are exposed to.

Nevertheless, we can get some intuition regarding the effect of room light by roughly calculating the effect of a BBR spectrum in the visible range, as shown on the left of Fig. 7.6. We model a visible light as a 100 W BBR spherical emitter located 1 m away from the atoms. Using the polarizability data provided in Ref. [81], we calculate the shift in response to such an emitter. Interestingly, the shift is actually largest with a BBR emitter near 100 K. At this temperature, the center of the BBR peak is near 30 μm, and virtually the entire shift is due to the rather large DC polarizability difference between states. At shorter wavelengths, the many different transitions out of both clock states force the polarizability to cross (there are a number of visible magic wavelengths!), and the overall shift is

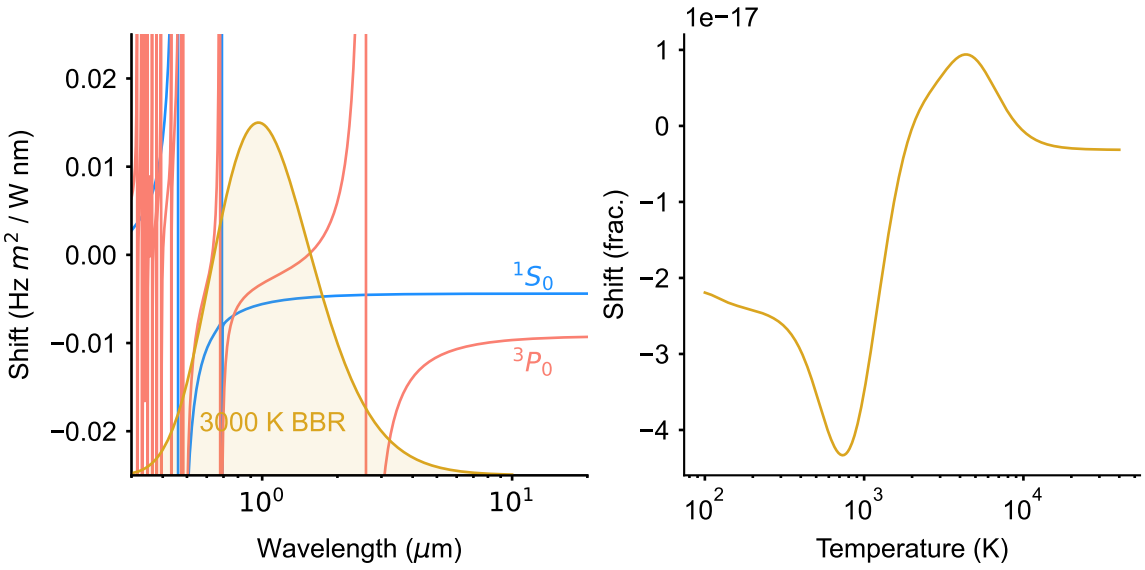

Figure 7.6: The effect of a visible BBR spectrum on the clock. Left: the shift for the two clock states as a function of wavelength and the BBR spectrum of a 3000 K emitter. Right: the calculated shift of the clock transition in fractional frequency units as a function of BBR temperature, assuming a spherical 100 W BBR emitter located 1 m away from the atoms.

closer to 0. Fluorescent and LED bulbs both have a non-thermal spectrum, typically trading broad IR spectrum for peaks in the visible. Thus, this calculation is not entirely representative of the light environment of any modern lab.

During operation, the Sr1 system is always enclosed with panels on the sides and a top shelf, blocking much of the room light from reaching the atoms. This enclosure is not light tight, with small gaps between panels and around the table. There is certainly far less light entering the enclosure than is used to calculate Fig. 7.6, however it is rather difficult to determine exactly what the atoms are seeing as we cannot measure the light inside the vacuum chamber.

Instead, we decided to measure if there is any observable frequency shift by significantly increasing the light in the enclosure. Using a lamp on a switchable outlet, we interleave a dark (off) condition and a bright (on) condition and measure the frequency shift on the clock transition, $\nu^{\text{off}} - \nu^{\text{on}}$. Images of this experiment are shown at the top of Fig. 7.7. The lamp is placed within the enclosure at the corner of the system about 1 m from the atoms with no direct line of sight. With

the light off, the atoms experience only the light that makes it through cracks in the enclosure. With the light on, some light scatters off various surfaces and towards the sample. The light is on only during clock spectroscopy and off during all other phases of the experiment. We also measure the magnetic sublevel splitting Δ_{meas} to see if there is any vector light shift or systematic effect from switching on a current.

The room lights are mostly large fixture fluorescent bulbs, with some LED bulbs and incandescent bulbs. For this measurement, we try three different bulbs, a 60W incandescent bulb, a 9W LED, and a 13W fluorescent. We confirm these power draws are within 10% using a outlet power meter.

The results of these three bulb measurements are shown in Fig. 7.7. The error bars are from a white noise fit to the Allan deviation extrapolated to full measurement time. All bulb types are consistent with zero, indicating no measurable shift from ambient visible light at the low 10^{-18} level. The Δ_{meas} is also consistent with zero, again indicating no appreciable effect from this visible light source, plotted in the bottom panel of Fig. 7.7. With the light off and the system enclosed, the light in the system is orders of magnitude lower than the condition tested here, and should cause a shift far below 10^{-19}.

Perhaps a null result in this measurement is rather disappointing, as we can only control a shift if we can measure it. To better quantify the effect of room light on the system, this shift should be directly measured, with high intensity light aimed at the atoms. Further work should also be done to determine the intensity and spectrum of light at the atoms. To assuage all worries about this systematic shift, a better light-tight enclosure may also be installed.

7.8 Other Shifts

Line pulling occurs if population in other magnetic sublevels is off-resonantly driven, distorting the carrier lineshape. With a low intensity 2.43 s clock pulse, even at our modest 0.4 G bias field other transitions are highly suppressed. We bound the possible shift by first calculating the maximum excitation fraction that another transition could contribute at the operational transition frequency. Given a Lorentzian lineshape, the excitation fraction of the other transition under a operational

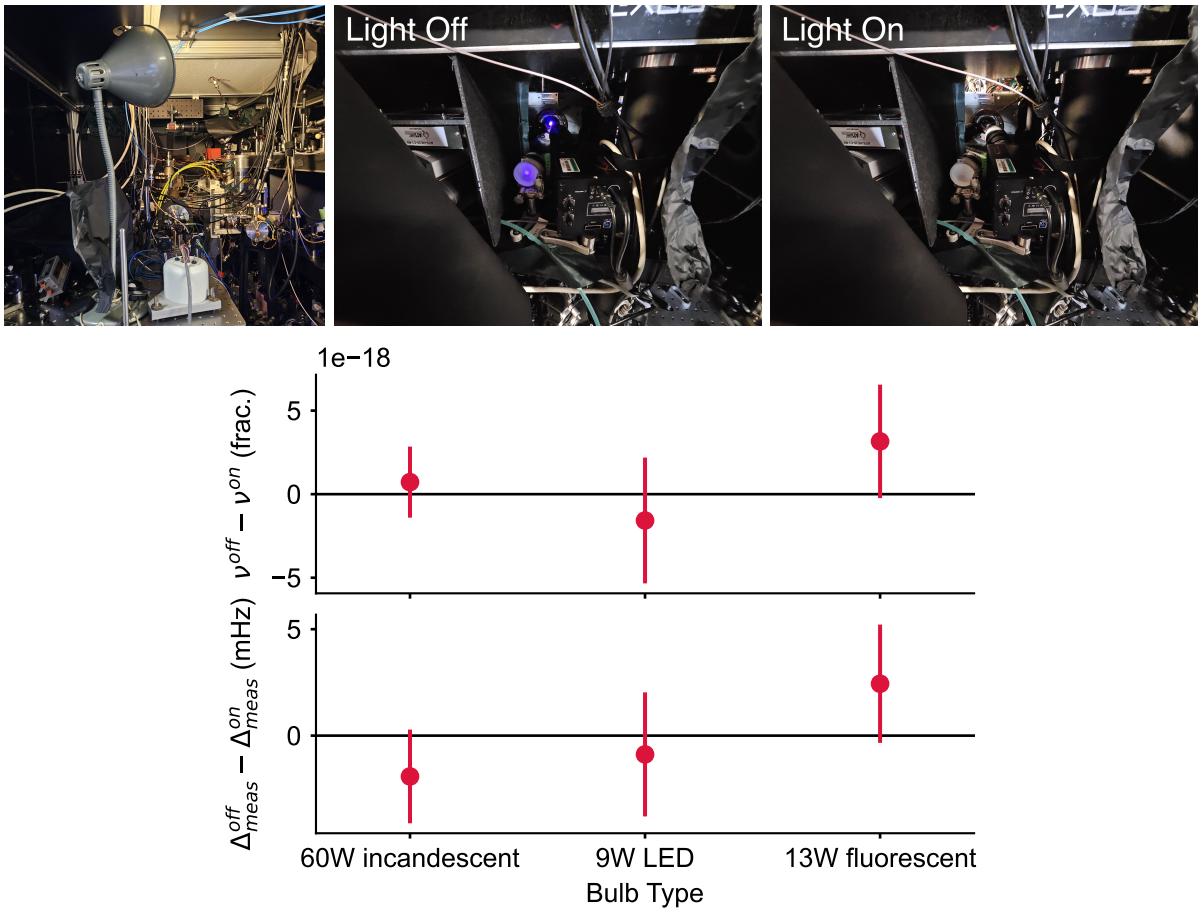

Figure 7.7: Measuring the effect of light in our system. A lamp is placed inside the Sr1 enclosure and switched to measure differential light shifts from different bulbs, shown in the top images. The plot at the bottom shows the results of this test. Top plot: frequency difference between the light off and the light on, $\nu^{\text{off}} - \nu^{\text{on}}$ with 1σ uncertainty shown as error bars. All bulbs are consistent with zero shift. Bottom plot: the frequency difference between the measured splitting of magnetic sublevels, Δ_{meas}. A null result indicates no effect from vector light shifts or switching lamp current.

clock drive is

$$\rho^{ee}_{\text{other}} = \left(\frac{C_{\text{other}}}{C}\right)^2 \frac{\Omega^2}{\sqrt{(2\pi\delta)^2 + \Omega^2}}, \tag{7.9}$$

where C is the Clebsch-Gordon coefficient of the operational transition, C_{other} is the Clebsch-Gordon coefficient of the other transition, Ω is the operational Rabi frequency, and δ is the frequency difference between the operational transition and the other transition. The maximum frequency shift from this effect is simply the effect of this excitation fraction pulling one side of the line. Additionally, other transitions from the same magnetic sublevel can similarly cause line pulling, but

these transitions are far detuned from the operational transition under our standard bias field. The upper bound on the line pulling frequency shift is a sum of all possible transitions weighted by the magnetic sublevel populations. We regularly see lineshape contrast of 96%, likely limited due to Rabi frequency inhomogeneity and laser dephasing. Assuming instead that this contrast reduction is due to other magnetic sublevel populations, we sum the effect of line pulling with 4% of the population in each magnetic sublevel. In this worst case scenario, we estimate a line pulling shift of $< 10^{-21}$.

Similarly, a low intensity Rabi drive significantly reduces the light shift from the clock laser. Using the coefficient measured in Ref. [157], and accounting for the increased intensity due to both light polarizations, we estimate the probe AC stark shift to be -4×10^{-22}, which we treat as the uncertainty.

Thermal transients in the acousto-optic modulator (AOM) due to switching may lead to an uncorrected Doppler shift. As in [21], we path length stabilize the same AOM order that drives the atomic transition. The AOM drive frequency is ramped onto the atomic resonance after these thermal transients have settled, leading to an estimated probe chirp shift $< 10^{-21}$.

7.9 Final Accuracy Budget

A single systematic budget does not entirely capture the uncertainty of a clock at any given operating time. In Tab. 7.9 we illustrate an systematic shift and accuracy budget for a characteristic operational run. For a certain systematic shifts are evaluated for each measurement, while others are evaluated for each lock point of a clock lock. For example, as the vacuum lifetime has remained constant since completing vacuum work in winter 2024, the background gas shift does not change between locks. However the magnetic field is not static over even a few hours, so for each lock point we use the measuring splitting to evaluate the second order Zeeman shift. The shift reported in Tab. 7.9 is an average for this characteristic run.

Our total systematic accuracy is 8.1×10^{19} in fractional frequency units, which corresponds to approximately a 1 second uncertainty over 40 billion years. As of April 2025, this is the most accurate clock ever built, surpassing the NIST Al^+ ion clock evaluated in 2019 [26]. As previously

discussed in Ch. 1 and illustrated in Fig. 1.2, clock accuracy has made remarkable strides in the past 25 years. This evaluation continues a tradition of JILA Sr OLCs pushing the accuracy of optical standards by carefully evaluating all known systematic effects.

The question inevitably arises: how can we push the strontium clock to even lower systematic uncertainties? There seem to be two types of errors: those that can be reduced with more measurement, and those that require a new approach. It is clear that BBR remains a persistent limitation on this platform. While more measurements of the $^3D_1$ lifetime may help reduce the largest source of uncertainty, making accurate oscillator strength measurements is a time-consuming and error-prone task. Our lifetime measurement work lasted over one year and resulted in only a factor of 2 reduction in uncertainty. A different experimental approach, perhaps using pump-probe spectroscopy in a beam, might yield more precise measurements. Cryogenic operation enables far lower systematic uncertainty at the cost of a more complicated apparatus [54, 144]. This would also solve the temperature measurement issue, as lower temperatures have less stringent requirements on thermometry uncertainty, but it does introduce a more complicated thermal environment through necessary line-of-sight to room temperature surfaces. The lattice light shift remains the second largest source of uncertainty, though higher precision measurements may enable further uncertainty reduction. Synchronous operation with other clocks may reduce measurement instabilities by over an order of magnitude for fast determination of frequency shifts at the 10^{-19} level [114]. Operating with lower uncertainty often requires dividing the lineshape even further, with increased sensitivity to small variations in excitation fraction. While this process should not introduce any frequency uncertainty, it makes me *uneasy*. With a better laser, we can trade longer spectroscopy times for improved frequency resolution. This can be accomplished with current laser systems through synchronous spectroscopy. One Sr clock running with a short duty cycle updates the laser frequency with the short time phase information with a duty cycle shorter than the laser coherence time. This generates an atom stabilized synthetic laser that can be used with extended spectroscopy times on a second clock, as demonstrated in Refs. [33, 42]. There is no apparent limit to systematic uncertainty of atomic clocks, with clear strategies to lower uncertainty on all known systematics.

Table 7.2: Sr1 systematic shifts [2]. The second order Zeeman and density shift corrections are mean corrections evaluated for every lock point during a characteristic clock lock.

Shift Name	Shift (10^{-19})	Uncertainty (10^{-19})
BBR	-48417.2	7.3
Lattice Light	0	3.2
Second Order Zeeman	-855.1	1.0
Density	-1.1	0.9
First order Zeeman	0.0	0.7
Background Gas	-4.7	0.5
DC Stark	-1.0	0.1
Tunneling	0.0	<0.1
Minor Shifts	0.0	<0.1
Total Shift	-49279.2	8.1

As new clock technologies emerge, new systematics will need to be considered in order to continue reducing systematic uncertainty.

Chapter 8

Clock Frontiers

Since evaluating the most accurate and stable clock to date, we have now turned to applying this tremendous platform in interesting directions. As Sr is a secondary definition of the SI second, Sr1 has become in-lab frequency reference for other experiments, including referencing the Thorium nuclear transition and YO narrowline transition frequencies [99, 167]. In this chapter, I will discuss some other directions advancing the "frontiers" of precision frequency metrology. Pushing limits of precision spectroscopy necessarily happens on many fronts. In this chapter, we will discuss understanding the sources of decoherence that limit spectroscopy with the goal of extending the atomic coherence time. Under optimal conditions, we measure atomic coherence over 100 s. While there are techniques to perform spectroscopy beyond the atom-light coherence time, a better laser always makes for a better clock. Averaging the frequency of two silicon cavities reduces laser noise, and we show true clock improvement from this approach. At the shallowest lattice depths, we can use the strontium clock as an interferometer, precisely measuring local gravitational acceleration and opening the door to studying all sorts of interesting physics. At very shallow depths, an enduring mystery has emerged: frequency shifts that appear to suggest atoms are moving upwards. Finally, we discuss recent work comparing our system with other optical clocks at NIST, truly testing the performance of this rebuilt Sr1 clock.

8.1 Extending Coherence

Quantum projection noise is the fundamental noise limit in spectroscopy of unentangled atoms [62]. Entangling atoms to reduce this noise source is an approach undertaken in the Ye lab [129] as well as elsewhere [30, 119]. In the mean time, we aim to make quantum projection noise as low as possible by increasing the spectroscopy time and the number of interrogated atoms. As the spectroscopy time increases, the spectroscopy feature gains frequency resolution but loses contrast. The contrast scales with atomic coherence, and exponentially decays due to various effects. In the absence of laser noise, quantum projection noise is minimized at the atomic coherence time. In this section, we discuss work to characterize the atomic coherence in our system.

We first investigated this effect on the new Sr1 machine during the redshift measurement and found a coherence time of 36.5 ± 0.7 s [22]. This measurement was performed one late night at one lattice depth near 10 E_r—a measurement lacking a systematic approach. Since installation of the auxiliary temperature probe chamber and subsequent vacuum work, we have observed far longer vacuum lifetimes, increasing from < 15 s to over 1 minute. With a vacuum lifetime far lower than the measured coherence time, the initial data set may have been compromised by quick decay out of the trap modifying the density at long dark times. With longer vacuum lifetimes and a desire to push the limits of the optical lattice clock, we set out to map out the coherence of our system.

In the simplest approximation, the decoherence rate Γ_C is a sum of a single particle decoherence rate Γ_0 and a density dependent term:

$$\Gamma_C = \Gamma_0 + \Gamma_{\text{dens}} \times N_{\text{loc}}, \tag{8.1}$$

where Γ_{dens} is the density dependent coefficient and N_{loc} is average atoms per site. Γ_0 is a sum of all single particle effects, primarily lattice Raman scattering γ_{lat}, the $^3P_0$ natural lifetime decay rate $1/\tau_{Sr}$, and BBR pumping out of $^3P_0$, γ_{BBR}.

We determine γ_{lat} by holding a $^3P_0$ sample in the lattice for a range of times and then measuring the populations. The excited state has four decay mechanisms: natural spontaneous

Table 8.1: Summary of the decay rates in an optical lattice [71]. We observe the decay of an excited state population over various hold times and lattice depths U. We observe some depth dependence in γ^e_{BG}.

Quantity	Value
$\gamma^e_{BG}(U)$	$1.3(3) \times 10^{-4} U + 2.7(4) \times 10^{-2}$ s^{-1}
γ^g_{BG}	$1.2(4) \times 10^{-2}$ s^{-1}
γ_{lat}	$4.30(7) \times 10^{-4}$ s^{-1} E_r^{-1}
$\tau_{Sr} + \tau_{BBR}$	123(8) s
γ_{ee}	$4(1) \times 10^{-6}$ cm^{-3}s^{-1}K^{-1}

decay, lattice Raman scattering, background loss γ_{BG}, and two particle loss, γ_{ee}. The ground state is filled with atoms from the excited state undergoing spontaneous decay and lattice Raman scattering. Thus, two coupled differential equations govern the evolution of populations in this idealized two level system:

$$\begin{aligned} \dot{N}_e &= -\gamma^e_{BG} N_e - (\gamma_{\text{lat}} \times U) N_e - \frac{1}{\tau_{Sr} + \tau_{BBR}} N_e - \gamma_{ee} \kappa N_e^2 \\ \dot{N}_g &= -\gamma^g_{BG} N_g + (\gamma_{\text{lat}} \times U) N_e + \frac{1}{\tau_{Sr} + \tau_{BBR}} N_e, \end{aligned} \tag{8.2}$$

where $\dot{N}_i$ is the change in population for state i, U is the lattice depth, and κ is a conversion factor that depends on the trapping volume and the atomic temperature. Two particle loss and lattice Raman scattering in the ground state is negligible. We measure decay curves for many lattice depths and fit Eq. 8.2 for each lattice depth. The fitted parameters are listed in Tab. 8.1. We observe lattice depth dependence on γ^e_{BG}, likely due to lattice Raman scattering to different states ($^3P_2$) affecting the population readout.

To measure decoherence, we perform a Ramsey experiment, measuring the contrast decay as a function of dark time as in Refs. [22, 94, 166]. The final $\pi/2$ pulse randomly samples all phases, so this measurement is independent of the laser coherence time. Using in-situ imaging, we can simultaneously resolve contrast decay over different densities. In Fig. 8.1, we plot this experimental approach as well as the coherence results. On the top row we demonstrate extraction of Γ_{dens} and Γ_0

at 10 E_r. On the top left, we prepare a sample with up to 80 atoms per site, and bin into 10 pixel regions. The green and yellow boxes indicate high and low density regions. In the center panel, we plot the Ramsey contrast as a function of dark time for these two regions, indicating faster contrast decay at denser regions. The lines are exponential decay fits, allowing us to extract Γ_C for each region. On the right, we plot the fitted Γ_C for each region as a function of N_{loc}, with error bars originating from the uncertainty in the exponential decay fit. To this data, we fit Eq. 8.1, shown as the black line. We exclude regions where $N_{\mathrm{loc}} < 10$, shown as the red shaded region, where low densities lead to poor signals at long measurement times.

The lower plots in Fig. 8.1 show Γ_{dens} on the left and Γ_0 on the right over a range of lattice depths. We can connect the behavior of Γ_{dens} to the density shift discussion presented in Ch. 4. At deep lattice depths, on-site p-wave interactions dominate, causing decoherence through mode changing collisions, a similar process to that discussed in the dynamical phase transition, Ch. 4.4. As the trap depth is relaxed, the trap volume increases and the radial temperature decreases, reducing this decoherence source. At the shallowest depths, off-site s-wave interactions dominate, leading to a strong increase in Γ_{dens} where $U < 10\ E_r$. Near the magic depth of 10 E_r, Γ_{dens} is minimized. The analysis here is a very simple, first order approximation. Indeed, the actually coherence decay dynamics are more complicated as the sample is held for prolonged dark times. As population decays from the trap, the interactions are modified and decay should not be exponential. We also do not account for two body loss and more complicated interactions that lead to non-linearity. A more comprehensive approach to understanding interactions in this experiment is under review [71].

The single particle decoherence rate Γ_0 is dominated by lattice Raman scattering, and is thus optimized at the shallowest lattice depths. The dashed black line is a sum of lattice Raman scattering determined in Tab. 8.1, as well as the limits from BBR photon pumping and natural lifetime decay. The data seems to be well captured by this simple three process model.

At the shallowest depths, it appears that Γ_0 is below the expected rate, and even below the natural lifetime limit. With the caveat that this data is very sensitive to fitting parameters, the exceedingly long coherence times may be explained with an energy selection process. As atoms scatter

lattice and BBR photons and decay from the excited clock state, they experience a recoil kick of one to a few photons. At the shallowest lattice depths, this additional energy is high enough to remove atoms from the trap. With a fully excited state, we observe the excitation fraction does not decay as atoms that decay to g do not remain in the trap. Thus the single particle decoherence effects are now mapped onto atom loss. This is effectively an "erasure conversion" process, preserving contrast at the expense of atom number and decreasing instability by a factor of $\sqrt{2}$. Other approaches to building an erasure clock have involved reading out only the operational spin state [111]. The possible mechanism here is broadly applicable to any two level system, allowing spectroscopy beyond the natural lifetime, but so far no gain in actual clock performance is observed.

With these coherence measurements, we now seek to find the optimal density and spectroscopy time to reduce QPN. We write the experimental contrast as a function of N_{loc}, Assuming instantaneous $\pi/2$ pulses, the single site QPN limit for Ramsey spectroscopy is

$$\delta_{QPN} = \frac{1}{2\pi T_{dark}} \sqrt{\frac{T_{dark} + T_{dead}}{N_{\mathrm{loc}}}} \frac{1}{C_0 e^{-T_{dark}\Gamma_C(U,N_{\mathrm{loc}})}} \frac{1}{\sqrt{\tau}}, \tag{8.3}$$

where T_{dark} is the dark time, T_{dead} is the dead time and τ is the averaging time. With an initial Ramsey fringe contrast of 1, the optimal dark time becomes

$$\mathrm{opt}\left(T_{dark}\right) = \frac{1}{4}\left(\Gamma_C^{-1} - 2T_{dead} + \sqrt{\Gamma_C^{-2} + 12T_{dead}\Gamma_C^{-1} + 4T_{dead}^2}\right). \tag{8.4}$$

Using the experimentally measured Γ_0 and Γ_{dens}, we can determine the optimal N_{loc} and T_{dark} for a given T_{dead} and U. The results of this calculation are plotted in Fig. 8.2 with $T_{dead} = 1$ s. On the left of Fig. 8.2, we plot the optimal QPN as a function of N_{loc} over the range of experimentally measured lattice depths. For $N_{\mathrm{loc}} > 8$, the optimal lattice depth is 12 E_r, near the magic depth for Rabi spectroscopy as Γ_{dens} is minimized. On the right of Fig. 8.2, we plot T_{dark}, N_{loc}, and QPN for the optimal condition at each lattice depth. Remarkably, the best stabilities can be $< 10^{-17}\ 1/\sqrt{\tau/s}$ for a single lattice site. Optimal spectroscopy times are generally < 10 s, 7 s for the 12 E_r case,

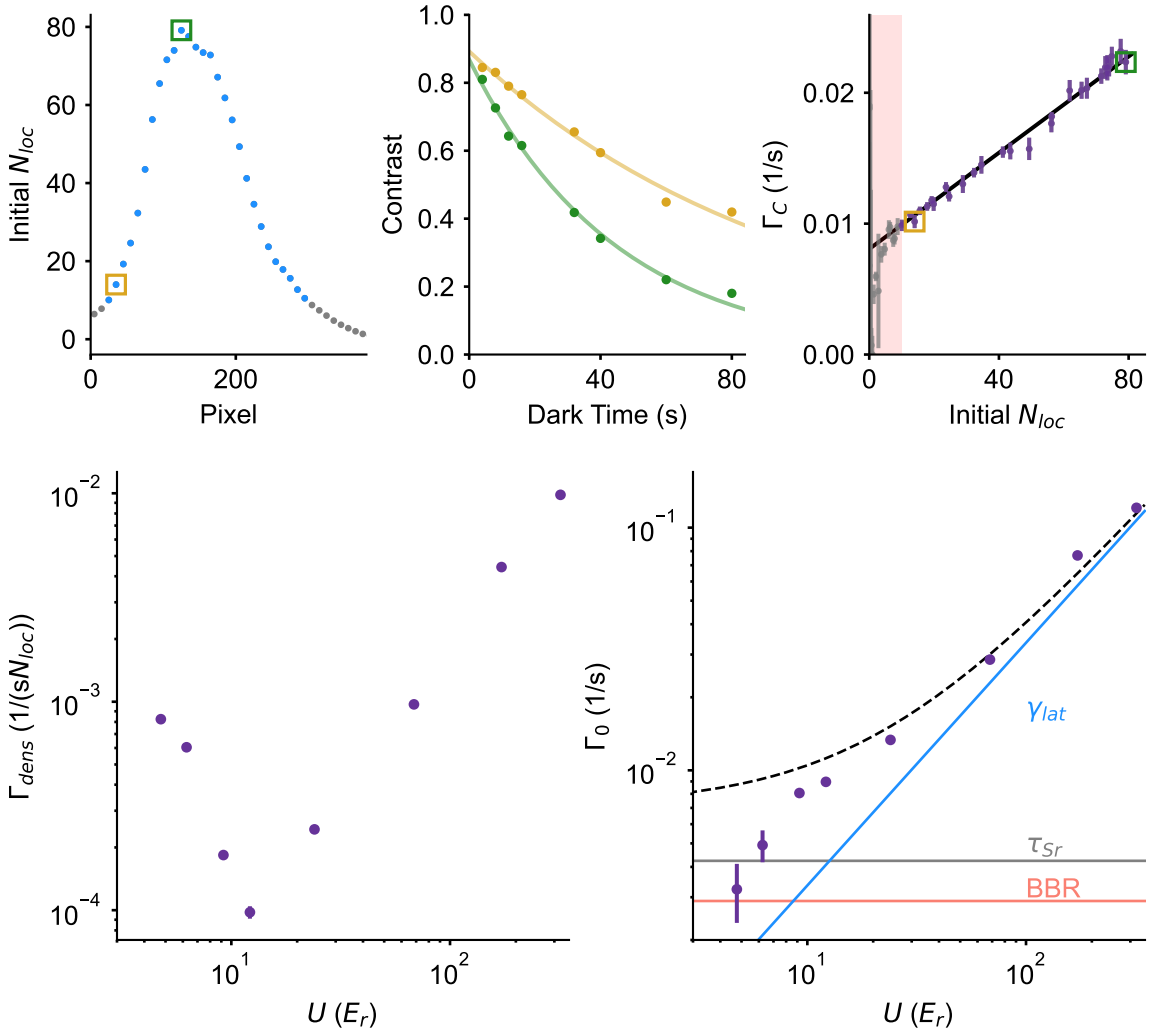

Figure 8.1: Measuring the atomic coherence using in-situ imaging. Top: we prepare a high density sample with peak on-site density $N_{loc} \approx 80$, shown on left binning 10 pixels at 9 E_r. We perform Ramsey sequence with a variable dark time, randomly sampling the final phase. This leads to a decay fringe contrast, shown in the center panel for a region near the edge (gold) and the center (green) of the sample. For each region the experimentally determine contrast, shown as points, we fit an exponential decay, plotted as the solid line. On the right, we plot the exponential contrast decay rate Γ_C as a function of initial on-site density, N_{loc}. To this data, we fit a linear function, Eq. 8.1. We exclude pixels where initially $N_{loc} < 10$, shown as the red region. Bottom: the extracted multiparticle dephasing rate Γ_{dens} (left) and single particle dephasing rate Γ_0 (right). Γ_{dens} has a p-wave dominated regime > 10 E_r and an s-wave regime < 10 E_r. We can explain the Γ_0 trend based mostly on lattice photon scatter γ_{lat}. Decay due to the natural lifetime τ_{Sr} and BBR pumping also contribute to decoherence.

which should be achievable once next generation silicon cavities are operational. Achieving this

stability requires loading about 700 atoms onto a single site, less than a factor of three higher that the peak densities we observed in Ch. 4.4. It remains to be seen if the simple mean field model for the frequency shift is workable at such densities. With 10^4 lattice sites of 700 atoms, the QPN limit is $< 10^{-19}\ 1/\sqrt{\tau/s}$. Loading a uniform sample, this would be a 4 mm sample of 7 million atoms. While all these parameters are not feasible at the moment on Sr1, a few small advancements along all fronts may allow operation at this level. This would represent about a factor of 20 reduction in instability from our previously published lowest synchronous instability, Ref. [22], allowing nearly a one part in ten measurement of the gravitational redshift in a single experimental cycle.

It is clear that interactions significantly limit coherence times in the 1D lattice, so a 3D lattice might allow for even longer spectroscopy times. Unfortunately, three confining beams generate stronger lattice Raman scattering, adversely affecting single particle coherence. Blue detuned lattices solve this issue by trapping atoms at the nodes of the standing wave, and may be a key technology for next generation clocks [153]. Without significantly modifying our system, how can we reduce decoherence from interactions? Ideally we want to operate at the shallowest depths where lattice Raman scattering and p-wave dephasing is minimized, but we need to remove off-site s-wave interactions. As in Ch. 3.7, we can use a standing wave of incommensurate spacing to select certain lattice sites. With a standing wave of wavelength $\lambda = 1626$ nm overlapped with the lattice, we create a clock shift for every other lattice site, allowing us to remove half the atoms with a clock drive. This eliminates nearest-neighbor interactions, so Γ_{dens} will continue to decrease with lower U until next-nearest-neighbor interactions are significant at far lower U. Driving Wannier-Stark transitions to shuffle atoms onto every other site, we should be able to operate with the same number of atoms. In June 2025, we demonstrated this technique and are excitedly exploring the improvements to clock spectroscopy through site selection.

8.2 Laser Averaging

We are fortunate our silicon laser (Si3) is one of the best in the world, allowing us to perform seconds long optical spectroscopy. Much of the work presented in this thesis was possible only

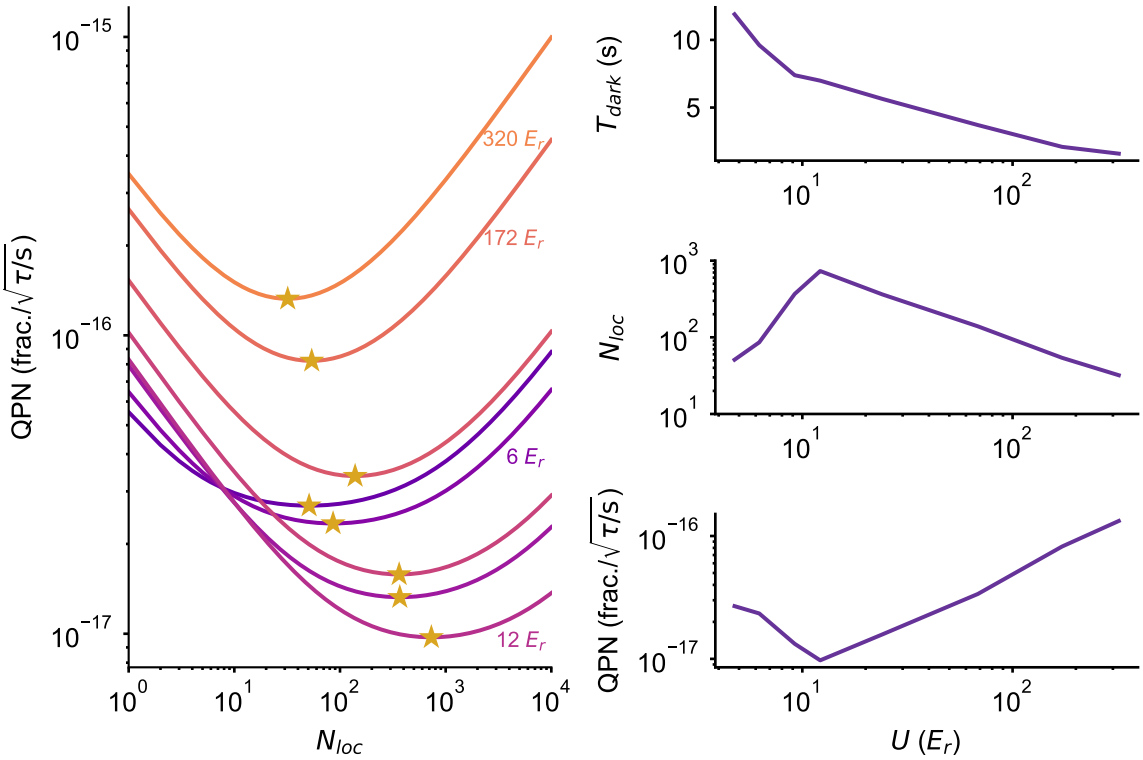

Figure 8.2: Calculated optimal stability using measured coherence parameters. Left: for each on-site density N_{loc} and each measured lattice depth U, we calculate the optimal QPN stability, assuming a dead time of 1 s. The stars indicate the minimum instability point. Right: The optimal dark time T_{dark} (top), N_{loc} (center), and QPN instability (bottom) at each lattice depth.

because we had access to this wonderful oscillator. Nevertheless, a better laser would allow for longer spectroscopy times and a lower Dick effect, making our job even easier. The Stable Lasers team, currently staffed by Dahyeon Lee, Ben Lewis, and Zoey Hu, has been working hard on two new systems, Si6 and Si7. Si7 is currently under construction with the goal of being a lower noise Si3 replacement. Si6 is a 6 cm cavity with crystalline coatings operating at 16 K in a closed cycle cryostat. A previous iteration of this system is described in Ref. [68]. After much diligent work and new crystalline coatings, this small cavity is approaching the stability level of Si3, especially at times < 100 s [77].

With two cavities of similar noise in the lab, the question becomes how to best utilize these oscillators. The idea is quite simple: the average of two identical oscillators containing uncorrelated

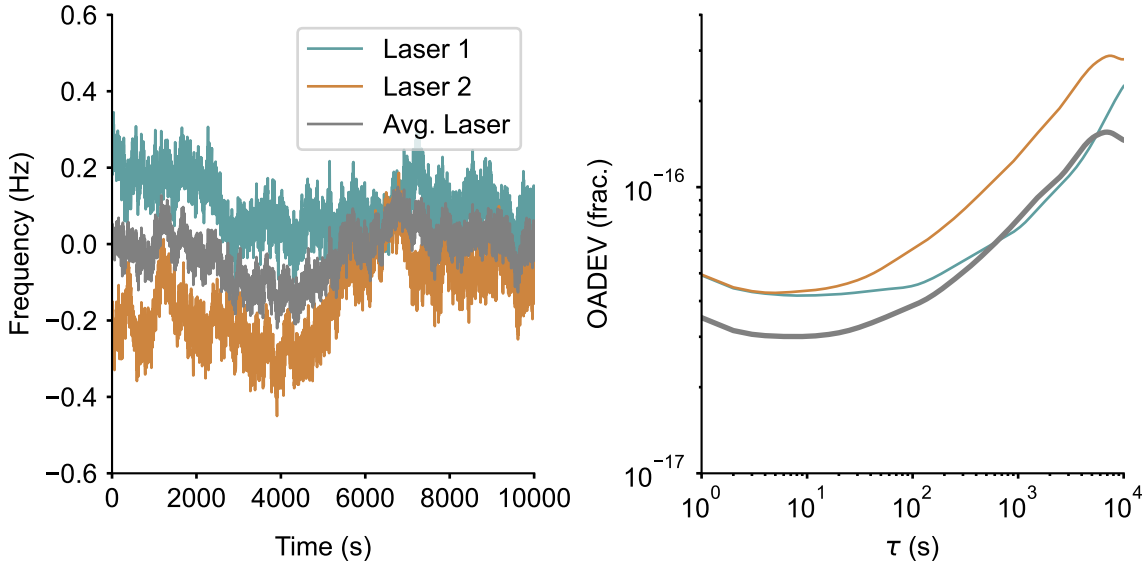

Figure 8.3: Averaging two oscillators with similar noise results in a $1/\sqrt{2}$ reduction in noise. Consider two lasers with flicker frequency noise and random walk frequency noise at longer times, simulated and plotted on the left. Averaging these two noises, shown in gray, results in spectrum that immediately seems to have lower peak-to-peak noise. On the right, we plot an overlapping Allan deviation (OADEV) of these frequency series. At short times where the two lasers have similar noise performance, averaging results in a $\sqrt{2}$ improvement in instability. At longer times where one laser is worse than the other, the average instability does not exceed the better laser. This scenario is reflective of the two silicon lasers in our lab, Si3 and Si6.

noise will reduce the overall noise by $1/\sqrt{2}$. This principle is illustrated in Fig. 8.3. On the left, we plot a time series of frequencies of two simulated oscillators, roughly corresponding to Si3 in teal and Si6 in brown. These oscillators have noise that is dominated by frequency flicker at short times and random walk frequency noise at long times, as shown in the overlapping Allan deviations on the right. The frequency average is shown in gray on both plots. In the time series, the average has a smaller spread of frequencies at short times. In the overlapping Allan deviation, the frequency average has lower noise than both oscillators with $\tau < 500$ s. At long times, the Allan deviation is lower than laser 2 but slightly higher than laser 1. On timescales where the noise is similar, the average leads to a clear improvement in performance.

We have discussed laser averaging for a number of years in the Ye group, but the first experimental demonstration of this approach was implemented with noisier systems in Ref. [83].

This work demonstrated reduction of frequency fluctuations from 40 Hz to 28 Hz. By averaging two silicon cavities, our hope is to truly build a better clock. To accomplish this, a beat between Si3 and Si6 is formed containing the frequency information, $\Delta f = f_{\mathrm{Si6}} - f_{\mathrm{Si3}}$. Dividing this RF beat by a factor of 2 and then adding it to the Si3 light, via an AOM or another actuator, gives a frequency average: $f_{\mathrm{avg}} = f_{\mathrm{Si3}} + \Delta f/2 = \frac{1}{2}\left(f_{\mathrm{Si6}} + f_{\mathrm{Si3}}\right)$. Typically, the frequency comb repetition rate is locked via a comb tooth beat against Si3 with an offset frequency 35 MHz. We swap out this constant RF offset with one that contains the $\Delta f/2$ frequency plus some static offset, so the frequency comb, and thus our clock laser, is stabilized to a frequency average of the two cavities. Using the undivided beat frequency, we can also stabilize to Si6 alone. We implement RF switching for alternating between Si3, Si6, and a frequency average of the two.

In Fig. 8.4 we present the results of this approach. Using Sr1, we perform an interleaved comparison between Si3, Si6, and the laser average, shown as a frequency time series on the left of Fig. 8.4. While the average frequency clearly has more random walk noise, the short time noise appears smaller. This is obvious in the modified Allan deviation, plotted on the right of Fig. 8.4. In order to perform this 3 laser measurement, the dead time for each laser is much longer and the Dick effect is greatly increased. This mechanism is responsible for the degrade performance of all lasers when the averaging time $\tau < 30$ s, where we expect Si3 and Si6 to both operate near a flicker floor of 4×10^{-17}. Nevertheless, the averaged laser demonstrates the expected noise reduction. Where $\tau < 100$ s, the averaged laser has roughly $1/\sqrt{2}$ less noise than Si3 alone. At longer times, Si3 is superior and is near the historical thermal noise limited performance [114]. Since the atomic servo has a corner < 100 s, this improvement directly reduces the frequency noise of the combined clock system by a factor of $\sqrt{2}$, and reduces averaging time by half. For Dick effect limited interleaved comparisons, we see our instability reduce from 2×10^{-16} at 1 s for Si3 to 1.5×10^{-16} at 1 s for the averaged laser. If we had this system during the light shift evaluation, we might have saved half our measurement time. In short, the best laser in the world gets even better!

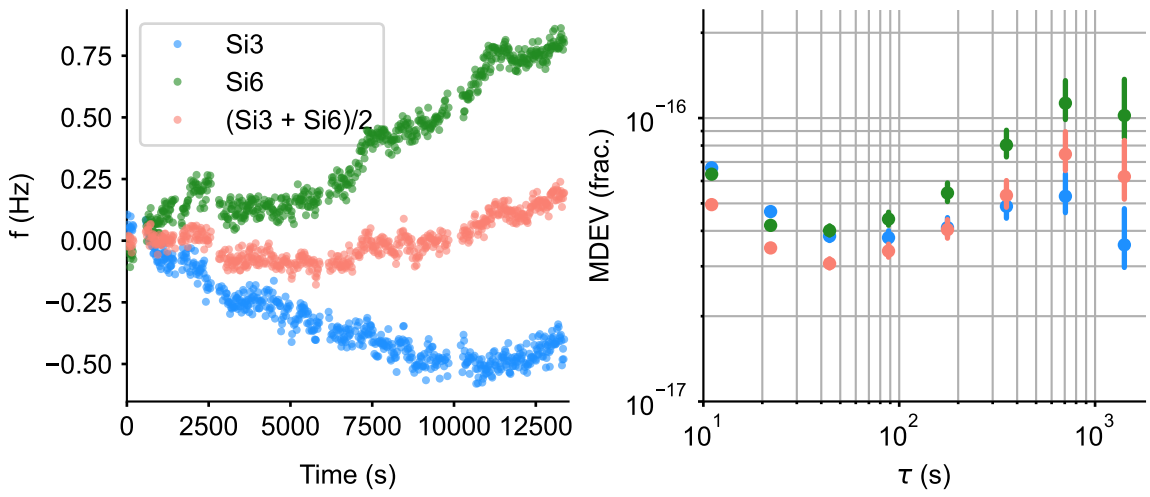

Figure 8.4: We interleave three laser conditions, using only Si3, using only Si6, and using a frequency average of Si3 and Si6. A frequency record of these two conditions is plotted on the left. As in the calculation, short time noise amplitude is reduce for the average laser compared to Si3 alone. Unfortunately the random walk noise of Si6 contributes to more instability at longer times. This becomes clear in the modified Allan deviation, plotted on the right. This Allan deviation is calculated after linear dedrifting of the frequency record. For times < 100 s we see clear improvement using an averaged laser, while at long time Si3 alone surpasses the laser average.

8.3 An Atom Interferometer

Already discussed extensively in Ch. 3, the Wannier-Stark ladder creates a set of transitions between lattice sites spaced by the potential energy difference. The energy of a transition of i lattice sites,

$$\mathrm{WS}{+}i = i \times \frac{Mg\lambda_L}{2}\cos(\theta), \tag{8.5}$$

where M is the mass of the atom, g is the gravitational acceleration, λ_L is the lattice wavelength, and θ is the angle between the lattice and the direction of gravity.

Due to the purity of these motional states, it is natural to regard transitions between lattice sites as a new kind of atomic interferometer. Cold atom interferometers use the spatial displacement of the atomic sample to measure gravity effects to excellent effect [65]. A cold cloud in split into a superposition of two atom packets which undergo free fall at different heights. The resultant phase difference is due to the gravitational acceleration, allowing for 10^{-9} precision measurements of g

in just a few seconds [121]. When atoms are placed into a superposition of electronic states on a WS+i transition, the internal state undergoes phase evolution due to the spatial displacement of the superposed state. Recent advancements in atom interferometers follow a similar path, using lattice supported atomic ensembles to overcome free fall constraints and probe for many seconds [158]. Using strontium, we can perform measurements that measure both the low energy gravitational effects as well as the higher energy clock transition, joint interferometers for the internal (spin) and external (motional) degrees of freedom.

8.3.1 WS Coherence

Towards using WS transitions for precision spectroscopy, we determine the coherence of these transitions. With the same approach as in the Ch. 8.1, we perform an uncontrolled Ramsey experiment and observe the contrast decay as a function of dark time. The extracted density dependent decoherence rate Γ_{dens} and single particle decoherence rate Γ_0 are presented in Fig. 8.5. To measure across all operational lattice depths, we perform the $\pi/2$ pulses at shallow lattice depths, where the WS+n transitions have high Rabi frequencies, and then increase and hold the lattice depth during the dark time.

As in the dynamical phase transition, Ch. 4.4, off-site transitions generate effectively on-site interactions, leading to far stronger density dependent decoherence. Γ_{dens} is higher across all U, nearly an order of magnitude higher than in the carrier transition case. As the depth increases, the density increases leading to a larger Γ_{dens}. All dominant interactions are on-site, so there is no Γ_{dens} minimum. Using alternating sites, we can avoid the large density shifts and go to even shallower lattice depths, which will further suppress Raman scattering. This technique, already under study in the lab, may extend coherence beyond 100s on the WS transitions.

Γ_0 is also larger across all depths, inconsistent with the lattice Raman scattering dominated decoherence observed on the carrier transition. One additional source of decoherence may be due to lattice Rayleigh scattering. In a magic wavelength lattice, Rayleigh scattering does not contribute to decoherence as the scattering rate is identical for both states [59]. However, in a Wannier-Stark

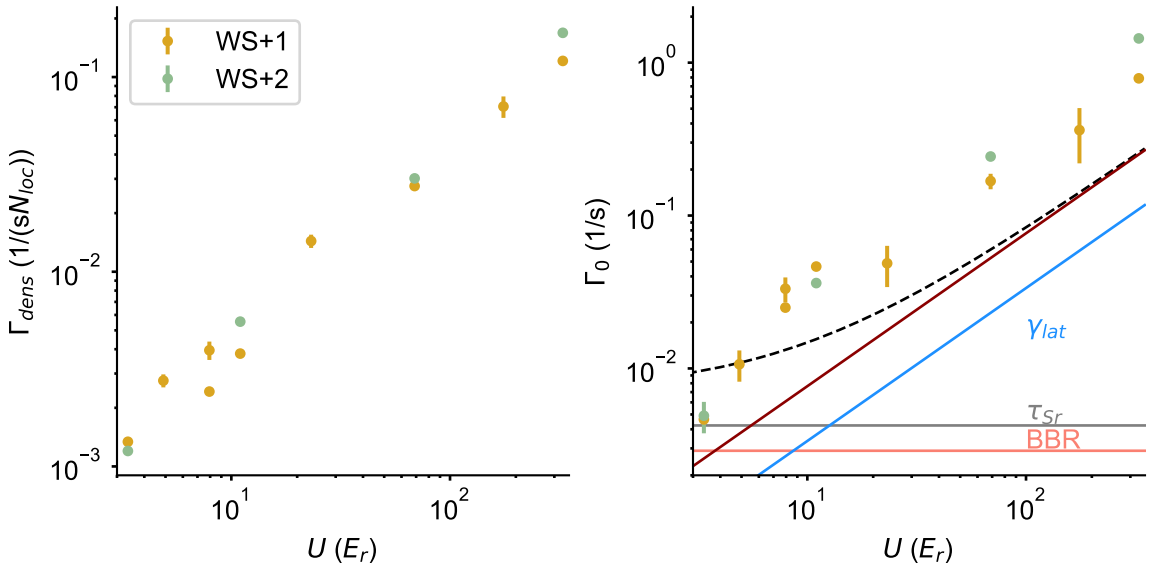

Figure 8.5: Coherence of offsite Wannier-Stark transitions. We follow the same approach as in Fig. 8.1, measuring the decoherence rate as a function of density over a range of lattice depths for the WS+1 and WS+2 transitions. The density dependent decoherence rate Γ_{dens} and single particle decoherence rate Γ_0 are plotted on the left and right respectively. The red line indicates the contribution to decoherence from Rayleigh scattering. The dashed line is a sum of all expected effects on Γ_0.

transition, the excited state occupies a different lattice site than the ground state, so Rayleigh scattered photons from each state can be distinguished leading to decoherence. This effect is plotted as the red line on the right of Fig. 8.5. Rayleigh scattering does not fully capture Γ_0—perhaps the much stronger density dependence is also corrupting the fit. There is also no clear decoherence difference between WS+1 and WS+2 transitions. With $N_{\text{loc}} \approx 10$, we can still achieve coherence times > 10 s, so this remains a viable platform for atom interferometry.

8.3.2 A Gravimeter

A natural application of off-site spectroscopy is gravimetry. As discussed in Ch. 2, optical clocks are sensitive to the gravitational redshift, and with proper comparisons can put bounds on relativistic effects [51, 140]. With the mass M, lattice wavelength λ_L, and angle with respect to gravity θ fixed, Wannier-Stark spectroscopy allows us to measure local gravitational acceleration.

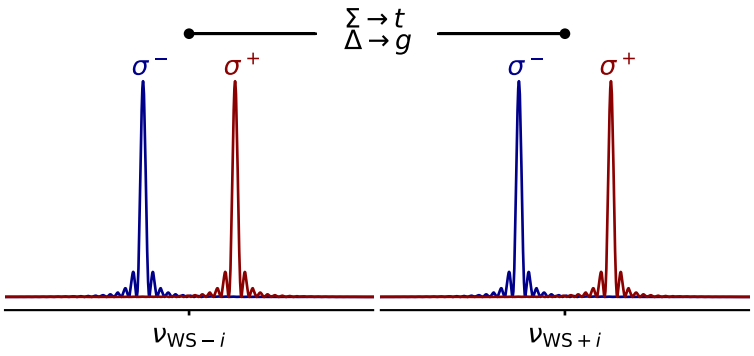

Figure 8.6: A schematic illustrating how we can use clock measurements to determine local g. Consider four independent atomic servos, locked to the $m_F = -5/2$ σ^+ and $m_F = +5/2$ σ^- spin internal transitions for WS$\pm i$ site-changing transitions. The magnetic field is encoded in the difference frequency of the $\sigma^\pm$ transitions. The average, $\sum$, of all four transition frequencies it the natural strontium frequency and can be uses to measure time t. The difference Δ between the WS$+i$ and WS$-i$ transitions encodes the local gravitational acceleration, g. Thus the clock becomes a simultaneous classical and relativistic gravimeter!

This was first experimentally implemented in a rubidium system [10, 120]. Using an optical lattice clock, we can measure gravity as well as operate as an accurate clock through a simple measurement scheme illustrated in Fig. 8.6. We drive both spin state ($\sigma^\pm$) WS$+i$ and WS$-i$ transitions. As in the carrier clock lock, the average of the two magnetic sublevel transitions rejects first order Zeeman shifts, and gives us the bare WS$\pm i$ transition frequency. The average of the two WS$\pm i$ transitions is identical to the carrier transition frequency ν_{Sr}, so we can operate as a standard OLC with proper systematic corrections. The difference of the WS$\pm i$ transitions allows us to determine g using Eq. 8.5. For the most accurate determination of ν_{Sr}, care must be taken to correct for the density shift, now a much stronger on-site s-wave shift. Again, preparing a sample with alternating lattice site filling will significantly reduce the density shift.

In Fig. 8.7, we present the results of a half day gravitational measurement implementing this scheme. The top panel shows the results using the average frequency of the two WS transitions. We recover frequency performance that is consistent with the Si3 laser. The lower plots indicate the results of using the WS difference channel to extract g. On the bottom left of Fig. 8.7, we plot the time record in MJD of the measured g_{meas} less the surveyed value g_{lab} in μGal (see Ref. [152]). We

do not have an accurate measurement of the lattice tilt with respect to gravity θ, so we set $\theta = 87.33°$ such that the average $\bar{g}_{meas} = g_{lab}$. To accurately measure g, we might borrow a technique from the corner cube gravimeters. By varying the tilt of the lattice, we can trace out θ and use the peak value as the true g. The purple line is a running average of the measurements within a 1 hour window. With averaging times $\tau < 10^3$ s, the fractional stability is Dick effect limited at $13 \times 10^{-6}/\sqrt{\tau/\mathrm{s}}$, as plotted on the lower right of Fig. 8.7. At longer times we notice fluctuations in g_{meas} the the 10^{-7} fractional level, apparent in both the time series and the Allan deviation. This fluctuation is a few times larger than the expected fluctuation due to tidal forces, unfortunately obscuring this effect. We do not have a complete understanding of this fluctuation, but it may be due to small chamber tilt over the course of a day. Tilt variation as small as 0.005° would cause such an effect. More work will be done to better stabilize the system or measure and correct for this effect. In sum, using Wannier-Stark spectroscopy we simultaneously make measurements of local g as well as the red shift sensitive optical transition, combining classical and relativistic geodesy on a single platform [45], perhaps allowing further tests of relativity [37, 130].

The WS interferometer is also a powerful tool for resolving local forces. The Dos Santos group at SYRTE uses a similar WS interferometer to measure quectonewton level Casimir-Polder forces [7]. On our system, we make use of in-situ imaging to resolve gradients in frequency and g. As before, these are synchronous measurements, so g gradient measurements should be QPN limited. The expected g gradient measured in the JILA gravity survey [152] found a -2.55 μGal/cm gradient in S1B60, which corresponds to a fractional g gradient of -2.6×10^{-10} g/mm. In the same test lock presented in Fig. 8.7, we measure synchronous g gradient instabilites of 2.8×10^{-6} g/mm at 1 s. Resolving this remarkably small effect remains out of reach, but since this measurement is only QPN limited, reasonable advances in experimental conditions may allow for such a measurement. Increasing atom number, spectroscopy time, and number of sites may allow for combined measurements of both gravity gradients as well as the gravitational redshift.

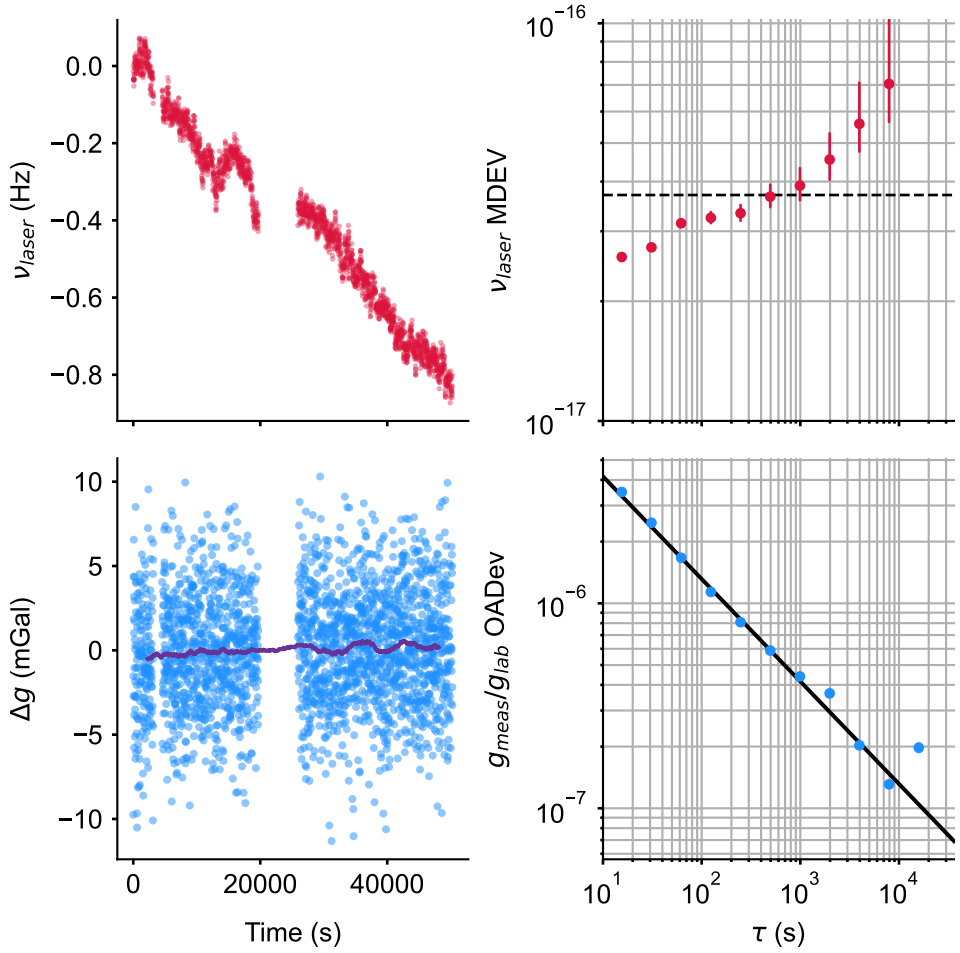

Figure 8.7: Measuring gravity and time in our 1D Sr OLC. The top row illustrates measurements of the clock laser using the WS lock average frequency. Top left: the frequency record of the Si3 laser as a function of time indicates the expected long term drift. Top right: a modified Allan deviation (MDEV) of the frequency record indicates performance consistent with the Si3 thermal noise floor, shown as a dashed black line. Bottom left: the measured gravity g_{meas} using the approach presented in Fig. 8.6 less the professional measured g_{lab} [152]. We adjust the lattice tilt with respect to gravity such that the average difference is 0. A running average of the blue data with 1 hour window is shown as a purple line. Bottom right: an overlapping Allan deviation (OADEV) of g_{meas}. A stability of $13 \times 10^{-6}/\sqrt{\tau/\mathrm{s}}$ plotted in black, captures the measurement stability $< 10^4$ s. Long term variations, likely due to system tilt, may prohibit our system from reaching ultimate stability as a gravimeter.

8.3.3 Proposals

In addition to measuring g, Wannier-Stark spectroscopy is a powerful tool to measure effects beyond the clock transition. For example, if θ, g, and M are well known, we can measure λ_L at

around 10^{-7}, so this spectroscopy can act as a very expensive wavemeter! Another interpretation of the Wannier-Stark ladder is as a precise, single-atom [7]. Swapping in a different isotope of Sr, we can use this spectroscopy to make measurements of mass ratios. Alternating between two isotopes in an interleaved fashion should reject most common systematics to first order, such as lattice tilt.

We may even use this to probe the mass defect and study the effect of relativity on an optical clock. The clock photon carries energy $h\nu_{Sr}$, so the excited state mass contains an additional photon of energy:

$$M_e = M + h\nu_{Sr}/c^2, \tag{8.6}$$

where M is the rest mass of the ground state Sr atom. As Eq. 8.5 depends on the mass, the Wannier-Stark ladder is modified depending on the internal state of the atom. With $\theta = 0$, the difference in frequency between the ground state and excited state site splitting $w_e - w_g = \left(h\nu_{Sr}/c^2\right)\left(g\lambda_L/(2h)\right) = 19$ nHz. This is equivalent to the single site gravitational redshift on the clock transition, $r = \nu_{Sr} g\lambda_L/2c^2$. We can write an WS+1 transition as a carrier transition plus an excited state site change, $\nu_{\mathrm{WS+1}} = \nu_{Sr} + w_e$, or a ground state site change plus a carrier transition with a single site gravitational redshift $\nu_{\mathrm{WS+1}} = w_g + \nu_{Sr} + r$. This energy landscape is illustrated on the left of Fig. 8.8.

The next question is, of course, can we measure this remarkably small effect? The stability required to make this measurement in a reasonable time is daunting. An ideal Ramsey sequence with $T_{dark} = 1$ s, 2 s cycle time, and 10^6 atoms has a QPN limited instability of 3.8 $\mu\mathrm{Hz}/\sqrt{\tau/\mathrm{hr}}$, so measuring 19 nHz is unreasonable. Extending T_{dark} to 10 s with the same atom number and dead time reduces averaging time by over an order; measuring the effect over 20 lattice sites quadratically reduces averaging time by this factor, so we can measure this effect in less than 10 hours. Perhaps this experiment is feasible!

One approach is to measure the gravitational redshift between lattice sites, perhaps measuring the difference between WS+i transitions with an optical photon. Unfortunately, the effect will be broadened by many orders over the sample, as in the in-situ redshift measurement [22]. Instead, we

desire to measure w_g and w_e without directly measuring the clock transition. Direct interferometry of a site change, perhaps using a Raman process, will allow the atoms to remain in either the ground or excited state manifold and can be extended to many lattice sites. The difference between the transition frequency in either internal state corresponds to the mass defect. An added feature of this approach is the experiment signal being encoded in a microwave frequency, not an optical frequency. If we can purely transfer the Si3 performance to the kHz range, we can make interleaved measurements of the WS spacing where the Dick effect is below QPN. As described in Ref. [10], we need state-labeling to determine whether or not the atom has transitioned between lattice sites. We might consider using the magnetic sublevels as labels, however with 10 nuclear spins in Sr, this becomes a far more complicated process. An atom like ^{171}Yb with $I = 1/2$ is a possible candidate for this experimental scheme. Other atoms that have metastable states with hyperfine structure are perhaps ideal for this endeavor.

8.4 Shallow Lattice Physics

During the first lattice light shift evaluation, we observed inexplicable shifts at shallow depths. During this campaign, we made measurements at one lattice depth shallower than the 10 E_r reference at all lattice frequencies. While each point at 7 E_r had fit residuals generally consistent with zero, the average of the residuals was $\sim 2 \times 10^{-18}$ above zero. No other light shift points had this behavior, so this observation warranted further investigation. Additionally, we observed significant positive residuals on the (n_Z) modulation data when $U < 30\ E_r$. Measuring more shallow lattice depths, we saw consistent results indicating an increase in transition frequency at lower lattice depths, and up to a 5×10^{-17} shift at 3 E_r. These measurement results are presented on the left of Fig. 8.9.

This frequency shift is rather puzzling. We observe no dependence on lattice frequency, spectroscopy time, density shift, initial clock state, or magnetic field. We observe a similar effect when measuring the transition with a different clock path. Our standard clock path originates at the bottom chamber and travels upwards. We have another clock path that originates at the top of the chamber and propagates down. Measuring the frequency difference between these paths,

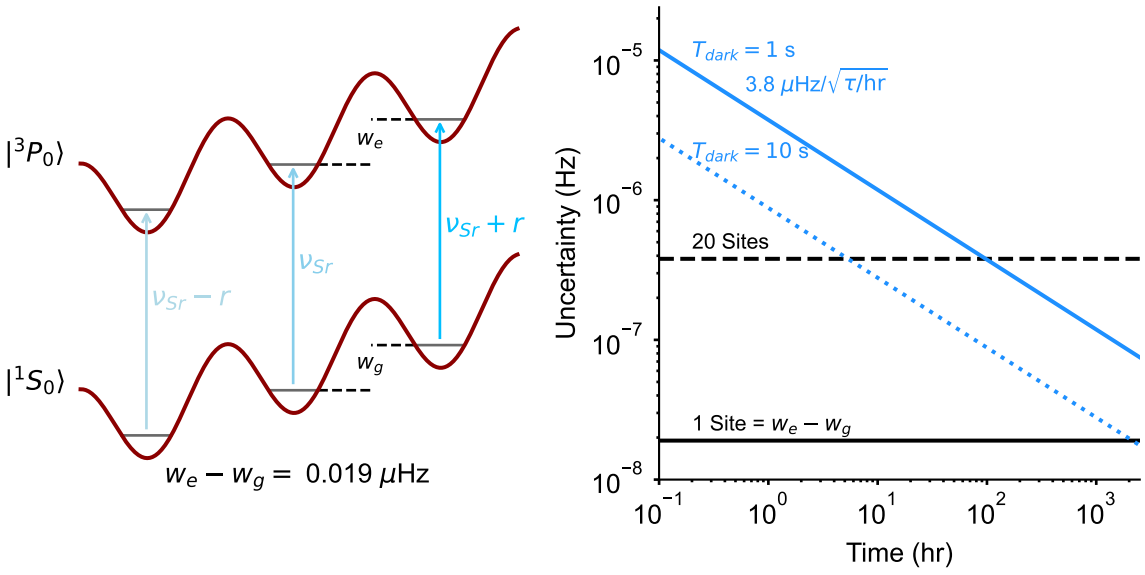

Figure 8.8: Proposal for measuring the mass defect using Wannier-Stark state spectroscopy. The lattice creates a Wannier-Stark ladder in both the ground and excited states, shown on the left. The mass defect means that the energy spacing between ground and excited states, w_g and w_e respectively, differs by 19 nHz. This is equivalent to the single site gravitational redshift, r. To measure such an effect, we need exceptional stability. On the right we plot the QPN frequency stability of a 1 s ramsey sequency with 10^6 atoms in solid blue, indicating that it would take $> 10^4$ hours to measure this effect, shown as a solid black line. With an optimistic $T_{dark} = 10$ s plotted as a dashed blue line, measuring the effect over 20 lattice sites, plotted as a dashed black line, would require less than 10 hours.

$\nu_{bottom} - \nu_{top}$, results in a frequency shift twice what we observe in the light shift residuals for the $n_Z = 0$ case, as presented on the right of Fig. 8.9.

We also investigate this shift for the $n_Z = 1$ state, observing generally noisier data. We believe one of the primary culprits for this noise is the top clock path. Instead of phase noise stabilizing the path that directly drives the atoms as in the bottom path, the top path stabilizes the 0th order, not the 1st order light that shines on the atoms. The large differential path length between these leads to greater instability and perhaps even frequency offsets from drift during the duty cycle. Nevertheless, the common features between the light shift and path comparison results indicates a shared systematic.

The origin of this shift remains a mystery. A naive explanation is a Doppler shift—atoms

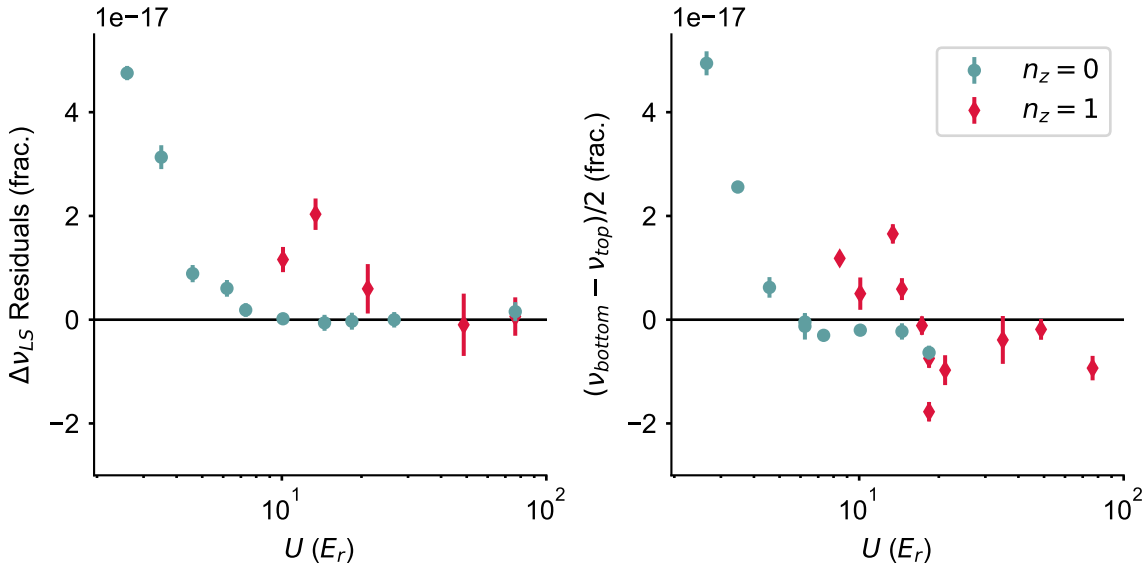

Figure 8.9: Shallow lattice light shift $\Delta\nu_{LS}$ residuals (left) and path comparison results (right). The residuals are an average of all lattice frequencies at each depth. Below 7 E_r (30 E_r) the light shift model does not capture the behavior of the $n_Z = 0$ ($n_Z = 1$) state, apparent in the fit residuals. The behavior is echoed in the frequency difference between the bottom clock path and the top clock path for both states.

moving upwards during spectroscopy would appear blue shifted with the bottom path and red shifted with the top path. A velocity of 3 nm/s is a 10^{-17} frequency shift, so the shallowest points have velocities $\sim$ 20 nm/s. If this is indeed the mechanism that creates this frequency shift, the generator of this motion is unclear. Long spectroscopy times do not lead to a different frequency shift, so the velocity must be static and not due to some mechanical transient. Wannier-Stark states are metastable, that is under long enough times atoms should tunnel to the continuum, falling out of the trap under gravity. This tunneling rate is enhanced at shallow depths, leading to shorter trapped lifetimes, although we have been unable to demonstrate this effect experimentally. Further investigation is necessary, include more precise spectroscopy especially on $n_Z > 0$ states. For the lattice light shift measurement, we decide to fit only points with $U > 8$ E_r. In the Ref. [70] supplement, we investigate the effect on the fitting results as a function of this depth cut off, and we believe it does not affect the lattice light shift results. At our standard operational depth, this effect should be highly suppressed, and we do not believe it contributes to an appreciable frequency shift

at our accuracy level.

8.5 Comparison

Clock comparisons are a critical step towards redefinition of the SI second [40]. While the exact atomic transition(s) have not been specified by the BIPM, regular comparisons between different atomic species are necessary to establish the repeatability of such high precision measurements and help identify the best candidates for redefinition [126]. Clock comparisons take two forms: same-species and intra-species. At NIST and JILA, multiple Al^+, Yb, and Sr clocks allow for same species comparison as well as intra-species comparisons between these labs.

In Boulder, the Boulder Research and Administrative Network (BRAN) has constructed miles of optical fiber throughout the city [125]. This network allows us to share light between JILA and NIST for optical clock comparison, that with proper care, might even be QPN limited [164]. In 2006 and 2008, the previous strontium system was compared against a NIST Cs and Ca clocks [86, 89]. In 2019, optical ratios using the BRAN network were measured with the NIST Al^+ and Yb clocks, known as the Boulder Atomic Clock Optical Network (BACON) [23]. This measurement campaign resulted in some of the most accurate clock ratios ever measured. Since this work, both the JILA Sr1 clock and the NIST Al^+ clock were completely rebuilt, with the Al^+ systematic evaluation published in July 2025 [93].

The goal of this new comparison is to remeasure ratios with better accuracy and precision. To reduce the laser noise, both NIST clocks make use of the Si3 stability. We send Si3 light to NIST using a fiber-noise-cancelled BRAN link, Nick Nardelli locks a Er/Yb:glass comb to this light [106], and then transfers the Si3 stability to the Al^+ and Yb clock wavelengths. All optical clocks can probe for extended periods of time with a common oscillator. We have checked loopback measurement to determine the frequency stability of this process as well as verifying any frequency offsets. Si3 light is free-running, and each clock reports their offset from the Si3 light after correcting for each systematic shift. After a few trial runs observing stability and working out comparison kinks, we decided to devote a few months in early 2025 to periodic ratio measurements between the three

clocks.

Our nominal operation conditions mirror the parameters described in Ch. 7. We use a shallow near magic wavelength lattice near the magic depth of 10 E_r, the least magnetically sensitive clock transition, and a single band readout sequence. We typically use 3×10^4 atoms loaded with a 400 °C oven, a 0.5 G bias field, and a spectroscopy time of $1.0 - 1.3$ s. In summer 2024, we reevaluated a number of systematics to ensure the corrections were reliable. This included a lattice light shift evaluation documented in Ch. 5 and a DC stark shift measurement reported in Tab. 7.6. In-vacuum temperatures were measured before and after each comparison run.

Starting in January, 2025, we ran a total of thirteen comparison days, with Al^+ joining for nine days. To test the robustness of each clock's uncertainty evaluation, each clock operated under different conditions. As documented in Appendix B, Sr1 tested different operational conditions for four days, including the bias field, spectroscopy time, lattice depth, oven temperature, and environment temperature. In Fig. 8.10, we plot the total shifts applied to the Sr clock frequency correction over this data set. The narrow range of points, highlighted in blue on the left and plotted with a smaller range on the right, indicate our nominal operational correction. The outliers are from operating with a different bias field and environment temperature. The blue error bars are the total systematic uncertainty. Less the redshift, our standard operational uncertainty is $< 10^{-18}$. These results are preliminary and may change before the final ratio is published.

In Fig. 8.11 we plot preliminary results of the 2025 BACON comparison. On the left, we plot an overlapping Allan deviation of the concatenated data sets for all three ratios. On the right we plot the resultant clock ratios as a difference from the previous BACON comparison. The black error bars are the total statistical uncertainty of each measurement day, and the blue error bars contain the systematic uncertainty added in quadrature.

To my knowledge, this is the lowest instability remote frequency ratio measurement ever performed, with the Yb/Sr ratio at $1.1 \times 10^{-16}/\sqrt{\tau/\mathrm{s}}$ and Al^+ ratios at $3 \times 10^{-16}/\sqrt{\tau/\mathrm{s}}$. All ratio stabilities represent a substantial improvement over the 2019 comparison, allowing us to average to the systematic uncertainties of each clock in just a few hours. Al^+ ratios in particular are aided by a

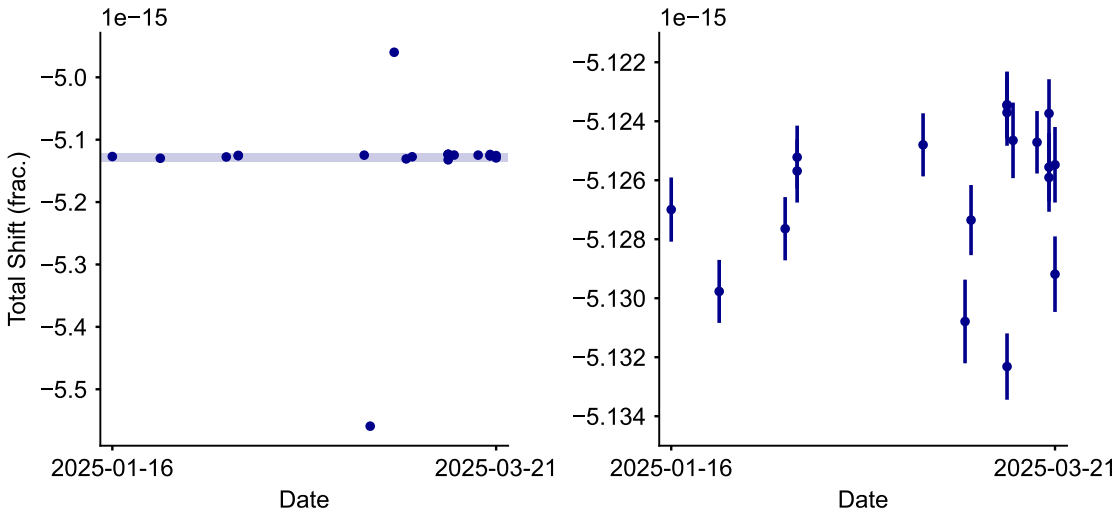

Figure 8.10: Strontium frequency corrections during the 2025 BACON comparison. On the left we show all corrections, and on the right we zoom in on the nominal frequency shift correction, highlighted in light blue on the left. The blue error bars represent the total systematic uncertainty.

reduction in QPN though longer spectroscopy times afforded by the Si3 performance. Flicker appears in the concatenated data set over a few hours, likely due to daily variation as most comparison days are less than five hours in duration and are individually consistent with white noise.

Perhaps the most notable result from this comparison is ratio difference with the previous BACON measurement. The right of Fig. 8.11 shows the ratios in terms of the difference with the previous results. While the final ratio value is not finalized, significant disagreement on all three ratios is apparent. The most notable difference is with the Sr ratios; both ratios disagree with the previous comparison by $\sim 10^{-16}$. It is unclear where this offset originates, and systematic checks have yielded no clues. A 10^{-16} error is consistent with a ~ 1 K temperature error, a ~ 1 m redshift error, or a 70% error on the second order Zeeman coefficient at our operational field. In addition to the two in-vacuum temperature sensors, the dozens of NTCs surrounding the chamber and enclosure all report consistent temperatures. We reduced the system temperature by 2.5 °C and continued to observe the ratio difference. To correct for the gravitational redshift, we measure a height of -7.9 cm with respect to a geodetic marker (S1B60V1) on the north wall of the lab [152], so a meter error would represent roughly a 1000% error. We operate with different bias fields, generating a

4×10^{-16} difference in second order Zeeman shift, yet the ratio offset remains. These systematic modulations are the outliers in the Sr correction presented in Fig. 8.10.

Perhaps an enduring lesson of optical comparisons is their challenge. Disseminating an optical frequency with 10^{-18} accuracy requires each AOM and phase lock to be properly referenced. Spanning multiple wavelengths involves careful use of multiple frequency combs. Finally, operating an atomic clock at 10^{-18} is its own challenge, requiring dividing down a 1 Hz Rabi line by over a factor of 1000. This is difficult even for same-lab same-species comparison, where the technical challenges are significantly reduced. An international clock comparison incorporating Sr clocks built at NPL in England, RIKEN in Japan, and PTB in germany, reports frequency ratios that disagree at the mid 10^{-17} level [61]. At PTB, the transportable Sr clock disagrees with the in-lab clock at 3×10^{-17}. Also measured at PTB, ratios between Sr, Yb^+ and In^+, differ by $\sim 4 \times 10^{-17}$ between 2022 and 2024 [56]. The messy state of optical frequency ratios in 2025 highlights the need for continued precision frequency measurements, with international comparisons as well as transportable clocks [19, 76, 140] key to the success of optical frequency references.

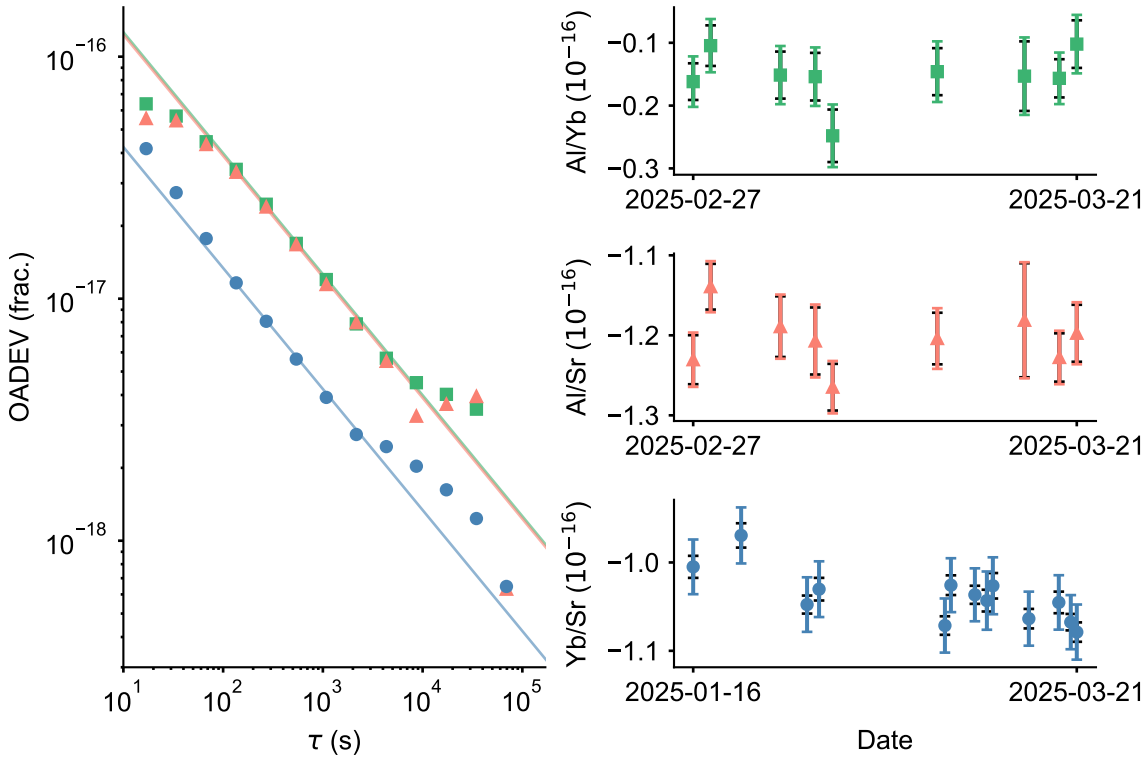

Figure 8.11: Preliminary results of the 2025 BACON comparison. Left: an overlapping Allan deviation of the concatenated frequency ratio measurements. The solid lines are white frequency noise fits to the OADEV between 10^2 and 10^3 s, with the Yb/Sr ratio at $1 \times 10^{-16}/\sqrt{\tau/\mathrm{s}}$ and Al^+ ratios at $3 \times 10^{-16}/\sqrt{\tau/\mathrm{s}}$. Right: ratio measurements of the three species plotted as the difference with the previous comparison [23]. The black error bars are statistical error bars, and the colored error bars are a sum of statistical and systematic uncertainties.

References

[1] A. Aeppli, A. Chu, T. Bothwell, C. J. Kennedy, D. Kedar, P. He, A. M. Rey, and Jun Ye, "Hamiltonian engineering of spin-orbit coupled fermions in a Wannier-Stark optical lattice clock", Science Advances **8**, eadc9242 (2022) (Cited on pp. ii, 9, 10, 68, 71, 73, 78).

[2] A. Aeppli, K. Kim, W. Warfield, M. S. Safronova, and J. Ye, "Clock with 8×10^{-19} systematic uncertainty", Phys. Rev. Lett. **133**, 023401 (2024) (Cited on pp. ii, 9, 26, 113, 122, 130, 131, 148).

[3] T. Akatsuka, K. Hashiguchi, T. Takahashi, N. Ohmae, M. Takamoto, and H. Katori, "Three-stage laser cooling of Sr atoms using the $5s5p\,^3P_2$ metastable state below doppler temperatures", Phys. Rev. A **103**, 023331 (2021) (Cited on p. 13).

[4] D. Allan, "Statistics of atomic frequency standards", Proceedings of the IEEE **54**, 221 (1966) (Cited on p. 5).

[5] B. X. R. Alves, Y. Foucault, G. Vallet, and J. Lodewyck, "Background gas collision frequency shift on lattice-trapped strontium atoms", in 2019 joint conference of the ieee international frequency control symposium and european frequency and time forum (eftf/ifc) (2019) (Cited on p. 137).

[6] K. J. Arnold and M. D. Barrett, "Suppression of clock shifts at magnetic-field-insensitive transitions", Phys. Rev. Lett. **117**, 160802 (2016) (Cited on p. 8).

[7] Y. Balland, L. Absil, and F. Pereira Dos Santos, "Quectonewton local force sensor", Phys. Rev. Lett. **133**, 113403 (2024) (Cited on pp. 163, 165).

[8] D. S. Barker, B. P. Acharya, J. A. Fedchak, N. N. Klimov, E. B. Norrgard, J. Scherschligt, E. Tiesinga, and S. P. Eckel, "Precise quantum measurement of vacuum with cold atoms", Review of Scientific Instruments **93**, 121101 (2022) (Cited on p. 139).

[9] J. P. Bartolotta, M. A. Norcia, J. R. K. Cline, J. K. Thompson, and M. J. Holland, "Laser cooling by sawtooth-wave adiabatic passage", Phys. Rev. A **98**, 023404 (2018) (Cited on p. 15).

[10] Q. Beaufils, G. Tackmann, X. Wang, B. Pelle, S. Pelisson, P. Wolf, and F. P. dos Santos, "Laser Controlled Tunneling in a Vertical Optical Lattice", Physical Review Letters **106**, 213002 (2011) (Cited on pp. 162, 166).

[11] K. Beloy, N. Hinkley, N. B. Phillips, J. A. Sherman, M. Schioppo, J. Lehman, A. Feldman, L. M. Hanssen, C. W. Oates, and A. D. Ludlow, "Atomic clock with 1×10^{-18} room-temperature blackbody stark uncertainty", Phys. Rev. Lett. **113**, 260801 (2014) (Cited on pp. 18, 107, 123).

[12] K. Beloy, W. F. McGrew, X. Zhang, D. Nicolodi, R. J. Fasano, Y. S. Hassan, R. C. Brown, and A. D. Ludlow, "Modeling motional energy spectra and lattice light shifts in optical lattice clocks", Physical Review A **101**, 053416 (2020) (Cited on p. 86).

[13] K. Beloy, J. A. Sherman, N. D. Lemke, N. Hinkley, C. W. Oates, and A. D. Ludlow, "Determination of the $5d6s\ ^3D_1$ state lifetime and blackbody-radiation clock shift in Yb", Phys. Rev. A **86**, 051404 (2012) (Cited on pp. 108, 109, 113, 117, 123).

[14] M. Bishof, X. Zhang, M. J. Martin, and J. Ye, "Optical spectrum analyzer with quantum-limited noise floor", Phys. Rev. Lett. **111**, 093604 (2013) (Cited on p. 25).

[15] S. Blatt, J. W. Thomsen, G. K. Campbell, A. D. Ludlow, M. D. Swallows, M. J. Martin, M. M. Boyd, and J. Ye, "Rabi spectroscopy and excitation inhomogeneity in a one-dimensional optical lattice clock", Physical Review A **80**, 052703 (2009) (Cited on pp. 48, 54).

[16] F. Bloch, "Über die Quantenmechanik der Elektronen in Kristallgittern", Zeitschrift für Physik **52**, 555 (1929) (Cited on pp. 37, 39).

[17] R. Bondarescu, A. Schärer, A. Lundgren, G. Hetényi, N. Houlié, P. Jetzer, and M. Bondarescu, "Ground-based optical atomic clocks as a tool to monitor vertical surface motion", Geophysical Journal International **202**, 1770 (2015) (Cited on p. 9).

[18] T. Bothwell, "A Wannier-Stark optical lattice clock with extended coherence times", Available at https://jila.colorado.edu/sites/default/files/2022-05/Bothwell_thesis_2022.pdf, PhD thesis (University of Colorado, Boulder, CO, 2022) (Cited on pp. 12, 16, 139).

[19] T. Bothwell, W. Brand, R. Fasano, T. Akin, J. Whalen, T. Grogan, Y.-J. Chen, M. Pomponio, T. Nakamura, B. Rauf, I. Baldoni, M. Giunta, R. Holzwarth, C. Nelson, A. Hati, F. Quinlan, R. Fox, S. Peil, and A. Ludlow, "Deployment of a transportable yb optical lattice clock", Opt. Lett. **50**, 646 (2025) (Cited on p. 172).

[20] T. Bothwell, B. D. Hunt, J. L. Siegel, Y. S. Hassan, T. Grogan, T. Kobayashi, K. Gibble, S. G. Porsev, M. S. Safronova, R. C. Brown, K. Beloy, and A. D. Ludlow, "Lattice light shift evaluations in a dual-ensemble Yb optical lattice clock", Phys. Rev. Lett. **134**, 033201 (2025) (Cited on pp. 55, 97).

[21] T. Bothwell, D. Kedar, E. Oelker, J. M. Robinson, S. L. Bromley, W. L. Tew, J. Ye, and C. J. Kennedy, "JILA SrI optical lattice clock with uncertainty of 2.0×10^{-18}", Metrologia **56**, 065004 (2019) (Cited on pp. 10, 75, 88, 123, 135, 146, 190).

[22] T. Bothwell, C. J. Kennedy, A. Aeppli, D. Kedar, J. M. Robinson, E. Oelker, A. Staron, and J. Ye, "Resolving the gravitational redshift across a millimetre-scale atomic sample", Nature **602**, 420 (2022) (Cited on pp. ii, 2, 10, 34–36, 74, 141, 150, 151, 155, 165).

[23] Boulder Atomic Clock Optical Network (BACON) Collaboration, "Frequency ratio measurements at 18-digit accuracy using an optical clock network", Nature **591**, 564 (2021) (Cited on pp. 2, 6, 11, 169, 173).

[24] M. M. Boyd, "High precision spectroscopy of strontium in an optical lattice: towards a new standard for frequency and time", Available at https://jila.colorado.edu/~junye/yelabsOLD/pubs/theses/2007/theses_2007_08_martyboyd.pdf, PhD thesis (University of Colorado, Boulder, CO, 2007) (Cited on p. 12).

[25] M. M. Boyd, T. Zelevinsky, A. D. Ludlow, S. Blatt, T. Zanon-Willette, S. M. Foreman, and J. Ye, "Nuclear spin effects in optical lattice clocks", Physical Review A **76**, 022510 (2007) (Cited on pp. 13, 20, 134).

[26] S. M. Brewer, J.-S. Chen, A. M. Hankin, E. R. Clements, C. W. Chou, D. J. Wineland, D. B. Hume, and D. R. Leibrandt, "$^{27}Al^{+}$ quantum-logic clock with a systematic uncertainty below 10^{-18}", Phys. Rev. Lett. **123**, 033201 (2019) (Cited on pp. 9, 146).

[27] S. L. Bromley, S. Kolkowitz, T. Bothwell, D. Kedar, A. Safavi-Naini, M. L. Wall, C. Salomon, A. M. Rey, and J. Ye, "Dynamics of interacting fermions under spin–orbit coupling in an optical lattice clock", Nature Physics **14**, 399 (2018) (Cited on pp. 37, 68).

[28] R. C. Brown, N. B. Phillips, K. Beloy, W. F. McGrew, M. Schioppo, R. J. Fasano, G. Milani, X. Zhang, N. Hinkley, H. Leopardi, T. H. Yoon, D. Nicolodi, T. M. Fortier, and A. D. Ludlow, "Hyperpolarizability and operational magic wavelength in an optical lattice clock", Phys. Rev. Lett. **119**, 253001 (2017) (Cited on pp. 83, 104).

[29] G. K. Campbell, M. M. Boyd, J. W. Thomsen, M. J. Martin, S. Blatt, M. D. Swallows, T. L. Nicholson, T. Fortier, C. W. Oates, S. A. Diddams, N. D. Lemke, P. Naidon, P. Julienne, J. Ye, and A. D. Ludlow, "Probing interactions between ultracold fermions", Science **324**, 360 (2009) (Cited on p. 68).

[30] A. Cao, W. J. Eckner, T. Lukin Yelin, A. W. Young, S. Jandura, L. Yan, K. Kim, G. Pupillo, J. Ye, N. Darkwah Oppong, and A. M. Kaufman, "Multi-qubit gates and Schrödinger cat states in an optical clock", Nature **634**, 315 (2024) (Cited on pp. 9, 150).

[31] J. Cao, X. Lu, B. Lu, and H. Chang, *SI-traceable temperature calibration based on optical lattice clocks*, 2025 (Cited on p. 122).

[32] A. Chu, J. Will, J. Arlt, C. Klempt, and A. M. Rey, "Simulation of xxz spin models using sideband transitions in trapped bosonic gases", Phys. Rev. Lett. **125**, 240504 (2020) (Cited on p. 78).

[33] E. R. Clements, M. E. Kim, K. Cui, A. M. Hankin, S. M. Brewer, J. Valencia, J.-S. Chen, C.-W. Chou, D. R. Leibrandt, and D. B. Hume, "Lifetime-limited interrogation of two independent $^{27}Al^{+}$ clocks using correlation spectroscopy", Phys. Rev. Lett. **125**, 243602 (2020) (Cited on p. 147).

[34] B. J. Dalton, "Theory of cascade effects on quantum beats", Journal of Physics B: Atomic and Molecular Physics **12**, 2625 (1979) (Cited on pp. 110, 111).

[35] H. G. Dehmelt, "Mono-ion oscillator for ultimate resolution laser spectroscopy", in Laser spectroscopy v, edited by A. R. W. McKellar, T. Oka, and B. P. Stoicheff (1981), pp. 353–359 (Cited on pp. 8, 52).

[36] U. Design, *Mppl - linear guided motion*, See https://www.uhvdesign.com/products/push-pull-devices/magnetically-coupled-devices/mppl-linear-guided-motion/ (Cited on p. 123).

[37] F. Di Pumpo, C. Ufrecht, A. Friedrich, E. Giese, W. P. Schleich, and W. G. Unruh, "Gravitational redshift tests with atomic clocks and atom interferometers", PRX Quantum **2**, 040333 (2021) (Cited on p. 163).

[38] G. J. Dick, "Local oscillator induced instabilities in trapped ion frequency standards", in Proceedings of the nineteenth annual precise time and time interval (ptti) applications and planning meeting, redondo beach, ca, 1-3 dec 1987, Available at https://archive.org/details/DTIC_ADA502386. (1987) (Cited on p. 25).

[39] S. A. Diddams, T. Udem, J. C. Bergquist, E. A. Curtis, R. E. Drullinger, L. Hollberg, W. M. Itano, W. D. Lee, C. W. Oates, K. R. Vogel, and D. J. Wineland, "An optical clock based on a single trapped $^{199}Hg^{+}$ ion", Science **293**, 825 (2001) (Cited on p. 8).

[40] N. Dimarcq, M. Gertsvolf, G. Mileti, S. Bize, C. W. Oates, E. Peik, D. Calonico, T. Ido, P. Tavella, F. Meynadier, G. Petit, G. Panfilo, J. Bartholomew, P. Defraigne, E. A. Donley, P. O. Hedekvist, I. Sesia, M. Wouters, P. Dubé, F. Fang, F. Levi, J. Lodewyck, H. S. Margolis, D. Newell, S. Slyusarev, S. Weyers, J.-P. Uzan, M. Yasuda, D.-H. Yu, C. Rieck, H. Schnatz, Y. Hanado, M. Fujieda, P.-E. Pottie, J. Hanssen, A. Malimon, and N. Ashby, "Roadmap towards the redefinition of the second", Metrologia **61**, 012001 (2024) (Cited on pp. 8, 169).

[41] S. Dörscher, J. Klose, S. M. Palli, and C. Lisdat, "Experimental determination of the E2-M1 polarizability of the strontium clock transition", Phys. Rev. Res. **5**, L012013 (2023) (Cited on pp. 94, 95).

[42] S. Dörscher, A. Al-Masoudi, M. Bober, R. Schwarz, R. Hobson, U. Sterr, and C. Lisdat, "Dynamical decoupling of laser phase noise in compound atomic clocks", Communications Physics **3**, 185 (2020) (Cited on pp. 9, 147).

[43] R. Fasano, Y. Chen, W. McGrew, W. Brand, R. Fox, and A. Ludlow, "Characterization and Suppression of Background Light Shifts in an Optical Lattice Clock", Physical Review Applied **15**, 044016 (2021) (Cited on p. 90).

[44] R. Finkelstein, R. B.-S. Tsai, X. Sun, P. Scholl, S. Direkci, T. Gefen, J. Choi, A. L. Shaw, and M. Endres, "Universal quantum operations and ancilla-based read-out for tweezer clocks", Nature **634**, 321 (2024) (Cited on p. 9).

[45] J. Flury, "Relativistic geodesy", Journal of Physics: Conference Series **723**, 012051 (2016) (Cited on p. 163).

[46] K. Gibble, "Scattering of cold-atom coherences by hot atoms: frequency shifts from background-gas collisions", Phys. Rev. Lett. **110**, 180802 (2013) (Cited on p. 137).

[47] K. Gibble, "Comment on 'first accuracy evaluation of nist-f2'", Metrologia **52**, 163 (2015) (Cited on p. 6).

[48] M. Glück, A. R. Kolovsky, and H. J. Korsch, "Resonant tunnelling of Wannier-Stark states", Journal of Optics B: Quantum and Semiclassical Optics **2**, 694 (2000) (Cited on p. 46).

[49] M. Glück, A. R. Kolovsky, and H. J. Korsch, "Wannier–Stark resonances in optical and semiconductor superlattices", Physics Reports **366**, 103 (2002) (Cited on p. 44).

[50] A. V. Gorshkov, M. Hermele, V. Gurarie, C. Xu, P. S. Julienne, J. Ye, P. Zoller, E. Demler, M. D. Lukin, and A. M. Rey, "Two-orbital SU(N) magnetism with ultracold alkaline-earth atoms", Nature Physics **6**, 289 (2010) (Cited on pp. 9, 68).

[51] J. Grotti, I. Nosske, S. Koller, S. Herbers, H. Denker, L. Timmen, G. Vishnyakova, G. Grosche, T. Waterholter, A. Kuhl, S. Koke, E. Benkler, M. Giunta, L. Maisenbacher, A. Matveev, S. Dörscher, R. Schwarz, A. Al-Masoudi, T. Hänsch, T. Udem, R. Holzwarth, and C. Lisdat, "Long-distance chronometric leveling with a portable optical clock", Phys. Rev. Appl. **21**, L061001 (2024) (Cited on p. 161).

[52] "Guide to secondary thermometry: industrial platinum resistance thermometers", Bureau International des Poids et Mesures (2021) (Cited on p. 123).

[53] S. E. Hamann, D. L. Haycock, G. Klose, P. H. Pax, I. H. Deutsch, and P. S. Jessen, "Resolved-Sideband Raman cooling to the ground state of an optical lattice", Phys. Rev. Lett. **80**, 4149 (1998) (Cited on p. 53).

[54] Y. S. Hassan, K. Beloy, J. L. Siegel, T. Kobayashi, E. Swiler, T. Grogan, R. C. Brown, T. Rojo, T. Bothwell, B. D. Hunt, A. Halaoui, and A. D. Ludlow, *Cryogenic optical lattice clock with* 1.7×10^{-20} *blackbody radiation Stark uncertainty*, 2025 (Cited on p. 147).

[55] Y. S. Hassan, T. Kobayashi, T. Bothwell, J. L. Seigel, B. D. Hunt, K. Beloy, K. Gibble, T. Grogan, and A. D. Ludlow, "Ratchet loading and multi-ensemble operation in an optical lattice clock", Quantum Science and Technology **9**, 045023 (2024) (Cited on p. 133).

[56] H. N. Hausser, J. Keller, T. Nordmann, N. M. Bhatt, J. Kiethe, H. Liu, I. M. Richter, M. von Boehn, J. Rahm, S. Weyers, E. Benkler, B. Lipphardt, S. Dörscher, K. Stahl, J. Klose, C. Lisdat, M. Filzinger, N. Huntemann, E. Peik, and T. E. Mehlstäubler, "$^{115}In^{+}$-$^{172}Yb^{+}$ coulomb crystal clock with 2.5×10^{-18} systematic uncertainty", Phys. Rev. Lett. **134**, 023201 (2025) (Cited on p. 172).

[57] A. Heinz, A. J. Park, N. Šantić, J. Trautmann, S. G. Porsev, M. S. Safronova, I. Bloch, and S. Blatt, "State-dependent optical lattices for the strontium optical qubit", Physical Review Letters **124**, 203201 (2020) (Cited on pp. 12, 122).

[58] M.-S. Heo, H. Kim, D.-H. Yu, W.-K. Lee, and C. Y. Park, "Evaluation of the blackbody radiation shift of an Yb optical lattice clock at KRISS", Metrologia **59**, 055002 (2022) (Cited on p. 123).

[59] R. B. Hutson, A. Goban, G. E. Marti, L. Sonderhouse, C. Sanner, and J. Ye, "Engineering quantum states of matter for atomic clocks in shallow optical lattices", Phys. Rev. Lett. **123**, 123401 (2019) (Cited on p. 160).

[60] T. Ido, H. Ito, H. Hachisu, N. Nemitz, N. Ohtsubo, Y. Miyauchi, M. Morikawa, M. Tønnes, and K. Matsubara, "Incorporation of hydrogen masers into a free ensemble timescale aimed for optically steered UTC(k)", Journal of Physics: Conference Series **2889**, 012023 (2024) (Cited on p. 4).

[61] International Clock and Oscillator Networking and Collaboration, A. Amy-Klein, E. Benkler, P. Blondé, K. Bongs, E. Cantin, C. Chardonnet, H. Denker, S. Dörscher, C.-H. Feng, J.-O. Gaudron, P. Gill, I. R. Hill, W. Huang, M. Y. H. Johnson, Y. B. Kale, H. Katori, J. Klose, J. Kronjäger, A. Kuhl, R. L. Targat, C. Lisdat, O. Lopez, T. Lücke, M. Mazouth, S. Mukherjee, I. Nosske, B. Pointard, P.-E. Pottie, M. Schioppo, Y. Singh, K. Stahl, M. Takamoto, M. Tønnes, J. Tunesi, I. Ushijima, and C. Vishwakarma, *International comparison of optical frequencies with transportable optical lattice clocks*, 2024 (Cited on p. 172).

[62] W. M. Itano, J. C. Bergquist, J. J. Bollinger, J. M. Gilligan, D. J. Heinzen, F. L. Moore, M. G. Raizen, and D. J. Wineland, "Quantum projection noise: population fluctuations in two-level systems", Phys. Rev. A **47**, 3554 (1993) (Cited on pp. 26, 150).

[63] P. S. Jessen, C. Gerz, P. D. Lett, W. D. Phillips, S. L. Rolston, R. J. C. Spreeuw, and C. I. Westbrook, "Observation of quantized motion of Rb atoms in an optical field", Phys. Rev. Lett. **69**, 49 (1992) (Cited on p. 37).

[64] Z.-P. Jia, X.-Y. Cui, Y.-J. Xie, X. Zhang, G.-Z. Niu, X.-Y. Liu, Q.-Q. Zhu, J. Li, and H.-N. Dai, "Suppressing background spectra of lattice lasers in strontium optical clocks", Phys. Rev. Appl. **23**, 014014 (2025) (Cited on p. 90).

[65] M. Kasevich and S. Chu, "Measurement of the gravitational acceleration of an atom with a light-pulse atom interferometer", Applied Physics B **54**, 321 (1992) (Cited on p. 159).

[66] H. Katori, T. Ido, Y. Isoya, and M. Kuwata-Gonokami, "Magneto-optical trapping and cooling of strontium atoms down to the photon recoil temperature", Phys. Rev. Lett. **82**, 1116 (1999) (Cited on pp. 12, 15).

[67] H. Katori, V. D. Ovsiannikov, S. I. Marmo, and V. G. Palchikov, "Strategies for reducing the light shift in atomic clocks", Physical Review A **91**, 052503 (2015) (Cited on pp. 85, 86, 95).

[68] D. Kedar, J. Yu, E. Oelker, A. Staron, W. R. Milner, J. M. Robinson, T. Legero, F. Riehle, U. Sterr, and J. Ye, "Frequency stability of cryogenic silicon cavities with semiconductor crystalline coatings", Optica **10**, 464 (2023) (Cited on p. 156).

[69] C. J. Kennedy, E. Oelker, J. M. Robinson, T. Bothwell, D. Kedar, W. R. Milner, G. E. Marti, A. Derevianko, and J. Ye, "Precision metrology meets cosmology: improved constraints on ultralight dark matter from atom-cavity frequency comparisons", Phys. Rev. Lett. **125**, 201302 (2020) (Cited on p. 9).

[70] K. Kim, A. Aeppli, T. Bothwell, and J. Ye, "Evaluation of lattice light shift at low 10^{-19} uncertainty for a shallow lattice Sr optical clock", Phys. Rev. Lett. **130**, 113203 (2023) (Cited on pp. ii, 2, 46, 53, 82, 88, 93–95, 103, 105, 122, 168).

[71] K. Kim, A. Aeppli, W. Warfield, A. Chu, A. M. Rey, and J. Ye, *Atomic coherence of 2 minutes and instability of* 1.5×10^{-18} *at 1 s in a Wannier-Stark lattice clock*, 2025 (Cited on pp. 151, 152).

[72] C. Kittel, *Introduction to solid state physics* (John Wiley and Sons, Inc, 2005) (Cited on p. 40).

[73] V. Klüsener, S. Pucher, D. Yankelev, J. Trautmann, F. Spriestersbach, D. Filin, S. G. Porsev, M. S. Safronova, I. Bloch, and S. Blatt, "Long-lived coherence on a μHz scale optical magnetic quadrupole transition", Phys. Rev. Lett. **132**, 253201 (2024) (Cited on p. 12).

[74] S. Kolkowitz, S. L. Bromley, T. Bothwell, M. L. Wall, G. E. Marti, A. P. Koller, X. Zhang, A. M. Rey, and J. Ye, "Spin-orbit-coupled fermions in an optical lattice clock", Nature **542**, arXiv: 1608.03854, 66 (2017) (Cited on pp. 37, 42).

[75] S. Kolkowitz, I. Pikovski, N. Langellier, M. D. Lukin, R. L. Walsworth, and J. Ye, "Gravitational wave detection with optical lattice atomic clocks", Phys. Rev. D **94**, 124043 (2016) (Cited on p. 9).

[76] S. B. Koller, J. Grotti, S. Vogt, A. Al-Masoudi, S. Dörscher, S. Häfner, U. Sterr, and C. Lisdat, "Transportable optical lattice clock with 7×10^{-17} uncertainty", Phys. Rev. Lett. **118**, 073601 (2017) (Cited on p. 172).

[77] D. Lee, B. Lewis, Z. Hu, and J. Ye, In preparation. (2025) (Cited on p. 156).

[78] P. Lemonde, G. Santarelli, P. Laurent, F. Dos Santos, A. Clairon, and C. Salomon, "The sensitivity function: a new tool for the evaluation of frequency shifts in atomic spectroscopy", in Proceedings of the 1998 ieee international frequency control symposium (cat. no.98ch36165) (1998), pp. 110–115 (Cited on p. 25).

[79] P. Lemonde and P. Wolf, "Optical lattice clock with atoms confined in a shallow trap", Physical Review A **72**, 033409 (2005) (Cited on pp. 37, 46, 136).

[80] E. Lindroth and A. Ynnerman, "Ab initio calculations of g_j factors for Li, Be^+, and Ba^+", Phys. Rev. A **47**, 961 (1993) (Cited on p. 95).

[81] C. Lisdat, S. Dörscher, I. Nosske, and U. Sterr, "Blackbody radiation shift in strontium lattice clocks revisited", Phys. Rev. Res. **3**, L042036 (2021) (Cited on pp. 107, 119, 122, 142).

[82] J. Lodewyck, M. Zawada, L. Lorini, M. Gurov, and P. Lemonde, "Observation and cancellation of a perturbing DC Stark shift in strontium optical lattice clocks", IEEE Transactions on Ultrasonics, Ferroelectrics, and Frequency Control **59**, 411 (2012) (Cited on pp. 17, 139).

[83] W. Loh, R. T. Maxson, A. P. Medeiros, G. N. West, P. W. Juodawlkis, and R. P. McConnell, "Optical frequency averaging of light", Opt. Express **31**, 25507 (2023) (Cited on p. 157).

[84] B. Lu, X. Lu, J. Li, and H. Chang, "Theoretical calculation of the quadratic Zeeman shift coefficient of the $^3P_0^o$ clock state for strontium optical lattice clock", Chin. Phys. B **31** (2022) 10.1088/1674-1056/ac29a6 (Cited on p. 135).

[85] X.-T. Lu, F. Guo, Y.-Y. Liu, J.-J. Xia, G.-D. Zhao, Y.-X. Chen, Y.-B. Wang, B.-Q. Lu, and H. Chang, "Determining the lifetime of the $5s5p^3P_0^o$ metastable state in ^{87}Sr from the electric dipole matrix element", Phys. Rev. Appl. **21**, 024042 (2024) (Cited on p. 51).

[86] A. Ludlow, T. Zelevinsky, G. Campbell, S. Blatt, M. Boyd, M. de Miranda, M. Martin, J. Thomsen, S. Foreman, J. Ye, T. Fortier, J. Stalnaker, S. Diddams, Y. L. Coq, Z. Barber, N. Poli, N. Lemke, K. Beck, and C. Oates, "Sr lattice clock at 1×10^{-16} fractional uncertainty by remote optical evaluation with a Ca clock", Science **319**, 1805 (2008) (Cited on p. 169).

[87] A. Ludlow, "The strontium optical lattice clock: optical spectroscopy with sub-hertz accuracy", Available at https://jila.colorado.edu/sites/default/files/2020-11/theses_2008_AndrewLudlow.pdf, PhD thesis (University of Colorado, Boulder, CO, 2008) (Cited on p. 12).

[88] A. D. Ludlow, M. M. Boyd, J. Ye, E. Peik, and P. O. Schmidt, "Optical atomic clocks", Reviews of Modern Physics **87**, 637 (2015) (Cited on p. 12).

[89] A. D. Ludlow, M. M. Boyd, T. Zelevinsky, S. M. Foreman, S. Blatt, M. Notcutt, T. Ido, and J. Ye, "Systematic study of the ^{87}Sr clock transition in an optical lattice", Phys. Rev. Lett. **96**, 033003 (2006) (Cited on p. 169).

[90] K. W. Madison, M. C. Fischer, and M. G. Raizen, "Observation of the Wannier-Stark fan and the fractional ladder in an accelerating optical lattice", Phys. Rev. A **60**, R1767 (1999) (Cited on pp. 37, 45).

[91] H. J. Manetsch, G. Nomura, E. Bataille, K. H. Leung, X. Lv, and M. Endres, *A tweezer array with 6100 highly coherent atomic qubits*, 2024 (Cited on p. 139).

[92] H. S. Margolis, G. Panfilo, G. Petit, C. Oates, T. Ido, and S. Bize, "The CIPM list 'recommended values of standard frequencies': 2021 update", Metrologia **61** (2024) 10.1088/1681-7575/ad3afc (Cited on p. 51).

[93] M. C. Marshall, D. A. R. Castillo, W. J. Arthur-Dworschack, A. Aeppli, K. Kim, D. Lee, W. Warfield, J. Hinrichs, N. V. Nardelli, T. M. Fortier, J. Ye, D. R. Leibrandt, and D. B. Hume, "High-stability single-ion clock with 5.5×10^{-19} systematic uncertainty", Phys. Rev. Lett. **135**, 033201 (2025) (Cited on p. 169).

[94] G. E. Marti, R. B. Hutson, A. Goban, S. L. Campbell, N. Poli, and J. Ye, "Imaging optical frequencies with 100 μHz precision and 1.1 μm resolution", Phys. Rev. Lett. **120**, 103201 (2018) (Cited on pp. 28, 29, 151).

[95] M. J. Martin, M. Bishof, M. D. Swallows, X. Zhang, C. Benko, J. von-Stecher, A. V. Gorshkov, A. M. Rey, and J. Ye, "A quantum many-body spin system in an optical lattice clock", Science **341**, 632 (2013) (Cited on pp. 9, 68, 77).

[96] M. J. Martin, "Quantum metrology and many-body physics: pushing the frontier of the optical lattice clock", Available at https://jila.colorado.edu/bibcite/reference/3282, PhD thesis (University of Colorado, Boulder, CO, 2013) (Cited on p. 23).

[97] D. G. Matei, T. Legero, S. Häfner, C. Grebing, R. Weyrich, W. Zhang, L. Sonderhouse, J. M. Robinson, J. Ye, F. Riehle, and U. Sterr, "1.5 μm Lasers with Sub-10 mHz Linewidth", Physical Review Letters **118**, 263202 (2017) (Cited on p. 23).

[98] W. F. McGrew, X. Zhang, R. J. Fasano, S. A. Schäffer, K. Beloy, D. Nicolodi, R. C. Brown, N. Hinkley, G. Milani, M. Schioppo, T. H. Yoon, and A. D. Ludlow, "Atomic clock performance enabling geodesy below the centimetre level", Nature **564**, 87 (2018) (Cited on p. 9).

[99] K. Mehling, J. J. Burau, L. E. Hillberry, M. Chen, P. Aggarwal, L. Cheng, J. Ye, and S. Scheidegger, *Narrowline laser cooling and spectroscopy of molecules via stark states*, 2025 (Cited on p. 149).

[100] B. Merkel, K. Thirumalai, J. E. Tarlton, V. M. Schäfer, C. J. Ballance, T. P. Harty, and D. M. Lucas, "Magnetic field stabilization system for atomic physics experiments", Review of Scientific Instruments **90**, 044702 (2019) (Cited on p. 133).

[101] T. Middelmann, S. Falke, C. Lisdat, and U. Sterr, "High accuracy correction of blackbody radiation shift in an optical lattice clock", Phys. Rev. Lett. **109**, 263004 (2012) (Cited on p. 122).

[102] W. R. Milner, S. Lannig, M. Mamaev, L. Yan, A. Chu, B. Lewis, M. N. Frankel, R. B. Hutson, A. M. Rey, and J. Ye, "Coherent evolution of superexchange interaction in seconds-long optical clock spectroscopy", Science **388**, 503 (2025) (Cited on p. 9).

[103] W. R. Milner, J. M. Robinson, C. J. Kennedy, T. Bothwell, D. Kedar, D. G. Matei, T. Legero, U. Sterr, F. Riehle, H. Leopardi, T. M. Fortier, J. A. Sherman, J. Levine, J. Yao, J. Ye, and E. Oelker, "Demonstration of a timescale based on a stable optical carrier", Phys. Rev. Lett. **123**, 173201 (2019) (Cited on p. 23).

[104] J. A. Muniz, D. Barberena, R. J. Lewis-Swan, D. J. Young, J. R. K. Cline, A. M. Rey, and J. K. Thompson, "Exploring dynamical phase transitions with cold atoms in an optical cavity", Nature **580**, 602 (2020) (Cited on p. 78).

[105] J. A. Muniz, D. J. Young, J. R. K. Cline, and J. K. Thompson, "Cavity-QED measurements of the ^{87}Sr millihertz optical clock transition and determination of its natural linewidth", Phys. Rev. Res. **3**, 023152 (2021) (Cited on pp. 45, 51).

[106] N. V. Nardelli, H. Leopardi, T. R. Schibli, and T. M. Fortier, "Optical and microwave metrology at the 10^{-18} level with an Er/Yb:glass frequency comb", Laser & Photonics Reviews **17**, 2200650 (2023) (Cited on p. 169).

[107] N. Nemitz, A. A. Jørgensen, R. Yanagimoto, F. Bregolin, and H. Katori, "Modeling light shifts in optical lattice clocks", Phys. Rev. A **99**, 033424 (2019) (Cited on p. 86).

[108] T. L. Nicholson, M. J. Martin, J. R. Williams, B. J. Bloom, M. Bishof, M. D. Swallows, S. L. Campbell, and J. Ye, "Comparison of Two Independent Sr Optical Clocks with 1×10^{-17} Stability at 10^3 s", Physical Review Letters **109**, 230801 (2012) (Cited on pp. 88, 188).

[109] T. Nicholson, S. Campbell, R. Hutson, G. Marti, B. Bloom, R. McNally, W. Zhang, M. Barrett, M. Safronova, G. Strouse, W. Tew, and J. Ye, "Systematic evaluation of an atomic clock at 2×10^{-18} total uncertainty", Nature Communications **6**, 6896 (2015) (Cited on pp. 10, 108, 109, 113, 119, 123, 187).

[110] T. L. Nicholson, "A new record in atomic clock performance", Available at https://jila.colorado.edu/sites/default/files/2019-03/nicholson_thesis.pdf, PhD thesis (University of Colorado, Boulder, CO, 2015) (Cited on pp. 12, 108, 139).

[111] P. Niroula, J. Dolde, X. Zheng, J. Bringewatt, A. Ehrenberg, K. C. Cox, J. Thompson, M. J. Gullans, S. Kolkowitz, and A. V. Gorshkov, "Quantum sensing with erasure qubits", Phys. Rev. Lett. **133**, 080801 (2024) (Cited on p. 153).

[112] Q. Niu, X.-G. Zhao, G. A. Georgakis, and M. G. Raizen, "Atomic landau-zener tunneling and wannier-stark ladders in optical potentials", Phys. Rev. Lett. **76**, 4504 (1996) (Cited on p. 45).

[113] M. A. Norcia, J. R. K. Cline, J. P. Bartolotta, M. J. Holland, and J. K. Thompson, "Narrow-line laser cooling by adiabatic transfer", New J. Phys. **20** (2018) 10.1088/1367-2630/aaa950 (Cited on p. 15).

[114] E. Oelker, R. B. Hutson, C. J. Kennedy, L. Sonderhouse, T. Bothwell, A. Goban, D. Kedar, C. Sanner, J. M. Robinson, G. E. Marti, D. G. Matei, T. Legero, M. Giunta, R. Holzwarth, F. Riehle, U. Sterr, and J. Ye, "Demonstration of 4.8×10^{-17} stability at 1 s for two independent optical clocks", Nature Photonics **13**, 714 (2019) (Cited on pp. 23, 25, 28, 132, 147, 158).

[115] L. Olschewski, "Messung der magnetischen Kerndipolmomente an freien ^{43}Ca-,^{87}Sr-,^{135}Ba-,^{137}Ba-,^{171}Yb- und ^{173}Yb-Atomen mit optischem Pumpen", Zeitschrift für Physik **249**, 205 (1972) (Cited on p. 20).

[116] V. D. Ovsiannikov, S. I. Marmo, V. G. Palchikov, and H. Katori, "Higher-order effects on the precision of clocks of neutral atoms in optical lattices", Physical Review A **93**, 043420 (2016) (Cited on p. 95).

[117] V. D. Ovsiannikov, V. G. Pal'chikov, A. V. Taichenachev, V. I. Yudin, and H. Katori, "Multipole, nonlinear, and anharmonic uncertainties of clocks of Sr atoms in an optical lattice", Physical Review A **88**, 013405 (2013) (Cited on p. 95).

[118] T. Parker, S. Jefferts, and T. Heavner, "Medium-term frequency stability of hydrogen masers as measured by a cesium fountain", in 2010 ieee international frequency control symposium (2010), pp. 318–323 (Cited on p. 4).

[119] E. Pedrozo-Penafiel, S. Colombo, C. Shu, A. F. Adiyatullin, Z. Li, E. Mendez, B. Braverman, A. Kawasaki, D. Akamatsu, Y. Xiao, and V. Vuletić, "Entanglement on an optical atomic-clock transition", Nature **588**, 414 (2020) (Cited on p. 150).

[120] B. Pelle, A. Hilico, G. Tackmann, Q. Beaufils, and F. Pereira dos Santos, "State-labeling wannier-stark atomic interferometers", Phys. Rev. A **87**, 023601 (2013) (Cited on p. 162).

[121] A. Peters, K. Y. Chung, and S. Chu, "High-precision gravity measurements using atom interferometry", Metrologia **38**, 25 (2001) (Cited on p. 160).

[122] S. G. Porsev, M. G. Kozlov, and M. S. Safronova, "Contribution of negative-energy states to multipolar polarizabilities of the Sr optical lattice clock", Phys. Rev. A **108**, L051102 (2023) (Cited on pp. 9, 95).

[123] S. G. Porsev, M. S. Safronova, U. I. Safronova, and M. G. Kozlov, "Multipolar polarizabilities and hyperpolarizabilities in the Sr optical lattice clock", Physical Review Letters **120**, 063204 (2018) (Cited on pp. 9, 94, 95).

[124] D. Reens, H. Wu, A. Aeppli, A. McAuliffe, P. Wcisło, T. Langen, and J. Ye, "Beyond the limits of conventional Stark deceleration", Phys. Rev. Res. **2**, 033095 (2020) (Cited on p. vi).

[125] B. Research and A. Network, Available at https://www.bran.ucar.edu (Cited on p. 169).

[126] F. Riehle, P. Gill, F. Arias, and L. Robertsson, *The cipm list of recommended frequency standard values: guidelines and procedures*, 2018 (Cited on pp. 2, 169).

[127] W. Riley, *Handbook of frequency stability analysis* (National Institute of Standards and Technology, 2008) (Cited on p. 5).

[128] J. M. Robinson, "Enhancing optical clocks with ultrastable lasers and spin-squeezing", Available at https://jila.colorado.edu/sites/default/files/2023-05/Robinson_thesis_Final.pdf, PhD thesis (University of Colorado, Boulder, CO, 2023) (Cited on p. 190).

[129] J. M. Robinson, M. Miklos, Y. M. Tso, C. J. Kennedy, T. Bothwell, D. Kedar, J. K. Thompson, and J. Ye, "Direct comparison of two spin-squeezed optical clock ensembles at the 10^{-17} level", Nature Physics **20**, 208 (2024) (Cited on p. 150).

[130] A. Roura, "Gravitational redshift in quantum-clock interferometry", Phys. Rev. X **10**, 021014 (2020) (Cited on p. 163).

[131] M. S. Safronova, S. G. Porsev, U. I. Safronova, M. G. Kozlov, and C. W. Clark, "Blackbody-radiation shift in the Sr optical atomic clock", Phys. Rev. A **87**, 012509 (2013) (Cited on pp. 107, 108).

[132] M. S. Safronova, Z. Zuhrianda, U. I. Safronova, and C. W. Clark, "Extracting transition rates from zero-polarizability spectroscopy", Phys. Rev. A **92**, 040501 (2015) (Cited on p. 121).

[133] H. L. Schwartz, T. M. Miller, and B. Bederson, "Measurement of the static electric dipole polarizabilities of barium and strontium", Physical Review A **10**, 1924 (1974) (Cited on p. 122).

[134] C. Shi, J.-L. Robyr, U. Eismann, M. Zawada, L. Lorini, R. Le Targat, and J. Lodewyck, "Polarizabilities of the ^{87}Sr clock transition", Physical Review A **92**, 012516 (2015) (Cited on pp. 97, 98, 100, 112).

[135] D. Sukachev, S. Fedorov, I. Tolstikhina, D. Tregubov, E. Kalganova, G. Vishnyakova, A. Golovizin, N. Kolachevsky, K. Khabarova, and V. Sorokin, "Inner-shell magnetic dipole transition in Tm atoms: a candidate for optical lattice clocks", Phys. Rev. A **94**, 022512 (2016) (Cited on p. 8).

[136] M. D. Swallows, M. Bishof, Y. Lin, S. Blatt, M. J. Martin, A. M. Rey, and J. Ye, "Suppression of collisional shifts in a strongly interacting lattice clock", Science **331**, 1043 (2011) (Cited on p. 68).

[137] M. Takamoto, H. Katori, S. I. Marmo, V. D. Ovsiannikov, and V. G. Pal'chikov, "Prospects for optical clocks with a blue-detuned lattice", Physical Review Letters **102**, 063002 (2009) (Cited on pp. 97, 122).

[138] M. Takamoto, F.-L. Hong, R. Higashi, and H. Katori, "An optical lattice clock", Nature **435**, 321 (2005) (Cited on pp. 12, 82).

[139] M. Takamoto and H. Katori, "Spectroscopy of the $^1S_0 - ^3P_0$ clock transition of ^{87}Sr in an optical lattice", Phys. Rev. Lett. **91**, 223001 (2003) (Cited on p. 14).

[140] M. Takamoto, I. Ushijima, N. Ohmae, T. Yahagi, K. Kokado, H. Shinkai, and H. Katori, "Test of general relativity by a pair of transportable optical lattice clocks", Nature Photonics **14**, 411 (2020) (Cited on pp. 9, 161, 172).

[141] W. L. Tew, T. L. Nicholson, and R. B. Huston, "Calibration of thin-film platinum sensors for use in the JILA Sr II Clock", NIST Technical Report (2015) doi.org/10.6028/NIST.IR.8046 (Cited on pp. 125, 126, 187, 188).

[142] P. Thekkeppatt, Digvijay, A. Urech, F. Schreck, and K. van Druten, *Measurement of the g factor of ground-state ^{87}Sr at the parts-per-million level using co-trapped ultracold atoms*, 2025 (Cited on p. 20).

[143] J. Trautmann, D. Yankelev, V. Klüsener, A. J. Park, I. Bloch, and S. Blatt, "$^1S_0 - {}^3P_2$ magnetic quadrupole transition in neutral strontium", Phys. Rev. Res. **5**, 013219 (2023) (Cited on p. 12).

[144] I. Ushijima, M. Takamoto, M. Das, T. Ohkubo, and H. Katori, "Cryogenic optical lattice clocks", Nature Photonics **9**, 185 (2015) (Cited on pp. 107, 147).

[145] I. Ushijima, M. Takamoto, and H. Katori, "Operational magic intensity for Sr optical lattice clocks", Physical Review Letters **121**, 263202 (2018) (Cited on pp. 88, 91–95, 102, 103, 105).

[146] K. R. Vogel, T. P. Dinneen, A. C. Gallagher, and J. L. Hall, "Experiments with strontium in a vapor cell magneto-optic trap", in Methods for ultrasensitive detection, Vol. 3270, edited by B. L. Fearey (International Society for Optics and Photonics, 1998), pp. 77–84 (Cited on p. 12).

[147] M. L. Wall, A. P. Koller, S. Li, X. Zhang, N. R. Cooper, J. Ye, and A. M. Rey, "Synthetic spin-orbit coupling in an optical lattice clock", Phys. Rev. Lett. **116**, 035301 (2016) (Cited on p. 68).

[148] P. Wcisło, P. Ablewski, K. Beloy, S. Bilicki, M. Bober, R. Brown, R. Fasano, R. Ciuryło, H. Hachisu, T. Ido, J. Lodewyck, A. Ludlow, W. McGrew, P. Morzyński, D. Nicolodi, M. Schioppo, M. Sekido, R. L. Targat, P. Wolf, X. Zhang, B. Zjawin, and M. Zawada, "New bounds on dark matter coupling from a global network of optical atomic clocks", Science Advances **4**, eaau4869 (2018) (Cited on p. 9).

[149] P. Wcisło, H. Wu, D. Reens, A. Aeppli, and J. Ye, "Detection and manipulation of the transverse motion of neutral molecules in a Stark decelerator", Measurement **183**, 109888 (2021) (Cited on p. vi).

[150] C. I. Westbrook, R. N. Watts, C. E. Tanner, S. L. Rolston, W. D. Phillips, P. D. Lett, and P. L. Gould, "Localization of atoms in a three-dimensional standing wave", Phys. Rev. Lett. **65**, 33 (1990) (Cited on p. 37).

[151] P. G. Westergaard, J. Lodewyck, L. Lorini, A. Lecallier, E. A. Burt, M. Zawada, J. Millo, and P. Lemonde, "Lattice-Induced Frequency Shifts in Sr Optical Lattice Clocks at the 10^{-17} Level", Physical Review Letters **106**, 210801 (2011) (Cited on pp. 83, 95).

[152] D. van Westrum, *Geodetic survey of nist and jila clock laboratories*, tech. rep. (National Geodetic Survey, 2019) (Cited on pp. 33, 162–164, 171).

[153] M. Witkowski, S. Bilicki, M. Bober, D. Kovačić, V. Singh, A. Tonoyan, and M. Zawada, "Photoionization cross sections of ultracold ^{88}Sr in $^1P_1$ and $^3S_1$ states at 390 nm and the resulting blue-detuned magic wavelength optical lattice clock constraints", Opt. Express **30**, 21423 (2022) (Cited on pp. 86, 97, 155).

[154] F.-F. Wu, T.-Y. Shi, W.-T. Ni, and L.-Y. Tang, "Contribution of negative-energy states to the $E2 - M1$ polarizability of optical clocks", Phys. Rev. A **108**, L051101 (2023) (Cited on pp. 9, 95).

[155] F.-F. Wu, Y.-B. Tang, T.-Y. Shi, and L.-Y. Tang, "Dynamic multipolar polarizabilities and hyperpolarizabilities of the Sr lattice clock", Physical Review A **100**, 042514 (2019) (Cited on pp. 94, 95).

[156] J. Xia, F. Guo, Y. Zhou, X. Lu, and H. Chang, "Determining the magic wavelength without modulation of the trap depth", Optics **5**, 534 (2024) (Cited on p. 97).

[157] Q. Xu, X. Lu, J. Xia, Y. Wang, and H. Chang, "Measuring the probe Stark shift by frequency modulation spectroscopy in an ^{87}Sr optical lattice clock", Applied Physics Letters **119**, 101105 (2021) (Cited on p. 146).

[158] V. Xu, M. Jaffe, C. D. Panda, S. L. Kristensen, L. W. Clark, and H. Müller, "Probing gravity by holding atoms for 20 seconds", Science **366**, 745 (2019) (Cited on p. 160).

[159] X. Xu, T. H. Loftus, J. L. Hall, A. Gallagher, and J. Ye, "Cooling and trapping of atomic strontium", J. Opt. Soc. Am. B **20**, 968 (2003) (Cited on p. 15).

[160] L. Yan, S. Lannig, W. R. Milner, M. N. Frankel, B. Lewis, D. Lee, K. Kim, and J. Ye, "High-power clock laser spectrally tailored for high-fidelity quantum state engineering", Phys. Rev. X (2025) 10.1103/qw53-8b8r (Cited on p. 25).

[161] M. Yasuda and H. Katori, "Lifetime measurement of the $^3P_2$ metastable state of strontium atoms", Phys. Rev. Lett. **92**, 153004 (2004) (Cited on p. 12).

[162] M. Yasuda, T. Kishimoto, M. Takamoto, and H. Katori, "Photoassociation spectroscopy of Sr 88 : Reconstruction of the wave function near the last node", Physical Review A **73**, 011403 (2006) (Cited on p. 122).

[163] J. Ye, H. J. Kimble, and H. Katori, "Quantum state engineering and precision metrology using state-insensitive light traps", Science **320**, 1734 (2008) (Cited on pp. 12, 82).

[164] J. Ye, J.-L. Peng, R. J. Jones, K. W. Holman, J. L. Hall, D. J. Jones, S. A. Diddams, J. Kitching, S. Bize, J. C. Bergquist, L. W. Hollberg, L. Robertsson, and L.-S. Ma, "Delivery of high-stability optical and microwave frequency standards over an optical fiber network", J. Opt. Soc. Am. B **20**, 1459 (2003) (Cited on p. 169).

[165] M.-J. Yin, X.-T. Lu, T. Li, J.-J. Xia, T. Wang, X.-F. Zhang, and H. Chang, "Floquet engineering Hz-level rabi spectra in shallow optical lattice clock", Phys. Rev. Lett. **128**, 073603 (2022) (Cited on p. 37).

[166] A. W. Young, W. J. Eckner, W. R. Milner, D. Kedar, M. A. Norcia, E. Oelker, N. Schine, J. Ye, and A. M. Kaufman, "Half-minute-scale atomic coherence and high relative stability in a tweezer clock", Nature **588**, 408 (2020) (Cited on p. 151).

[167] C. Zhang, T. Ooi, J. S. Higgins, J. F. Doyle, L. von der Wense, K. Beeks, A. Leitner, G. A. Kazakov, P. Li, P. G. Thirolf, T. Schumm, and J. Ye, "Frequency ratio of the ^{229m}Th nuclear isomeric transition and the ^{87}Sr atomic clock", Nature **633**, 63 (2024) (Cited on p. 149).

[168] X. Zhang, K. Beloy, Y. S. Hassan, W. F. McGrew, C.-C. Chen, J. L. Siegel, T. Grogan, and A. D. Ludlow, "Subrecoil clock-transition laser cooling enabling shallow optical lattice clocks", Phys. Rev. Lett. **129**, 113202 (2022) (Cited on p. 55).

[169] X. Zhang, M. Bishof, S. L. Bromley, C. V. Kraus, M. S. Safronova, P. Zoller, A. M. Rey, and J. Ye, "Spectroscopic observation of SU(N)-symmetric interactions in sr orbital magnetism", Science **345**, 1467 (2014) (Cited on p. 68).

[170] Z. Zhang, T.-W. Hsu, T. Y. Tan, D. H. Slichter, A. M. Kaufman, M. Marinelli, and C. A. Regal, "High optical access cryogenic system for Rydberg atom arrays with a 3000-second trap lifetime", PRX Quantum **6**, 020337 (2025) (Cited on p. 139).

[171] X. Zheng, J. Dolde, and S. Kolkowitz, "Reducing the instability of an optical lattice clock using multiple atomic ensembles", Phys. Rev. X **14**, 011006 (2024) (Cited on p. 9).

Appendix A

Temperature Sensors

As discussed in Ch. 6, we use two thin film platinum resistance thermometers (TFPRTs) to measure the radiant temperature at the center of our chamber. This appendix is dedicated to discussing the culling and calibration of these sensors, serving as a record for the final accuracy evaluation.

To calibrate and cull the TFPRTs, we compare with two NIST calibrated wire wound PRTs. The NIST calibrated sensors are labeled R17 and R18 with NIST IDs 2611 and 2612 respectively and appear with the same NIST IDs and names in the 2015 technical report [141]. The calibration of these sensors was revised in 2020, as handling lead to disagreement with the 2015 calibration. The in-vacuum sensors are Hereaus-Nexensos (now YAGEO-Nexensos) C416 TFPRTs (part no. 32208519). These are nominally 100 Ω thermometers which consist of a small platinum trace on a ceramic substrate, soldered leads, and a strain relief feature covering these solder points. While the strain relief appears to be some sort of plastic or epoxy, it has not significantly affected vacuum performance. To these sensor leads, two wires each are soldered for a four point resistance measurement. The sensor is then slid into a alumina double bore tube and the leads are glued after the solder joint using Epotek 353ND vacuum compatible epoxy. This alumina tube acts as a robust mounting structure, allowing us to compare in the dry block and affix to the in-vacuum translation arm.

To switch between different resistors, we use a relay circuit designed and built by JILA electronics legend Terry Brown, the same relay system used in [109]. The current source is a Keithley 6220 with the operating range set to twice the desired current. The 100 Ω reference resistor is a

Fluke 742A-100. Over the course of this calibration campaign, we use two different voltmeters. For the measurements presented in A.2, we used a higher noise Keithley 2001 multimeter. The voltage measurements used for calibration in A.3 and for in-vacuum measurement are made with a Keithley 2182A nanovoltmeter. The noise of the voltmeter is modified by the number of 60 Hz line power cycles (NPLCs) the device averages over. In A.2 we use NPLC = 10, and in A.3 and for in-vacuum measurement we use NPLC = 5.

An image of the calibration setup is shown in Fig. A.1. NIST calibrated R17 and R18 are mounted closely in a copper block with an additional 0.19 in diameter hole placed between. To calibrate the TFPRTs, we insert alumina tube with the mounted sensors into this hole and compare them with R17 and R18. The copper block is placed within an aluminum enclosure, with the temperature of this aluminum enclosure controlled by a thermoelectric cooler (TEC) that is servoed to a 35k NTC sensor. This enclosure is placed within a larger plastic housing that has a liquid cooled base plate and circulating fan with a liquid-to-air heat exchanger. These elements are stabilized to within 100 mK of a setpoint by actuating on the liquid temperature.

A.1 NIST Calibrated Sensors

In January 2020, Weston Tew at NIST Maryland calibrated three wire wound PRTs. Two of these PRTs, R17 and R18 (2611 and 2612), had previously been calibrated for the 2015 Sr2 accuracy evaluation [108, 141]. Likely due to handling over the years, the recent calibration differs significantly from the previous one. For each sensor, this calibration includes two fixed point realizations at the water triple point as well as four temperature comparisons against NIST sensors in a water bath. There are two temperature sensors located in the water bath-we take half the difference as the water bath temperature uncertainty. For the triple point, we use a standard uncertainty of 0.1 mK. The January 2020 calibration data is shown in tables A.1 and A.2. The data has been processed to remove self heating and calculate the relevant uncertainties.

Using this data, we fit eq. 6.7 centering at 22 °C. This modifies the uncertainty such that the calibration uncertainty is minimized at 22 °C. The data is fit using an orthogonal distance regression

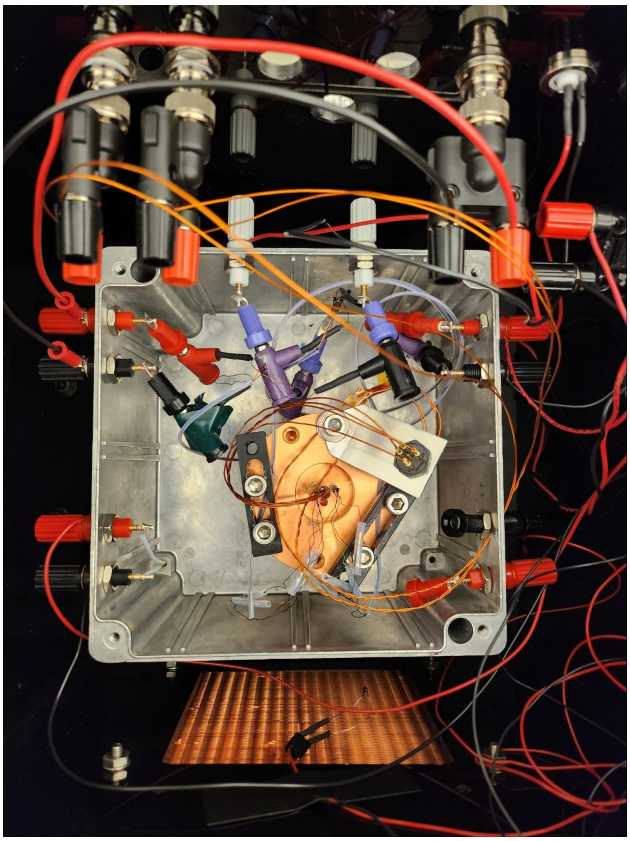

Figure A.1: A top-down view of the calibration setup. The circular copper block contains reference sensors R17 and R18 as well as the TFPRT A3, inserted in the center. The copper block is placed within an aluminum box, shown here with the top removed. This box sits on a TEC and is rigidly connected to a black breadboard on the bottom and is surrounded on the other five sides by an plastic enclosure. The breadboard is mounted on a liquid stabilized coldplate, with the in-loop temperature sensors affixed to the breadboard. A copper liquid to air heat exchanger stabilizes the temperature within the external enclosure. The in-loop sensor is visible near this heat exchanger.

T (°C)	δT (°C)	R @ $I = 0$mA (Ω)	δR (Ω)
9.9995	0.00090	103.95915	0.00066
20.00445	0.00075	107.92776	0.00021
25.00205	0.00035	109.90628	0.00020
29.997	0.00050	111.88039	0.00049
0.01	0.0001	99.98345	0.00012
0.01	0.0001	99.98364	0.00010

Table A.1: R17 (NIST ID 2611) January 2020 calibration data.

T (°C)	δT (°C)	R @ $I = 0$mA (Ω)	δR (Ω)
9.9995	0.00090	104.01831	0.00041
20.00445	0.00075	107.98761	0.00015
25.00205	0.00035	109.96621	0.00028
29.997	0.00050	111.94061	0.00027
0.01	0.0001	100.04221	0.00011
0.01	0.0001	100.042279	0.00012

Table A.2: R18 (NIST ID 2612) January 2020 calibration data.

Sensor	$R_{22°C}$ (Ω)	$\delta R_{22°C}$ ($m\Omega$)	a (°C)$^{-1}$	δa (°C)$^{-1}$	b (°C)$^{-2}$	δb (°C)$^{-2}$
R17	108.71824	0.194	0.0036415	3.5×10^{-7}	-5.485×10^{-7}	0.1817×10^{-7}
R18	108.77811	0.114	0.0036399	1.5×10^{-7}	-5.548×10^{-7}	0.0815×10^{-7}

Table A.3: R17 and R18 calibration centered at 22 °C.

(ODR) routine in order to account for uncertainties in both temperature and resistance. The results of these fits are shown in Fig. A.2 and table A.3. There is good agreement with all measured points, and this calibration will allow us to measure temperatures with ~ 1 mK uncertainties.

A.2 Culling

To operate at UHV, we need to bake the auxiliary chamber with the sensors before installation, so the temperature sensors must be stable over multiple baking cycles. The previous approach in our group was to thermally cycle sensors, measuring the ice point between each thermal cycle. The sensors that demonstrated the most repeatable ice points over these thermal cycles were chosen to be used in vacuum [21, 128]. Here, we utilize a similar approach, however instead of ice points, we compare the resistance difference between a NIST calibrated sensor and the TFPRTs. This has proven to be a reliable technique that avoids the difficulty of generating identical ice point measurements.

In March 2023, 10 thin film PRTs were wired and glued into alumina housings and given

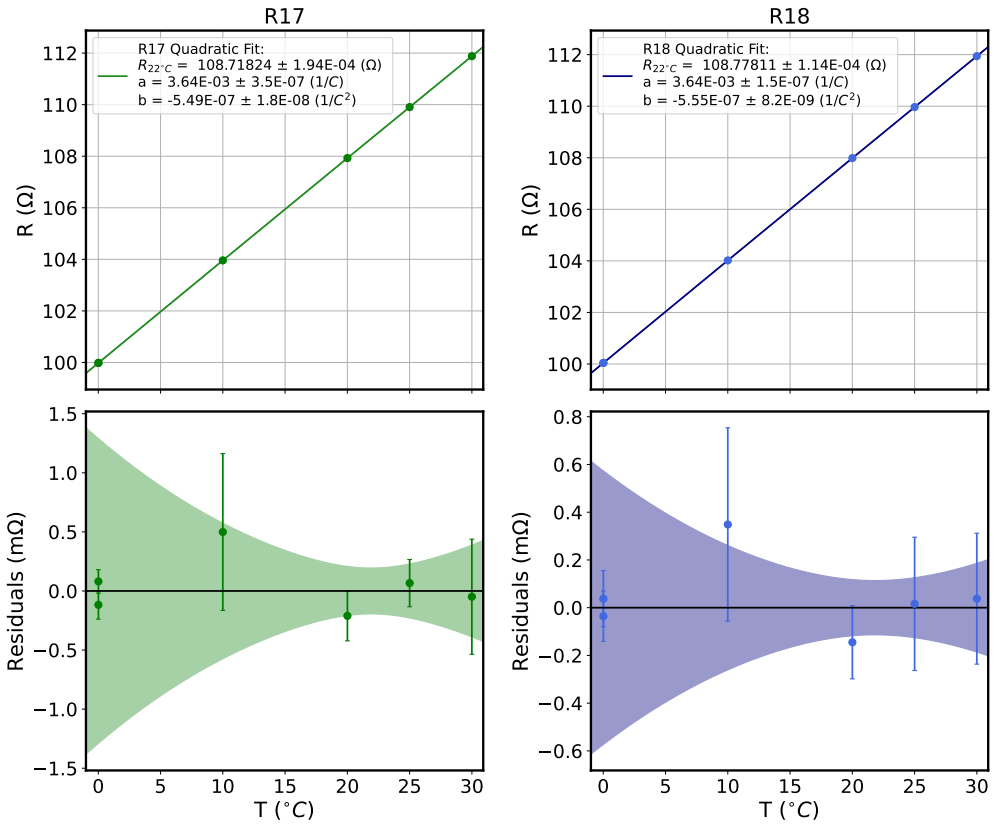

Figure A.2: Thermometer fits for R17 (left, green) and R18 (right, blue). The top panels show the data and the fit. The bottoms panels show the residuals and fit uncertainty in the shaded region. All the data includes errorbars with uncertainty in both resistance and temperature. The center of the fit is chosen to be 22 °C to minimize uncertainty around room temperature

alphanumeric identifiers A1-5 and B1-5. Before any measurements were performed, the sensors were thermally cycled between 200 °C and room temperature 6 times. Sensor A2 was immediately discarded as the sensor leads were sheared off, likely from rough handling or poor soldering. The 9 remaining sensors were thermally cycled between room temperature and 200 °C for a few hours. After each thermal cycle, the sensors were compared with reference sensor R18. Of these 9 remaining sensors, most demonstrated exemplary performance with stability better than 1 mK over 5 additional thermal cycles. Sensors A3 and A5 demonstrate the best stability and were chosen to be calibrated for in vacuum use.

A summary of the thermal cycling results are presented in fig A.3. We plot the measured resistance difference with respect to the first measurement, shown in black, after each thermal cycle.

The shaded region indicates the initial measured resistance statistical uncertainty. Only statistical errors are plotted. Although no sensors have all thermal cycles agree, the systematic uncertainty from thermal transients is liked larger than the statistical uncertainty. This measurement relies on excellent thermal stability of the dry block, which is not easy to achieve as sensors are quickly swapped. For calibration, the sensors remain in the dry block for upwards of one day at each temperature, which has resulted in more reliable temperature measurements. Nevertheless, most sensors agree within 1 mΩ, with the exemplary A3 and A5 agreeing better than 0.3 mΩ when removing a single measurement point. No obvious trends occur with thermal cycling, perhaps due to the initial round of thermal stress.

A.3 Sensor Calibration

We calibrate in vacuum sensors using R17 and R18 in much the same way. The TFPRTs are inserted into the copper block and the resistance is measured at different temperatures. R17 and R18 are measured to determine the temperature of the copper block. Since the TFPRTs and R17,18 are of different construction, self heating is different. To remove this effect, the resistance is measured with 2 currents and extrapolated to zero.

Fig. A.4 shows a representative calibration measurement for a single data point, showing excellent temperature stability over the course of the 45 minute run. We alternate measuring the resistance of a NIST calibrated sensor and the TFPRT, typically for 20 to 60 minutes. The resistance of A3 and R18 is shown in the top plot, the difference in resistance is shown in the center plot, and overlapping Allan deviations of the resistances are plotted in the bottom. In order to achieve good temperature stability and homogeneity across the copper block, we typically wait 24 hours after changing the temperature setpoint to make a measurement. If the temperature has not stabilized, the drift is observable in an Allan deviation of the resistance. We make measurements across a range of temperatures, from 17 °C to 30 °C, changing both the block temperature and the external enclosure temperature.

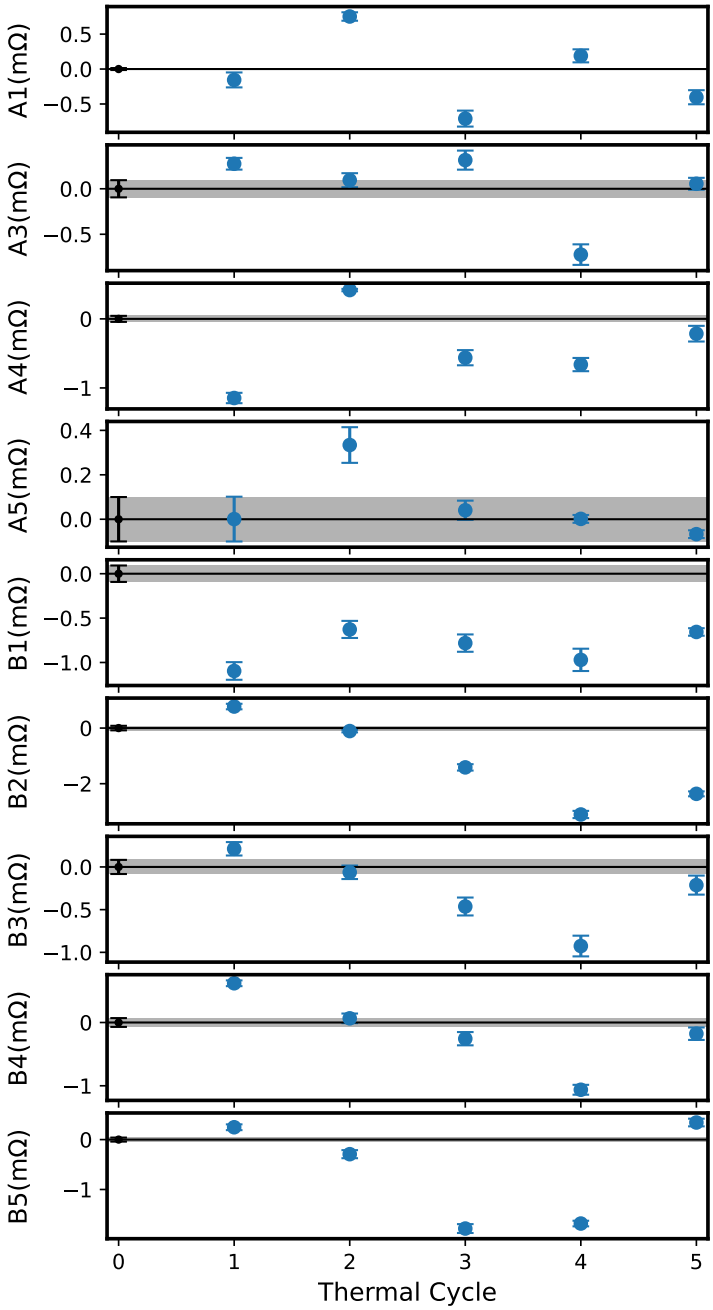

Figure A.3: Results from sensor culling. Nine sensors are compared with reference sensor R18. The resistance difference between these sensors and R18 are shown in mΩ over 5 thermal cycles, with the the initial difference subtracted. The statistical uncertainty of each point is plotted as error bars, with the shaded region indicating the initial uncertainty. Sensors A3 and A5 were chosen to be used in-vacuum.

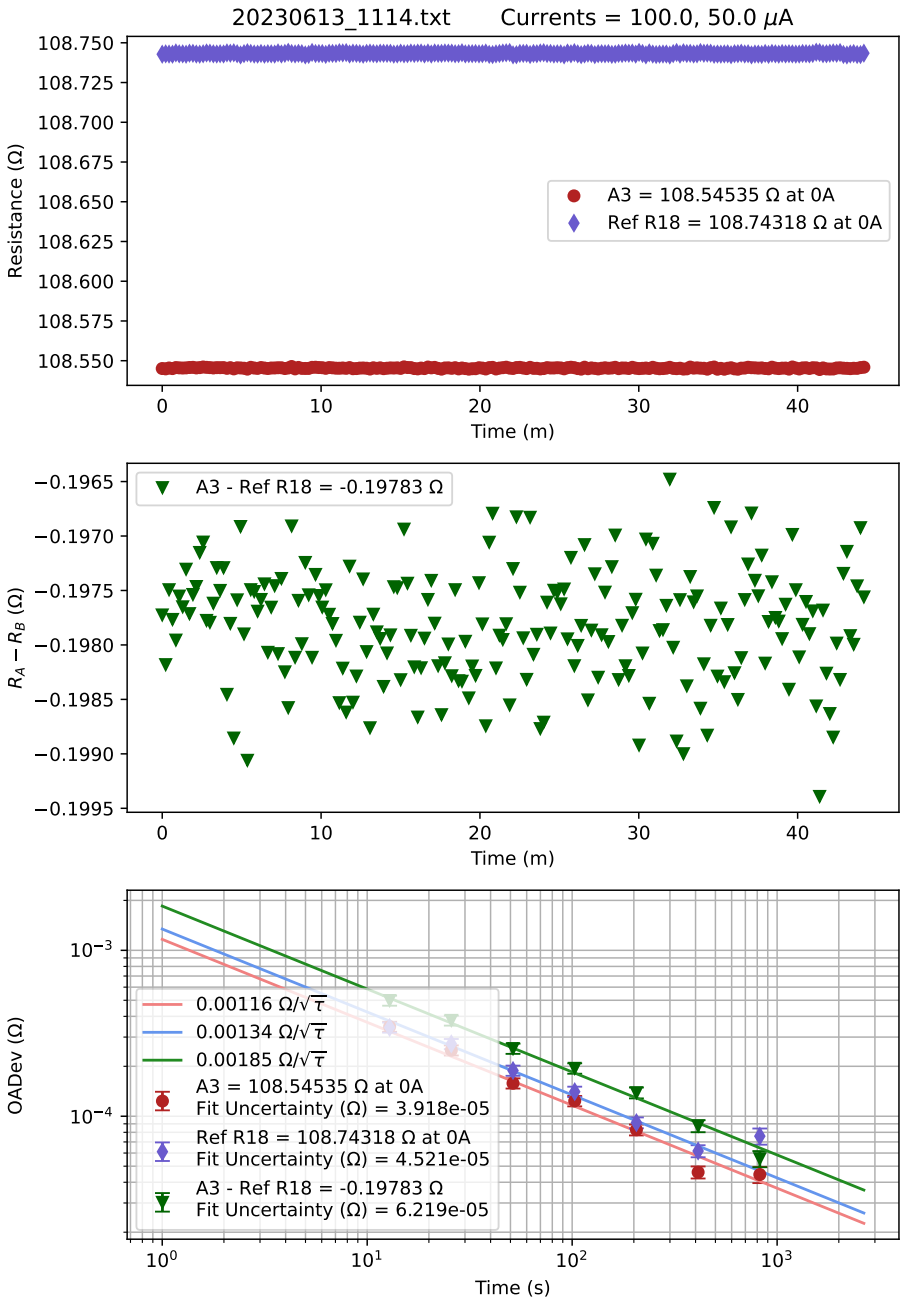

Figure A.4: Representative calibration measurement. Top: over 45 minutes, the resistance of A3 and R18 are measured at two currents, 100 and 50 μA. The resistance plotted is extrapolated to a 0A condition. Middle: the resistance difference between A3 and R18. Bottom: overlapping Allan deviation of the sensor resistances and difference in resistance. The OADev is fit with with a function of the form $\Omega/\sqrt{\tau}$. The fit uncertainty is the calculated using the slope of the OADev fit at 1/3 the averaging time.

A.3.1 Differential Immersion Error

One systematic that arises from temperature measurements with a thermally conductive probe is immersion error. When the thermometer is inserted into the environment, thermal conduction along the wire leads and the mounting structure can lead to errors in temperature measurement. In our calibration system, this is generally common between the reference resistors and the TFPRTs. However, since the leads are not common, there still exists a differential immersion error that could corrupt our calibration.

To determine this effect, we modify the external enclosure while maintaining the temperature of the aluminum box that contains the copper calibration block. The resistance difference between A3 and the reference sensors over a range of enclosure setpoints is plotted in Fig. A.5. We observe a similar linear trend between A3 and both the reference resistors, with a slope of ~ 1.6 mΩ/C. The enclosure setpoint is maintained by temperature servos using 50k NTC commercial bead sensors with a quoted uncertainty of 0.2 °C. During calibration, all temperature setpoints of the aluminum box and the external enclosure are made the same, and we observe a temperature difference between the setpoints and the reference resistors of -100 to 10 mK. The enclosure temperature is always well stabilized, so we simply use an enclosure temperature uncertainty of 0.2 °C due to the NTC uncertainty. Thus the differential immersion error results in a constant 0.32 mΩ resistance uncertainty, which we treat as a correlated error between all temperature measurements. This is listed in final temperature uncertainty Tab. 6.3 as "JILA calibration immersion error," and results in a 1.2 mK uncertainty.

A.3.2 Final Calibration

Three temperature sensors were chosen for calibration, A3, A5, and B1. A3 and A5 eventually were placed in vacuum and are the current sensors used for the BBR correction on Sr1. For each sensor, two calibrations were derived from the two NIST calibrated sensors R17 and R18. The calibration curves are shown in Figs. A.6 and A.7. The final calibration results are listed in Tabs. A.4

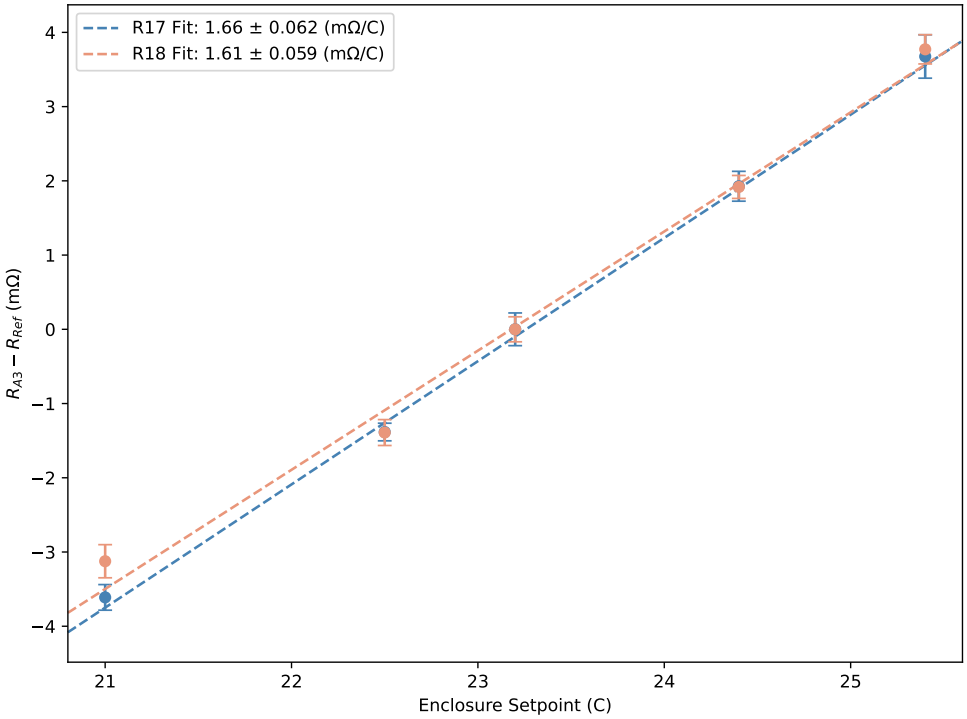

Figure A.5: Differential immersion error. The resistance difference between A3 and the reference resistors as a function of the enclosure setpoint. The interior aluminum box is set to 23 °C and then external enclosure temperature is varied. The resistance difference at 23.3 °C is subtracted to center the plot near zero. The difference is fit with a linear form, shown as dashed lines for R17,18.

and A.5. The resistance uncertainty is from a quadrature sum of immersion error and statistical uncertainty.

A3 and A5 are mounted to the in-vacuum extension arm on Sr1. Measuring the temperature can proceed in much the same way as all the measurements described in this document. Typically, we interleave measurements between A3 and A5. For both sensors we calculate a temperature using both calibrations. We then use the average of all four point, and calculate the statistical and calibration uncertainty through a linear pooling technique. The final temperature uncertainties are documented in Ch. 6.

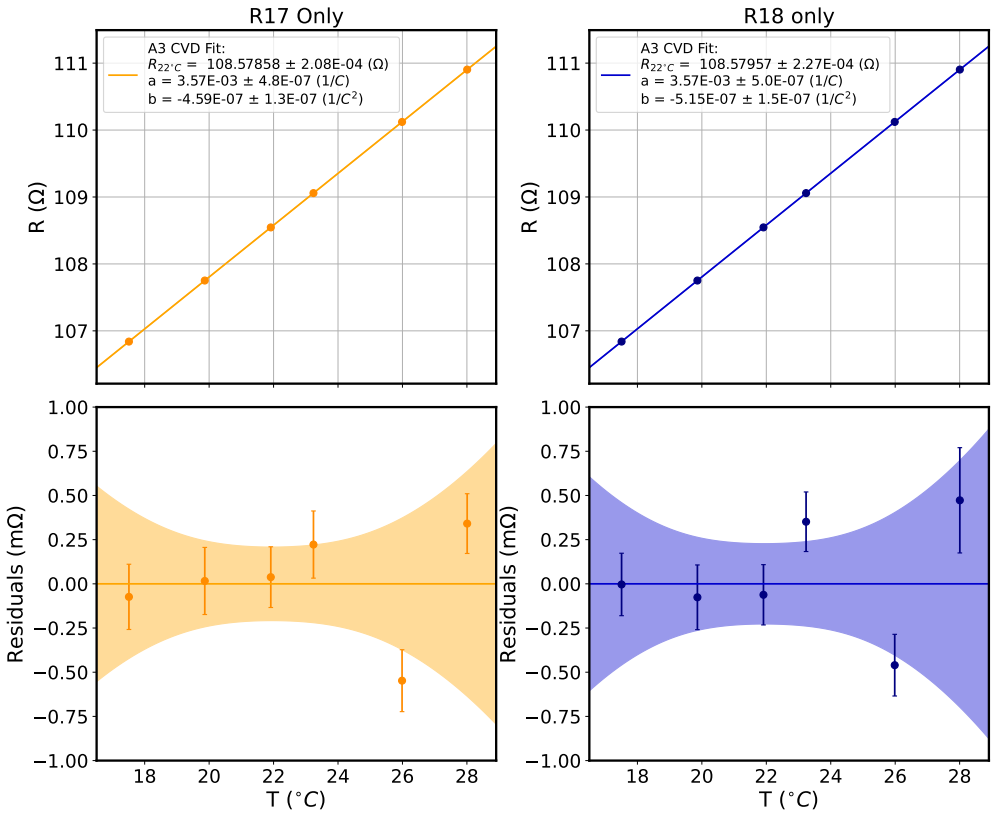

Figure A.6: Thermometer fits for PRT A3, to be used in vacuum. The left column uses the R17 NIST calibrated sensor, and the right column uses R18. The top panels show the data and the fit. The bottoms panels show the residuals and fit uncertainty in the shaded region. All the data includes errorbars with uncertainty in both resistance and temperature. The center of the fit is chosen to be 22 °C to minimize uncertainty around room temperature

A3	$R_{22°C}$ (Ω)	$\delta R_{22°C}$ ($m\Omega$)	a $(°C)^{-1}$	δa $(°C)^{-1}$	b $(°C)^{-2}$	δb $(°C)^{-2}$
R17	108.578581	0.208	0.003566	4.83×10^{-7}	-4.595×10^{-7}	1.3008×10^{-7}
R18	108.57957	0.227	0.003566	4.95×10^{-7}	-5.147×10^{-7}	1.4643×10^{-7}

Table A.4: R17 and R18 calibrations for sensor A3 centered at 22 °C.

A5	$R_{22°C}$ (Ω)	$\delta R_{22°C}$ ($m\Omega$)	a $(°C)^{-1}$	δa $(°C)^{-1}$	b $(°C)^{-2}$	δb $(°C)^{-2}$
R17	108.505334	0.084	0.003564	1.74×10^{-7}	-4.494×10^{-7}	0.345×10^{-7}
R18	108.506250	0.088	0.003564	1.73×10^{-7}	-3.980×10^{-7}	0.338×10^{-7}

Table A.5: R17 and R18 calibrations for sensor A5 centered at 22 °C.

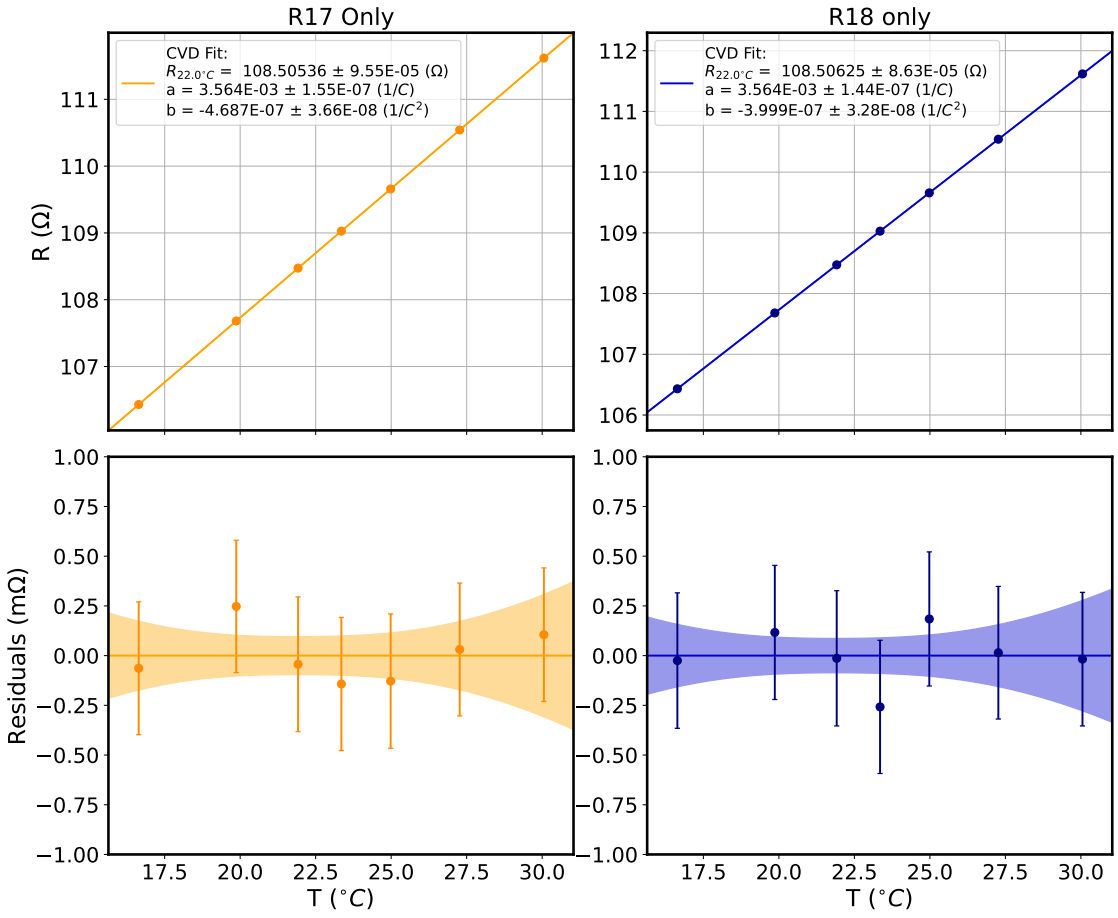

Figure A.7: Thermometer fits for PRT A5, to be used in vacuum. The left column uses the R17 NIST calibrated sensor, and the right column uses R18. The top panels show the data and the fit. The bottoms panels show the residuals and fit uncertainty in the shaded region. All the data includes errorbars with uncertainty in both resistance and temperature. The center of the fit is chosen to be 22 °C to minimize uncertainty around room temperature

Appendix B

Comparison Conditions

Over 13 days between January and March 2025, we compared Sr1 with NIST Al^+ and Yb optical clocks. All clocks operated a majority of the time in a "high accuracy" configuration, and for a few days, each clock modulated systematics to test correction robustness. A comparison schedule is presented in Tab. B, with "nominal" conditions indicating the clock was operating in a standard or near standard configuration. The nominal Sr clock conditions are: $U = 12\ E_r$, 0.5 G bias; 295.3 K environment temperature; 3×10^4 atoms; 400 °C oven temperature; $T_{rabi} = 1.0$ s (some measurements with $T_{rabi} = 1.3$), ground band cooled, single band selected sample near 100 nK; $\nu_{lat} = \nu_{magic} + 9$ MHz; 60 s vacuum lifetime.

In Figs. B.1 and B.2, we plot the measurement and calculated shift for the BBR and second order Zeeman corrections. The environment temperature is typically 22.1 °C, with the temperature record plotted on the top of Fig. B.1. On March 4, 2025 we reduced the system temperature to 19.6 °C, which is apparent as the one temperature outlier on the left plot. The average BBR shift under nominal conditions is near -4.981×10^{-15}, plotted in the bottom of Fig. B.1. The temperature modulation leads to a shift difference of approximately 2×10^{-16}. Since ratios agree $< 4 \times 10^{-18}$, this measurement leads to a direct characterization of the BBR correction to approximately a part in 50.

The second order Zeeman correction is applied in a point by point fashion using the measured splitting between magnetic sublevel clock transitions, Δ_{m_F}. The vector shift is also calculated using this splitting and the cavity parameters measured in Fig. 5.8. The average Δ_{m_F} for each

Table B.1: Schedule of the comparison days during early 2025. March 14 was intended to be a comparison day, but issues on all clocks and combs prevented measurement. March 14 is not included in the ratio, but is reported in the shift plots, Figs. B.1 and B.2.

Day	Sr Condition	Al^+ Condition	Yb Condition
Jan. 16, 2025	Nominal	N/A	Nominal
Jan. 24, 2025	Nominal	N/A	Nominal
Feb. 04, 2025	Nominal	N/A	Nominal
Feb. 06, 2025	Nominal	N/A	Nominal
Feb. 27, 2025	370 °C oven temperature	Nominal	Nominal
Feb. 28, 2025	T_{rabi} = 420 ms, 1 G bias	Nominal	Nominal
Mar. 04, 2025	19.6 °C system temperature	Nominal	Nominal
Mar. 06, 2025	$U = 20\ E_r$	Nominal	Nominal
Mar. 07, 2025	Nominal	Nominal	Nominal
Mar. 13, 2025	Nominal	High Doppler temperature	Nominal
Mar. 14, 2025	Nominal	Comb issue	Comb issue
Mar. 18, 2025	Nominal	Nominal	T_{dead} + 200 ms
Mar. 20, 2025	Nominal	Nominal	High bias
Mar. 21, 2025	Nominal	Nominal	Nominal

comparison clock lock is plotted on the top of Fig. B.2, with the highlighted region indicating the nominal operational field near 0.5 G. On February 28, 2024, we nearly doubled the bias field, which is the outlier point on this plot. The average second order Zeeman shift is plotted on the bottom of Fig. B.2. The ratio measurement on February 28, 2024 is consistent with other days despite generating a 4×10^{-16} shift difference, so we are confident that the second order Zeeman shift is properly corrected.

The lattice light shift corrections are applied globally to each comparison day. Lattice light shift evaluations were completed before the comparison in July 2024 and after the comparison in

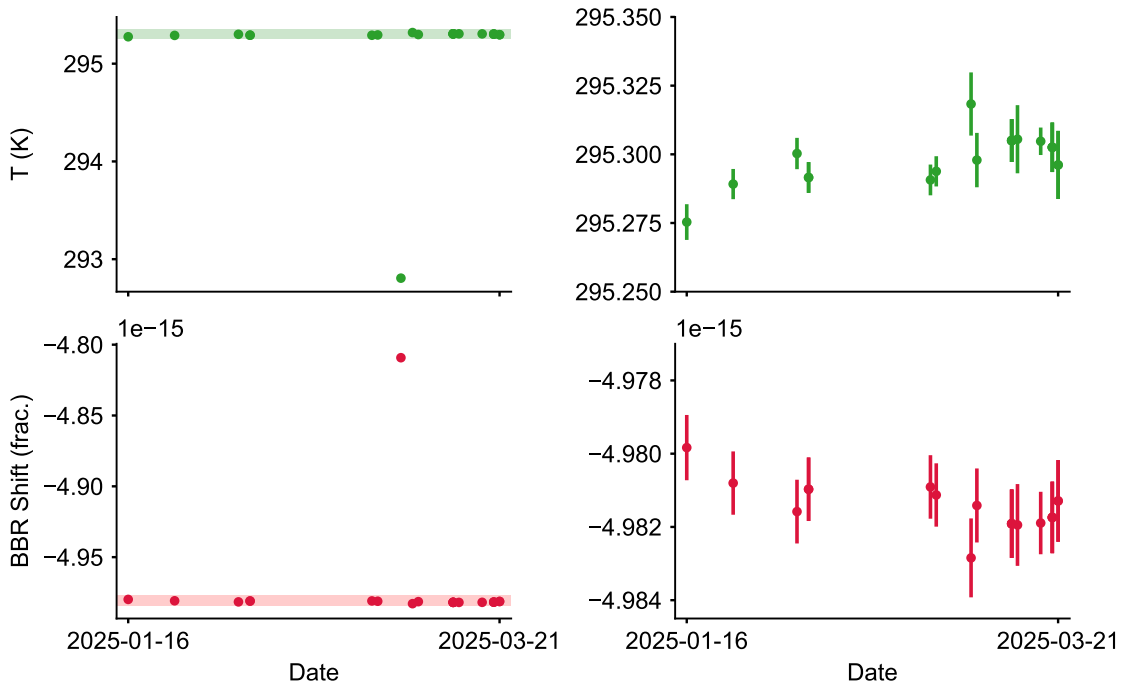

Figure B.1: BBR corrections. Top: the measured radiant temperature at the atom's location, a technique described in Ch. 6. The green shaded area highlight the nominal operation point, and is plotted on the right. Error bars are calculated as described in Ch. 6. Bottom: the BBR shift, with the nominal operation condition highlighted in red and plotted on the right.

May 2025, with the more extensive 2024 evaluation discussed in Ch. 5. Both shift evaluations agree within statistical uncertainty and differ slightly from the 2022 light shift evaluation. For the final comparison light shift correction, we use a combined fit of shift data measured in 2024 and 2025. We fit Eq. 5.5 with all atomic parameters free, leading to typical light shift uncertainties of $< 5 \times 10^{-19}$ during the comparison.

To evaluate the gravitational redshift with respect to the NIST clocks, we determine the atom height from the S1B60 survey markers. We implement a procedure that relies on a number of independent steps including a water leveling trick. We begin by determining the height of the blue MOT with respect to the in-vacuum temperature probe using a camera and known dimensions. We then align a laser level to the probe and project a marker to the 80-20 structure around the table. We fill a plastic tube with water to this marker level, and take the other end to the north wall of the

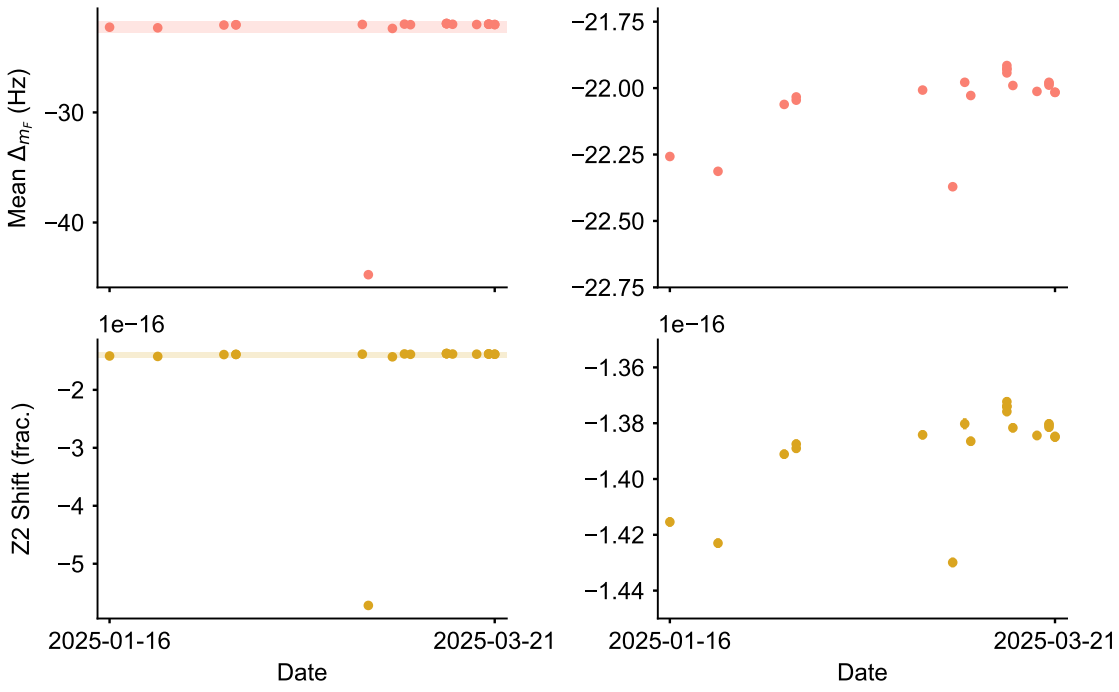

Figure B.2: Second order Zeeman shift. Top: the mean measured between magnetic sublevel transition Δ_{m_F} for each lock. The nominal operation is highlighted and plotted on the right. Bottom: the second order Zeeman shift calculated using Eq. 7.2. This correction is applied in a point by point fashion, so this data represents only the average of each lock.

lab. Finally, we measure the height of the water with respect to the survey marker using a ruler with NIST traceable calibration. With respect to the marker on the north end of the room, S1B60V1, we find an atomic height of -7.86 ± 0.32 cm, corresponding with a redshift of $-(8.56 \pm 0.34) \times 10^{-18}$.